Master's thesis

NTNU
Norwegian University of
Science and Technology
Faculty of Information Technology,
Mathematics and Electrical Engineering
Department of Electric Power Engineering

Thomas Sagvold Haugan

Smart Grid: Shunt Compensation in Non-Sinusoidal Regimes

Trondheim, October 2012

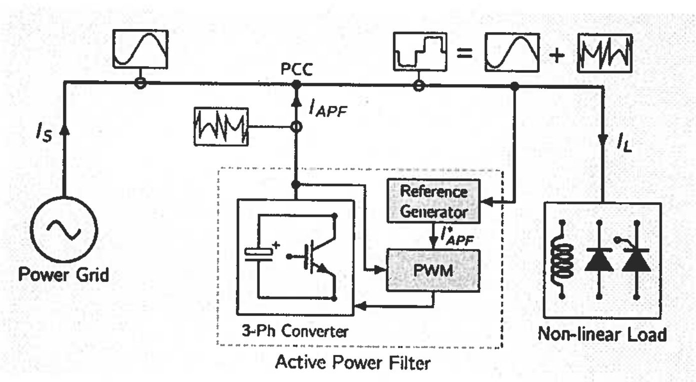

NTNU – Trondheim
Norwegian University of
Science and Technology

NTNU – Trondheim
Norwegian University of Science and Technology

Smart Grid: Shunt Compensation in Non-Sinusoidal Regimes

Thomas Sagvold Haugan

Master of Science in Electric Power Engineering
Submission date: October 2012
Supervisor: Marta Molinas, ELKRAFT

Norwegian University of Science and Technology
Department of Electric Power Engineering

Problem Description

Presently there are well established methods for optimizing operating conditions in electric power system; i.e. shunt compensation of reactive power and current harmonics. Shunt compensation has become more demanding as the operating conditions in the grid tend towards unbalanced and distorted voltages or currents, or sometimes combinations of both. The scientific community has still not come up with a final compensation strategy for non-sinusoidal regimes. This thesis will review properties of the popular *pq*-power theory, and the more recent conservative power theory.

Experimental Part

Attempt to conduct experimental verification of the conservative power theory.

Simulation Part

Extensive comparison between *pq*-theory and the conservative power theory applied in compensation application, both under balanced sinusoidal and unbalanced non-sinusoidal voltage regimes.

Assignment given: Trondheim - 28.03.11
Supervisor: Professor Marta Molinas, Department of Electric Power Engineering

Abstract

The electric power theory is of fundamental importance in most aspects of electric power engineering, enabling to analyze and control the grid based on an unambiguous physical interpretation of the power and current flow. The futuristic *SmartGrid* concept will include scenarios of potentially very challenging network conditions, due to large impact of non-linear loads, combined with unsymmetric and non-sinusoidal voltage regimes. New and more advanced power theories are needed, in order to maintain correct physical understanding of the power grid, independently of voltage conditions. Moreover sophisticated power theories can help identify and eliminate detrimental effects induced by loads; i.e. unsymmetry, reactive power consumption and harmonic pollution. This project has reviewed the recent and promising conservative power theory (*CPT*).

Major part of the project was dedicated to experimental research, evaluating the CPT purely from a power theory perspective. Central part of these experiments was a real-time rapid prototyping system (*RPS*) and three-phase voltage source converter. Control system for the programmable voltage source, data acquisition and CPT-algorithm were implemented by the RPS. Based on extensive tests it was found that the CPT offers enhanced and physical correct interpretation of current and power flow, in all tested voltage conditions. Obtained results from the virtual instrumentation are principally consistent with and support previous research presented in the literature.

Second part evaluated the CPT in context of shunt active power filter (*SAPF*). Experimental implementation of SAPF failed, mainly as the RPS did not provide sufficient sampling rate. Selected cases of reactive and harmonic compensation were demonstrated, utilizing computer modeling tools (*MATLAB/Simulink*). The results conclude that the CPT performs excellent selective compensation, only when grid voltages are balanced sinusoidal. In scenarios of unsymmetric or distorted voltages, the compensation strategies provided by the CPT are apparently less versatile and effective, compared to the popular *pq*-theory. Overall this study demonstrated that optimal network operation can only be achieved, through the joint action of series and parallel compensators. Future work will amongst others include further in-depth study of the rapid prototyping system, and experimental implementation of SAPF.

Keywords: active power filter, conservative power theory, experimental implementation, non-sinusoidal voltage regime, rapid prototyping, smartgrid, virtual instrumentation, xPC Target Turnkey.

Sammendrag

Den elektriske kraftteorien er av fundamental betydning i de fleste områder av fagfeltet elkraft, ettersom den muliggjør analyse og regulering av kraftnettet, basert på en entydig fysisk forståelse av kraftflyten. I forbindelse med innførelse av såkalte smarte nett vil det kunne oppstå meget krevende nettdrift grunnet ulineære laster, kombinert med harmonisk og usymmetrisk nettspenning. Nye og mer avanserte kraftteorier er nødvendig for å kunne forstå kraftnettet ut fra prinsippet om korrekt fysisk tolkning, uavhenging av spenningsregimer. Videre kan sofistikerte kraftteorier tilby identifisering og eliminering av ugunstige fenomener forårsaket av nettbrukere; f.eks. skjevlast, reaktiv effektflyt samt harmonisk forurensning. I denne sammenheng har dette prosjektet betraktet den nye og lovende konservative kraftteorien (*KKT*).

Storparten av prosjektet ble dedikert til eksperimentell forskning, hvor KKT ble evaluert ut fra et kraftteoretisk perspektiv. En viktig del av forsøkene var et sanntids-kontrollsystem (*SKS*) og en trefase vekselretter. Styring av vekselretteren, datainnsamling samt KKT-algoritme ble implementert av SKS. Basert på omfattende tester ble det konkludert at den nye kraftteorien åpner for forbedret analyse av strøm og kraftflyt, for alle de spenningsregimer som ble testet. Resultatene fra undersøkelsen sammenfaller med, og underbygger resultat fra tidligere publisert forskning.

Andre del evaluerte bruken av KKT som del av styringssystemet til et aktivt shuntfilter (*ASF*). Eksperimentell implementering av shuntkompensering var desverre ikke mulig, ettersom kontrollsystemet ikke har tilstrekkelig samplingsfrekvens. Basert på datasimulering *(MATLAB/Simulink)*, ble utvalgte tilfeller av reaktiv og harmonisk kompensering demonstrert. Resultatene viser til at den nye kraftteorien muliggjør tilfredsstillende selektiv kompensering, så lenge nettspenning er ideell. I tilfelle usymmetrisk eller harmonisk nettspenning vil kompseringsmetoder tilbydt av KKT tilsynelatende være mindre allsidig og effektiv, sammelignet med den populære *pq*-teorien. Denne studien viser at optimale nettforhold bare kan oppnåes gjennom samhandling av spenning og strømkompensering. Fremtidig arbeid vil blant annet inkludere videre studie av SKS, samt eksperimentell implementering av aktivt shuntfilter.

Nøkkelord: aktivt shuntfilter, konservativ kraftteori, eksperimentell implementering, smarte nett, virtuell instrumentering, sanntids-kontrollsystem, harmonisk spenningsregime, xPC Target Turnkey.

Acknowledgments

Before going into details about the thesis work, there are a number of persons that deserves my deepest gratitude. I want to thank everyone that I shared time with at the power electronics lab, and contributed to a great working atmosphere: Dr. Anandarup Das and Alejandro Garcés Ruiz, and PhD students Alejandro Garcés Ruiz, Fritz Schimpf, Raymundo Torres, Hamed Nademi and Santiago Sanchez. Special thanks to PhD student Muhammad Jafar for many good conversations and discussions.

Even though the thesis has been an independent work, many persons have helped along the way. In the beginning having no clue where to start, Research Scientist Kjell Ljøkelsøy at SINTEF acted as a good contributing mentor. Thanks to Department Engineers Bård Almås and Thor Lohse and to Senior Engineer Vladimir Klubicka at the departments service lab, sharing many intricate tips and tricks. Special thanks to Thor for all the help. Staff Engineer Jan Erik Molde at the workshop has been generously supportive. Thanks to Martin Stoller at Speedgoat, providing quick and helpful support.

My thankful mind goes to supervisor Professor Marta Molinas for being a superior inspiration source, and for having an endless patience...

Last but not least thanks to my family for support, especially Marit Ingeborg and Marta. And of course the ladies Eli, Ingrid, Jorid and Anngjerd.

Norway's oil production peaked in 2001, and is currently declining annually. This is a common situation in many countries, the petroleum industry is desperate. The coming decades might be challenging, not only from an energy perspective.

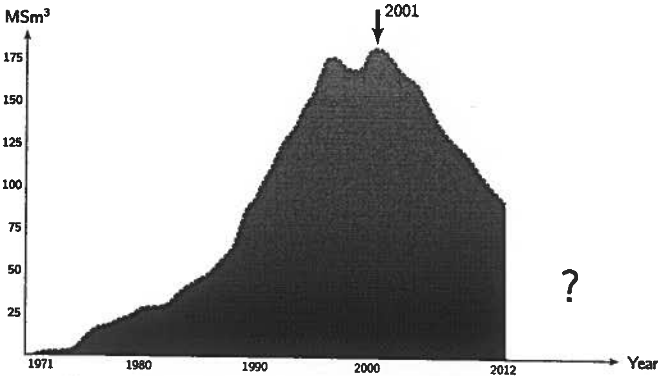

Source: Norwegian Petroleum Directorate, www.npd.no/en/news/Production-figures

Contents

List of Figures

List of tables

Nomenclature

Symbol	Parameter	Unit
General fundamental electric quantities		
ω	Angular frequency	*rad s⁻¹*
f	Fundamental grid frequency	*Hz*
T	Averaging time period	*ms*
t	Time	*ms*
$V_{a(b)}$	Phase/line voltage (effective value)	*V*
$V_{b(c)}$	Phase/line voltage (effective value)	*V*
$V_{c(a)}$	Phase/line voltage (effective value)	*V*
V_N	Voltage, phase N (effective value)	*V*
I_a	Line current, phase A (effective value)	*A*
I_b	Line current, phase B (effective value)	*A*
I_c	Line current, phase C (effective value)	*A*
I_N	Line current, phase N (effective value)	*A*
THD_v	Total harmonic distortion, voltage	*%*
THD_i	Total harmonic distortion, current	*%*
K_{v0}	Zero sequence unbalance index, voltage	*%*
K_{v-}	Negative sequence unbalance index, voltage	*%*
K_{i0}	Zero sequence unbalance index, current	*%*
K_{i-}	Negative sequence unbalance index, current	*%*
PF	Power factor (traditonal)	-
R_{abc}	Symmetric resistance	*Ω*
L_{abc}	Symmetric inductance	*mH*
$R_{a,b,c}$	Unsymmetric resistance (per phase)	*Ω*
$L_{a,b,c}$	Unsymmetric inductance (per phase)	*mH*
C_{DC}	DC-Link capacitance	*µF*
R_{DC}	DC-Link resistance	*Ω*
α_{th}	Thyristor gate-pulse firing angle	*(°)*
S^*	Apparent power (traditional)	*VA*
P^*	Active power (traditional)	*W*
Q^*	Reactive power (traditional)	*VAR*
U_{h1}	Fundamental voltage (effective value)	*V*
$u_f(t)$	Fundamental voltage harmonic	*V*
$U_h(t)$	Harmonic voltage of h-th order (effective value)	*V*
$u_h(t)$	Instantaneous harmonic voltage of h-th order	*V*
$u_n(t)$	Instantaneous voltage, phase n	*V*
$I_h(t)$	Harmonic current of h-th order (effective value)	*A*
$i_h(t)$	Instantaneous harmonic current of h-th order	*A*

continued on next page . . .

... continued from previous page

Symbol	**Parameter**	**Unit**
Conservative Power Theory		
$x(t)$	Generic voltage variable	*V*
$y(t)$	Generic current variable	*A*
$\overline{x}$	Average value	*V*
$\widehat{x}(t)$	Homo-integral	*V*
$\breve{x}(t)$	Homo-derivative	*V*
X	Root-mean-square value	*V*
$\boldsymbol{x}(t)$	Generic voltage vector (polyphase)	*V*
$x_k(t)$	Generic voltage variable, phase *k* (polyphase)	*V*
$\boldsymbol{y}(t)$	Generic current vector (polyphase)	*A*
$y_k(t)$	Generic current variable, phase *k* (polyphase)	*A*
$\boldsymbol{x}(t) \circ \boldsymbol{y}(t)$	Scalar product (polyphase)	*W*
$\lvert\boldsymbol{x}(t)\rvert$	Vector magnitude (polyphase)	*V*
$\langle\boldsymbol{x}(t)\rangle$	Average value (polyphase)	*V*
$\langle\boldsymbol{x}(t),\boldsymbol{y}(t)\rangle$	Internal product (polyphase)	*W*
$\lVert\boldsymbol{x}(t)\rVert$	Norm (polyphase)	*V*
$\boldsymbol{u}(t)$	Voltage vector (polyphase)	*V*
$\widehat{\boldsymbol{u}}(t)$	Homo-integral voltage vector (polyphase)	*V*
$\breve{\boldsymbol{u}}(t)$	Homo-derivative voltage vector (polyphase)	*V*
$\boldsymbol{i}(t)$	Current vector (polyphase)	*A*
$\widehat{\boldsymbol{i}}(t)$	Homo-integral current vector (polyphase)	*A*
$\breve{\boldsymbol{i}}(t)$	Homo-derivative current vector (polyphase)	*A*
$\boldsymbol{s}(t)$	Instantaneous complex power	*VA*
$\boldsymbol{p}(t)$	Instantaneous real power	*W*
$\boldsymbol{q}(t)$	Instantaneous imaginary power	*VAR*
A	Apparent power	*VA*
S	Complex power	*VA*
P	Active power	*W*
Q	Reactive power	*VAR*
N_a^u	Unbalanced active power (polyphase)	*W*
N_r^u	Unbalanced reactive power (polyphase)	*VAR*
D	Distortion power	*VA*
$D_{\boldsymbol{u}}$	Voltage distortion power	*VA*
$D_{\boldsymbol{i}}$	Current distortion power	*VA*
$f_c(HP)$	Cut frequency high-pass filter, algorithm input	*Hz*
$f_c(LP)$	Cut frequency low-pass filter, algorithm input	*Hz*
f_{CPT}	Averaging fundamental frequency, CPT-algorithm	*Hz*
T_{CPT}	Averaging fundamental time-period, CPT-algorithm	*ms*
$\boldsymbol{i}_a(t)$	Active current	*A*

continued on next page ...

... continued from previous page

Symbol	Parameter	Unit
$i_r(t)$	Reactive current	*A*
$i_v(t)$	Void current	*A*
$i_{sa}(t)$	Active scattering current	*A*
$i_{sr}(t)$	Reactive scattering current	*A*
$i_{an}(t)$	Active current, phase n (polyphase)	*A*
$\boldsymbol{i}_a(t)$	Basic active current vector (polyphase)	*A*
$i_{a0}(t)$	Neutral active current (polyphase)	*A*
$i_{rn}(t)$	Reactive current, phase n (polyphase)	*A*
$\boldsymbol{i}_r(t)$	Basic reactive current vector (polyphase)	*A*
$i_{r0}(t)$	Neutral reactive current (polyphase)	*A*
$i_{vn}(t)$	Void current, phase n (polyphase)	*A*
$\boldsymbol{i}_v(t)$	Basic void current vector (polyphase)	*A*
$i_{v0}(t)$	Neutral void current (polyphase)	*A*
$\boldsymbol{i}_a^b(t)$	Balanced active current vector (polyphase)	*A*
$i_{a0}^b(t)$	Balanced neutral active current (polyphase)	*A*
$\boldsymbol{i}_a^u(t)$	Unbalanced active current vector (polyphase)	*A*
$i_{a0}^u(t)$	Unbalanced neutral active current (polyphase)	*A*
$\boldsymbol{i}_r^b(t)$	Balanced reactive current vector (polyphase)	*A*
$i_{r0}^b(t)$	Balanced neutral reactive current (polyphase)	*A*
$\boldsymbol{i}_r^u(t)$	Unbalanced reactive current vector (polyphase)	*A*
$i_{r0}^u(t)$	Unbalanced neutral reactive current (polyphase)	*A*
λ	Power factor	-
σ_u	Voltage distortion factor	-
σ_i	Current distortion factor	-
G_e	Equivalent conductance	*S*
G_h	Conductance at h-th harmonic	*S*
G_n	Equivalent conductance, phase n (polyphase)	*S*
G^b	Global balanced conductance (polyphase)	*S*
B_e	Equivalent susceptance	*S*
B_h	Susceptance at h-th harmonic	*S*
B_n	Equivalent susceptance, phase n (polyphase)	*S*
B^b	Global balanced susceptance (polyphase)	*S*
P_n	Active power associated to phase n (polyphase)	*W*
Q_n	Reactive power associated to phase n (polyphase)	*VAR*
$P_a(t)$	Active power associated to active current	*W*
$P_r(t)$	Active power associated to reactive current	*W*
$P_v(t)$	Active power associated to void current	*W*
$Q_a(t)$	Reactive power associated to active current	*VAR*
$Q_r(t)$	Reactive power associated to reactive current	*VAR*
$Q_v(t)$	Reactive power associated to void current	*VAR*

continued on next page ...

... continued from previous page

Symbol	**Parameter**	**Unit**
P_h	Active power at h-th harmonic	W
Q_h	Reactive power at h-th harmonic	VAR
$\mathbf{N}_u$	Set of harmonic content in voltage	-
$\mathbf{N}_i$	Set of harmonic content in current	-
$\mathbf{N}_c$	Common set of harmonics in voltage and current	-
α_h	Voltage phase shift at h-th harmonic order	degree (°)
β_h	Current phase shift at h-th harmonic order	degree (°)
φ_h	Harmonic phase shift at h-th harmonic	degree (°)
$i_g(t)$	Load generated current	A
$i_k(t)$	Homo-frequential current	A
$i_{ah}(t)$	Active current at h-th harmonic	A
$i_{rh}(t)$	Reactive current at h-th harmonic	A
$i_{Ha}(t)$	Total harmonic active current	A
$i_{Hr}(t)$	Total harmonic reactive current	A
$u_k(t)$	Homo-frequential voltage	V
$u_g(t)$	Source generated voltage	V
f_{ref}	Sampling rate of current reference generator	A
f_{PWM}	Sampling rate of current control loop	V
f_{cpt}	Sampling rate of CPT-algorithm	V

Abbreviations

Abbreviation	**Description**
APF	Active Power Filter (shunt)
CPT	Conservative Power Theory
CPU	Central Processing Unit
D-Configuration	Delta-connected circuitry
DER	Distributed Energy Resource
DSP	Digital Signal Processor
FACTS	Flexible AC Transmission System
FFT	Fast Fourier Transform
FIR	Finite Impulse Response
FPGA	Field-Programmable Gate Array
HF	High Frequency
IGBT	Insulated-Gate Bipolar Transistor
IIR	Infinit Impulse Response
IT	Isolated Terra, 3-Ph Three-wire system
MOSFET	Metal–Oxide–Semiconductor Field-Effect Transistor
PF	Classical Power Factor
PCC	Point of Common Connection
PWM	Pulse-Width Modulation
RMS	Root Mean Square
STM	Speedgoat Target Machine
TCPU	Target Central Processor Unit
TN	Terra Neutral, 3-Ph Four-wire system
VSC	Voltage Source Converter
VSI	Voltage Source Inverter
VI	Virtual Instrument(ation)
YF-Configuration	Floating Star-connected circuitry
YG-Configuration	Grounded Star-connected circuitry

Chapter 1

Introduction

1.1 Background and motivation

The traditional electric power system has been characterized by balanced sinusoidal voltages and currents. These network conditions are of fundamental importance in most aspects of electric power engineering; i.e. power system design and operation, power metering, power compensation and conditioning. Associated with these network characteristics there is a well established electric power theory[E53,E61], as the mathematical and theoretical tool. The power theory deals with the relation between network voltages and currents, providing decomposition of current and power flow, which can be linked to real physical phenomenas. The proof that the classic power theory is correct can be demonstrated by the fact that its implementation has been successful for over a century.

Since the invention of power electronics in late 1960s[B21], electric power networks have been subjected to increasingly challenging operating conditions, due to the ever escalating usage of unlinear and time-variant loads. These origin from electronic consumer products commonly found in domestics and office buildings; i.e. computers, smartphones, lightning and heating, TVs etc. High-power equivalents can be seen in industrial appliances like electric drives, arc furnaces etc. Related to these loads comes a number of phenomenas such as reactive power consumption and harmonic distortion. These often cause negative effects on the nearby or upstream network; i.e. overheating of electric machines like transformers and motors, voltage waveform distortion, voltage flicker and interference with sensitive electrical apparatus.

Unfortunately the electric power theory most commonly utilized by electric power engineers all around the world, has limited validity and consequently not been universally adopted; its restricted only to power networks of ideal operation, meaning symmetric sinusoidal state. Ever since the origin of electric power grid there has been an ongoing debate, resulting in several proposed power theories to handle network operations of unsymmetric and distorted waveforms. Noteworthy contributors are Budeanu, Fryze-Buchholz-Depenbrock, Kusters-Moore and Czarnecki, thought neither of these frameworks have proven general enough to perform correct physical interpretation of current and power flow.[A2]

There are several motivation factors for developing new power theories; advancement in power theories can provide enhanced information regarding power and current flow, enabling better understanding and operation of the power network, particularly in unbalanced non-sinusoidal regimes. Moreover as advanced power theories provide identification of unwanted phenomenas like unsymmetry, distortion and reactive power consumption, this can be utilized to generate compensation targets for various compensator devices such as APFs and FACTS.

This study focuses particularly on shunt compensation using shunt active power filters (*AFPs*) as depicted in **Figure 1.1**. The shunt APF is a controllable current source, connected in parallel with a load which is drawing current $i_L(t)$. Part of the load current may contain reactive power consumption or harmonic pollution, which act detrimental on the upstream power network. Using proper mathematical techniques the undesired part of the load current is extracted by the APFs current *reference generator*, providing a *current reference* $i^*_{APF}(t)$ for the controllable current source. The APF power circuit is some form of power electronics converter, operating in *current-controlled* mode.
Ultimately the APF injects a current $i_{APF}(t)$ into the power network, being an ideal replica but anti-phased version of the part of the load current to be removed. The detrimental effects are effectively cancelled by the APF, leaving the compensated source current $i_s(t)$ in ideal state, optimizing the network performance and utilization. Mitigating negative load interference becomes even more challenging when the grid voltage itself is non-sinusoidal, and the results are often less successful compared to shunt compensation in sinusoidal voltage regimes.

The last decades the pq-theory developed by H.Akagi[B21] has gained great attention in the industry and scientific community, as its being employed with great success both for series and shunt active compensation. Despite its versatility regardless of voltage conditions, the pq-theory has certain flaws when evaluated as a power theory.
In this thesis a more recent contribution will be comprehensively reviewed. The conservative power theory (*CPT*) consolidated by P.Tenti and P.Mattavelli, has established itself as a promising alternative since it was firstly presented in 2002[A4]. Notably the CPT is greatly influenced by previous time-domain power theories.

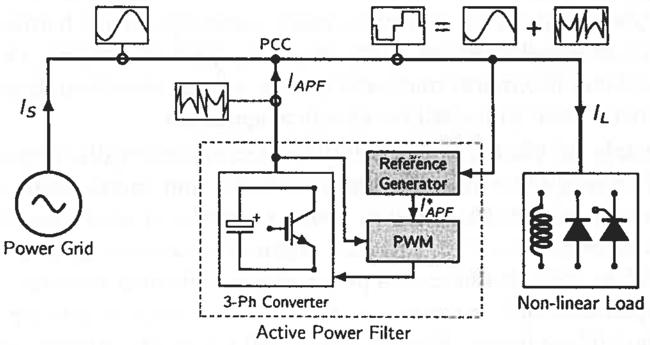

Figure 1.1 – *Simplified conceptual presentation of active shunt compensation. The active power filter extracts and cancels out undesired current harmonics and reactive power induced by the load.*

The agenda of this thesis work is twofold; initially the properties of the CPT when its operating as a power theory are investigated. Secondly the CPT will be employed as a current reference generator for an high-performance APF, so to implement reactive and harmonic compensation both in sinusoidal and non-sinusoidal voltage regimes. Larger share of the project is based on experimental lab work, where a real-time rapid prototyping system fabricated by the Swiss company Speedgoat plays an important role. The Speedgoat target machine is employed as a virtual instrument,[F65–F68] and controlling a programmable voltage source to mimic various network voltage conditions. Overall the work can be characterized as diverse, as its been including both simulative, experimental and practical challenges.

1.2 Report outline

The structure and general outline of this Master of Science thesis is as following:

Chapter 1 Briefly sets the thesis work in context by addressing the initial problem, and defining the scope of the project.

Chapter 2 Mainly based on the author's research report from TET5500 Specialization project[A1], however rewritten as the original text suffered from many errors which now have been corrected. Examines the most important theoretical aspects from the conservative power theory. Introduction of the algorithmic implementation of the new power theory, utilized in simulative work and real-time virtual instrumentation.

Chapter 3 Presentation and evaluation of experimental results. Using Speedgoat rapid prototyping system, the current and power decomposition qualities of the conservative power theory is tested, for a variety of load types and voltage conditions. Results are benchmarked with the classic power theory implemented by a state-of-the-art power quality analyzer. Accuracy and credibility of the experimental data are discussed. The chapter is completed by considering challenges encountered using the Speedgoat rapid prototyping system, and further proposing future user strategies.

Chapter 4 Demonstrates selected cases of shunt compensation modeled in software using MATLAB® and Simulink®. The structure and parametrization of the active power filter model are outlined; voltage source inverter and grid interfacing, current reference generator and current controller. Chapter 4 is particularly constricted towards reactive compensation in non-sinusoidal voltage conditions, supplemented by harmonic filtering of unlinear loads under sinusoidal voltage regime. Finally the active power filter performance and behavior depending on various important parameters are demonstrated and discussed, focusing extensively on the influence of control system sampling rate. The chapter culminates with an attempt to experimentally implement an hysteresis current controller.

Chapter 5 The last chapter summarizes the obtained results, and proposes relevant topics in future work.

Appendix Supplementary material can be found in the Appendix; additional data and photos from the experimental work, MATLAB source code for virtual instrument graphical user interface, technical data sheets for voltage source converter, along with construction drawings used during assembly of the experimental lab setup.

1.3 Publications

A brief abstract of the thesis work was delivered and accepted for the Technoport 2012 Conference held in Trondheim. The author was in that context also invited to submit a full article to be presented in Energy Procedia *(ISSN: 1876-6102)*, however the Procedia article was not prioritized. After the publication there have been several petitions expressing interest in the research; Journal of Energy and Power Engineering *(ISSN: 1934-8975)*, and Journal of Materials Science and Engineering A & B *(ISSN: A: 2161-6213; B: 2161-6221)*. Along with the listed future plans, this thesis will be followed up by the process of extracting one or several scientific articles.

Chapter 2

The Conservative Power Theory

Introduction

The conservative power theory *(CPT)* is a relatively new supplement to the existing power theories. Professors P.Tenti, P.Mattavelli and Doctor E.Tedeschi can be considered as the main developers of this new and promising theory. Other contributors to mention are D.Trombetti and more lately H.Paredes which has greatly contributed to the research on an experimental level.

The theory remains more or less as it was originally presented in the first publications, but has undergone minor revisions and refinements. The theoretic background is familiar from many of the older power theories, as the CPT aims to incorporate their most successful concepts. A brief timeline of the development through the last ten years:

2002 Developers of the CPT launch the first public presentation. The framework was principally presented from a theoretical approach.[A4]

2003 The second paper presents the conservative power theory in more theoretical depth. Perhaps considered as one of the most significant theoretical articles.[A7]

2005 First introduction of applied harmonic and reactive compensation using an hybrid filter. The paper deals with distributed filtering of a diode rectifier load.[A11]

2007 Case studies of distributed compensation focusing on control in the discrete time-domain. Relevant for future implementation in DSPs and similar devices.[A3,A10]

2008 Discusses how network transformers affect cooperative distributed compensation, and how these issues are solved from a control system perspective.[A12,A18]

2009a Presently 2009 stands out as the peak-year regarding number of CPT-related technical articles. First independent critical reviews comparing the *pq* and *FBD* power theories with the CPT.[B22–B24]

2009b The first and presently only experimental verification of compensation in the single-phase domain. Also evaluation based on virtual instrumentation.[A13,A16]

2009c E.Tedeschi finalizing PhD thesis which to this day is the most extensive theoretical dissertation of the conservative power theory. Critical concepts of the CPT are thoroughly demonstrated in a mathematical approach. This chapter is largely based on selected topics from Doctor Tedeschi's research.[A2]

2010a More experiments presented based on virtual instrumentation. The CPT is tested in non-ideal voltage regimes in conjunction with a revisited definition of sequence components. This thesis work is greatly influenced by articles from 2010.[A6,A20]

2010b The flexibility of CPT when applied in shunt compensation is demonstrated through simulations. To reduce the CPT-algorithm convergence time, a revisited method for average value computation is presented.[A5,A15]

2011 NTNU adds to the list of contributors. Various strategies for compensation of a thyristor load *(HVAC)* are discussed.[A17]

2012 At medio 2012 no related research has presently been made public. Experimental verification of many important aspects are yet to be implemented.

As the conservative power theory was developed for application in shunt compensation, its framework is based on the *time-domain* as this offers instantaneous processing of powers and currents. Another essential property of the CPT is to define power terms that fulfill Tellegen's conservation theorem, and thus maintain their conservativity in all network operating conditions. This important characteristic allows adoption of fundamental concepts known from power system analysis in sinusoidal state; i.e. the control and synergetic action of a set of distributed power plants, governed to maintain stability of power grid frequency and voltage, or other important network parameters.[C26]

Also the proposed theory attempts to deal with the challenge related to encoding instantaneous power and line currents under non-ideal state, into appropriate parcels that can be linked to physical phenomenas. The conservative power theory therefore aims to define a set of quantities that must have the same specific physical interpretation, irrespective of network conditions. Thus sinusoidal operation must be considered only as a particular case of the general mode.

CPT is valid both for single-phase and both types of three-phase systems, such as three-wire or four-wire topologies *(IT and TN respectively).* Contrary to the *pq*-theory it does not have the duality property, as it cannot decompose both currents and voltages. However in one of the first presentations of the framework[A4], the authors suggested several alternative load models, where residual part of the current (i.e. harmonic content that does not contribute to active or reactive power flow), was modeled either as an harmonic current source or harmonic voltage source. As P.Tenti and P.Mattavelli further developed the theory for load modeling and compensation purposes, the conservative power theory is presently focusing towards current decomposition and compensation exclusively.

2.1 Basis for a new power theory

A central element of CPT is the introduction of so-called *homo-variables.* Here they are defined and their mathematical properties demonstrated. A basic variable $x(t)$ is defined with the **constraints** of having constant period T and frequency $f = 1/T$, or equivalently angular frequency $\omega = 2\pi/T = 2\pi f$. It is also required to be a real, continuous and periodic function, with no DC-offset, thus average value is zero:

$$\overline{x} = \frac{1}{T}\int_0^T x(t)\,dt = 0 \tag{2.1}$$

The impact of biased $x(t)$ will be demonstrated by experimental work next chapter. Corresponding calculus variables time-derivative $x'(t)$ and time-integral $x_{\int}(t)$ renders:

$$x_{\int}(t) = \int_0^T x(\tau)\,d\tau \tag{2.2}$$

$$x'(t) = \frac{d}{dt}x(t) \tag{2.3}$$

the average value of the time-integral can be found as:

$$\overline{x}_{\int}(t) = \frac{1}{T}\int_0^T x_{\int}(t)\,dt \tag{2.4}$$

Next comes the definition of the homo-variables which must be considered as one of the greatest contributions by the CPT, particularly for reactive power compensation:

$$\overset{\frown}{x}(t) = \omega\big(x_{\int}(t) - \overline{x}_{\int}(t)\big) \tag{2.5a}$$

$$\overset{\smile}{x}(t) = \frac{1}{\omega}x'(t) \tag{2.5b}$$

The time-integral of $x(t)$ will contain an average value component which sets it off the time axis. Also it will be scaled down from its original variable by a factor equal to the angular frequency ω. To obtain *homo-integral* $\overset{\frown}{x}(t)$ the integral is normalized by subtracting the offset-value $\overline{x}_{\int}$, and rescaling it by the same angular frequency ω.

In a similar fashion the time-derivative of $x(t)$ will be scaled up by the factor $\omega = 2\pi f$, thus to get the *homo-derivative* it must be normalized. The variables $\overset{\frown}{x}(t)$ and $\overset{\smile}{x}(t)$ will now appear as homogeneous copies of their original $x(t)$ as they have the same physical dimensions, but time shifted in a quadrature phase relation.

Scalar operators

In the derivation of the various CPT-variables there are two mathematical operations commonly used, namely the internal product $\langle x(t), y(t)\rangle$ and euclidean norm $\|x(t)\|$. A second variable $y(t)$ is introduced as eventually both fundamental electric quantities voltages and currents have to be dealt with:

$$\langle x(t), y(t)\rangle = \frac{1}{T}\int_0^T x(t)\cdot y(t)\, dt \tag{2.6}$$

$$\|x(t)\| = \sqrt{\langle x(t), x(t)\rangle} = \sqrt{\frac{1}{T}\int_0^T x^2(t)\, dt} = X \tag{2.7}$$

Useful mathematical properties of variable $x(t)$ and its associated homo-variables gives:

Property 1

$$\widehat{\breve{x}} = \breve{\widehat{x}} = x \tag{2.8}$$

Proof: This follows from the definition of the homo-derivative and homo-integral, as an integrating operation cancels a derivative, and vice versa.

Property 2

$$\langle x, \breve{x}\rangle = \langle x, \widehat{x}\rangle = 0 \tag{2.9a}$$

Proof:

$$\langle x, \breve{x}\rangle = \left\langle x, \frac{1}{\omega}\frac{dx}{dt}\right\rangle = \frac{1}{\omega T}\int_0^T x(t)\frac{dx(t)}{dt}\, dt = \frac{1}{\omega T}\left[\frac{x^2(t)}{2}\right]_0^T = 0 \tag{2.9b}$$

$$\langle x, \widehat{x}\rangle = \langle \breve{\widehat{x}}, \widehat{x}\rangle = \frac{1}{\omega T}\int_0^T \widehat{x}(t)\frac{d\widehat{x}(t)}{dt}\, dt = \frac{1}{\omega T}\left[\frac{\widehat{x}^2(t)}{2}\right]_0^T = 0 \tag{2.9c}$$

Property 3

$$\langle x, \breve{y}\rangle = -\langle \breve{x}, y\rangle \tag{2.10a}$$

Proof:

$$f = x\cdot y \tag{2.10b}$$

$$\frac{df}{dt} = \frac{dx}{dt}y + x\frac{dy}{dt} = \omega\breve{x}y + \omega x\breve{y} = \omega(\breve{x}y + x\breve{y}) \tag{2.10c}$$

$$\langle \breve{x}, y\rangle + \langle x, \breve{y}\rangle = \frac{1}{\omega T}\int_0^T \frac{df}{dt}\, dt = \frac{1}{2\pi}\,[f(t)]_0^T = 0 \tag{2.10d}$$

Property 4

$$\langle x, \widehat{y}\rangle = -\langle \widehat{x}, y\rangle \tag{2.11}$$

Proof: From Equation (2.8) yields $\langle x, \widehat{y}\rangle = \langle \breve{\widehat{x}}, \widehat{y}\rangle$ which leads to $\langle \breve{\widehat{x}}, \widehat{y}\rangle = -\langle \widehat{x}, \breve{\widehat{y}}\rangle = -\langle \widehat{x}, y\rangle$

Property 5

$$\langle \widehat{x}, \breve{y} \rangle = \langle \breve{x}, \widehat{y} \rangle = -\langle x, y \rangle \tag{2.12a}$$

Proof:

$$f = \widehat{x} \cdot y \tag{2.12b}$$

$$\frac{df}{dt} = \frac{d\widehat{x}}{dt} y + \widehat{x} \frac{dy}{dt} = \omega x y + \widehat{x} \omega \breve{y} = \omega (x y + \widehat{x} \breve{y}) \tag{2.12c}$$

$$\langle x, y \rangle + \langle \widehat{x}, \breve{y} \rangle = \frac{1}{\omega T} \int_0^T \frac{df}{dt} \, dt = \frac{1}{2\pi} \left[f(t) \right]_0^T = 0 \tag{2.12d}$$

Property 6

$$\langle \widehat{x}, \breve{x} \rangle = -\langle x, x \rangle = -\| x \|^2 \tag{2.13}$$

Proof: This property follows directly from the fifth property.

Properties under sinusoidal operation If the variable $x(t)$ is defined as sinusoidal $x(t) = \sqrt{2}X \sin(\omega t + \phi)$, associated homo-variables will be $\widehat{x}(t) = -\sqrt{2}X \cos(\omega t + \phi)$ and $\breve{x}(t) = \sqrt{2}X \cos(\omega t + \phi)$. Then also follows that in any instant of period T:

$$\widehat{x}(t) + \breve{x}(t) = 0 \tag{2.14a}$$

$$x^2(t) + \widehat{x}^2(t) = x^2 + \breve{x}^2 = x^2 - \widehat{x} \cdot \breve{x} = 2X^2 \tag{2.14b}$$

where variable X is the *RMS* value known from the classical power theory.

Vector operators

In order to make the CPT-framework valid in polyphase systems, the scalar operators must be expanded to vector format. Assuming a system of N conductors, electric quantities are represented by generic variables collected in vectors $\boldsymbol{x}(t)$ and $\boldsymbol{y}(t)$:

$$\boldsymbol{x}(t) = \begin{bmatrix} x_1 \\ \vdots \\ x_n \\ \vdots \\ x_N \end{bmatrix} = \begin{bmatrix} x_1(t) \\ \vdots \\ x_n(t) \\ \vdots \\ x_N(t) \end{bmatrix} \qquad \boldsymbol{y}(t) = \begin{bmatrix} y_1 \\ \vdots \\ y_n \\ \vdots \\ y_N \end{bmatrix} = \begin{bmatrix} y_1(t) \\ \vdots \\ y_n(t) \\ \vdots \\ y_N(t) \end{bmatrix} \tag{2.15}$$

The conservative power theory is founded on a number of mathematical operations:
Scalar product:

$$\boldsymbol{x}(t) \circ \boldsymbol{y}(t) = \sum_{n=1}^{N} x_n(t) \cdot y_n(t) \tag{2.16}$$

Vector magnitude:

$$|\boldsymbol{x}(t)| = \sqrt{\boldsymbol{x}(t) \circ \boldsymbol{x}(t)} = \sqrt{\sum_{n=1}^{N} x_n^2(t)} \tag{2.17}$$

Average value:

$$\langle \boldsymbol{x}(t) \rangle = \bar{\boldsymbol{x}}(t) = \frac{1}{T} \int_0^T \boldsymbol{x}(t)\, dt = \begin{bmatrix} \overline{x}_1 \\ \vdots \\ \overline{x}_N \end{bmatrix} \tag{2.18}$$

Internal product:

$$\langle \boldsymbol{x}(t), \boldsymbol{y}(t) \rangle = \langle x_n \circ y_n \rangle = \sum_{n=1}^{N} \frac{1}{T} \int_0^T x_n(t) \cdot y_n(t)\, dt \tag{2.19}$$

Norm:

$$\|\boldsymbol{x}(t)\| = \sqrt{\langle \boldsymbol{x}(t), \boldsymbol{x}(t) \rangle} = \sqrt{\sum_{n=1}^{N} X_n^2} \tag{2.20}$$

At last the Cauchy-Schwartz inequality will become useful when considering power terms and quality indexes:

$$\left|\langle \boldsymbol{x}(t), \boldsymbol{y}(t) \rangle\right| \leq \|\boldsymbol{x}(t)\| \cdot \|\boldsymbol{y}(t)\| \tag{2.21a}$$

$$\left|\langle \widehat{\boldsymbol{x}}(t), \breve{\boldsymbol{x}}(t) \rangle\right| = \|\boldsymbol{x}(t)\|^2 \leq \left\|\widehat{\boldsymbol{x}}(t)\right\| \cdot \left\|\breve{\boldsymbol{x}}(t)\right\| \tag{2.21b}$$

2.2 Conservativity

Considering that a generic electric power network is described by vector $\boldsymbol{u}(t)$ containing branch voltages, and vector $\boldsymbol{i}(t)$ containing branch currents. When these currents and voltages satisfy Kirchhoff's first and second law respectively, they are said to be *consistent* and Tellegen's theorem will be valid for the specified circuit.

Referring to simultaneous electrical quantities this corresponds to conservation of instantaneous power, which is one of the fundamental principles in electric power engineering. According to energy physics there must at all times be a corresponding balance between produced and consumed electric power and energy.

Now by applying the aforementioned mathematical concepts on elements from $\boldsymbol{u}(t)$ and $\boldsymbol{i}(t)$, a new set of electrical quantities can be introduced. The voltage homo-integral $\widehat{\boldsymbol{u}}(t)$, voltage homo-derivative $\breve{\boldsymbol{u}}(t)$, current homo-integral $\widehat{\boldsymbol{i}}(t)$ and lastly current homo-derivative $\breve{\boldsymbol{i}}(t)$. As the homo-quantities are homogenous to their original signals, it follows that they will also be consistent and thereby obey Tellegen's theorem.

Consistence of homo-derivatives

The consistency can be proven by means of a set of voltage homo-variables, which equivalently applies for a cut set of currents. Having a network mesh μ made up from M branches can be described by voltage vector $\boldsymbol{u}^{\mu}(t)$, then it follows from Kirchhoff's voltage law that $\sum_{m=1}^{M} u_m^{\mu}(t) = 0$. If the summation of voltages around the mesh is derived, the consistence of homo-derivative is demonstrated:

$$\sum_{m=1}^{M} \frac{d}{dt}[u_m^{\mu}(t)] = \omega \cdot \sum_{m=1}^{M} \breve{u}_m^{\mu}(t) = 0 \tag{2.22}$$

Extending the procedure to every mesh in the network, the homo-derivative indeed gives a consistent description of the system.

Consistence of homo-integrals

By integrating Kirchhoff's voltage law for mesh μ induce following results:

$$\int_0^t \sum_{m=1}^{M} u_m^{\mu}(\tau)\, d\tau = 0 \tag{2.23a}$$

suggesting that the integrand is null:

$$u_{\int m}^{\mu}(t) = \int_0^t u_m^{\mu}(\tau)\, d\tau \tag{2.23b}$$

$$\sum_{m=1}^{M} u_{\int m}^{\mu}(t) = 0 \tag{2.23c}$$

so the mean value of Equation (2.23a) has to be zero as well:

$$\frac{1}{T}\int_0^t \sum_{m=1}^{M} u_{\int m}^{\mu}(t)\, dt = \sum_{m=1}^{M} \overline{u}_{\int m}^{\mu}(t) = 0 \tag{2.23d}$$

Rearranging the definition of the homo-integral yields:

$$u_{\int m}^{\mu}(t) = \frac{\widehat{u}_m^{\mu}(t)}{\omega} + \overline{u}_{\int m}^{\mu} \tag{2.23e}$$

$$\frac{1}{\omega}\sum_{m=1}^{M} \widehat{u}_m^{\mu}(t) + \sum_{m=1}^{M} \widehat{u}_{\int m}^{\mu}(t) = 0 \tag{2.23f}$$

By substituting Equation (2.23c) into (2.23f) the demonstration is complete:

$$\sum_{m=1}^{M} \overset{\frown}{u}{}^{\mu}_{m}(t) = 0 \tag{2.23g}$$

If the analysis is extended to every mesh in the network, homo-integrals are truly consistent with the system. These six variables form the set of fundamental quantities in the conservative power theory, and can be utilized to define scalar products that according to Tellegen's theorem are zero. These are possible combinations of homo-variables:

$$\boldsymbol{u} \circ \boldsymbol{i} = \overset{\frown}{\boldsymbol{u}} \circ \boldsymbol{i} = \breve{\boldsymbol{u}} \circ \boldsymbol{i} = 0 \tag{2.24a}$$

$$\boldsymbol{u} \circ \overset{\frown}{\boldsymbol{i}} = \overset{\frown}{\boldsymbol{u}} \circ \overset{\frown}{\boldsymbol{i}} = \breve{\boldsymbol{u}} \circ \overset{\frown}{\boldsymbol{i}} = 0 \tag{2.24b}$$

$$\boldsymbol{u} \circ \overset{\smile}{\boldsymbol{i}} = \overset{\frown}{\boldsymbol{u}} \circ \overset{\smile}{\boldsymbol{i}} = \breve{\boldsymbol{u}} \circ \overset{\smile}{\boldsymbol{i}} = 0 \tag{2.24c}$$

According to the earliest presentation of the CPT-framework[A4], only five of the nine power-like terms above are independent. Power terms in Equations (2.24) and the ones to be presented shortly are at any instant of time conservative, and corresponds to the principle of *conservation of instantaneous homo-powers.* This fundamental property known from sinusoidal conditions, can now be transferred to a non-sinusoidal and unbalanced electric power system.

2.3 Single-phase application

2.4 Instantaneous powers definition

If the fundamental quantities $u(t)$, $\overset{\frown}{u}(t)$ and $\breve{u}(t)$ regarding voltages and similar to currents $i(t)$, $\overset{\frown}{i}(t)$ and $\overset{\smile}{i}(t)$ are instantaneous, the conservative power theory defines various instantaneous power terms. The authors propose a single quantity called *instantaneous complex power* $s(t)$ made up from *instantaneous real power* $p(t)$ and *instantaneous imaginary power* $q(t)$:

$$s(t) = p_{\alpha}(t) + jq_{\beta}(t) \quad (\alpha = 1 \ldots 3,\ \beta = 1 \ldots 4) \quad \mathit{(VA)} \tag{2.25}$$

Note the differentiation between an active and non-active power component which is in accordance to what found in the pq-theory and classic power theory. In the CPT there is not a final definition of instantaneous complex power, because the real and imaginary power terms have multiple definitions, and can tailored to fit specific needs and applications.

2.4.1 *Instantaneous real power*

This first definition of real instantaneous power coincides with the general definition of total power, and is simply the product of voltage and current:

$$p_1(t) = u(t) \circ i(t) \quad \mathit{(W)} \tag{2.26a}$$

This definition is the one most widely referred to in technical publications by P.Tenti and P.Mattavelli, and therefore also utilized in this work for easy comparison. Notably Equation (2.26a) is the only power definition being universally accepted across all instantaneous power theories. Similar definition can be seen both in the pq-theory[B21] and the classical power theory, and its physical interpretation and general validity for all network operating conditions will be demonstrated experimentally in next chapter.

There is a second definition used involving voltage homo-integral, and current homo-derivative that is especially applicable in compensation of unbalanced and distorted currents:

$$p_2(t) = \frac{u(t) \circ i(t) - \hat{u}(t) \circ \breve{i}(t)}{2} \quad (W) \tag{2.26b}$$

Also there has been suggested a third definition of instantaneous real power, which is symmetric in respect to the second definition:

$$p_3(t) = \frac{u(t) \circ i(t) - \breve{u}(t) \circ \hat{i}(t)}{2} \quad (W) \tag{2.26c}$$

The three power terms are all conservative, however they do not produce the same value at any instant of time. Note that for sinusoidal operation $p_2(t)$ and $p_3(t)$ will have a constant value at each instant of time, meaning they represent the unidirectional real power flow.

2.4.2 *Instantaneous imaginary power*

For the instantaneous reactive power there are four different definitions. The first can be found as the product of current and the homo-integral of voltage, and can be considered as the simplest and most widely used by the main developers:

$$q_1(t) = \hat{u}(t) \circ i(t) \quad (VAR) \tag{2.27a}$$

The second alternative is the so called dual version of the first definition, a minus sign must be added so that the two get same average value.

$$q_2(t) = -u(t) \circ \hat{i}(t) \quad (VAR) \tag{2.27b}$$

By combining the first two definitions and dividing by a factor of two, leads to third version also referred to as *integral imaginary power* as it only contains homo-integrals. Similar to $p_2(t)$ this power term is specifically intended for compensation purpose:

$$q_3(t) = \frac{\hat{u}(t) \circ i(t) - u(t) \circ \hat{i}(t)}{2} \quad (VAR) \tag{2.27c}$$

An imaginary power term based on homo-integral of voltage and current is desirable, as it enables connection to a physical phenomena. For network conditions having sinusoidal voltages and currents, the classical power theory recognizes reactive power as a part of the powerflow that does not present any useful real work, but more of a quantification of energy storage in the form of magnetic flux in electric machines and electric charge in capacitors.

Also reactive power is traditionally associated to electronic loads, while as demonstrated later in next chapter, the CPT does not link reactive power and non-linear loads in the same fashion as the classic power theory or the *pq*-theory do.

$$q_4(t) = \frac{u(t) \circ \breve{i}(t) - \breve{u}(t) \circ i(t)}{2} \quad \textit{(VAR)} \tag{2.27d}$$

The fourth definition is symmetrical to $q_3(t)$ and is termed *differential imaginary power* as it contains only homo-differentials. Using differential quantities is not recommended because of their noise sensitivity that may lead to instability. In general these four unique power terms offer conservativity, but they are not equal at each instant of time. In sinusoidal mode $q_1(t)$, $q_2(t)$, $q_3(t)$ and $q_4(t)$ will have a constant value equal to reactive power in Equation (2.29).

2.5 Average powers definition

In order to extract various current terms there is need to compute average value of the aforementioned instantaneous power terms. The uniqueness of these average power terms is to maintain their physical interpretation in both sinusoidal and distorted network conditions, thanks to homo-variables.

Whenever dealing with average terms its referred to *active power P* and *reactive power Q* instead of *instantaneous real power* and *instantaneous imaginary power* respectively. Average values are obtained by calculating internal product of each instantaneous power component.

2.5.1 *Active power*

As known from classic power theory the mean value of active instantaneous power represents permanent flow of power that can contribute to useful real work. Generally $p_1(t)$, $p_2(t)$ and $p_3(t)$ do not coincide, but once they are averaged over one time period $T_{CPT} = 20.0\,ms$ they will have equal values:

$$P = \overline{p}_1 = \overline{p}_2 = \overline{p}_3 = \langle u(t), i(t) \rangle = \frac{\langle u, i \rangle - \langle \widehat{u}, \breve{i} \rangle}{2} = \frac{\langle u, i \rangle - \langle \breve{u}, \widehat{i} \rangle}{2} \quad \textit{(W)} \tag{2.28}$$

2.5.2 *Reactive power*

For sinusoidal network conditions reactive power relates to reactive elements *(inductive and capacitive circuit components)*, and quantifies the amount of energy they store in the system. By aid of this new definition of reactive power it is possible to perform reactive compensation in distorted voltage regimes, no matter where the reactive load is located. This was demonstrated several times by P.Tenti et al.[A8,A9,A18] for the time being only in simulative work, thought this property has still not been experimentally verified.

$$Q = \bar{q}_1 = \bar{q}_2 = \bar{q}_3 = \langle \widehat{u}(t), i(t) \rangle = -\langle u, \widehat{i} \rangle = \frac{\langle \widehat{u}, i \rangle - \langle u, \widehat{i} \rangle}{2} \quad (VAR) \qquad (2.29)$$

The average value of the three first instantaneous imaginary powers $q_1(t)$, $q_2(t)$ and $q_3(t)$ is identical, however the average value of $q_4(t)$ is not equal to Q. The particular expression of $q_4(t)$ was introduced as it proves to be useful for control purposes. The average value of all imaginary powers becomes equal and constant during sinusoidal operation.

2.6 Current terms definition

Now after established a way of splitting up the total power flow into various average power terms that can be related to actual physical phenomenas, these can be utilized to derive corresponding decomposition of the load current. The current components constitute one of the great potentials and effectiveness of the conservative power theory.

2.6.1 Active current

The *active current* $i_a(t)$ is defined as the minimum port current that transports the same active power P as the original current $i(t)$. Notably $i_a(t)$ corresponds to the *Fryze* active current[B21] which is also utilized in the *pq* and *abc*-power theories:

$$i_a(t) = \frac{\langle u, i \rangle}{\|u\|^2} u = \frac{P}{\|u\|^2} u = G_e u \quad (A) \qquad (2.30a)$$

Here G_e is the equivalent conductance at the point of common connection *(PCC)*. The active current is responsible for the total active power P, but will by convention not contribute to the reactive power flow Q:

$$P_a(t) = \langle u, i_a \rangle = \|u\| \cdot \|i_a\| = \langle u, i \rangle = P \qquad (2.30b)$$

$$Q_a(t) = \langle \widehat{u}, i_a \rangle = G_e \langle u, \widehat{u} \rangle = 0 \qquad (2.30c)$$

2.6.2 Reactive current

The *reactive current* $i_r(t)$ is defined as the minimum current that transports the same reactive power Q as the original load current $i(t)$:

$$i_r(t) = \frac{\langle \widehat{u}, i \rangle}{\|\widehat{u}\|^2} \widehat{u} = \frac{Q}{\|\widehat{u}\|^2} \widehat{u} = B_e \widehat{u} \quad (A) \qquad (2.31a)$$

Here B_e is the equivalent susceptance at the PCC. The reactive current is responsible for total reactive power Q, while it does not contribute to active power flow P:

$$P_r(t) = \langle u, i_r \rangle = B_e \langle u, \widehat{u} \rangle = 0 \qquad (2.31b)$$

$$Q_r(t) = \langle \widehat{u}, i_r \rangle = \|\widehat{u}\| \cdot \|i_r\| = \langle \widehat{u}, i \rangle = Q \tag{2.31c}$$

2.6.3 Void current

Dealing with non-linear load conditions, the active $i_a(t)$ and reactive $i_r(t)$ currents are not fully sufficient to describe the measured load current. Therefore *void current* $i_v(t)$ is introduced as the last current component to account for residual terms:

$$i_v(t) = i(t) - i_a(t) - i_r(t) \quad (A) \tag{2.32a}$$

This residual current term is named void current simply because its not responsible for either active P nor reactive Q power transportation:

$$P_v(t) \quad = \quad \langle u, i_v \rangle = \langle u, i - i_a - i_r \rangle = P - P_a - P_r = 0 \tag{2.32b}$$

$$Q_v(t) = \langle \widehat{u}, i_v \rangle = \langle \widehat{u}, i - i_a - i_r \rangle = Q - Q_a - Q_r = 0 \tag{2.32c}$$

To gain a more meaningful explanation of the void current, the authors turn to Fourier analysis[A11]. Having a voltage $u(t)$ with the harmonic content $h \in \{\mathbb{N}_u\}$, it can be described in the time-domain as:

$$u(t) = \sum_{h \in \{\mathbb{N}_u\}} u_h(t) = \sum_{h \in \{\mathbb{N}_u\}} \sqrt{2} U_h \sin(h\omega t + \alpha_h) \tag{2.33a}$$

Equally the current $i(t)$ has the harmonic content $h \in \{\mathbb{N}_i\}$ and can be written as:

$$i(t) = \sum_{h \in \{\mathbb{N}_i\}} i_h(t) = \sum_{h \in \{\mathbb{N}_i\}} \sqrt{2} I_h \sin(h\omega t + \beta_h) \tag{2.33b}$$

The voltage and current may have a common set of harmonics defined as $\mathbb{N}_c = \{\mathbb{N}_u \cap \mathbb{N}_i\}$ such that:

$$u(t) = \sum_{h \in \{\mathbb{N}_c\}} u_h(t) + \sum_{h \in \{\mathbb{N}_u - \mathbb{N}_c\}} u_h(t) = u_k(t) + u_g(t) \tag{2.33c}$$

$$i(t) = \sum_{h \in \{\mathbb{N}_c\}} i_h(t) + \sum_{h \in \{\mathbb{N}_i - \mathbb{N}_c\}} i_h(t) = i_k(t) + i_g(t) \tag{2.33d}$$

Pointing out that voltage and current can be split into two main components; *homo-frequential* part $u_k(t)$ and $i_k(t)$ which are common harmonics in both voltage and current, and the so called *generated* part including those harmonics $u_g(t)$ and $i_g(t)$ that are unique for each quantity. The void current is said to contain those harmonics that cannot be found in the voltage, in other words the generated currents $i_g(t)$. This property is of great value when analyzing non-linear loads inducing harmonic line currents.

The homo-frequential current $i_k(t)$ can be projected into a corresponding active and reactive current component, for the h-th harmonic yields:

$$i_{ah}(t) = \frac{\langle u_h, i_h \rangle}{\|u_h\|^2} u_h = \frac{P_h}{U_h^2} u_h = G_h u_h \quad (A) \tag{2.34a}$$

$$i_{rh}(t) = \frac{\langle \widehat{u}_h, i_h \rangle}{\|\widehat{u}_h\|^2} \widehat{u}_h = \frac{h^2 Q_h}{U_h^2} \widehat{u}_h = B_h \widehat{u}_h \quad (A) \tag{2.34b}$$

By defining the phase shift between the h-th harmonic pair as $\varphi_h = \alpha_h - \beta_h$, corresponding active and reactive harmonic powers can be defined as:

$$P_h(t) = U_h I_h \cos\varphi_h, \quad Q_h(t) = \frac{U_h I_h \sin\varphi_h}{h} \tag{2.35a}$$

$$G_h(t) = \frac{I_h}{U_h} \cos\varphi_h, \quad B_h(t) = \frac{h I_h}{U_h} \sin\varphi_h \tag{2.35b}$$

According to the conservativity property, the sum of harmonic powers $P_h(t)$ and $Q_h(t)$ must be equal to total active P and reactive power Q:

$$\sum_{h \in \{N_c\}} P_h(t) = P \tag{2.36a}$$

$$\sum_{h \in \{N_c\}} Q_h(t) = Q \tag{2.36b}$$

Assuming that total current $i(t)$ is divided into three components; *generated current* $i_g(t)$, *total harmonic active current* $i_{Ha}(t)$ and *total reactive current* $i_{Hr}(t)$ gives:

$$i(t) = \sum_{h \in \{N_c\}} i_{ah}(t) + \sum_{h \in \{N_c\}} i_{rh}(t) + i_g(t) = i_{Ha} + i_{Hr} + i_g \tag{2.37}$$

however it can be demonstrated that $\|i_{Ha}\| \geq \|i_a\|$ and $\|i_{Hr}\| \geq \|i_r\|$. The total harmonic active and reactive currents generally do not match the active and reactive current respectively, so the authors have adopted[A3] the terms *active scattering current* $i_{sa}(t)$ and *reactive scattering current* $i_{sr}(t)$ where:

$$i_{sa}(t) = i_{Ha}(t) - i_a(t) \quad (A) \tag{2.38a}$$

$$i_{sr}(t) = i_{Hr}(t) - i_r(t) \quad (A) \tag{2.38b}$$

The final definition of void current can now be presented as:

$$i_v(t) = i_{sa}(t) + i_{sr}(t) + i_g(t) \quad (A) \tag{2.39}$$

Noting that terminology of scattering current components and generated current is adopted from *Czarneckis*[A2] power theory. The void current has proven to be a powerful element for current compensation techniques, as will be demonstrated later. In short the scattering currents account for a power networks frequency response as the general tendency[C26] is $G_h \neq G_e$ and $B_h \neq B_e$.

The complete decomposition of load current $i(t)$, and all terms having property of being mutually mathematical orthogonal:

$$\begin{aligned}\|i\|^2 &= \|i_a\|^2 + \|i_r\|^2 + \|i_v\|^2 \\ &= \|i_a\|^2 + \|i_r\|^2 + \|i_{sa}\|^2 + \|i_{sr}\|^2 + \|i_g\|^2 \end{aligned} \tag{2.40}$$

Orthogonal components are often used in advanced power engineering, such as modeling of various electric machines *(e.g. synchronous generator)*, or utilized in high-performance space vector control of electric drives and active FACTS devices. These control methods often incorporate the *$\alpha\beta\gamma$-transformation* and the very similar *dq0-transformation*, with the assumption of sinusoidal voltages and currents.

The conservative power theory ensures orthogonal current components independent of voltage regime, with the consequence that manipulation of one term will not affect the remaining parcels. This can be exploited to choose very specific current filtering strategies, as will be demonstrated later in simulation chapter.

2.7 Complete power description

2.7.1 Average power terms

The instantaneous complex power $s(t)$ can be extended to its average value S, which is simply called *complex power*. Its a complex quantity where the active power P is placed on the real axis, and the reactive power Q is located on the imaginary axis:

$$S = P + jQ \quad (VA) \tag{2.41}$$

The complex power possess the same properties as the apparent power S^* known from classical power theory, where P^* and Q^* quantify the power absorption and energy storage respectively.
However complex power does not give a complete description of the total power flow, as the void current also must be taken into account. The conservative power theory defines a new and more general form of the *apparent power A* given as:

$$A = \|u(t)\| \cdot \|i(t)\| \quad (VA) \tag{2.42a}$$

According to the Cauchy-Schwartz inequality in Equation (2.21) yields:

$$\left|\langle u(t), i(t)\rangle\right| \leq \|u(t)\| \cdot \|i(t)\| \quad \Leftrightarrow \quad |P| \leq A \tag{2.42b}$$

The apparent power A will only converge with modulus of apparent power S under sinusoidal operation. The apparent power A can be decomposed into:

$$\begin{aligned}A^2 &= \|u\|^2\|i_a\|^2 + \|u\|^2\|i_r\|^2 + \|u\|^2\|i_v\|^2 \\ &= P^2 + Q^2 + D^2 = S^2 + D^2\end{aligned} \tag{2.43}$$

Power term D origins from the void current, and is called the *distortion power*, made up from *voltage distortion power D_u* and *current distortion power D_i*:

$$D^2 = A^2 - P^2 - Q^2 = \frac{\left\|u\right\|^2 - \left\|\widehat{u}\right\|^2}{\left\|\widehat{u}\right\|^2} \cdot Q^2 + \left\|u\right\|^2 \cdot \left\|i_v\right\|^2 = D_u^2 + D_i^2 \qquad (2.44)$$

The distortion power terms D_u and D_i are given as:

$$D_u = Q\sqrt{\left(\frac{\left\|u(t)\right\|^2 - \left\|\widehat{u}(t)\right\|^2}{\left\|\widehat{u}(t)\right\|^2}\right)} \qquad D_i = \left\|u(t)\right\| \cdot \left\|i_v(t)\right\| \quad (VA) \qquad (2.45)$$

Revealing that D_v is non-zero in situations where the load draws reactive power, and the network voltage is distorted. Independently of reactive power consumption the voltage distortion power will disappear with sinusoidal voltage, as the homo-integral voltage and original voltage in Equation (2.45) become equal. The current distortion power is only present due to void current exclusively, meaning part of the current that does not contribute to complex power S.

It is worth to notice that distortion power D and apparent power A are **not** conservative quantities[A18]. This makes sense when observing the power system as a whole, harmonic phenomenas must be strictly treated as local events, they do not accumulate in the same physical manner as reactive and active powers do.

As depicted in **Figure 2.1** the traditional power theory describes the power flow in the way of a *power triangle*, where active power P and reactive power Q are mutually orthogonal, and their vector sum constitute the apparent power S. In case of distorted voltages and currents the CPT extends the decomposition by including distortion power D. Having three mutually orthogonal power terms where the vector sum equals a new apparent power A, these constitute a three dimensional power space *(power tetrahedron)*.

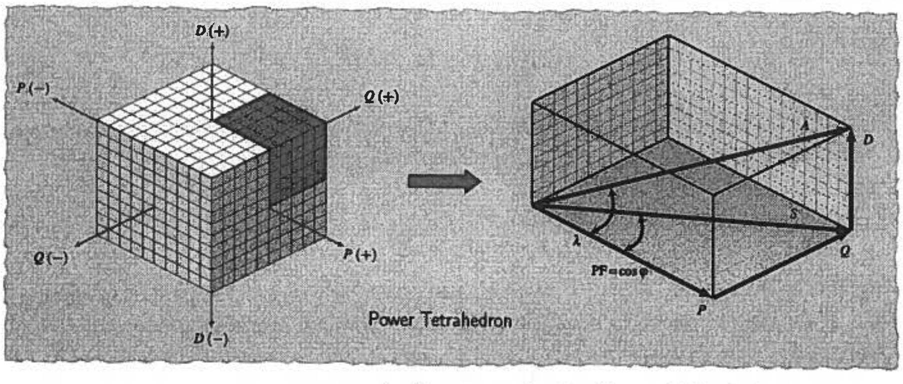

Figure 2.1 – *In case of unlinear loads the familiar power triangle will not sufficiently describe the power flow. This is solved by the inclusion of distortion power, and yields both for single-phase circuits and the basic three-phase approach. The concept of distortion power and associated tetrahedron power space, was introduced by Budeanu as early as 1927.*

2.7.2 Quality indexes

Under conditions where current and voltage are distorted, the amount of harmonic distortion is often quantified by means of the index called the *total harmonic distortion THD*. The index is defined as the ratio between RMS of total harmonic components and the fundamental component.

Consider voltage $u(t)$ with total effective value equal to U and the corresponding RMS value of fundamental part U_{h1}, total harmonic distortion can be assessed as:

$$THD_u = 100 \cdot \frac{\sqrt{U^2 - U_{hl}^2}}{U_{hl}} = 100 \cdot \sqrt{\sum_{n \neq 1} \left(\frac{U_{hn}}{U_{hl}} \right)^2} \tag{2.46}$$

In terms of the conservative power theory THD_u can be easily approximated; when computing the voltage homo-integral $\widehat{u}(t)$ most of the harmonic content in $u(t)$ will be removed by the integrator so that $\widehat{u}(t) \approx u_f(t)$, and the purity and quality of the voltage waveform can be quantified by the *voltage distortion factor* σ_u:

$$\sigma_u = \sqrt{\left(\frac{\|u\|^2 - \|\widehat{u}\|^2}{\|\widehat{u}\|^2} \right)} = \frac{D_u}{Q} \tag{2.47}$$

In the same fashion quantification of harmonic distortion in current can be approximated by the *current distortion factor* σ_i assuming that most of the harmonics are lumped into the void current, which holds true whenever the voltage is ideal:

$$\sigma_i = \frac{\|i_v(t)\|}{\|i(t)\|} = \frac{D_i}{A} \tag{2.48}$$

For the classical power theory its also custom to measure the quality or efficiency of the powerflow by means of the conventional power factor $PF = \cos\varphi = \frac{P}{S}$. The developers have introduced a similar power quality index for the CPT. In terms of complex power S and distortion factors σ_v and σ_i apparent power A can be written as:

$$A^2 = P^2 + Q^2 + D^2 = \frac{P^2 + Q^2 \cdot (1 + \sigma_u^2)}{1 - \sigma_i^2} \tag{2.49}$$

Normally the voltage distortion is limited while the current can be severely distorted, thus when assuming that $\sigma_u \approx 0$ the apparent power can be expressed as:

$$A \approx \frac{S}{\sqrt{1 - \sigma_i^2}} \tag{2.50}$$

Similar to the power factor PF from classic theory the power factor λ implemented in CPT, is defined as the ratio between active power P and apparent power A:

$$\lambda = \frac{P}{A} \approx \frac{P}{S} \cdot \sqrt{1 - \sigma_i^2} \tag{2.51}$$

If operating conditions suggest pure sinusoidal current and voltage, the current distortion factor will diminish to null, and as numerously demonstrated in the next chapter the proposed power factor λ will converge with the classical power factor PF:

$$\lambda = PF = \cos\varphi = \frac{P}{S} \tag{2.52}$$

The distortion powers D_u and D_i from Equations (2.45) and associated distortion factors σ_v and σ_i from Equations (2.47) and (2.48), can be easily computed as the variables are already embedded in the CPT-algorithm. However these quantities were omitted in this work, but could be interesting to evaluate in future investigations.

2.8 Three-phase application

2.9 Instantaneous powers definition

In previous section the conservative power theory was defined for single-phase systems, and its general validity in both sinusoidal and non-sinusoidal regimes was presented. In order to make it even more general, it can with minor adjustment be extended to three-phase systems, or any arbitrary N-polyphase network by replacing scalar with vector quantities.

The CPT is valid both in *three-phase three-wire* and *three-phase four-wire* systems provided that system voltages are measured against a proper reference potential.[1] Assume having a three-phase system where measured voltages ***u(t)*** and currents ***i(t)*** and their associated homo-variables are given as:

$$\boldsymbol{u}(t) = \begin{bmatrix} u_1(t) \\ u_2(t) \\ u_3(t) \end{bmatrix} \quad \overset{\frown}{\boldsymbol{u}}(t) = \begin{bmatrix} \overset{\frown}{u}_1(t) \\ \overset{\frown}{u}_2(t) \\ \overset{\frown}{u}_3(t) \end{bmatrix} \quad \breve{\boldsymbol{u}}(t) = \begin{bmatrix} \breve{u}_1(t) \\ \breve{u}_2(t) \\ \breve{u}_3(t) \end{bmatrix} \tag{2.53}$$

$$\boldsymbol{i}(t) = \begin{bmatrix} i_1(t) \\ i_2(t) \\ i_3(t) \end{bmatrix} \quad \overset{\frown}{\boldsymbol{i}}(t) = \begin{bmatrix} \overset{\frown}{i}_1(t) \\ \overset{\frown}{i}_2(t) \\ \overset{\frown}{i}_3(t) \end{bmatrix} \quad \breve{\boldsymbol{i}}(t) = \begin{bmatrix} \breve{i}_1(t) \\ \breve{i}_2(t) \\ \breve{i}_3(t) \end{bmatrix} \tag{2.54}$$

Instantaneous real power terms previously defined for single-phase environment in Equations (2.26a), are valid for three-phase systems when introducing scalar product:

$$p_1(t) = \boldsymbol{u} \circ \boldsymbol{i} \quad (W) \tag{2.55a}$$

$$p_2(t) = \frac{\boldsymbol{u} \circ \boldsymbol{i} - \overset{\frown}{\boldsymbol{u}} \circ \breve{\boldsymbol{i}}}{2} \quad (W) \tag{2.55b}$$

$$p_3(t) = \frac{\boldsymbol{u} \circ \boldsymbol{i} - \breve{\boldsymbol{u}} \circ \overset{\frown}{\boldsymbol{i}}}{2} \quad (W) \tag{2.55c}$$

and the instantaneous imaginary power terms from Equations (2.27) yield:

---

[1] The CPT only accepts phase voltages. Using line voltages provoke erroneous detection of active and reactive unbalanced elements, in addiction to balanced reactive elements.

$$q_1(t) = \widehat{\boldsymbol{u}} \circ \boldsymbol{i} \quad (VAR) \tag{2.56a}$$

$$q_2(t) = -\boldsymbol{u} \circ \widehat{\boldsymbol{i}} \quad (VAR) \tag{2.56b}$$

$$q_3(t) = \frac{\widehat{\boldsymbol{u}} \circ \boldsymbol{i} - \boldsymbol{u} \circ \widehat{\boldsymbol{i}}}{2} \quad (VAR) \tag{2.56c}$$

$$q_4(t) = \frac{\boldsymbol{u} \circ \breve{\boldsymbol{i}} - \breve{\boldsymbol{u}} \circ \boldsymbol{i}}{2} \quad (VAR) \tag{2.56d}$$

Both real and imaginary power terms in Equations (2.55) and (2.56) possess same physical interpretation as those defined for single-phase power systems. However the given instantaneous powers only apply for the power network as a whole, so that information regarding each separate phase is lost.

This is in fact a fundamental requirement in Tellegen's theorem; the calculated power quantities are only conservative when the network is analyzed as an unified system. Extracting instantaneous powers for each separate phase is however not an issue if required, as the information is already embedded in the CPT-algorithm.

On the other hand such a procedure cannot be used for a distributed compensation strategy, which is dependent on the conservative feature to work successfully.
The instantaneous complex power for a three-phase system is obtained by summing the contributions from each individual phase:

$$s(t) = p(t) + jq(t) = \sum_{n=1}^{3} p_n(t) + j \sum_{n=1}^{3} q_n(t) \tag{2.57a}$$

or

$$s(t) = p_\alpha(t) + jq_\beta(t) \quad (\alpha = 1 \ldots 3,\ \beta = 1 \ldots 4) \quad (VA) \tag{2.57b}$$

2.10 Average powers definition

Average power terms can be expanded in similar way if replacing scalar with vector operators. Independently of unsymmetric or harmonic properties of current and voltage waveforms, the average value of all alternative expressions in Equations (2.57) becomes equal when averaged over one fundamental time period:

2.10.1 Active power

$$P = \overline{p}_1 = \overline{p}_2 = \overline{p}_3 = \langle \boldsymbol{u}, \boldsymbol{i} \rangle = \frac{\langle \boldsymbol{u}, \boldsymbol{i} \rangle - \langle \widehat{\boldsymbol{u}}, \breve{\boldsymbol{i}} \rangle}{2} = \frac{\langle \boldsymbol{u}, \boldsymbol{i} \rangle - \langle \breve{\boldsymbol{u}}, \widehat{\boldsymbol{i}} \rangle}{2} \tag{2.58}$$

2.10.2 Reactive power

$$Q = \overline{q}_1 = \overline{q}_2 = \overline{q}_3 = \overline{q}_4 = \langle \widehat{u}, i \rangle = -\langle u, \widehat{i} \rangle = \frac{\langle \widehat{u}, i \rangle - \langle u, \widehat{i} \rangle}{2} = \frac{\langle u, \breve{i} \rangle - \langle \breve{u}, i \rangle}{2} \tag{2.59}$$

Here power absorption and energy storage for each phase are lumped into a single unit *(active power P and reactive power Q respectively)*. They are conservative in all grid operating conditions, which is interesting in terms of reactive power regulation or compensation under non-sinusoidal voltage regimes.

2.11 Current terms definition

When dealing with polyphase systems of N conductors, there are basically two ways to utilize the conservative power theory. One of the two versions is more elaborate as it pays more detailed attention to any unsymmetry in line currents.

2.11.1 Basic approach

The first approach is exactly the same as used in a single-phase system. By considering the n-th phase as a single-phase system results in the extraction of *basic current terms*. Terms $i_{an}(t)$, $i_{rn}(t)$ and $i_{vn}(t)$ can be recognized as *active*, *reactive* and *void* currents:

$$i_a(t) = \{i_{an}\}_{n=1}^{N}, \quad i_{an}(t) = \frac{\langle u_n, i \rangle}{\|u_n\|^2} u_n = \frac{P_n}{\|u_n\|^2} u_n = G_n u_n \quad (A) \tag{2.60a}$$

$$i_r(t) = \{i_{rn}\}_{n=1}^{N}, \quad i_{rn}(t) = \frac{\langle \widehat{u}_n, i \rangle}{\|\widehat{u}_n\|^2} \widehat{u}_n = \frac{Q_n}{\|\widehat{u}_n\|^2} \widehat{u}_n = B_n \widehat{u}_n \quad (A) \tag{2.60b}$$

$$i_v(t) = \{i_{vn}\}_{n=1}^{N}, \quad i_{vn}(t) = i_n(t) - i_{an}(t) - i_{rn}(t) \quad (A) \tag{2.60c}$$

The void current $i_{vn}(t)$ can theoretically be split into *scattered* and *generated* terms, however it was reported problems[A5] achieving this in practice. Consequently the void current defined in Equation (2.60c) was employed in this work. As three-phase systems are often connected to ground or a neutral conductor *(three-phase four-wire topology)*, there may be instances of unsymmetric loads where current flows in the neutral conductor:

$$i_{a0}(t) = -\sum_{n=1}^{N} i_{an}(t) \qquad \textit{neutral active current} \tag{2.61a}$$

$$i_{r0}(t) = -\sum_{n=1}^{N} i_{rn}(t) \qquad \textit{neutral reactive current} \tag{2.61b}$$

$$i_{v0}(t) = -\sum_{n=1}^{N} i_{vn}(t) \qquad \textit{neutral void current} \tag{2.61c}$$

Neutral currents are denoted with minus sign as they flow upstream back towards the source or feeding point. In terms of current decomposition the basic approach clearly processes each phase separately in terms of respective phase voltage, current and powers. The basic approach is often utilized by H.Paredes et al. in their reviews of the conservative power theory.[A13–A16,B22–B24]

2.11.2 *Extended approach*

When dealing with three phase systems the simplified approach outputs correct results, however there is possible to split up the currents into even more segments accounting for unsymmetry in the system. The first step is to recalculate the active and reactive current terms into *balanced current* terms:

2.11.3 *Balanced active currents*

$$\boldsymbol{i}_a^b(t) = \frac{\langle \boldsymbol{u},\boldsymbol{i}\rangle}{\|\boldsymbol{u}\|^2}\boldsymbol{u} = \frac{P}{\|\boldsymbol{u}\|^2}\boldsymbol{u} = G^b\boldsymbol{u}, \quad \Rightarrow \langle \boldsymbol{u},\boldsymbol{i}_a^b\rangle = P \tag{2.62a}$$

Where $\boldsymbol{i}_a^b(t)$ are called *balanced active currents* while G^b is equivalent balanced conductance, and is equal for all phases as they are assumed to be symmetric. The *balanced neutral active current* $i_{a0}^b(t)$ is simply the sum of phase currents:

$$i_{a0}^b(t) = -\sum_{n=1}^{N} i_{an}^b(t) \tag{2.62b}$$

2.11.4 *Balanced reactive currents*

$$\boldsymbol{i}_r^b(t) = \frac{\langle \widehat{\boldsymbol{u}},\boldsymbol{i}\rangle}{\|\widehat{\boldsymbol{u}}\|^2}\widehat{\boldsymbol{u}} = \frac{Q}{\|\widehat{\boldsymbol{u}}\|^2}\widehat{\boldsymbol{u}} = B^b\boldsymbol{u}, \quad \Rightarrow \langle \boldsymbol{u},\boldsymbol{i}_r^b\rangle = Q \tag{2.62c}$$

Where $\boldsymbol{i}_r^b(t)$ are termed *balanced reactive currents* while B^b is equivalent balanced susceptance, and is equal for all phases by intentionally assuming they are symmetric. The *balanced neutral reactive current* $i_{r0}^b(t)$ is simply the sum of phase currents:

$$i_{r0}^b(t) = -\sum_{n=1}^{N} i_{rn}^b(t) \tag{2.62d}$$

The active and reactive balanced currents are computed by the simple assumption that powers from Equations (2.58) and (2.59) are shared equally among all three phases. Unlike the pq-theory[B21] the CPT does not account the neutral conductor as taking part of the powerflow, which is more in accordance with the general interpretation.

After computed the balanced current components the decomposition is expanded further by introducing *unbalanced current* terms, obtained by subtracting balanced currents from their basic current terms.

2.11.5 *Unbalanced active currents*

$$\boldsymbol{i}_a^u(t) = \boldsymbol{i}_a(t) - \boldsymbol{i}_a^b(t), \quad \Rightarrow \boldsymbol{i}_a(t) = \{i_{an}^u(t)\}_{n=1}^N = \left\{(G_n - G^b)u_n\right\}_{n=1}^N \tag{2.63a}$$

The *unbalanced active currents* $\boldsymbol{i}_a^u(t)$ are only present if the equivalent phase conductances are unsymmetric. The *unbalanced neutral active current* $i_{a0}^u(t)$ becomes:

$$i_{a0}^u(t) = -\sum_{n=1}^{N} i_{an}^u(t) \tag{2.63b}$$

2.11.6 *Unbalanced reactive currents*

$$\boldsymbol{i}_r^u(t) = \boldsymbol{i}_r(t) - \boldsymbol{i}_r^b(t), \quad \Rightarrow \boldsymbol{i}_r(t) = \{i_{rn}^u(t)\}_{n=1}^N = \left\{(B_n - B^b)\widehat{u}_n\right\}_{n=1}^N \tag{2.64a}$$

The *unbalanced reactive current* $\boldsymbol{i}_r^u(t)$ only appear when equivalent phase susceptances are unsymmetric. Equally the *unbalanced neutral reactive current* $i_{r0}^u(t)$ yields:

$$i_{r0}^u(t) = -\sum_{n=1}^{N} i_{rn}^u(t) \tag{2.64b}$$

2.11.7 *Final current decomposition*

Now arriving at the final and most general decomposition of the measured load currents. According to the conservative power theory (**Figure 2.2**) it incorporates parcels that are linked to real physical phenomenas like, power absorption and energy storage in the network. Also there are terms that can be linked to impedance unsymmetry, and finally components that origin directly from harmonic pollution in voltage or the load itself:

$$\boldsymbol{i}(t) = \boldsymbol{i}^b(t) + \boldsymbol{i}^u(t) + \boldsymbol{i}_v(t) = \boldsymbol{i}_a^b(t) + \boldsymbol{i}_a^u(t) + \boldsymbol{i}_r^b(t) + \boldsymbol{i}_r^u(t) + \boldsymbol{i}_v(t) \quad (A) \tag{2.65}$$

It was mathematically demonstrated[A2] that all terms in Equation (2.65) are mutually orthogonal, so that similar to classic theory resulting line currents can be written:

$$\begin{aligned}\left\|\boldsymbol{i}(t)\right\|^2 &= \left\|\boldsymbol{i}^b(t)\right\|^2 + \left\|\boldsymbol{i}^u(t)\right\|^2 + \left\|\boldsymbol{i}_v(t)\right\|^2 \\ &= \left\|\boldsymbol{i}_a^b(t)\right\|^2 + \left\|\boldsymbol{i}_a^u(t)\right\|^2 + \left\|\boldsymbol{i}_r^b(t)\right\|^2 + \left\|\boldsymbol{i}_r^u(t)\right\|^2 + \left\|\boldsymbol{i}_v(t)\right\|^2\end{aligned} \tag{2.66}$$

2.12 Complex powers

As the current components have property of being orthogonal, the apparent power can similar to Equation (2.43) be described as:

$$\begin{aligned}A^2 &= \left\|\boldsymbol{u}\right\|^2\left\|\boldsymbol{i}\right\|^2 = \left\|\boldsymbol{u}\right\|^2 \cdot \left(\left\|\boldsymbol{i}_a^b\right\|^2 + \left\|\boldsymbol{i}_a^u\right\|^2 + \left\|\boldsymbol{i}_r^b\right\|^2 + \left\|\boldsymbol{i}_r^u\right\|^2 + \left\|\boldsymbol{i}_v\right\|^2\right) \\ &= \left\|\boldsymbol{u}\right\|^2\left\|\boldsymbol{i}_a^b\right\|^2 + \left\|\boldsymbol{u}\right\|^2\left\|\boldsymbol{i}_r^b\right\|^2 + \left\|\boldsymbol{u}\right\|^2\left\|\boldsymbol{i}_a^u\right\|^2 + \left\|\boldsymbol{u}\right\|^2\left\|\boldsymbol{i}_r^u\right\|^2 + \left\|\boldsymbol{u}\right\|^2\left\|\boldsymbol{i}_v\right\|^2 \\ &= P^2 + Q^2 + N_a^{u2} + N_r^{u2} + D^2\end{aligned} \tag{2.67}$$

Compared to the basic definition of apparent power in Equation (2.49), there are two power terms added, which naturally origin from the unbalanced current terms. N_a^u is called *unbalanced active power* while N_r^u is referred to as *unbalanced reactive power.* Similarly to single-phase systems the apparent power A and distortion power D, do not possess the property of being conservative. Note that currents and power terms presented in the extended approach, are the most general form of the conservative power theory. However the extended framework boils down to the basic version when having either a single-phase system, or a three-phase system that is fully symmetric with ideal sinusoidal current waveforms.

In the three-phase extended mode the power decomposition contains five mutually orthogonal power components. In single-phase and basic three-phase modes the power mix can be adequately described in a $\mathbb{R}^3$ power space, while the extended mode defines a $\mathbb{R}^5$ space which cannot be easily graphically illustrated. Apparently all current and power quantities have units that are in fully agreement with the conventional power theory from the sinusoidal voltage regime. Contrary to H.Akagi's *pq*-theory which introduces new physical units *(volt ampere imaginary-vai)*, the CPT framework contains variables that retain the original nomenclature. They are related to physical phenomenas, and not relying on mathematical transformation *(Park transform).*

2.13 Basic theorems of compensation

Because the CPT offers three different alternations of both voltages and currents, there are in total six fundamental quantities presented in Equations (2.24), which can be combined to define either instantaneous real or imaginary power. The authors take selected power terms and define two compensation theorems.

2.13.1 The First Theorem of Compensation

States that voltages and currents will be proportional if the integral imaginary power $q_3(t)$ is zero at any instant of time, $q_3(t) = 0 \quad \forall t \Leftrightarrow u = R \cdot i$

$$q_3(t) = \frac{\overset{\frown}{u} \circ i - u \circ \overset{\frown}{i}}{2} = 0 \quad \Rightarrow \frac{i}{\overset{\frown}{i}} = \frac{u}{\overset{\frown}{u}} \quad \frac{1}{\omega \overset{\frown}{i}} \frac{d\overset{\frown}{i}}{dt} = \frac{1}{\omega \overset{\frown}{u}} \frac{d\overset{\frown}{u}}{dt} \quad \Rightarrow \frac{d\overset{\frown}{i}}{\overset{\frown}{i}} = \frac{d\overset{\frown}{u}}{\overset{\frown}{u}} \tag{2.68a}$$

$$\ln(\overset{\frown}{i}) + K = \ln(\overset{\frown}{u}) \quad \Rightarrow \ln \frac{\overset{\frown}{u}}{\overset{\frown}{i}} = K \quad \Rightarrow \overset{\frown}{u} = e^K \cdot \overset{\frown}{i} \quad \overset{\frown}{u} = R \cdot \overset{\frown}{i} \tag{2.68b}$$

$$\frac{1}{\omega} \frac{d\overset{\frown}{u}}{dt} = \frac{1}{\omega} \frac{d}{dt} [R \cdot \overset{\frown}{i}] \quad \Rightarrow u = R \cdot i \tag{2.68c}$$

$$u = R \cdot i \quad \Rightarrow \overset{\frown}{u} = R \cdot \overset{\frown}{i} \quad \Rightarrow \frac{\overset{\frown}{u}}{u} = \frac{\overset{\frown}{i}}{i} \quad \Rightarrow q_3(t) = \frac{\overset{\frown}{u} \circ i - u \circ \overset{\frown}{i}}{2} = 0 \tag{2.68d}$$

The same condition can be demonstrated for the differential imaginary power $q_4(t)$.

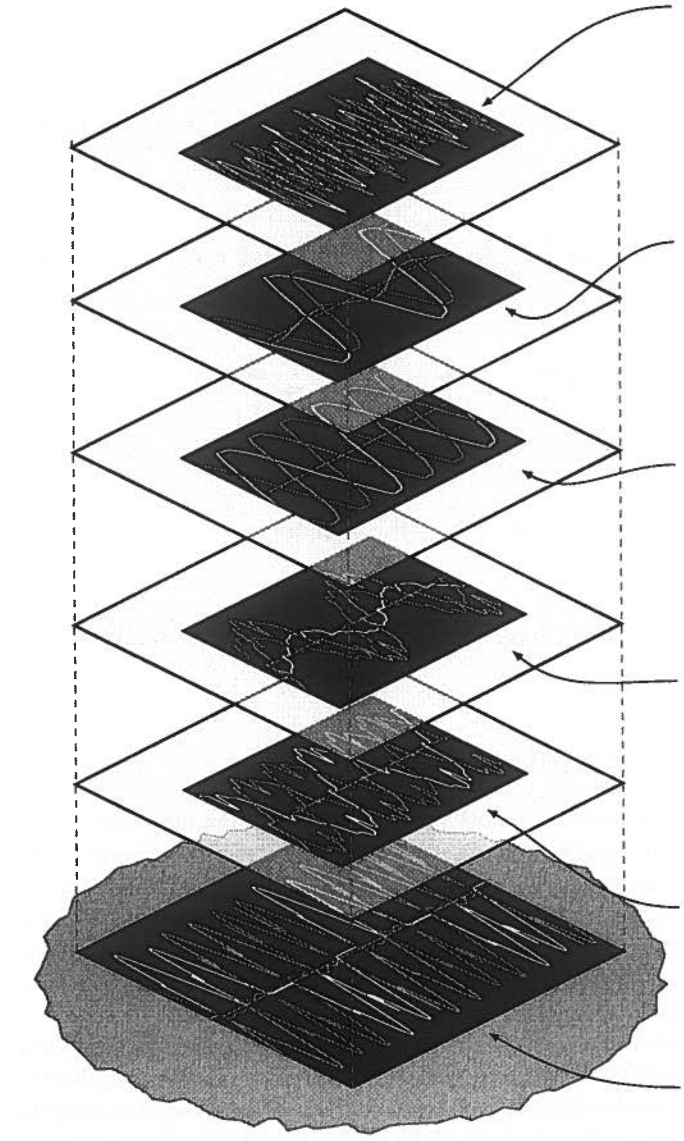

Void Currents - $i_v(t)$

- Transport distortion power exclusively.
- Contain three sub-components:
  - *Generated currents* account for current harmonics only found in line currents, but not in the voltage.
  - *Active scattering currents* account for harmonic active power.
  - *Reactive scattering currents* account for harmonic reactive power.
- Induce high order oscillation in instantaneous real and imaginary power.
- Important in context of current filtering applications.

Unbalanced Reactive Currents - $i_r^u(t)$

- Transport unbalanced reactive power exclusively.
- Account for negative and zero sequence currents, depending on system grounding and load type.
- Always appear in a fixed ±90° quadrature phase relation with respective phase voltages.
- Completes reactive compensation under unbalanced current conditions.
- Inherit harmonic content from homo-integrated voltage.
- Produce 100 Hz oscillation in instantaneous imaginary power.

Balanced Reactive Currents - $i_r^b(t)$

- Transport reactive power exclusively.
- Fully reproduce line currents drawn by a symmetric L-load.
- Inherit same harmonic spectrum as homo-integrated voltages.
- Adopts symmetric qualities from measured phase voltages.
- Ideal reference for reactive compensation in all voltage conditions.
- Appear always in fixed quadrature -90° phase-shift relation with respect to phase voltages.

Unbalanced Active Currents - $i_a^u(t)$

- Transport unbalanced active power exclusively.
- Account for negative and zero sequence currents, depending on system grounding and load type.
- Always appear in a fixed 0° or 180° phase-shift relation with respective phase voltages.
- Inherit harmonic content from measured phase voltages.
- Produce 100 Hz oscillation in instantaneous real power.

Balanced Active Currents - $i_a^b(t)$

- Transport active power exclusively.
- Fully reproduce line currents drawn by a symmetric R-load.
- Inherit same harmonic spectrum as found in measured phase voltages.
- Adopts positive and negative sequence components from measured phase voltages.
- Always appear aligned with respect to phase voltages.

Measured Line Currents - $i(t)$

3-Ph Thyristor Rectifier *(experiment 47)*.

Figure 2.2 – *In terms of the CPT operating in extended three-phase mode, the current decomposition splits the original current into five "layers" depending on load characteristics. Waveforms are taken from experiment 47, presented along with important observations from the experimental work.*

2.13.2 *The Second Theorem of Compensation*

The sort of dual to the first theorem suggests that if instantaneous real power $p_2(t)$ is zero at any instant of time, the current will be proportional to homo-integral voltage, $p_2(t) = 0 \quad \forall t \Leftrightarrow i = B \cdot \overset{\frown}{u}$

$$p_2(t) = \frac{u \circ i - \overset{\frown}{u} \circ \breve{i}}{2} = 0 \quad \Rightarrow \frac{u}{\overset{\frown}{u}} = \frac{\breve{i}}{i} \quad \Rightarrow \frac{\breve{\overset{\frown}{u}}}{\overset{\frown}{u}} = \frac{\breve{i}}{i} \quad \Rightarrow \frac{d\overset{\frown}{u}}{\overset{\frown}{u}} = \frac{di}{i} \qquad (2.69a)$$

$$\ln(\overset{\frown}{u}) = \ln(i) + K \quad \Rightarrow \ln(\frac{\overset{\frown}{u}}{i}) = K \quad \Rightarrow \frac{\overset{\frown}{u}}{i} = e^K \quad \Rightarrow i = B \cdot \overset{\frown}{u} \qquad (2.69b)$$

$$i(t) = B \cdot \overset{\frown}{u} \quad \Rightarrow \frac{di}{dt} = B\frac{d\overset{\frown}{u}}{dt} \quad \Rightarrow \frac{di}{dt} = \frac{i}{\overset{\frown}{u}}\frac{d\overset{\frown}{u}}{dt} \quad \Rightarrow \frac{di}{i} = \frac{d\overset{\frown}{u}}{\overset{\frown}{u}} \qquad (2.69c)$$

$$\frac{\omega}{i}\frac{di}{dt} = \frac{\omega}{\overset{\frown}{u}}\frac{d\overset{\frown}{u}}{dt} \quad \Rightarrow \frac{u}{\overset{\frown}{u}} = \frac{\breve{i}}{i} \quad \Rightarrow ui - \overset{\frown}{u}\,\overset{\frown}{i} = 0 \quad \Rightarrow p_2(t) = \frac{u \circ i - \overset{\frown}{u} \circ \overset{\frown}{i}}{2} = 0 \qquad (2.69d)$$

In context of reactive power compensation especially the first compensation theorem will be very useful.

2.14 Algorithmic implementation

In the early stage of the experimental work it became evident that the original CPT-algorithm[A1] was useless in a real-time application. The general tendency from previous work was that Simulink simulations incorporating the CPT-algorithm often took five to ten minutes, and many times abruptly terminating because of overloaded CPU. Running the same algorithm on the STM made the TCPU overload within few microseconds. This rapid collapse of the control system remained a mystery for almost a month before the virtual instrumentation was successful.

What can be considered as one of the most important discoveries during this thesis work, is that Simulink models must be optimized before applied in a real-time application. This process can involve block reduction and discretizing the model, in order to minimize loading of the TCPU. Final implementation of the CPT is depicted in **Figure 2.3**.

All quantities related to load bus voltage *(homo-integral)* are computed in the lower left part. Instantaneous and average value of real and imaginary power are computed in upper left, along with complete current decomposition. For shunt compensation purposes only the left section is needed, while the right part derives the complete power decomposition and thus being more relevant for power metering applications.

Apparently the algorithm relies heavily on mean-value computations *(ten blocks)*, which is perhaps one of its biggest drawbacks. These blocks must be run in the discrete time-domain, or they will easily strangle the TCPU. In addition to occupying lots of processing power, mean-value calculations represent an inherent slowness of the CPT-algorithm, which is undesirable in terms of instantaneous active power filtering.

If for instance the load current transitions from one steady state to another, a new current reference for the APF must be computed. Assuming that load bus voltages are in the steady state, the new updated current decomposition needs *20.0 ms* to converge. In case of both voltages and currents being in the transient state, this requires that also voltage related variables are updated. Active currents will be updated first after two cycles *(40.0 ms)*, while reactive currents may converge after three cycles *(60.0 ms)* in the worst case. Notably also the integrator block producing the homo-integrated voltage had to be discretized. It was observed quite different results depending on selected integration method, presently the *Trapezoidal method* seemed to work best for this application.

It is once more worth mentioning that the algorithm does not perform decomposition of distortion power D into current distortion D_i and voltage distortion power D_v. And the void currents $\boldsymbol{i}_v(t)$ are not further split into generated $\boldsymbol{i}_g(t)$, active scattering $\boldsymbol{i}_{sa}(t)$ and reactive scattering currents $\boldsymbol{i}_{sr}(t)$.

In case of future improvements of this algorithm there should be focused on reducing the convergence time, perhaps by using discrete *IIR* or *FIR* filters. Further it would be interesting performing full decomposition of distortion power and void currents. Also it would be valuable including analysis of the neutral current, as there exist very little research on that topic. As the CPT-algorithm is largely based on arithmetic operations in addition to calculus and mean-value computations, its theoretically plausible to implement the CPT entirely in the FPGA-domain if that would have any reasonable advantage.

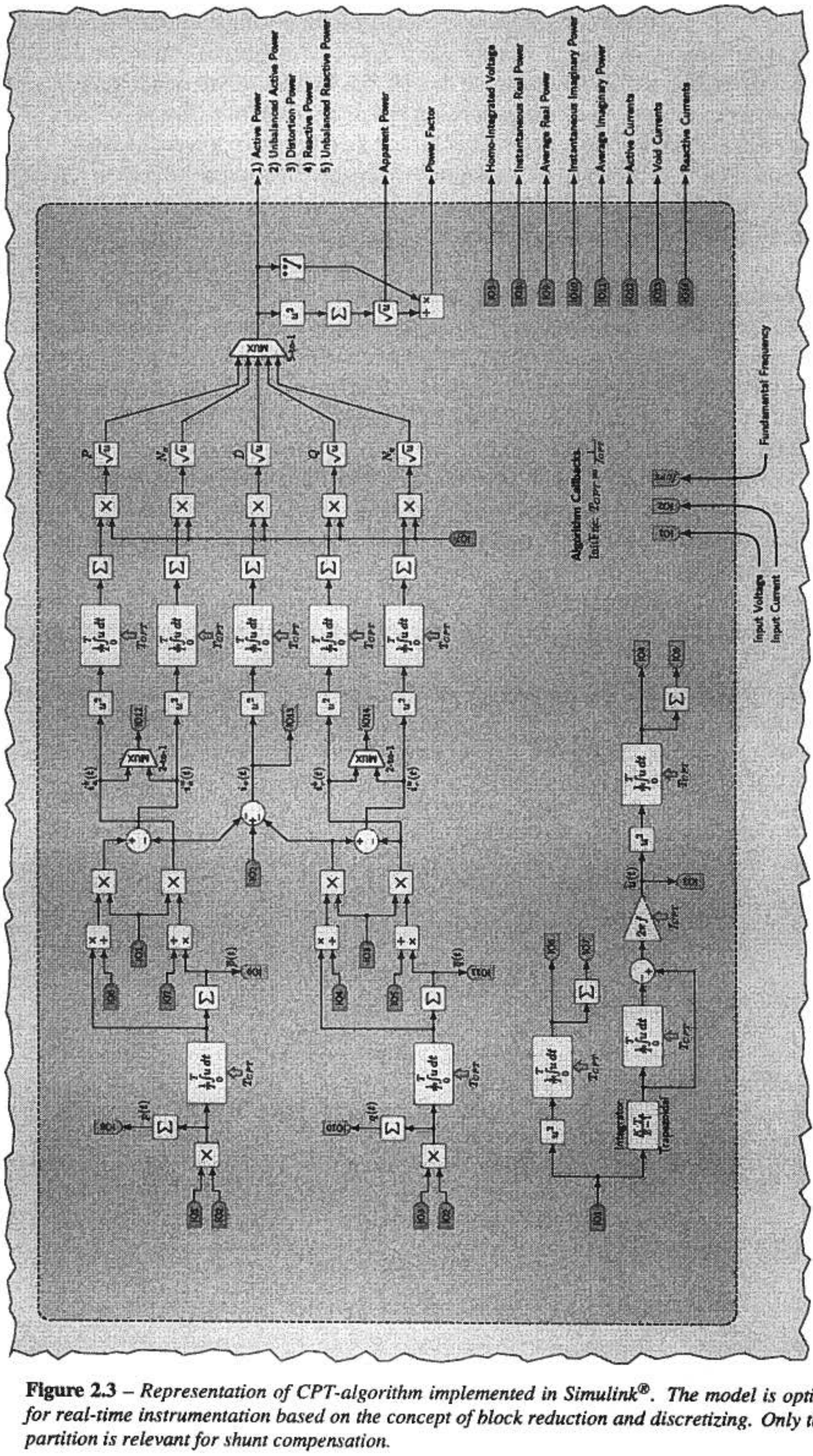

Figure 2.3 – *Representation of CPT-algorithm implemented in Simulink®. The model is optimized for real-time instrumentation based on the concept of block reduction and discretizing. Only the left partition is relevant for shunt compensation.*

Chapter 3

Virtual Instrumentation

Introduction

This chapter will in its entirety focus on presenting experimental data based on virtual instrumentation. The initial purpose of this master thesis work was to experimentally verify selected cases of active power filtering, using the conservative power theory as current reference generator. These goals soon proved to be to ambitious by several reasons; building up the experimental setup was very time consuming, limitations in the Speedgoat hardware and most crucially lacking knowledge of how to utilize the Speedgoat and xPC Target software.

Going for reactive and harmonic compensation was considered being a more original contribution as the CPT had already been tested several times supported by virtual instrumentation *(H.Paredes et al.)*

Although many of these former scientific articles have been used as inspiration, however this work must be considered as a much more comprehensive in-depth study than what is possible to present in the scope of a standard format scientific article. There has been put effort into presenting the experimental results in the best way possible.

During the experiments two virtual instruments were run in parallel, one based on the conservative power theory while the other was implementing H.Akagi's famous *pq*-theory. Data from both instruments were acquired and stored for post-analysis, however it later became clear that analyzing and presenting all the material would be to challenging. Most conclusive is the fact that the programmable voltage source was not able the generate zero-sequence voltage components. Consequently the comparison between the conservative power theory and the *pq*-theory becomes less valuable.

Also during the experiments a state-of-the-art power quality analyzer was included. The device is based on the classic power theory, and it will be used as benchmark to compare results from the virtual instrument. In this chapter the discussion will focus towards the CPT current decomposition, as it indirectly proves how compensating selected current components will alter the compensated grid current. Further in the next chapter selected cases will be tested through computer simulations, thus confirming the observations.

Reading instructions

Each individual experiment will be commented separately, or in instances where several experimental results are similar, these will be commented as a group. The study will be solely on a qualitative level. Experiments are organized and presented in more or less the same chronological order as they were conducted at the power electronics lab. Quality indexes related to harmonic distortion and unsymmetry in the voltage and current will be commented, as these are valuable when evaluating the decomposition of power and current and their associated waveforms. Further the load and resulting line currents of each scenario are discussed, as they are important in order to understand the performance of the conservative power theory.

The run-through of all experiments is long and exhausting, so initially the reader should consult tables presented in next section. These tables present the experimental data in a compact and effective format. Just as important are the current and power waveforms which are presented throughout the chapter. Lastly the qualitative observations made through the chapter are conveniently summarized in an own separate table. As all graphics are given in vector format, they are well suited for magnification on a PC screen. The reader is advised to do so for enhanced detail and clarity.

Notation

- In this chapter when using the term "ground" it is actually referred to a metallic connection to the floating neutral point of the three-phase dY11N-transformer *(neutral conductor)*. The power circuit was never connected to actual ground potential, except the mandatory protective earth *(PE)* used for safety measure.
- Whenever referring to $u(t)$ and $i(t)$ this indicate load voltage and load current respectively, measured at the output of the LCL-filter. Different notation will be used in next chapter when dealing with simulated shunt-compensation.

3.1 Experimental data

This section presents experimental data in table format collected from the CPT-based virtual instrument, and the Fluke™434 Power Quality Analyzer intended for benchmark comparison. Each table is adequately organized into five segments qualitatively describing all 87 experiments. Ten experiments are included in each table as their characteristics are usually in close relation to one another.

The first segment provides true root-mean-square values for voltages and currents recorded with the Fluke™434 instrument, and gives the reader a sort of impression of the voltage and current level involved in each respective experiment.
In case of IT-mode line voltages and line currents are measured, while under TN-mode phase voltages are measured in addition to corresponding voltage and current for the neutral conductor. These RMS values can be seen in correlation with voltage and current waveforms acquired by the virtual instrument.

Second subpart contains quality indexes also recorded with the power quality analyzer, reflecting harmonic and unsymmetric properties of voltage and current waveforms. These are valuable when evaluating the current and power decomposition suggested by each of the two instruments.

Total harmonic distortion (THD_v) quantifies the voltage distortion relative to the fundamental $50\,Hz$ voltage component. Negative sequence unbalance factor (K_{v-}) and the zero sequence unbalance factor (K_{v0}), account for presence of negative and zero sequence voltage components at $50\,Hz$. Identical quality indexes equally apply for line currents.

Figures reproduced in the third section is the five-dimensional power decomposition as proposed by the CPT-algorithm. For easy readability and comparison with the classic power theory, powers are presented in the per-unit-system using the apparent power as base power. Remaining subset of powers are given as the relative percentage of the base power, rather then stating each power in its physical unit. Apparent power is also listed by its Volt-Ampere value so to give the reader a physical sense of the actual power level.

Apparent power A_{Sum} is manually calculated in order to verify that the power decomposition always sum to 100 %, and thus confirming orthogonal decoding of current and power. Also is the new proposed power factor (λ) included for comparison with the classic power factor. The experience gained during the experiments is that per-unit powers contra the current decomposition, generally give a much better impression of the CPT-performance. Admittedly this is partly because there was not possible to devise any effective method for visualizing waveforms. Nonetheless power and current decomposition act as sort of complementary to each other, and studying both gives better understanding of the CPT.

Surveying the scientific tables a systematic tendency is revealing; the CPT performs fairly robust and independent of load bus voltage condition. Whether the voltage is balanced or unbalanced, sinusoidal or distorted and any combinations in between, comparison demonstrate that the conservative power theory pays exclusively attention to the load characteristics.

The fourth segment of the table contains powerflow analysis from the Fluke™434, implementing the classic two-dimensional power decomposition, hence it should be regarded as the benchmark. All powers are similarly presented as the magnitude relative to base power. Also here the powers are manually summed up (S^*_{Sum}), in order to invalidate the orthogonality of power decomposition under demanding network conditions.

The last portion of each table is divided into five columns, containing important detailed information regarding how each experiment was actually executed:

Topology indicates if the Fluke™434 Analyzer was configured to IT or TN-mode, while the roman numeral in parentheses refers to the corresponding electrical circuit diagram relevant for each respective case. Schematics are presented in the text.

Network Voltage Status categorizes each experiment into the sinusoidal or non-sinusoidal voltage regime. Also listed is the voltage symmetry included. These qualities were in certain occasions provoked by the load, due to high source impedance.

Figure column indicates if waveforms of measured phase voltages, line currents and corresponding CPT current decomposition are visualized for the particular experiment. Only representative cases are selected for observation.

At last Load Description supplements the electrical diagrams introduced throughout the chapter, by listing load parameter values; the wiring-topology, specifying load impedance and if the load classifies as symmetric or unsymmetric.

- In case of bipolar loads (D) translates to delta-connection, while (YF) and (YG) indicate a floating or grounded star-connection respectively.
- $Z_{a,b,c}$ is the phase impedance given either commonly for all three phases, or explicitly in case of an unsymmetric load. Z_{ac} is connection from line A to C.
- Dealing with diode and thyristor rectifiers, R_{DC} and C_{DC} are the DC-bus load impedance. For the thyristor rectifier α_{th} equals the delayed thyristor firing angle.

Table 3.1 – *Case 1 - 10: Symmetric resistive loads alternated between floating or grounded star and delta-configuration. Voltages balanced sinusoidal and unbalanced sinusoidal. Decomposition of powerflow comply with classic power theories.*

Quantity	Unit	1	2	3	4	5	6	7	8	9	10
$V_{A(B)}$	$[V]$	230.3	188.0	133.1	133.0	107.4	107.4	230.2	185.6	107.7	230.8
$V_{B(C)}$	$[V]$	228.9	251.9	132.8	132.9	128.8	129.1	229.4	242.5	129.0	229.6
$V_{C(A)}$	$[V]$	228.7	219.2	132.4	132.4	144.1	144.6	229.4	201.5	144.4	229.8
V_N	$[V]$			35.9	35.6	27.6	27.3	4.3		13.4	
I_A	$[A]$	5.8	4.7	5.8	5.8	4.7	4.7	4.3	3.2	3.5	4.4
I_B	$[A]$	5.8	5.6	5.8	5.8	5.6	5.6	4.3	4.1	4.2	4.4
I_C	$[A]$	5.7	6.3	5.7	5.7	6.2	6.2	4.3	4.3	4.7	4.3
I_N	$[A]$			0.1	0.0	0.1	0.0	0.0		0.0	
Quality Indexes											
THD_v	[%]	2.1	2.4	1.7	1.7	2.7	2.7	1.5	2.2	2.6	1.8
THD_i	[%]	1.7	1.7	1.7	1.7	2.6	2.7	1.5	2.7	2.5	1.6
K_{v-}	[%]	0.2	17.1	0.4	0.2	17.0	16.9	0.5	16.9	16.9	0.4
K_{v0}	[%]			0.0	0.0	0.0	0.0	0.0		0.0	
K_{i-}	[%]	0.5	16.6	0.7	0.5	16.6	16.4	0.8	17.6	16.5	0.5
K_{i0}	[%]			0.5	0.3	0.5	0.3	0.4		0.4	
Virtual Instrument - CPT											
A	$[kVA]$	2.322/100	2.157/100	2.326/100	2.325/100	2.154/100	2.153/100	1.719/100	1.439/100	1.619/100	1.761/100
P	$[pu]$	99.99	99.99	99.99	99.98	99.99	99.99	99.99	99.99	99.99	99.99
N_a	$[pu]$	0.26	0.25	0.37	0.31	0.22	0.25	0.34	0.47	0.20	0.27
Q	$[pu]$	0.09	0.09	0.12	0.12	0.07	0.07	0.16	0.15	0.35	0.33
N_q	$[pu]$	0.12	0.11	0.23	0.19	0.21	0.09	0.30	0.10	0.29	0.42
D	$[pu]$	0.54	0.52	0.46	0.39	0.44	0.39	0.35	1.46	0.38	0.41
A_{Sum}	$[pu]$	99.99	99.99	99.99	99.98	99.99	99.99	99.99	100.00	99.99	99.99
λ	$[-]$	1.000	1.000	1.000	1.000	1.000	1.000	1.000	0.999	1.000	1.000
Fluke 434 Scope											
S^*	$[pu]$	99.05	98.75	98.88	98.92	98.89	98.93	100.06	98.68	99.44	98.24
P^*	$[pu]$	99.05	98.75	98.88	98.92	98.89	98.93	100.06	98.68	99.44	98.24
Q^*	$[pu]$	5.17	6.03	1.72	1.72	1.86	1.86	2.33	8.34	2.47	7.38
S^*_{Sum}	$[pu]$	99.18	98.93	98.89	98.93	98.91	98.95	100.09	99.03	99.47	98.52
$\cos\phi$	$[-]$	1.00	1.00	1.00	1.00	1.00	1.00	1.00	1.00	1.00	1.00

Case	Topology	Network Voltage Status	Figure	Load Description
1	**IT ▷ (I)**	**Balanced ▷ Sinusoidal**	*Figure 3.2*	**YF-Connected, $R_{a,b,c} = 23\,\Omega$ (Symmetric)**
2	**IT ▷ (I)**	**Unbalanced ▷ Sinusoidal**		**YF-Connected, $R_{a,b,c} = 23\,\Omega$ (Symmetric)**
3	**TN ▷ (I)**	**Balanced ▷ Sinusoidal**		**YG-Connected, $R_{a,b,c} = 23\,\Omega$ (Symmetric)**
4	**TN ▷ (I)**	**Balanced ▷ Sinusoidal**		**YF-Connected, $R_{a,b,c} = 23\,\Omega$ (Symmetric)**
5	**TN ▷ (I)**	**Unbalanced ▷ Sinusoidal**	*Figure 3.3*	**YG-Connected, $R_{a,b,c} = 23\,\Omega$ (Symmetric)**
6	**TN ▷ (I)**	**Unbalanced ▷ Sinusoidal**		**YF-Connected, $R_{a,b,c} = 23\,\Omega$ (Symmetric)**
7	**TN ▷ (II)**	**Balanced ▷ Sinusoidal**	*Figure 3.8*	**D-Connected, $R_{a,b,c} = 96\,\Omega$ (Symmetric)**
8	**IT ▷ (II)**	**Unbalanced ▷ Sinusoidal**	*Figure 3.9*	**D-Connected, $R_{a,b,c} = 96\,\Omega$ (Symmetric)**
9	**TN ▷ (II)**	**Unbalanced ▷ Sinusoidal**		**D-Connected, $R_{a,b,c} = 96\,\Omega$ (Symmetric)**
10	**IT ▷ (II)**	**Balanced ▷ Sinusoidal**		**D-Connected, $R_{a,b,c} = 96\,\Omega$ (Symmetric)**

Table 3.2 – *Case 11 - 20: Symmetric inductive loads alternated between floating or grounded star and delta-configuration. Voltages are balanced sinusoidal and unbalanced sinusoidal. Decomposition of powerflow comply with the classic power theories.*

Quantity	Unit	11	12	13	14	15	16	17	18	19	20
$V_{A(B)}$	$[V]$	231.6	192.1	133.2	133.3	108.3	107.9	183.8	147.5	89.9	102.0
$V_{B(C)}$	$[V]$	231.1	253.9	133.8	133.8	131.5	131.6	183.6	194.8	109.9	102.8
$V_{C(A)}$	$[V]$	230.3	218.2	133.2	133.3	144.6	144.5	182.2	166.5	120.6	101.9
V_N	$[V]$			13.7	13.2	14.2	13.9			15.0	14.8
I_A	$[A]$	3.0	2.4	3.0	3.0	2.4	2.4	7.2	5.5	6.1	7.0
I_B	$[A]$	3.0	2.9	3.0	3.0	3.0	2.9	7.3	6.9	7.6	7.0
I_C	$[A]$	3.0	3.2	2.9	2.9	3.2	3.2	7.2	7.5	8.3	6.9
I_N	$[A]$			0.2	0	0.2	0			0	0
Quality Indexes											
THD_v	[%]	2.0	2.1	1.7	1.8	2.2	2.2	4.1	4.6	4.9	4.1
THD_i	[%]	0.8	1.0	2.1	0.9	2.1	1.0	1.3	2.0	1.9	1.3
K_{v-}	[%]	0.4	16.6	0.4	0.4	16.6	16.6	0.4	16.9	16.9	0.5
K_{v0}	[%]			0.0	0.0	0.0	0.0			0.1	0.0
K_{i-}	[%]	0.6	17.0	0.6	0.6	17.0	17.0	0.6	17.8	17.9	0.7
K_{i0}	[%]			0.9	0.7	0.8	0.6			0.5	0.5
Virtual Instrument - CPT											
A	$[kVA]$	1.209/100	1.129/100	1.209/100	1.214/100	1.126/100	1.129/100	2.294/100	1.993/100	2.366/100	2.145/100
P	$[pu]$	2.98	3.02	2.97	2.98	3.05	3.02	2.83	2.81	2.79	2.82
N_a	$[pu]$	0.47	0.68	0.42	0.38	0.32	0.74	0.64	0.91	0.83	0.57
Q	$[pu]$	99.95	99.94	99.94	99.96	99.94	99.94	99.95	99.94	99.94	99.95
N_q	$[pu]$	0.15	0.43	0.61	0.15	0.89	0.33	0.51	0.92	1.03	0.59
D	$[pu]$	0.49	0.64	1.00	0.56	1.06	0.62	0.90	0.99	1.15	0.91
A_{Sum}	$[pu]$	100.00	99.99	99.99	100.01	100.00	99.99	100.00	99.99	99.99	100.00
λ	$[-]$	0.029	0.030	0.029	0.029	0.031	0.030	0.028	0.028	0.028	0.028
Fluke 434 Scope											
S^*	$[pu]$	98.43	98.32	98.43	98.85	98.58	98.32	99.83	99.35	96.79	99.77
P^*	$[pu]$	4.14	4.43	4.96	4.94	5.33	5.31	3.92	4.01	4.65	4.66
Q^*	$[pu]$	98.43	97.43	98.43	98.85	98.58	98.32	99.83	99.35	96.79	99.77
S^*_{Sum}	$[pu]$	98.52	97.53	98.55	98.97	98.72	98.46	99.91	99.43	96.90	99.88
$\cos\phi$	$[-]$	0.05	0.05	0.05	0.05	0.05	0.05	0.04	0.04	0.05	0.05

Case	Topology	Network Voltage Status	Figure	Load Description
11	IT ▷ (III)	Balanced ▷ Sinusoidal	*Figure 3.11*	YF-Connected, $L_{a,b,c} = 175\,mH$ (Symmetric)
12	IT ▷ (III)	Unbalanced ▷ Sinusoidal	*Figure 3.12*	YF-Connected, $L_{a,b,c} = 175\,mH$ (Symmetric)
13	TN ▷ (III)	Balanced ▷ Sinusoidal		YG-Connected, $L_{a,b,a} = 175\,mH$ (Symmetric)
14	TN ▷ (III)	Balanced ▷ Sinusoidal		YF-Connected, $L_{a,b,c} = 175\,mH$ (Symmetric)
15	TN ▷ (III)	Unbalanced ▷ Sinusoidal		YG-Connected, $L_{a,b,c} = 175\,mH$ (Symmetric)
16	TN ▷ (III)	Unbalanced ▷ Sinusoidal		YF-Connected, $L_{a,b,c} = 175\,mH$ (Symmetric)
17	IT ▷ (IV)	Balanced ▷ Sinusoidal		D-Connected, $L_{a,b,c} = 175\,mH$ (Symmetric)
18	IT ▷ (IV)	Unbalanced ▷ Sinusoidal		D-Connected, $L_{a,b,c} = 175\,mH$ (Symmetric)
19	TN ▷ (IV)	Unbalanced ▷ Sinusoidal	*Figure 3.13*	D-Connected, $L_{a,b,c} = 175\,mH$ (Symmetric)
20	TN ▷ (IV)	Balanced ▷ Sinusoidal		D-Connected, $L_{a,b,c} = 175\,mH$ (Symmetric)

Table 3.3 – *Case 21 - 30: Symmetric series connection of resistive and inductive loads, alternated between floating or grounded star and delta-configuration. Voltages being balanced sinusoidal and unbalanced sinusoidal. When network conditions includes sinusoidal voltages and currents, the CPT comply with the traditional power theories.*

Quantity	Unit	21	22	23	24[a]	25	26	27	28	29	30
$V_{A(B)}$	$[V]$	231.7	133.7	216.8		133.5	192.0	108.3	166.3	101.1	107.9
$V_{B(C)}$	$[V]$	230.0	133.5	215.2		133.9	254.1	130.8	220.5	122.2	130.7
$V_{C(A)}$	$[V]$	230.2	132.9	215.3		132.7	219.3	144.7	190.7	134.7	144.4
V_N	$[V]$		56.1			55.7		53.4		48.6	54.2
I_A	$[A]$	2.6	2.6	7.5		2.6	2.1	2.1	5.6	6.0	2.1
I_B	$[A]$	2.6	2.6	7.5		2.6	2.5	2.6	6.8	7.3	2.5
I_C	$[A]$	2.6	2.6	7.4		2.6	2.8	2.8	7.5	8.1	2.8
I_N	$[A]$		0.1			0		0.1		0	0
Quality Indexes											
THD_v	[%]	1.8	1.8	3.2		1.8	2.3	2.2	4.3	4.1	2.3
THD_i	[%]	0.8	2.2	1.2		0.7	0.9	2.0	1.7	1.8	1.0
K_{v-}	[%]	0.5	0.4	0.5		0.3	16.6	16.6	16.7	16.7	16.6
K_{v0}	[%]		0.1			0.0		0.1		0.1	0.0
K_{i-}	[%]	0.2	0.2	0.3		0.2	17.2	17.3	17.1	17.4	17.3
K_{i0}	[%]		0.9			0.7		0.9		0.5	0.6
Virtual Instrument - CPT											
A	$[kVA]$	1.052/100	1.053/100	2.823/100	2.809/100	1.055/100	0.982/100	0.984/100	2.269/100	2.627/100	0.978/100
P	$[pu]$	48.15	48.15	48.45	48.44	48.12	47.99	48.03	48.34	48.48	48.07
N_a	$[pu]$	0.55	0.79	0.43	0.49	0.55	0.84	1.14	0.63	0.78	0.85
Q	$[pu]$	87.63	87.62	87.48	87.48	87.65	87.73	87.69	87.54	87.46	87.68
N_q	$[pu]$	0.35	0.08	0.38	0.42	0.35	0.49	0.49	0.43	0.71	0.49
D	$[pu]$	0.53	1.09	0.43	0.49	0.54	0.61	1.05	0.49	0.45	0.61
A_{Sum}	$[pu]$	99.99	99.99	100.00	100.00	99.99	100.00	100.00	100.00	100.00	100.00
λ	$[-]$	0.482	0.482	0.484	0.484	0.481	0.479	0.480	0.483	0.485	0.481
Fluke 434 Scope											
S^*	$[pu]$	97.91	98.77	98.48		97.63	97.76	97.56	98.28	98.59	98.16
P^*	$[pu]$	48.48	49.38	48.53		49.29	48.88	48.78	48.48	49.11	49.08
Q^*	$[pu]$	85.55	85.47	85.72		84.36	85.54	84.35	85.50	85.27	84.87
S^*_{Sum}	$[pu]$	98.33	98.71	98.50		97.70	98.52	97.44	98.29	98.40	98.04
$\cos\phi$	$[-]$	0.50	0.50	0.49		0.50	0.49	0.50	0.49	0.50	0.50

Case	Topology	Network Voltage Status	Figure	Load Description
21	**IT▹(V)**	**Balanced▹Sinusoidal**	*Figure 3.14*	**YF-Connected, $R_{a,b,c} = 23\,\Omega + L_{a,b,c} = 175\,mH$ (Series Symmetric)**
22	**TN▹(V)**	**Balanced▹Sinusoidal**		**YG-Connected, $R_{a,b,c} = 23\,\Omega + L_{a,b,c} = 175\,mH$ (Series Symmetric)**
23	**IT▹(VI)**	**Balanced▹Sinusoidal**		**D-Connected, $R_{a,b,c} = 23\,\Omega + L_{a,b,c} = 175\,mH$ (Series Symmetric)**
24	**TN▹(VI)**	**Balanced▹Sinusoidal**		**D-Connected, $R_{a,b,c} = 23\,\Omega + L_{a,b,c} = 175\,mH$ (Series Symmetric)**
25	**TN▹(V)**	**Balanced▹Sinusoidal**		**YF-Connected, $R_{a,b,c} = 23\,\Omega + L_{a,b,c} = 175\,mH$ (Series Symmetric)**
26	**IT▹(V)**	**Unbalanced▹Sinusoidal**		**YF-Connected, $R_{a,b,c} = 23\,\Omega + L_{a,b,c} = 175\,mH$ (Series Symmetric)**
27	**TN▹(V)**	**Unbalanced▹Sinusoidal**	*Figure 3.18*	**YG-Connected, $R_{a,b,c} = 23\,\Omega + L_{a,b,c} = 175\,mH$ (Series Symmetric)**
28	**IT▹(VI)**	**Unbalanced▹Sinusoidal**		**D-Connected, $R_{a,b,c} = 23\,\Omega + L_{a,b,c} = 175\,mH$ (Series Symmetric)**
29	**TN▹(VI)**	**Unbalanced▹Sinusoidal**		**D-Connected, $R_{a,b,c} = 23\,\Omega + L_{a,b,c} = 175\,mH$ (Series Symmetric)**
30	**TN▹(V)**	**Unbalanced▹Sinusoidal**		**YF-Connected, $R_{a,b,c} = 23\,\Omega + L_{a,b,c} = 175\,mH$ (Series Symmetric)**

[a] Recorded data from Fluke™ 434 Power Quality Analyzer were erroneous, and consequently ignored.

Table 3.4 – *Case 31 - 40: Unsymmetric bipolar loads, first half covers resistive loads and second half inductive loads. Resulting line currents drawn by unsymmetric loads and the corresponding CPT-decomposition, are very dependent on load-connection to neutral conductor. Unsymmetric bipolar loads cause interesting phase-shift relation between voltages and currents, which the conservative power theory elegantly sort out.*

Quantity	Unit	31	32	33[a]	34	35	36	37	38	39	40
$V_{A(B)}$	$[V]$	133.0	132.6	235.0	83.1	155.5	130.6	130.1	229.9	79.9	134.5
$V_{B(C)}$	$[V]$	135.4	136.5	229.8	96.4	167.4	134.1	134.4	231.0	82.9	155.1
$V_{C(A)}$	$[V]$	130.1	127.7	226.0	90.1	143.9	131.3	131.1	225.0	91.6	150.7
V_N	$[V]$	26.0	16.1		21.4		13.1	13.7		15.0	
I_A	$[A]$	1.9	1.4	1.9	7.1	7.1	4.1	5.2	4.1	5.4	5.4
I_B	$[A]$	1.9	1.5	1.9	3.1	3.1	3.4	3.0	3.4	7.8	7.8
I_C	$[A]$	2.8	5.6	2.8	7.3	7.3	3.2	2.9	3.2	3.5	3.5
I_N	$[A]$	0	4.2		0		0	2.3		0	
Quality Indexes											
THD_v[b]	[%]										
THD_i[c]	[%]										
K_{v-}	[%]	2.6	3.6	2.6	8.6	8.5	1.7	2.0	1.8	8.4	8.3
K_{v0}	[%]	0.0	0.3		0.1		0.0	0.1		0.0	
K_{i-}	[%]	31.3	47.8	31.2	44.8	45.0	15.8	19.8	15.8	51.8	51.9
K_{i0}	[%]	0.4	48.7		0.6		0.7	20.7		0.4	
Virtual Instrument - CPT											
A	$[kVA]$	0.913/100	1.378/100	0.913/100	1.683/100	1.686/100	1.444/100	1.545/100	1.444/100	1.503/100	1.491/100
P	$[pu]$	94.74	81.21	94.74	88.29	88.27	3.46	3.39	3.41	3.30	3.34
N_a	$[pu]$	22.92	58.36	22.92	32.08	32.02	11.20	1.17	11.22	36.42	36.48
Q	$[pu]$	0.15	0.09	0.15	0.13	0.06	98.61	95.92	98.61	86.13	86.10
N_q	$[pu]$	22.34	0.25	22.34	34.29	34.37	11.78	28.02	11.73	35.26	35.25
D	$[pu]$	0.29	0.14	0.28	0.79	0.84	0.57	1.42	0.52	1.40	1.41
$A_{S_{sum}}$	$[pu]$	100.00	100.01	100.00	100.00	99.99	100.00	100.00	100.00	100.00	100.00
λ	$[-]$	0.947	0.812	0.947	0.883	0.883	0.035	0.034	0.034	0.033	0.0334
Fluke 434 Scope											
S^*	$[pu]$	98.58	98.69		99.05	99.05	98.34	99.03	98.34	98.47	99.26
P^*	$[pu]$	93.10	79.83		87.34	86.60	5.54	5.18	4.85	4.66	4.69
Q^*	$[pu]$	3.29	2.18		1.78	46.86	96.95	94.50	98.34	85.16	99.26
$S^*_{S_{sum}}$	$[pu]$	93.16	79.86		87.36	98.47	97.11	94.64	98.46	85.29	99.37
$\cos\phi$	$[-]$	0.95	0.81		0.88	0.88	0.05	0.05	0.05	0.05	0.05

Case	Topology	Network Voltage Status	Figure	Load Description
31	TN ▹ (I)	Balanced ▹ Sinusoidal	*Figure 3.19*	YF-Connected, $R_{a,b} = 96\,\Omega + R_c = 25\,\Omega$ (Unsymmetric)
32	TN ▹ (I)	Balanced ▹ Sinusoidal	*Figure 3.20*	YG-Connected, $R_{a,b} = 96\,\Omega + R_c = 25\,\Omega$ (Unsymmetric)
33	IT ▹ (I)	Balanced ▹ Sinusoidal		YF-Connected, $R_{a,b} = 96\,\Omega + R_c = 25\,\Omega$ (Unsymmetric)
34	TN ▹ (II)	Unbalanced ▹ Sinusoidal	*Figure 3.21*	D-Connected, $R_{a,b} = 96\,\Omega + R_c = 25\,\Omega$ (Unsymmetric)
35	IT ▹ (II)	Unbalanced ▹ Sinusoidal		D-Connected, $R_{a,b} = 96\,\Omega + R_c = 25\,\Omega$ (Unsymmetric)
36	TN ▹ (III)	Balanced ▹ Sinusoidal		YF-Connected, $L_a = 87.5\,mH + L_{b,c} = 175\,mH$ (Unsymmetric)
37	TN ▹ (III)	Balanced ▹ Sinusoidal	*Figure 3.22*	YG-Connected, $L_a = 87.5\,mH + L_{b,c} = 175\,mH$ (Unsymmetric)
38	IT ▹ (III)	Balanced ▹ Sinusoidal		YF-Connected, $L_a = 87.5\,mH + L_{b,c} = 175\,mH$ (Unsymmetric)
39	TN ▹ (IV)	Unbalanced ▹ Sinusoidal		D-Connected, $L_a = 87.5\,mH + L_{b,c} = 175\,mH$ (Unsymmetric)
40	IT ▹ (IV)	Unbalanced ▹ Sinusoidal	*Figure 3.23*	D-Connected, $L_a = 87.5\,mH + L_{b,c} = 175\,mH$ (Unsymmetric)

[a] Recorded powerflow data from Fluke™ 434 Power Quality Analyzer were lost.

[b] Harmonic content in voltages were equal to previous cases, $THD_v < 3\%$. Quantity was not recorded to save time.

[c] $THD_i < 3\%$ in all cases. Thus THD_i was not recorded to save time.

Table 3.5 – *Case 41 - 50: Unlinear rectifier loads (three-phase diode and thyristor bridge) tested under harmonic voltage conditions. CPT matches active power with the conventional power theory, while reactive power is notably transformed as void power.*

Quantity	Unit	41	42	43	44	45	46	47[a]	48	49	50
$V_{A(B)}$	[V]	229.6	132.5	188.8	229.3	168.4	95.5	221.2	127.8	183.4	104.8
$V_{B(C)}$	[V]	228.5	132.6	250.1	228.4	202.4	108.3	220.4	127.5	237.8	123.0
$V_{C(A)}$	[V]	227.5	131.6	217.1	228.1	182.5	115.7	220.8	127.1	209.9	136.3
V_N	[V]		54.4	49.6			34.0		74.0	0	68.1
I_A	[A]	5.1	5.2	4.2	5.2	1.6	1.5	3.5	3.5	3.3	3.1
I_B	[A]	5.2	5.2	5.1	5.2	6.6	6.6	3.6	3.6	4.0	3.8
I_C	[A]	5.2	5.2	5.7	5.2	6.6	6.6	3.5	3.5	3.9	3.8
I_N	[A]		0	0			0		0	0	0
Quality Indexes											
THD_v	[%]	14.5	14.5	18.2	16.3	16.0	17.5	20.6	20.6	28.4	29.4
THD_i	[%]	22.1	22.0	31.1	23.3	87.1	87.3	56.1	56.2	82.9	82.9
K_{v-}	[%]	0.6	0.1	16.6	0.3	10.6	10.6	0.2	0.3	16.6	16.5
K_{v0}	[%]		0.0	0.0			0.0		0.0		0.0
K_{i-}	[%]	0.9	0.7	18.7	0.7	69.2	69.6	2.4	2.5	22.0	21.9
K_{i0}	[%]		0.2	0.2			0.2		0.2		0.1
Virtual Instrument - CPT											
A	[kVA]	2.044/100	2.055/100	1.917/100	2.075/100	1.765/100	1.759/100	1.311/100	1.328/100	1.281/100	1.289/100
P	[pu]	95.87	95.91	95.38	94.71	73.64	73.74	41.02	41.31	43.59	43.78
N_a	[pu]	0.65	0.56	2.48	1.17	33.09	32.80	1.91	2.08	5.66	5.63
Q	[pu]	6.30	6.27	7.43	8.51	16.71	16.67	75.01	74.91	70.93	70.83
N_q	[pu]	0.90	0.85	1.58	1.41	30.60	30.44	1.94	2.06	8.01	7.99
D	[pu]	27.69	27.58	28.98	30.89	47.61	47.77	51.80	51.69	54.53	54.49
$A_{\Sigma_{sum}}$	[pu]	99.99	100.00	100.01	100.00	100.00	100.00	100.00	99.99	100.00	99.99
λ	[−]	0.959	0.959	0.954	0.947	0.736	0.737	0.410	0.413	0.436	0.438
Fluke 434 Scope											
S^*	[pu]	99.80	99.76	99.63	99.28	99.15	99.49		101.66	102.26	101.63
P^*	[pu]	95.40	95.38	94.94	93.98	73.65	73.34		43.67	46.06	45.77
Q^*	[pu]	28.38	28.71	29.21	31.81	65.72	15.35		92.62	91.33	90.77
$S^*_{\Sigma_{sum}}$	[pu]	99.53	99.61	99.33	99.22	98.71	74.93		102.40	102.29	101.59
$\cos\phi$	[−]	0.96	0.96	0.95	0.95	0.75	0.74		0.43	0.45	0.45

Case	Topology	Network Voltage Status	Figure	Load Description
41	IT▹(VII)	Balanced▹Harmonic	*Figure 3.25*	3-Ph Diode rectifier▹ $R_{dc} = 45.5\,\Omega$
42	TN▹(VII)	Balanced▹Harmonic		3-Ph Diode rectifier▹ $R_{dc} = 45.5\,\Omega$
43	TN▹(VII)	Unblanced▹Harmonic	*Figure 3.26*	3-Ph Diode rectifier▹ $R_{dc} = 45.5\,\Omega$
44	IT▹(VII)	Balanced▹Harmonic		3-Ph Diode rectifier▹ $R_{dc} = 45.5\,\Omega + C_{dc} = 3300\,\mu F$
45	IT▹(VII)	Unbalanced▹Harmonic		3-Ph Diode rectifier▹ $R_{dc} = 45.5\,\Omega + C_{dc} = 3300\,\mu F$
46	TN▹VII	Unbalanced▹Harmonic	*Figure A.9*	3-Ph Diode rectifier▹ $R_{dc} = 45.5\,\Omega + C_{dc} = 3300\,\mu F$
47	IT▹(VIII)	Balanced▹Harmonic	*Figure 3.30*	3-Ph Thyristor rectifier ($\alpha_{th} \approx 60°$)▹ $R_{dc} = 32\,\Omega$+ 2x60W bulbs
48	TN▹(VIII)	Balanced▹Harmonic		3-Ph Thyristor rectifier ($\alpha_{th} \approx 60°$)▹ $R_{dc} = 32\,\Omega$+ 2x60W bulbs
49	IT▹(VIII)	Unbalanced▹Harmonic		3-Ph Thyristor rectifier ($\alpha_{th} \approx 50°$)▹ $R_{dc} = 32\,\Omega$+ 2x60W bulbs
50	TN▹(VIII)	Unbalanced▹Harmonic	*Figure 3.31*	3-Ph Thyristor rectifier ($\alpha_{th} \approx 50°$)▹ $R_{dc} = 32\,\Omega$+ 2x60W bulbs

[a] Data are not presented due to wrong figures.

Table 3.6 – *Case 51 - 60: 1) Severe unsymmetry created by coupling two phases with a bipolar impedance. 2) Testing symmetric and unsymmetric parallel connections of pure R and L-loads. 3) Rectifier loads connected to stiff grid voltage for comparison and reference. Both the conservative power theory and the classic power theory fails to correctly decipher single-phase bipolar loads.*

Quantity	Unit	51	52	53	54	55	56	57	58[a]	59	60
$V_{A(B)}$	[V]	116.4	221.2	117.2	214.6	213.5	213.5	117.8	229.0	225.7	232.2
$V_{B(C)}$	[V]	135.9	232.3	118.4	183.5	212.6	209.8	125.0	229.1	226.0	232.4
$V_{C(A)}$	[V]	123.8	198.4	98.3	181.5	213.1	204.6	113.0	229.4	226.0	232.6
V_N	[V]	66.2		12.4	0			24.1			
I_A	[A]	4.4	4.4	4.3	4.3	3.1	3.8	3.0	4.3	7.6	5.6
I_B	[A]	0	0	0	0	3.1	2.7	3.1	4.4	7.4	5.6
I_C	[A]	4.4	4.4	4.3	4.3	3.1	4.0	7.9	4.3	7.6	5.6
I_N	[A]	0		0				6.2			
Quality Indexes											
THD_v[b]	[%]								1.3	2.0	0.6
THD_i[c]	[%]								70.7	93.5	29.5
K_{v-}	[%]	9.1	9.2	11.5	11.5	0.1	2.4	5.5		0.2	0.1
K_{v0}	[%]	0.0		0.0				0.5			
K_{i-}	[%]	100.0	100.0	101.0	101.1	0.2	21.7	43.6		3.1	0.3
K_{i0}	[%]	0.4		0.8				46.6			
Virtual Instrument - CPT											
A	[kVA]	1.355/100	1.357/100	1.182/100	1.172/100	1.154/100	1.303/100	1.864/100	1.000/100	2.670/100	2.259/100
P	[pu]	64.34	64.41	1.67	1.66	46.43	61.45	64.23	51.51	72.94	95.98
N_a	[pu]	51.59	51.59	54.44	54.54	0.33	16.38	57.25	2.06	0.59	0.14
Q	[pu]	0.16	0.18	66.23	66.21	88.56	75.44	50.96	65.34	1.13	0.97
N_q	[pu]	56.54	56.46	51.38	51.29	0.11	16.27	0.33	1.75	0.49	0.18
D	[pu]	1.36	1.38	2.82	2.95	0.86	0.86	0.58	55.41	68.39	28.04
A_{Sum}	[pu]	100.00	100.00	100.00	100.00	100.00	100.01	100.00	100.00	100.00	100.00
λ	[−]	0.643	0.644	0.02	0.017	0.464	0.615	0.642	0.515	0.729	0.959
Fluke 434 Scope											
S^*	[pu]	99.63	99.48	98.98	99.83	98.79	99.00	99.25		110.11	99.60
P^*	[pu]	64.21	63.38	3.38	2.56	47.66	62.16	64.91		78.28	95.17
Q^*	[pu]	1.48	76.64	65.14	99.83	86.66	77.51	49.36		77.15	29.22
S^*_{Sum}	[pu]	64.23	99.45	65.23	99.86	98.90	99.36	81.55		109.91	99.55
$\cos\phi$	[−]	0.64	0.64	0.03	0.02	0.48	0.63	0.65		0.71	0.96

Case	Topology	Network Voltage Status	Figure	Load Description
51	TN ▹ (X)	Unbalanced ▹ Sinusoidal	*Figure 3.32*	Single-phasing between phase A and C, $R_{ac} = 98\,\Omega$
52	IT ▹ (X)	Unbalanced ▹ Sinusoidal		Single-phasing between phase A and C, $R_{ac} = 98\,\Omega$
53	TN ▹ (XI)	Unbalanced ▹ Sinusoidal		Single-phasing between phase A and C, $L_{ac} = 175\,mH$
54	IT ▹ (XI)	Unbalanced ▹ Sinusoidal	*Figure A.10*	Single-phasing between phase A and C, $L_{ac} = 175\,mH$
55	IT ▹ (IX)	Balanced ▹ Sinusoidal	*Figure A.11*	YRF/YLF, $R_{a,b,c} = 96\,\Omega + L_{a,b,c} = 175\,mH$ (Parallel Symmetric)
56	IT ▹ (IX)	Unbalanced ▹ Sinusoidal	*Figure 3.36*	YRF/YLF, $R_{a,b} = 96\,\Omega + R_c = 16\,\Omega + L_{a,b,c} = 175\,mH$ (Parallel Unsymmetric)
57	TN ▹ (IX)	Unbalanced ▹ Sinusoidal	*Figure 3.37*	YRG/YLF, $R_{a,b} = 96\,\Omega + R_c = 16\,\Omega + L_{a,b,c} = 175\,mH$ (Parallel Unsymmetric)
58	IT ▹ (VIII)	Balanced ▹ Sinusoidal	*Figure 3.40*	Same as case 47, connected to stiff grid voltage (thyristor rectifier)
59	IT ▹ (VIII)	Balanced ▹ Sinusoidal		Same as above, but connected to grid via variac (thyristor rectifier
60	IT ▹ (VII)	Balanced ▹ Sinusoidal	*Figure 3.41*	Same as case 41, connected to stiff grid voltage without variac (diode rectifier)

[a] Recorded data from Fluke™ 434 Power Quality Analyzer were lost.

[b] Total Harmonic Distortion (*THD*) of voltage were equal to previous cases, $THD_v < 3\%$.

[c] $THD_i < 3\%$. Recording this quantity was not prioritized to save time.

Table 3.7 – *Case 61-70: Miscellaneous experiments that demonstrate certain properties or behavior of the virtual instrument. Also presents some special scenarios where the CPT-algorithm was manipulated.*

Quantity	Unit	61	62[a]	63[a]	64[a]	65[a]	66[a]	67[a]	68[a]	69[a]	70
$V_{A(B)}$	[V]	231.7									131.5
$V_{B(C)}$	[V]	231.8									132.2
$V_{C(A)}$	[V]	231.6									132.1
V_N	[V]										1.1
I_A	[A]	9.3									2.9
I_B	[A]	7.0									3.0
I_C	[A]	8.8									3.0
I_N	[A]										0.2
Quality Indexes											
THD_v	[%]	0.6									0.6
THD_i	[%]	18.0									2.1
K_{v-}	[%]	0.0									0.3
K_{v0}	[%]										0.0
K_{i-}	[%]	17.4									1.1
K_{i0}	[%]										0.6
Virtual Instrument - CPT											
A	[kVA]	3.262/100	1.622/100	3.718/100	2.738/100	3.769/100	1.744/100	1.762/100	0.264/100	0.006/100	1.190/100
P	[pu]	95.17	99.99	53.92	77.14	97.74	99.99	99.69	72.53	99.96	3.07
N_a	[pu]	9.87	0.49	15.99	0.06	0.19	0.34	0.31	25.26	0.62	0.43
Q	[pu]	19.67	0.79	52.41	42.23	2.40	0.12	1.55	2.35	0.20	99.94
N_q	[pu]	11.49	0.28	20.48	0.32	0.39	0.26	0.37	26.19	0.79	0.33
D	[pu]	18.05	0.71	60.59	47.62	21.01	0.35	7.73	58.38	2.41	1.76
A_{Sum}	[pu]	100.00	100.00	100.00	100.01	100.00	99.99	100.00	99.99	99.99	100.00
λ	[–]	0.952	0.999	0.539	0.771	0.977	1.000	0.997	0.725	0.999	0.031
Fluke 434 Scope											
S^*	[pu]	103.31									98.32
P^*	[pu]	97.79									5.88
Q^*	[pu]	33.72									98.32
S^*_{Sum}	[pu]	103.4									98.50
$\cos\phi$	[–]	0.95									0.06

Case	Topology	Network Voltage Status	Figure	Load Description
61	**IT ⊳ (XII)**	**Balanced ⊳ Sinusoidal**	***Figure A.12***	**Thyristor rectifier ⊳ $R_{dc} = 46\,\Omega$ & Diode rectifier ⊳ $R_{dc} = 32\,\Omega$ & $R_{ac} = 96\,\Omega$**
62	**IT ⊳ (VII)**	**Balanced ⊳ Sinusoidal**	***Figure A.13***	**Diode rectifier ⊳ Input low-pass filter set to $f_c(LP) = 75$ Hz**
63	**IT ⊳ (VII)**	**Balanced ⊳ Sinusoidal**	***Figure A.14***	**Diode rectifier ⊳ Fundamental frequency in CPT-algorithm set to $f_{CPT} = 1.5$ kHz**
64	**IT ⊳ (VII)**	**Balanced ⊳ Sinusoidal**	***Figure A.15***	**Diode rectifier ⊳ Fundamental frequency in CPT-algorithm set to $f_{CPT} = 100$ Hz**
65	**TN ⊳ (I)**	**Balanced ⊳ Sinusoidal**	***Figure A.16***	**Balanced R-load connected to grid ⊳ Demonstration of saturated LEM LA 55-P**
66	**TN ⊳ (I)**	**Balanced ⊳ Sinusoidal**	***Figure A.17***	**Balanced R-load connected to grid ⊳ Demonstration of power generative mode**
67	**TN ⊳ (I)**	**Balanced ⊳ Sinusoidal**	***Figure A.18***	**Balanced R-load connected to grid ⊳ Input high-pass filter removed**
68	**TN ⊳ (-)**	**Balanced ⊳ Sinusoidal**	***Figure A.19***	**Demonstrating common type of load: cluster of PCs and monitors**
69	**IT ⊳ (I)**	**Balanced ⊳ Sinusoidal**	***Figure A.20***	**Balanced R-load connected to grid ⊳ Demonstration of unlinear LEM LV 25-P**
70	**TN ⊳ (I)**	**Balanced ⊳ Sinusoidal**		**Same as case 13, but connected to grid (symmetric L-load)**

[a] These cases were meant to demonstrate properties characteristic to the virtual instrument, thus data from Fluke™ 434 Scope were not recorded.

Table 3.8 – *Case 71-80: Selected set of experiments from cases 1-40, including various constellations of bipolar loads applied with harmonic voltages. Despite non-ideal voltage regime, the CPT manage to maintain correct decomposition of currents and power. This work include a very narrow set of harmonic voltage scenarios, thus more research is needed.*

Quantity	Unit	71	72	73	74	75	76	77	78	79	80
$V_{A(B)}$	$[V]$	229.3	131.5	223.8	264.3	150.1	91.0	144.9	144.9	88.1	241.1
$V_{B(C)}$	$[V]$	227.7	131.9	222.4	259.1	152.3	94.8	145.1	145.5	89.9	233.3
$V_{C(A)}$	$[V]$	227.9	131.1	222.2	255.9	147.2	91.5	141.9	141.9	86.8	228.8
V_N	$[V]$		24.0			25.2	18.6	23.4	21.5	17.5	
I_A	$[A]$	5.6	5.6	4.1	3.1	3.1	5.6	2.4	2.4	4.3	2.0
I_B	$[A]$	5.7	5.7	4.2	3.2	3.2	5.8	2.5	2.5	4.4	2.1
I_C	$[A]$	5.7	5.7	4.1	3.1	3.1	5.7	2.4	2.4	4.4	3.2
I_N	$[A]$		0.1			0.2	0.1	0	0.1	0.1	
Quality Indexes											
THD_v	[%]	19.7	19.7	11.1	43.3	40.3	41.5	37.6	37.6	43.1	18.0
THD_i	[%]	19.7	19.7	10.9	3.5	3.9	3.7	4.5	4.5	4.4	15.0
K_{v-}	[%]	0.3	0.5	0.3	0.5	0.5	0.5	0.6	0.5	0.4	2.9
K_{v0}	[%]		0.1			0.0	0.1	0.0	0.1	0.1	
K_{i-}	[%]	0.7	0.8	1.0	1.2	1.4	1.7	1.2	1.2	0.8	36.8
K_{i0}	[%]		0.5			1.4	0.5	1.2	1.1	0.5	
Virtual Instrument - CPT											
A	$[kVA]$	2.275/100	2.274/100	1.661/100	1.412/100	1.415/100	1.590/100	1.063/100	1.063/100	1.163/100	1.018/100
P	$[pu]$	99.98	99.99	99.98	2.90	2.88	2.82	55.05	55.13	53.86	93.01
N_a	$[pu]$	0.08	0.15	0.36	0.29	0.33	0.64	0.39	0.64	0.82	26.37
Q	$[pu]$	0.11	0.07	0.14	99.95	99.94	99.95	81.46	81.39	81.39	0.06
N_q	$[pu]$	0.28	0.23	0.44	0.32	0.56	0.05	0.12	0.17	0.47	25.33
D	$[pu]$	1.56	0.64	1.59	1.37	2.09	1.31	18.30	18.33	21.78	3.47
$A_{S_{um}}$	$[pu]$	99.99	99.99	99.99	100.00	100.01	100.00	100.01	100.00	100.00	100.00
λ	$[-]$	0.999	1.000	0.999	0.029	0.029	0.028	0.550	0.551	0.539	0.930
Fluke 434 Scope											
S^*	$[pu]$	98.90	98.50	98.78	99.15	98.94	99.37	98.78	98.78	99.74	99.21
P^*	$[pu]$	98.46	98.50	98.74	4.25	4.95	4.40	56.44	56.44	55.03	92.34
Q^*	$[pu]$	8.79	2.20	8.43	99.15	98.94	99.37	80.90	80.90	83.40	36.35
S^*_{Sum}	$[pu]$	98.85	98.52	99.10	99.24	99.06	99.47	98.64	98.64	99.92	99.24
$\cos\phi$	$[-]$	1.00	1.00	1.00	0.04	0.05	0.05	0.57	0.57	0.55	0.93

Case	Topology	Network Voltage Status	Figure	Load Description
71	IT ▹ (I)	Balanced ▹ Harmonic	*Figure 3.46*	YF-Connected, $R_{a,b,c} = 23\,\Omega$ (Symmetric)
72	TN ▹ (I)	Balanced ▹ Harmonic		YG-Connected, $R_{a,b,c} = 23\,\Omega$ (Symmetric)
73	IT ▹ (II)	Balanced ▹ Harmonic		D-Connected, $R_{a,b,c} = 96\,\Omega$ (Symmetric)
74	IT ▹ (III)	Balanced ▹ Harmonic	*Figure 3.47*	YF-Connected $L_{a,b,c} = 175\,mH$ (Symmetric)
75	TN ▹ (III)	Balanced ▹ Harmonic		YG-Connected $L_{a,b,c} = 175\,mH$ (Symmetric)
76	TN ▹ (IV)	Balanced ▹ Harmonic		D-Connected $L_{a,b,c} = 175\,mH$ (Symmetric)
77	TN ▹ (V)	Balanced ▹ Harmonic	*Figure 3.48*	YF-Connected, $R_{a,b,c} = 23\,\Omega + L_{a,b,c} = 175\,mH$ (Series Symmetric)
78	TN ▹ (V)	Balanced ▹ Harmonic		YG-Connected, $R_{a,b,c} = 23\,\Omega + L_{a,b,c} = 175\,mH$ (Series Symmetric)
79	TN ▹ (V)	Balanced ▹ Harmonic		D-Connected, $R_{a,b,c} = 30.3\,\Omega + L_{a,b,c} = 175\,mH$ (Series Symmetric)
80	IT ▹ (I)	Unbalanced ▹ Harmonic	*Figure 3.49*	YF-Connected, $R_{a,b} = 96\,\Omega + R_c = 25\,\Omega$ (Unsymmetric)

Table 3.9 – *Case 81-90: Selected set of defiant unsymmetric bipolar loads under harmonic voltage conditions. Verification how the CPT in terms of power flow only pays attention to characteristic in the load, while voltage conditions have less influence.*

Quantity	Unit	81	82	83	84	85	86	87	88	89	90
$V_{A(B)}$	[V]	134.0	118.4	148.0	266.7	66.5	134.9	136.3			
$V_{B(C)}$	[V]	140.2	136.0	155.7	259.9	72.5	151.0	136.2			
$V_{C(A)}$	[V]	127.1	129.9	144.3	249.3	72.7	138.2	114.3			
V_N	[V]	16.3	21.2	23.2		17.9	13.3	20.7			
I_A	[A]	1.4	10.0	5.4	4.3	5.7	2.4	4.5			
I_B	[A]	1.5	4.4	3.2	3.5	6.0	0	0			
I_C	[A]	8.3	10.5	3.0	3.4	4.4	2.4	4.6			
I_N	[A]	7.0	0	2.4		0.1	0	0			
Quality Indexes											
THD_v[a]	[%]	17.0	8.5	43.3	47.8	37.1	19.7	42.9			
THD_i[b]	[%]	16.7	5.9	4.8	3.7	3.6	13.0	4.1			
K_{v-}	[%]	5.0	7.6	2.0	1.7	4.1	6.0	9.5			
K_{v0}	[%]	0.4	0.1	0.1		0.0	0.0	0.0			
K_{i-}	[%]	60.8	45.9	19.1	14.8	17.2	100.0	100.0			
K_{i0}	[%]	60.6	0.1	21.1		0.4	0.8	0.4			
Virtual Instrument - CPT											
A	[kVA]	1.992/100	3.087/100	1.821/100	1.699/100	1.161/100	0.843/100	1.452/100			
P	[pu]	73.79	88.98	3.04	3.14	3.38	65.68	1.59			
N_a	[pu]	67.46	29.41	1.03	10.62	13.22	51.29	51.42			
Q	[pu]	0.14	0.03	95.88	98.62	97.98	0.08	66.73			
N_q	[pu]	0.28	33.48	28.06	11.78	13.82	54.13	51.27			
D	[pu]	1.92	9.83	2.91	3.73	4.85	11.25	16.50			
A_{Sum}	[pu]	100.00	100.00	100.00	100.01	100.00	100.01	100.00			
λ	[–]	0.734	0.890	0.031	0.030	0.034	0.657	0.016			
Fluke 434 Scope											
S^*	[pu]	99.40	109.17	98.85	98.88	99.05	98.46	99.86			
P^*	[pu]	73.29	96.53	4.94	4.12	5.17	65.24	4.13			
Q^*	[pu]	1.51	2.27	95.00	98.88	97.33	2.37	67.49			
S^*_{Sum}	[pu]	73.31	96.56	95.13	98.97	97.47	65.28	67.62			
$\cos\phi$	[–]	0.74	0.88	0.05	0.04	0.05	0.66	0.04			

Case	Topology	Network Voltage Status	Figure	Load Description
81	TN ▷ (I)	Unbalanced ▷ Harmonic	*Figure 3.50*	YG-Connected, $R_{a,b} = 67\,\Omega + R_c = 67\,\Omega$ (Unsymmetric)
82	TN ▷ (II)	Unbalanced ▷ Harmonic		D-Connected ▷ $R_{a,b} = 96\,\Omega + R_c = 24\,\Omega$ (Unsymmetric)
83	TN ▷ (III)	Unbalanced ▷ Harmonic	*Figure 3.51*	YG-Connected ▷ $L_a = 87.5\,mH + L_{b,c} = 175\,mH$ (Unsymmetric)
84	IT ▷ (III)	Unbalanced ▷ Harmonic		YF-Connected ▷ $L_a = 87.5\,mH + L_{b,c} = 175\,mH$ (Unsymmetric)
85	TN ▷ (IV)	Unbalanced ▷ Harmonic		D-Connected ▷ $L_a = 87.5\,mH + L_{b,c} = 175\,mH$ (Unsymmetric)
86	TN ▷ (X)	Unbalanced ▷ Harmonic	*Figure 3.52*	Single-phasing between phase A and C ▷ $R_{ac} = 96\,\Omega$
87	TN ▷ (XI)	Unbalanced ▷ Harmonic	*Figure 3.53*	Single-phasing between phase A and C ▷ $L_{ac} = 175\,mH$
88				
89				
90				

[a] Total Harmonic Distortion $THD_v < 3\%$ and $THD_i < 3\%$. Quantities were not recorded to save time.

3.2 Symmetric R-loads

Introductorily measured voltages $u(t)$ are as ideally balanced and sinusoidal as it was possible to achieve with the programmable voltage source. This first test generally sets the standard for all consequential symmetric sinusoidal voltage scenarios.

The source was programmed to output line voltages close to the usual $V_{LL} = 230.0\,V_{RMS}$ for convenient reference. The voltage negative sequence unbalance factor is approximately very close to zero $(K_{v-} = 0.2\,\%)$. A slight deformation of the waveforms occurs every time the voltages crosses one another (**Figure 3.2**). This deformation makes the total harmonic distortion nonzero $(THD_v = 2.1\,\%)$. According to the Fluke™ 434 Power Quality Analyzer, 3rd, 5th and 7th harmonics dominate the frequency spectrum (**Figure A.22**) along with the requested 50.0 Hz fundamental voltage component.

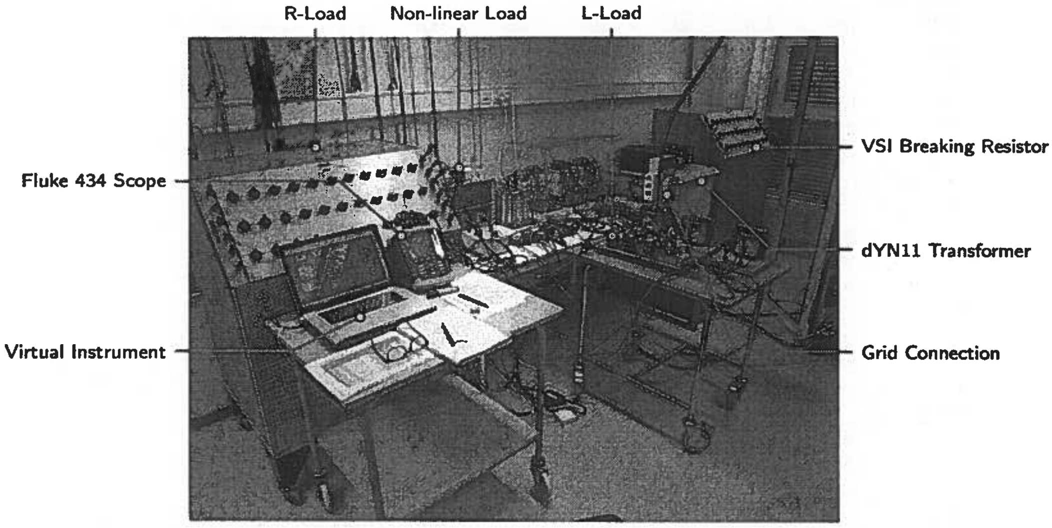

Figure 3.1 – *Overview picture of experimental setup. In the foreground laptop linked to Speedgoat Host computer via NTNUs WiFi network, used as a mobile virtual instrument controlling the programmable source, and acquiring experimental data.*
The Fluke 434 Oscilloscope was also connected to laptop via an optical USB-cable for convenient data transfer and storage. Resistive and inductive bipolar loads, and unlinear loads (thyristor- and diode rectifiers) can be observed in the background. Far back is the breaking resistor connected to the DC-bus breaking chopper, in case of DC-link overvoltage.

It was spent two weeks attempting to eliminate the voltage harmonics that were initially assumed to originate from erroneous pulse-width-modulation. However after numerous trials the conclusion is that the harmonics were caused by electromagnetic properties of the three-phase dYN11-transformer, used as coupling between voltage source converter and the load (**Figure 3.1**). As the harmonic content in voltages was kept within accepted limits[E53], it was decided not to further perfect the voltage quality.

3.2.1 *Case 1*

Starting with experiment 1 the load is purely symmetric resistive ($R_{a,b,c} = 23\,\Omega$), thus line currents $\boldsymbol{i}(t)$ inherit harmonic content ($THD_i = 1.7\,\%$) from respective voltages, as can be recognized by the slightly deformed waveforms in **Figure 3.2**.

The load is correctly interpreted by the CPT, as the entire powerflow is linked to active power P. Instantaneous real power $p(t)$ flows constant from the source to load, as voltages and currents are balanced sinusoidal. Notably balanced active currents $\boldsymbol{i}_a^b(t)$ fully account for acquired line currents $\boldsymbol{i}(t)$.

3.2.2 *Case 2*

Setting load bus voltages $\boldsymbol{u}(t)$ to sinusoidal and noticeably unbalance ($K_{v-} = 17.1\,\%$). Like previous experiment the load is a symmetric star-connected R-load, so that line currents $\boldsymbol{i}(t)$ are in-phase with, and inherit the exact same waveforms as their respective voltages. Measured voltages and currents, instantaneous real power $p(t)$ and current components for this case are identical to what observed in **Figure 3.3**.

Although line currents appear unbalanced ($K_{i-} = 16.6\,\%$), but they do sum up to zero at each instant of time due to load symmetry. Thus only active power P is identified, and line currents are made up of balanced active components $\boldsymbol{i}_a^b(t)$. Small and negligible unbalanced current terms $\boldsymbol{i}_a^u(t)$ along with void currents $\boldsymbol{i}_v(t)$ are observed, the former most likely due to unmatched impedance in the load circuitry. One important observation is that instantaneous real power $p(t)$ oscillate despite having a balanced resistive load.

3.2.3 *Case 3 and 4*

The setup is similar to experiment 1, but adding a neutral conductor in order to connect star point of load μ_M, to neutral point of the voltage source *(TN-mode)*. Also voltage reference is adequately chosen to be neutral conductor. As the load and voltages are identical to case 1, measured line currents $\boldsymbol{i}(t)$ remain unaltered nonetheless.

The load is almost perfectly symmetric so that phase N conducts insignificant amounts of current ($I_N = 0.10\,A$). Measured phase voltages $\boldsymbol{u}(t)$ are scaled down from line voltages by the usual $^{-1}\!\sqrt{3}$ factor.

The Fluke instrument is measuring a voltage on the neutral channel ($V_N = 35.9\,V$), however it has not been possible to determine exactly[D37] what reference this and phase voltages (V_A, V_B, V_C) are measured against, but they are most likely floating channels. Power and current decomposition match results from experiment 1, as the acquired currents $\boldsymbol{i}(t)$ and voltages $\boldsymbol{u}(t)$ are in their entirety unchanged.

In experiment 4 same TN-system applies but with the star point of the load floating. Theoretically as the load is symmetric no current flow in phase N, making the neutral conductor redundant. Consequently voltage level V_N and output from the CPT-algorithm should not be affected by the rewiring as confirmed by cases 3 and 4. Representative waveforms for these two tests can be viewed in **Figure 3.2**.

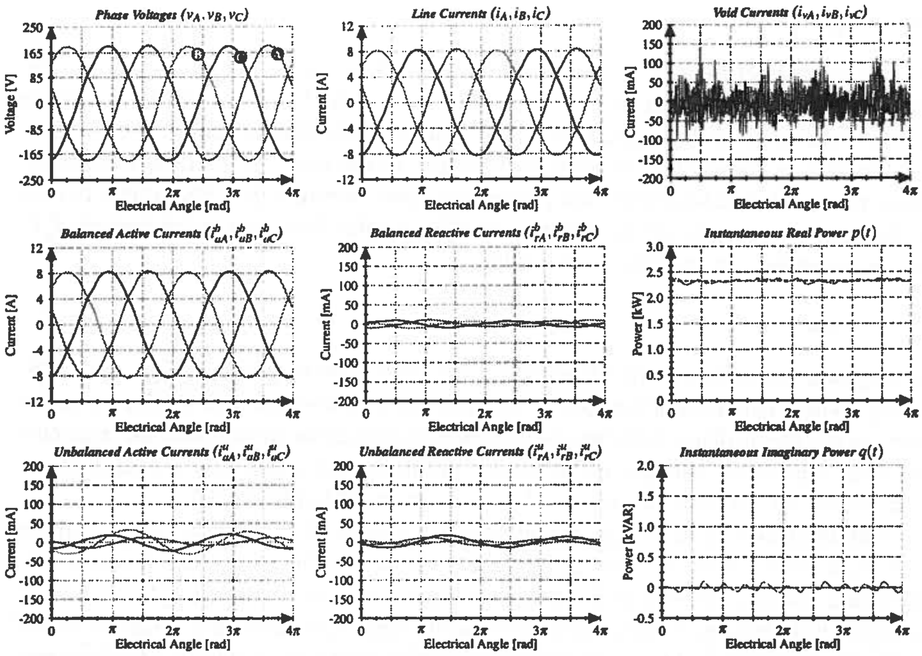

Figure 3.2 – *Case 1 - Symmetric YF-connected R-load. Only balanced active currents are detected. Instantaneous real power flow is fluctuating around average value.*

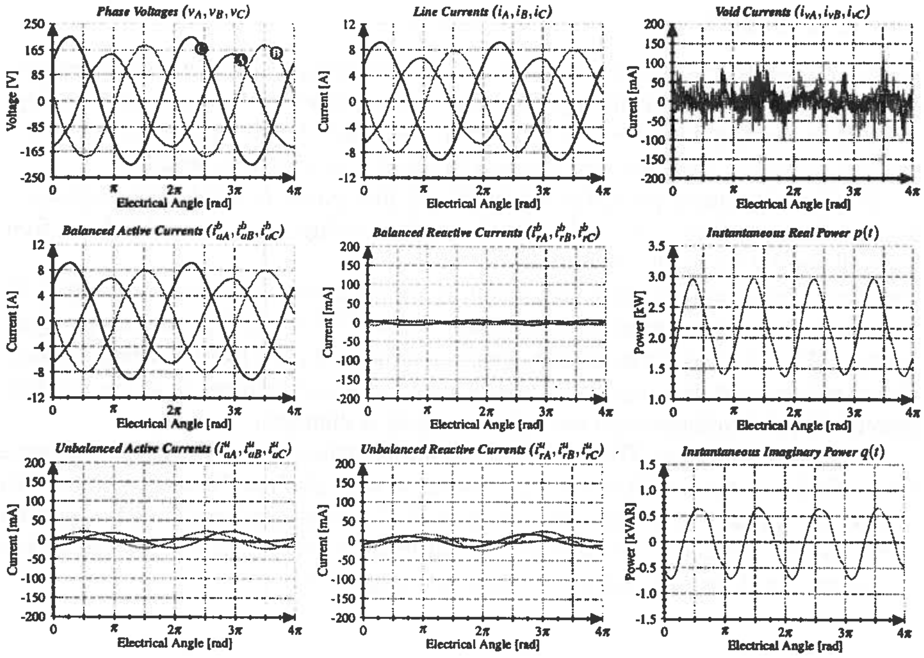

Figure 3.3 – *Case 5 - Symmetric YG-connected R-load. Despite unbalanced line currents the current decomposition remain similar to case 1 as the load is still purely symmetric.*

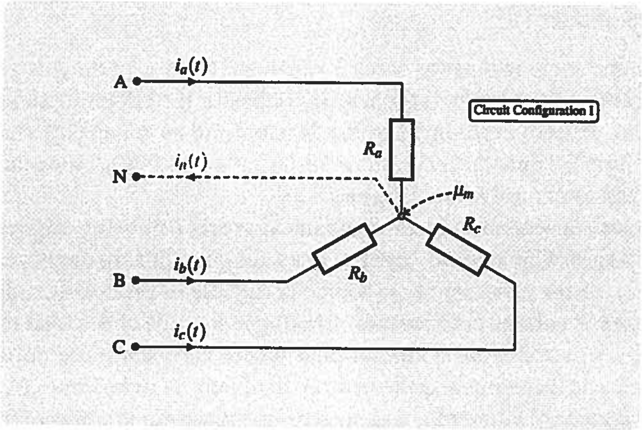

Figure 3.4 – *Load arrangement 1: Star-connected R-load.*

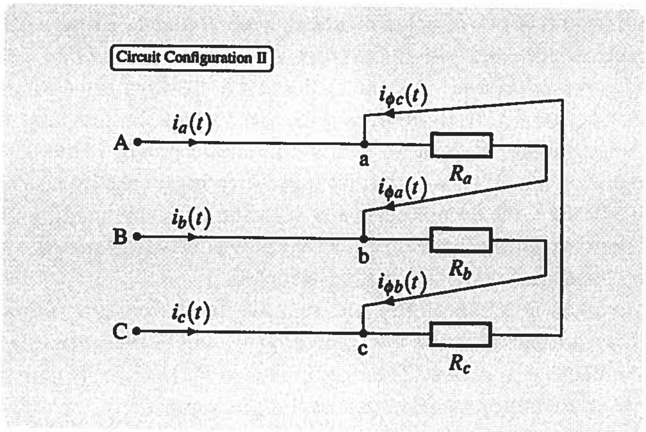

Figure 3.5 – *Load arrangement 2: Delta-connected R-load.*

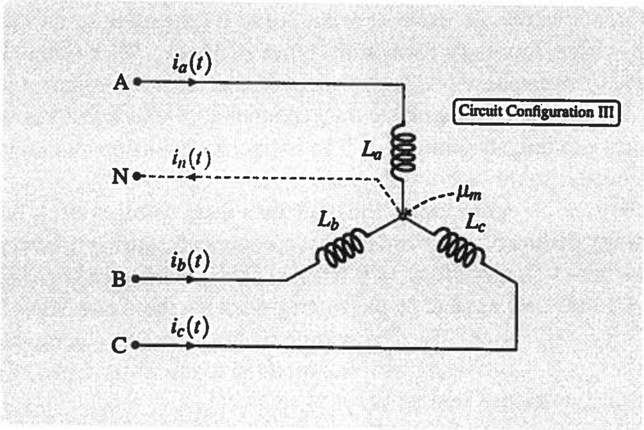

Figure 3.6 – *Load arrangement 3: Star-connected L-load.*

3.2.4 *Case 5 and 6*

Proceeding in the same manner as cases 3 and 4, next two experiments are meant as an opponent to case 2. By introducing a neutral conductor the circuit topology is classified as a TN-system. In both experiments phase N is utilized as voltage reference. Measured voltages $\boldsymbol{u}(t)$ appear unbalanced sinusoidal ($K_{v-} = 16.9\,\%$), independently of load being connected to neutral or not (**Figure 3.3**).

The resistive star-connected load drain line currents $\boldsymbol{i}(t)$ being aligned and linear to respective voltages. Unbalanced voltages does not contain zero-sequence components ($K_{v0} = 0.0\,\%$), as the programmable source is capable of producing only positive and negative-sequence voltage components. Linking star point of the load to neutral point of the source μ_N, establishes a current path where zero-sequence currents can flow. However similar to experiment 2 the neutral conductor is redundant ($K_{i0} = 0.5\,\%$) as the load impedance is symmetric, and no zero-sequence electromotive forces exist.

The conservative power theory correctly detects active power P only as the load is symmetric, and should not be affected by unbalanced voltages. **Figure 3.3** demonstrates how active power P coincide with the average value *(blue dashed line)* of instantaneous real power $p(t)$ *(red solid line)*. However the active power only contain information regarding unidirectional power flow, and do not reflect the fact that $p(t)$ oscillates at twice the fundamental frequency. Related to active power comes the detection of balanced active currents $\boldsymbol{i}_a^b(t)$, which fully reproduce measured line currents $\boldsymbol{i}(t)$.

Consequently the CPT do not offer any solution of compensating the unbalanced currents, and the oscillating instantaneous real power. These issues are solely voltage-related phenomenas while the CPT is load-oriented.
Interestingly even in absence of any true reactive load elements, there is noticeably fluctuation of instantaneous imaginary power $q(t)$, which is oscillating in quadrature with the instantaneous real power. The magnitudes of $\boldsymbol{i}_a^u(t)$ and $\boldsymbol{i}_r^u(t)$ are to small giving any perceptible contribution to these oscillation phenomenas.

3.2.5 *Case 7 - 10*

These experiments cover the delta or what some might refer to as π-configuration, an alternative wiring-topology for certain types of loads. With delta-connection the load impedance of each phase is directly connected across two adjacent phase voltages. Consequently the neutral conductor becomes redundant ($I_N = 0.0\,A$) as the load always floats due to non-existing star point μ_M. The harmonic distortion and unbalance indexes are generally similar to the star-topologies.

Figure 3.8 *(case 7)* representably illustrate measured voltages $\boldsymbol{u}(t)$, line currents $\boldsymbol{i}(t)$ and corresponding deduced power and current components, during network conditions of balanced sinusoidal voltages ($K_{v-} = 0.5\,\%$). As the load is purely resistive ($R_{a,b,c} = 96\,\Omega$), acquired currents appear in-phase and possess the same waveforms as their respective voltages ($K_{i-} = 0.8\,\%$). The symmetric load currents corresponds to balanced active currents $\boldsymbol{i}_a^b(t)$. Combined with balanced sinusoidal voltages, the load drains unidirectional instantaneous real power $p(t) = P$.

Figure 3.9 *(case 8)* depicts input and output signals from the CPT-algorithm when the system voltages $\boldsymbol{u}(t)$ are unbalanced sinusoidal ($K_{v-} = 16.9\,\%$). The delta-configuration draws unbalanced currents ($K_{i-} = 17.6\,\%$) which are classified as balanced active currents $\boldsymbol{i}_a^b(t)$. It is now apparent that balanced active currents occur as truly balanced specifically, only in cases where the voltages too are balanced. Therefore the active balanced currents $\boldsymbol{i}_a^b(t)$ may become unsymmetric despite their names suggest differently.

Going through the data in **Table 3.1**, obviously the power and current decomposition for symmetric delta-connected R-loads (case 9 and 10), are no different from the star-connected scenarios. These results are in agreement with the requirement that CPT must coincide with the classic power theory during sinusoidal operating conditions.

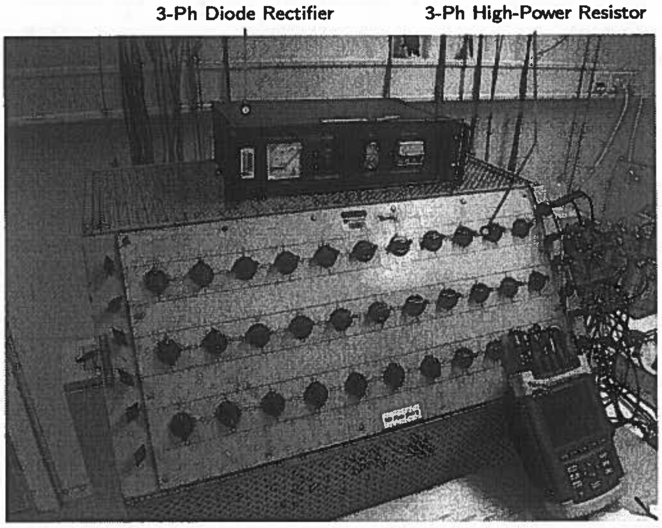

Figure 3.7 – *Three-phase reconfigurable resistor. Resistance in each phase is selectable from 15 to 455 Ω, offering a current rating up to 12.7 A and maximum power of 17.6 kW in total. On top is the 43 kW three-phase diode rectifier designed and built by NTNU. This is identical to the rectifier unit used to energize the DC-link in the programmable voltage source.*

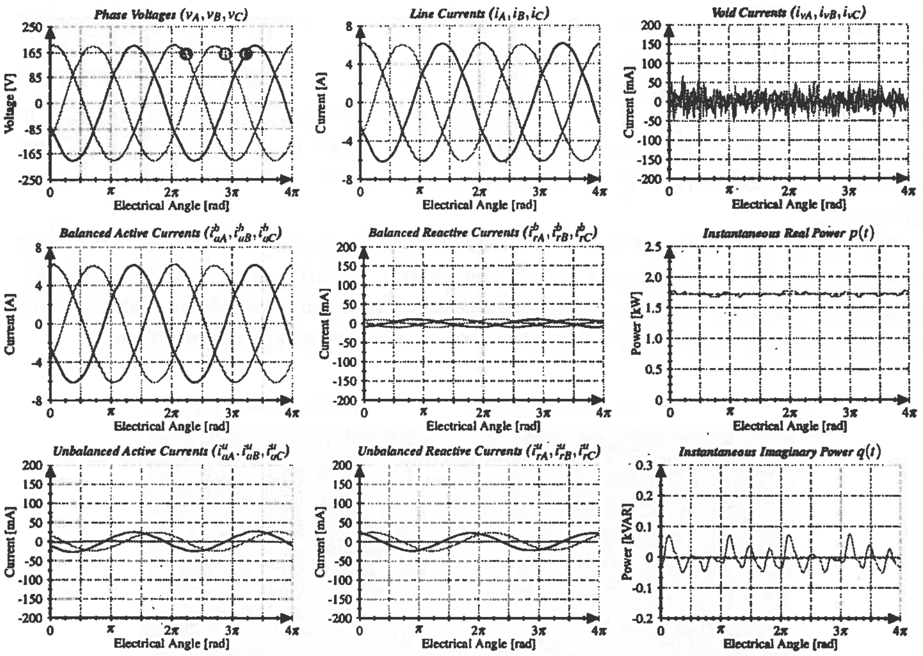

Figure 3.8 – *Case 7 - Symmetric D-connected R-load. Apparently current decomposition for symmetric R-loads are independent of star or delta-topology. Ground or virtual voltage reference give same results.*

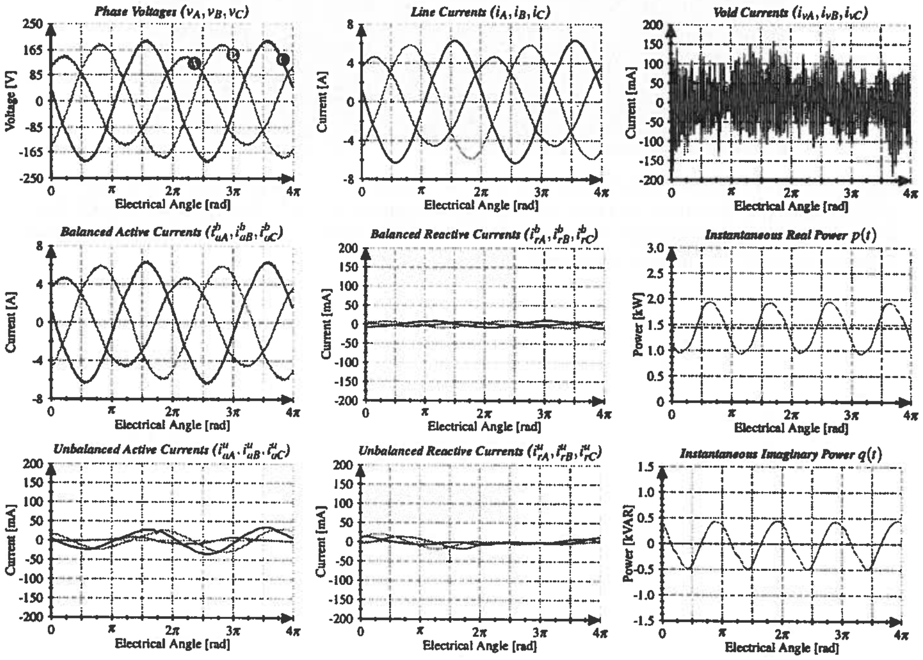

Figure 3.9 – *Case 8 - Symmetric D-connected R-load. Unbalanced voltages gives oscillating real and imaginary power flow, both for symmetric bipolar delta and star-configurations.*

3.3 Symmetric L-loads

The following next ten cases it is experimented with pure inductances as load. Although these cases represent an extreme example, as its unlikely to find similar loads in the regular power network. However the test are necessary in order to validate that the conservative power theory, is capable to correctly identify reactive elements in terms of power and current decomposition.

As the coils have very high inductance values ($L = 175\,mH$), they gave manageable current magnitudes when energized with the standard $V_{LL} = 230.0\,V_{RMS}$ voltage. The experimental results in **Table 3.2** testify that certain amount of resistance $R_L \approx 4.0\,\Omega$ is always present, due to the resistive nature of all copper conductors at room temperature. However the amount of resistance is ignorable compared to the coils inductance ($X_L \gg R_L$), so it can be characterized close to an ideal inductance $Z_L \approx j\omega L$.

Working with pure inductances demanded extra care to be taken during initiation of each test. Applying full voltage to an inductor at no-load status would be dangerous due to high inrush currents, and consequently high self-induced voltage across the inductors. The coils were energized gently as a safety precaution, and avoiding damaging the experimental setup.

3.3.1 Case 11

In experiment 11 applied voltages $\boldsymbol{u}(t)$ are balanced ($K_{v-} = 0.4\,\%$) and sinusoidal ($THD_v = 2.0\,\%$) as depicted in **Figure 3.11**. There were initially concerns regarding connecting a purely high-inductive load directly to the LCL-filter of the voltage source inverter, however it turned out to work nicely.

Acquired line currents $\boldsymbol{i}(t)$ are lagging their respective voltages by the compulsory $\varphi_1 \approx$ -90° phase shift. Currents are very close to being balanced ($K_{i-} = 0.6\,\%$) as the load impedance is symmetric ($L_{a,b,c} = 175\,mH$), resulting in unidirectional instantaneous imaginary power flow $q(t) = Q$, transported by the balanced reactive currents $\boldsymbol{i}_r^b(t)$. Minor balanced active currents $\boldsymbol{i}_a^b(t)$ are detected, and associated with a constant flow of real power $p(t)$. However as expected both quantities are very small, due to the aforementioned ratio of R_L and $j\omega L$.

As the coils naturally filters high order current harmonics, it can be seen in **Table 3.2** how the harmonic content THD_i always is lower than what found in the voltage THD_u, due to this filtering action. Compared to resistive loads line currents appear more close to a pure sinewave. This will generally yield for all following experiments involving these inductances.

3.3.2 Case 12

Applying sinusoidal unbalanced voltages ($K_{v-} = 16.6\,\%$) to a symmetric star-connected purely inductive load, makes the line currents $\boldsymbol{i}(t)$ obtain exact same waveform as their respective voltages $\boldsymbol{u}(t)$, but lagging nearly $\varphi_1 \approx$ -90°.

By properly scaling all current waveforms visualize (**Figure 3.12**) the relative impact of active currents $\boldsymbol{i}_a(t)$ and void current terms $\boldsymbol{i}_v(t)$, compared to the balanced reactive currents $\boldsymbol{i}_r^b(t)$. Despite having a symmetric inductive load, the instantaneous imaginary power $q(t)$ and instantaneous real power $p(t)$ oscillates, similar to what was observed for symmetric resistive loads. The powers mutually swing in quadrature relation at frequency of $100\,Hz$.

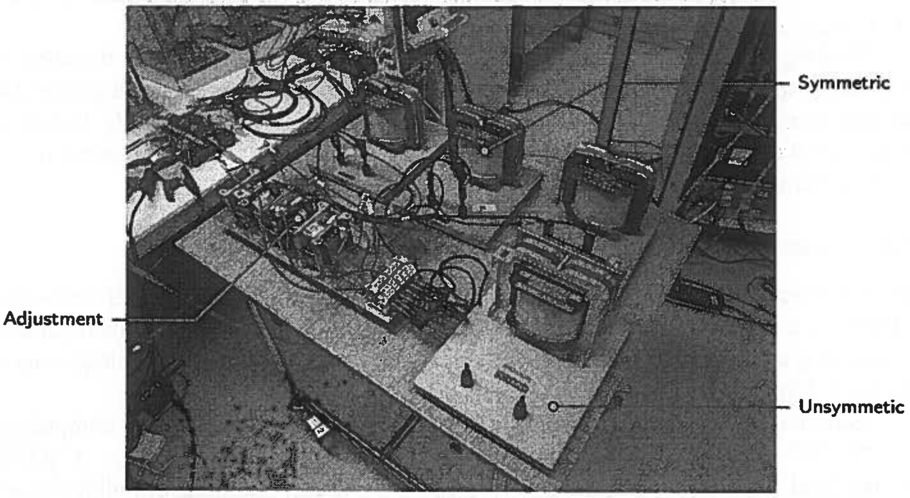

Figure 3.10 – *High-inductance coils* $L = 175\,mH@50\,Hz$ *used to emulate purely reactive bipolar loads. The coils were somewhat unmatched so phase C had to be adjusted by inserting a small inductance in series, in order to make the impedance symmetric.*
A fourth identical inductance was connected in parallel to one phase in order to create an unsymmetric reactive load. Dealing with these coils was the least pleasant part of the experiments.

3.3.3 Case 13 and 14

These two experiments mimic a TN-system where the star point of the inductive load μ_M, could be connected to the neutral conductor *(case 13)* or left floating *(case 14)*. Because the inductive load is symmetric, line currents $\boldsymbol{i}(t)$ will at each instant of time always sum up to zero at the star point, indicating that a TN-system in this context is redundant.

According to experimental results (**Table 3.2**), there are no qualitative or quantitative difference in CPT-power and current detection in these alternations. Symmetric inductive load impedance translates into balanced reactive currents $\boldsymbol{i}_r^b(t)$, associated with reactive power Q. Instantaneous imaginary power $q(t)$ flow constant from source to load, as the voltages $\boldsymbol{u}(t)$ are balanced $K_{v-} = 0.4\,\%$. **Figure 3.11** representably illustrate the suggested decomposition of current and power flow.

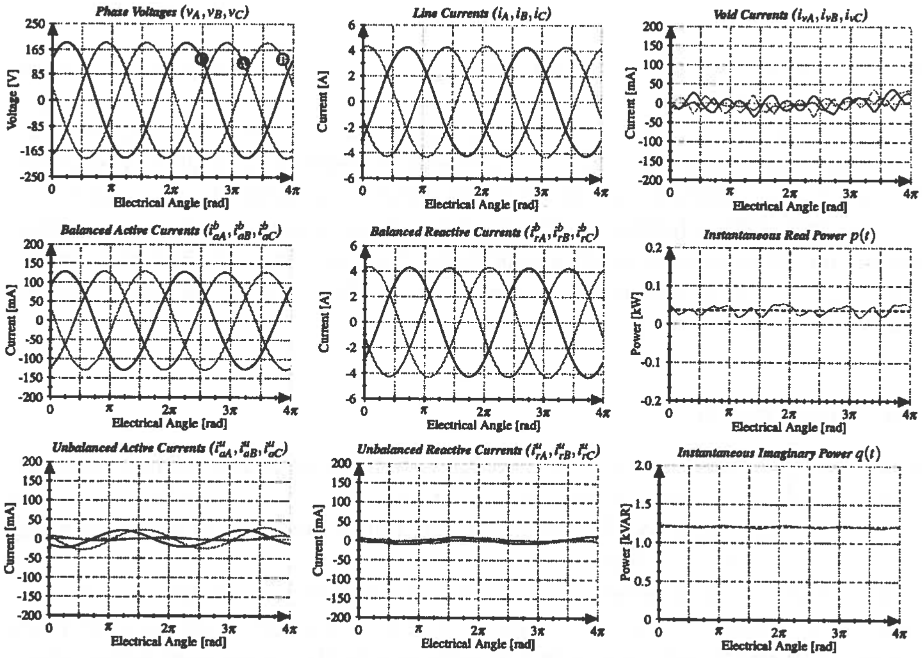

Figure 3.11 – *Case 11 - Symmetric YF-connected L-load. Balanced reactive current components dominates due to purely inductive load. Symmetry results in constant imaginary power flow.*

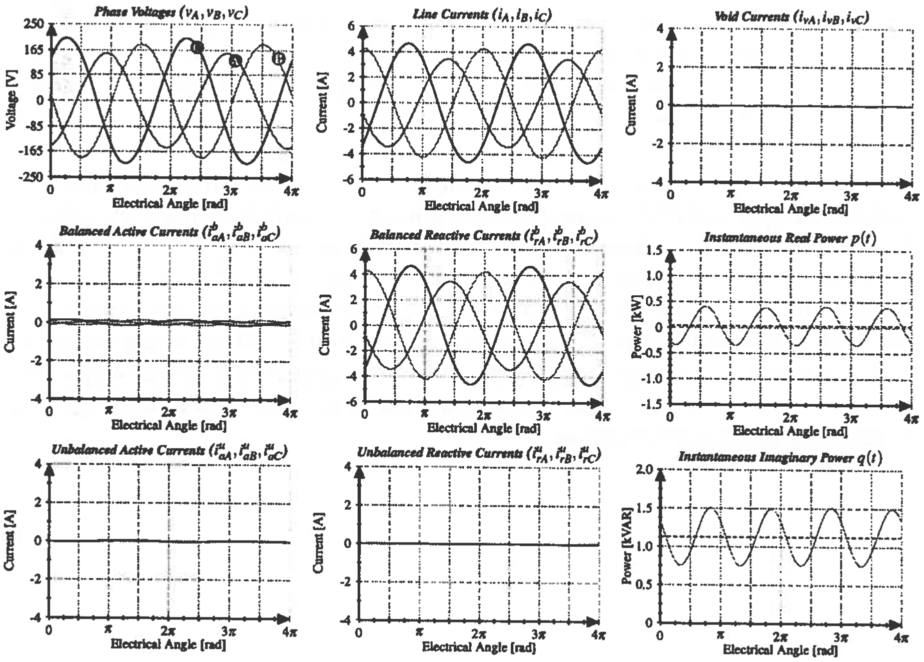

Figure 3.12 – *Case 12 - Symmetric YF-connected L-load. The symmetric L-load draws only balanced reactive currents despite unsymmetric voltage. Significant oscillation present in* $p(t)$ *and* $q(t)$*.*

3.3.4 Case 15 and 16

Further investigating the TN-topology now with preset unbalanced sinusoidal voltages $K_{v-} = 16.6\,\%$. Once more alternating between floating and grounded star point μ_M, the conservative power theory does not differentiate the two scenarios as the load still is symmetric. Observing representative waveforms in **Figure 3.12**, acquired line currents $\boldsymbol{i}(t)$ appear phase shifted, but with same characteristics as voltages $K_{v-} = 17.0\,\%$.

Because of the unbalanced voltages, instantaneous imaginary power $q(t)$ oscillate around an offset component which equals the reactive power Q. Balanced reactive currents $\boldsymbol{i}_r^b(t)$ equals measured line currents $\boldsymbol{i}(t)$, when ignoring the minor balanced active currents $\boldsymbol{i}_a^b(t)$.

3.3.5 Case 17 to 20

Investigating symmetric delta-connected inductive loads, generally yield the exact same results as observed and discussed in the star-topology. Acquired voltages $\boldsymbol{u}(t)$, line currents $\boldsymbol{i}(t)$ and decomposed current and power flow for unbalanced sinusoidal voltage scenarios are depicted in **Figure 3.13**.
A phenomena worth mentioning is that when applying full line voltage across the coils, resulted in degradation of source voltage $\boldsymbol{u}(t)$. Positive and negative peaks of the voltage curves (extrema) started to sort of pulsate at approximately 1-2 Hz, along with an audible humming sound from the dYN11-transformer. Total harmonic voltage distortion nearly doubled in these cases ($THD_v = 4.9\,\%$), while line currents as mentioned earlier remain much smoother $THD_i = 1.3\,\%$.

Figure 3.13 illustrates how the waveform of distorted voltages $\boldsymbol{u}(t)$ are directly transferred to the balanced active currents $\boldsymbol{i}_a^b(t)$, while the reactive analogue $\boldsymbol{i}_r^b(t)$ is more sinusoidal. The instantaneous imaginary power $q(t)$ is apparently less sensitive to the harmonic voltage than instantaneous real power $p(t)$.

Based on the past 20 experiments dealing with basic symmetric bipolar loads concludes that, $\boldsymbol{i}_a^b(t)$ and $\boldsymbol{i}_r^b(t)$ are the only components recognized by the CPT when the load is symmetric. This applies independently of voltage condition and selected voltage reference. Also what can be truly stated is that balanced active $\boldsymbol{i}_a^b(t)$ and reactive $\boldsymbol{i}_r^b(t)$ currents inherit positive and negative sequence components from the voltages. It is demonstrated that unbalanced voltages triggers oscillation of both instantaneous real $p(t)$ and imaginary $q(t)$ power flow, for both purely resistive and inductive symmetric loads. As these are voltage-related phenomenas, they can only be solved when addressed to series compensation techniques.

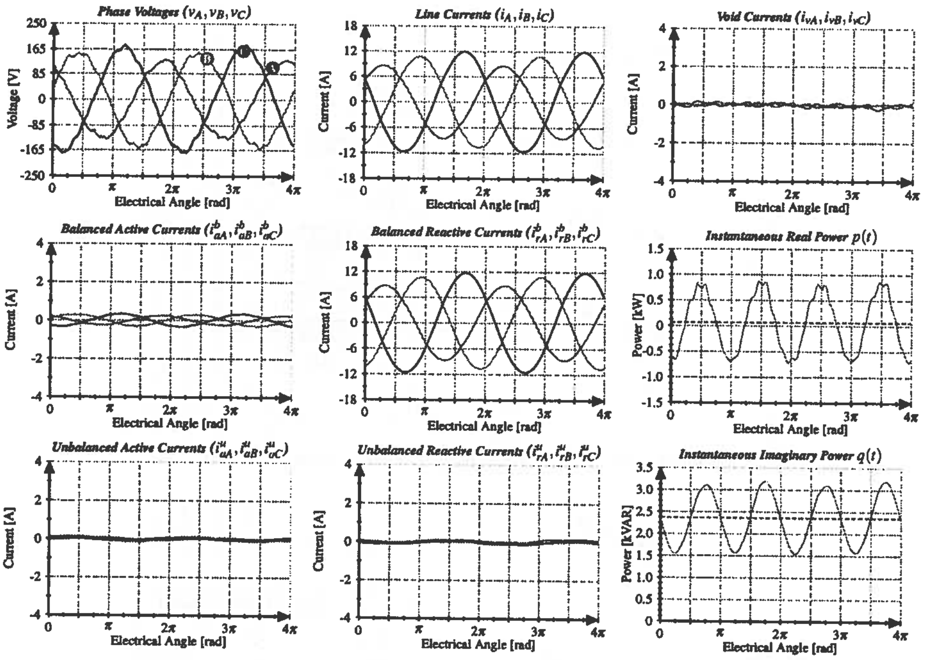

Figure 3.13 – *Case 19 - Symmetric D-connected L-load. Contrary to their names, balanced reactive and active currents appear unbalanced whenever the voltages are unbalanced.*

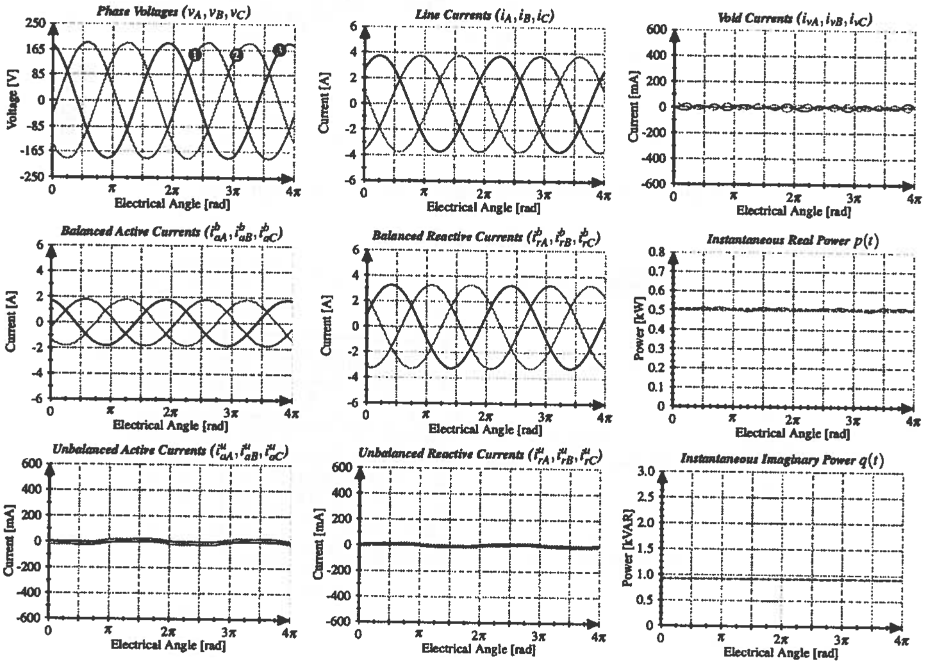

Figure 3.14 – *Case 21 - Symmetric YF-connected RL-load. Balanced active and reactive currents detected as anticipated. Real and imaginary power flow are flowing unidirectionally.*

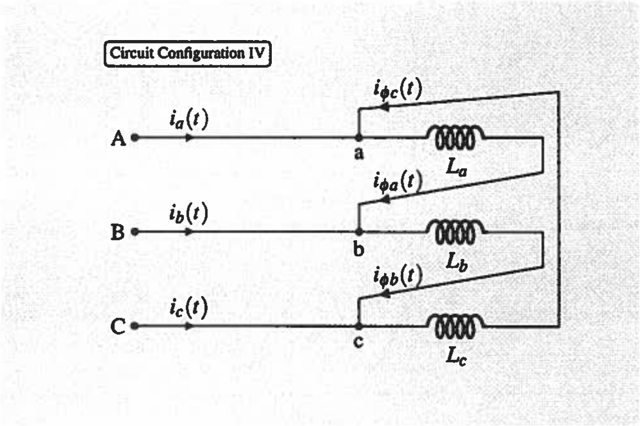

Figure 3.15 – *Load arrangement 4: Delta-connected L-load.*

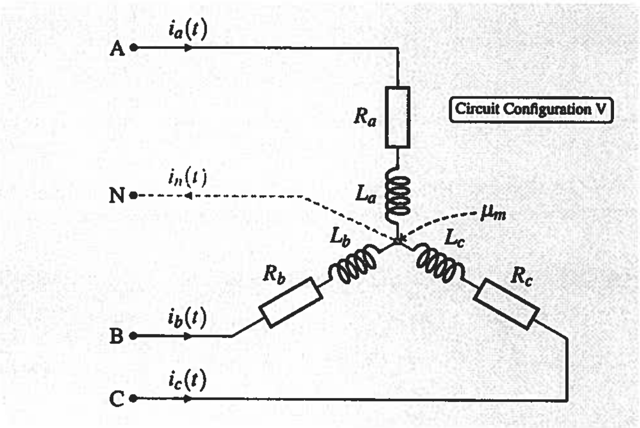

Figure 3.16 – *Load arrangement 5: Star-connected RL-load.*

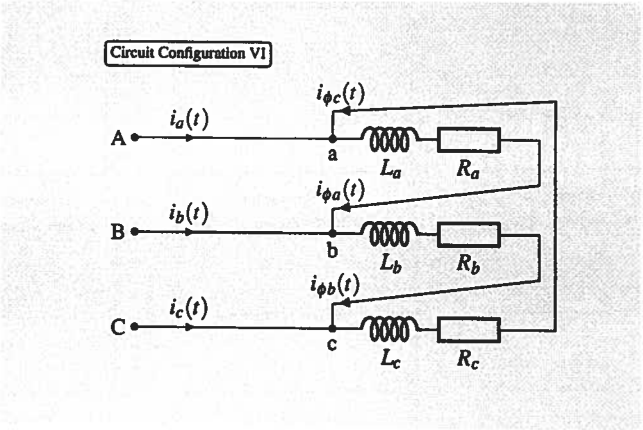

Figure 3.17 – *Load arrangement 6: Delta-connected RL-load.*

3.4 Symmetric series RL-loads

Now after studying both isolated cases of purely resistive and inductive loads, next natural step is to investigate the common RL-type of load. As larger share of the electric power grid is characterized by a mixed resistive and inductive impedance; i.e. generators, motors, transformers and power lines, the following experiments are of realistic valuable information.
The test-set with symmetric series connected RL-loads are divided in two parts, the first half dealing with balanced sinusoidal voltages ($K_{v-} = 0.5\,\%$), while the second part is covering the unbalanced sinusoidal voltage regime $K_{v-} = 16.7\,\%$.

3.4.1 Case 21 - 30

Observing the power decomposition presented as per-unit values in **Table 3.3**, it is evident how the ratio between active P and reactive power Q is unaltered from case to case. Experiments 21 to 30 include virtual and ground voltage reference, combined with alternating topologies delta and floating or grounded star-configuration. The fact that per-unit values are stable during all these variations, are anticipated as the load impedance is kept symmetric.

The impedance in each phase is made up from a resistance $R = 23\,\Omega$ connected in series with an inductive reactance of $X_L = 2\pi{\cdot}50\,Hz\cdot 175\,mH = j55\,\Omega$. This explain the ratio between reactive Q and active P powers, as well as magnitudes of balanced reactive $\boldsymbol{i}_r^b(t)$ and balanced active currents $\boldsymbol{i}_a^b(t)$ in **Figure 3.14**.

Notably when voltages $\boldsymbol{u}(t)$ become unbalanced, instantaneous real power $p(t)$ and imaginary power $q(t)$ oscillate around bias-values recognized as P and Q respectively. As illustrated in **Figure 3.18** detected $\boldsymbol{i}_a^b(t)$ and $\boldsymbol{i}_r^b(t)$ inherit same content of positive and negative sequence components as measured in the voltages $\boldsymbol{u}(t)$.

So far covering symmetric bipolar loads in various constellations, it is verified how the conservative power theory indeed translates current and power flow exactly like the traditional power theory.

3.5 Unsymmetric bipolar loads

Next experiments are interesting as they deal with unsymmetric bipolar loads, where previous simulative work revealed an odd phenomena[A1] that has not been covered in the literature up to this point. Firstly unsymmetric resistive loads are tested, followed by equal tests for unsymmetric inductive loads. In both instances the output from the voltage source were programmed to be balanced sinusoidal. However in cases involving inductive π-connected loads voltages unintentionally became unbalanced, most likely due to high internal impedance in the source, or due to electromagnetic issues in the dYN11-transformer.

As will be thoroughly demonstrated the performance of the programmable source becomes compromised in all cases dealing with highly unbalanced, or harmonic polluted line currents. Even if this effect in most experiments was unintended, it is not necessarily unwanted as it offers the opportunity to study very dramatic voltage scenarios, and the behavior of the CPT-algorithm in that context.

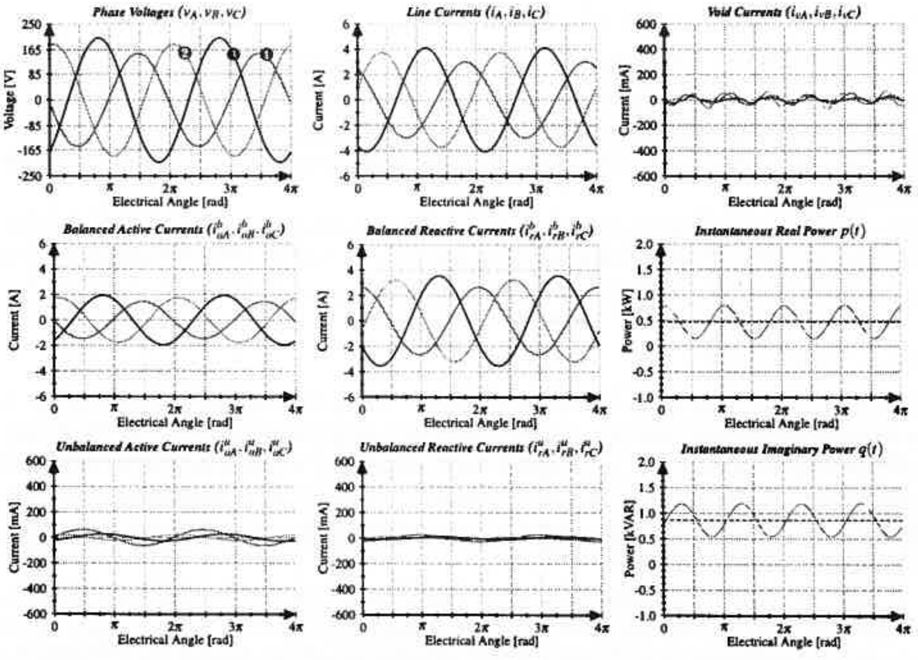

Figure 3.18 – *Case 27 - Symmetric YG-connected RL-load. Balanced active and reactive currents inherit positive and negative sequence components from unbalanced voltages.*

Compared to the pq-theory and the traditional power theory, the conservative power theory exclusively present the principle of active unbalanced power N_a and currents $\boldsymbol{i}^u_a(t)$, along with analogous reactive definitions N_q and $\boldsymbol{i}^u_r(t)$. Theoretically these must only occur when the load impedance is unsymmetric. The tests will further determine how additional factors like voltage regime, voltage reference and wiring-topology eventually might affect the detection of unbalanced components.

3.5.1 *Case 31*

For the unsymmetric R-loads according to **Table 3.4** impedance in phases A and B equals resistance $R_{a,b} = 96\,\Omega$, while in phase C the resistance is nearly four times lower $R_c = 25\,\Omega$. The system classifies as a TN-topology, but the neutral is not conveying any current ($I_N = 0.0\,A$) when the load star-point μ_M is floating. Consequently according to KCL the line currents *i(t)* will have to sum to zero at each instant of time.
The negative sequence currents are notably doubled ($K_{i-} = 31.3\,\%$), compared to previous cases where line currents became unbalanced because of unbalanced voltages.

Most of the power and current flow (**Figure 3.19**) are addressed to active power P and balanced active currents $\boldsymbol{i}^b_a(t)$ respectively. Balanced active currents are truly balanced because the voltages $\boldsymbol{u}(t)$ are balanced ($K_{v-} = 2.6\,\%$).
As expected because of the unsymmetric load impedance, the CPT-algorithm now also detects active unbalanced power N_a and corresponding unbalanced active currents $\boldsymbol{i}^u_a(t)$.

Interestingly only unbalanced active current in phase C is found to be truly in-phase with its voltage, while similar currents in phases A and B are in fact in anti-phase with voltages. This demonstrate how negative sequence components in line currents are adequately presented as unbalanced active currents $i_a^u(t)$.

One objection of the CPT is the suspicious detection of reactive unbalanced power N_q and currents $i_r^u(t)$. According to the algorithm there is supposedly unsymmetric inductive circuit elements in the load. This is principally not correct as the load is purely resistive. However observing closely the phase relationship between acquired voltages $u(t)$ and line currents $i(t)$ they are aligned in phase C (φ_{IC}= -240°), while the currents are lagging the voltages in remaining phases, φ_{IA}= -18° and φ_{IB}= -102°.
It has been demonstrated[A1] how measured currents $i(t)$ used as input to the CPT-algorithm, were reconstructed by adding together all current components output from the algorithm. It was clear that by omitting the unbalanced reactive currents $i_r^u(t)$, it was not possible to retain the same waveforms as the original measured currents. So the unbalanced reactive currents are indeed not a fictive, but integral part of the current flow.

Unbalanced reactive currents are only existent in phases A and B which are phase shifted, while no such component is identified in phase C where current is in-phase with its voltage. These reactive currents $i_r^u(t)$ are correctly lagging their respective voltages by φ_1 = -90°. Consequently instantaneous real $p(t)$ and imaginary $q(t)$ powers oscillates, this time exclusively because of the presence of unbalanced active and reactive currents respectively.

Case 31 is the first experiment to illustrate how the conservative power theory can be utilized in shunt compensation. By using for instance an APF to eliminate $i_a^u(t)$ and $i_r^u(t)$, line currents will have restored their symmetry along with cancelation of power oscillations.

3.5.2 Case 32

Pursuing the TN-system in previous case and now grounding the load star point to neutral conductor. According to waveforms in **Figure 3.20** this give very different results, both in terms of line currents $i(t)$ and related power and current decomposition. By linking the star point of the load to the neutral point of voltage source, currents are no longer forced summing to zero at the star point μ_M.

All three line currents become independent, and any resulting non-zero current flows back to programmable source via phase N (I_N = 4.2 A). Consequently line currents effectively become in-phase with their voltages $u(t)$. Negative and zero sequence unbalance factors in **Table 3.4** reveal equal amount of negative K_{i-} = 47.8 % and zero K_{i0} = 48.7 % sequence currents. As before balanced active currents $i_a^b(t)$ inherit the same symmetric waveforms as voltages.

Notably by grounding the star point unbalanced reactive currents $i_r^u(t)$ are practically eliminated, while unbalanced active currents $i_a^u(t)$ are now fully accounting for the negative and zero sequence components found in line currents. Phase C current is aligned while phase A and B currents are fully anti-phased with respective voltages.

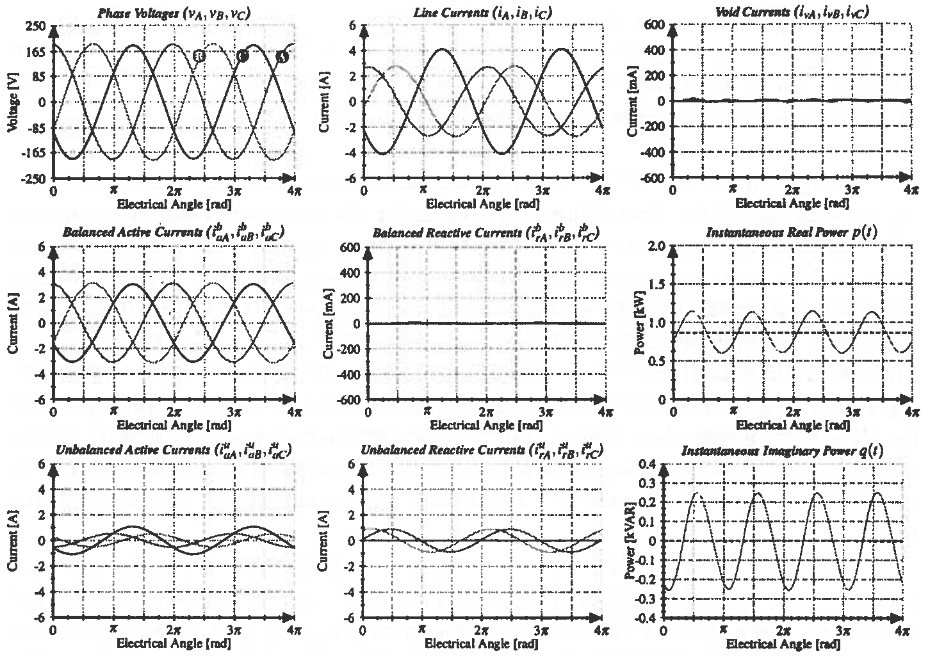

Figure 3.19 – *Case 31 - Unsymmetric YF-connected R-load. Unbalanced reactive currents are present, even in absence of inductive elements in the load circuit.*

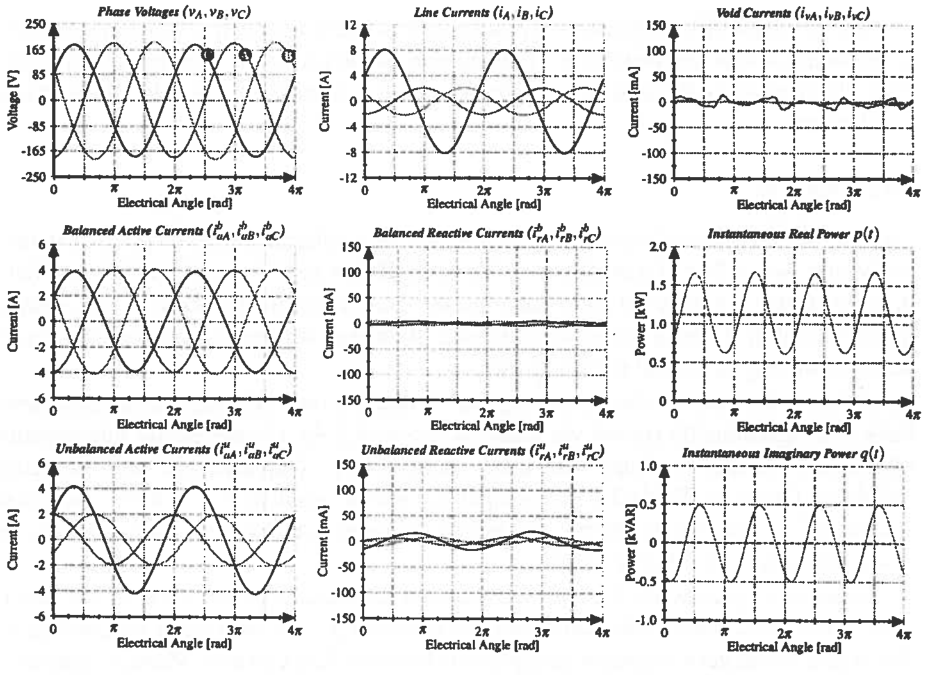

Figure 3.20 – *Case 32 - Unsymmetric YG-connected R-load. Grounding the load gives three independent in-phase line currents. Unbalanced reactive parcels vanish while power oscillations increase.*

Instantaneous powers $p(t)$ and $q(t)$ are oscillating as before. Interestingly the imaginary power $q(t)$ oscillates considerably thought the reactive unbalanced currents $\boldsymbol{i}_r^u(t)$ are not relatively very dominating compared to case 31.

3.5.3 Case 33

Similar to experiment 31 the load is an unsymmetric floating star-configuration, but now selecting virtual voltage reference rather than the neutral conductor. Resulting input and output signals from the CPT-algorithm are identical to what is presented in **Figure 3.19**. Comparing case 31 and 33 suggest that power and current decomposition for unsymmetric floating R-loads, do not change either quantitatively or qualitatively in respect to choice of voltage reference.

3.5.4 Case 34 and 35

These two cases involve the delta-topology where apparently both voltage references yields similar results. However the difference from the star-topology, are the resulting line currents $\boldsymbol{i(t)}$ and associated decomposition (**Figure 3.21**) of current and power flow. The internal wiring in the π-connection is more intricate, thus setting up KCL become a little more elaborate. Nonetheless super positioning of line currents will always sum up to zero, similar to unsymmetric floating star-topologies.

There are as anticipated detected equal amounts of unbalanced active N_a and reactive N_q powers. This particular delta-wiring drains currents that are more pronouncedly unbalanced ($K_{i-} = 44.8\,\%$) than observed for star-configuration, thus unbalanced powers take larger share of the apparent power A.

Examining waveforms in **Figure 3.21**, the unbalanced active current components $\boldsymbol{i}_a^u(t)$ are acting differently than demonstrated for floating stars, despite having exact same phase resistances. Unbalanced active currents in phase A and C are in-phase with voltage, while phase B is anti-phased. Only current in phase B is truly aligned with its voltage (φ_{IB}= -120°), thus unbalanced reactive currents $\boldsymbol{i}_r^u(t)$ are credited to remaining phases, φ_{IA}= -22° and φ_{IC}= -227°.

Acquired voltages are found to be minor unbalanced $K_{v-} = 8.6\%$ which is also reflected by the balanced active currents $\boldsymbol{i}_a^b(t)$. Instantaneous real $p(t)$ and imaginary $q(t)$ powers oscillates in the usual fashion.

The good news is that the conservative power theory is able to sort out these out-of-phase currents, as well as negative sequence components, in the way of unbalanced active $\boldsymbol{i}_a^u(t)$ and reactive $\boldsymbol{i}_r^u(t)$ currents. So even when dealing with unsymmetric delta-wired loads, an APF could be utilized to optimize line currents becoming in-phase and perfectly balanced. This is only true as long as load bus voltages $\boldsymbol{u(t)}$ are balanced of course.

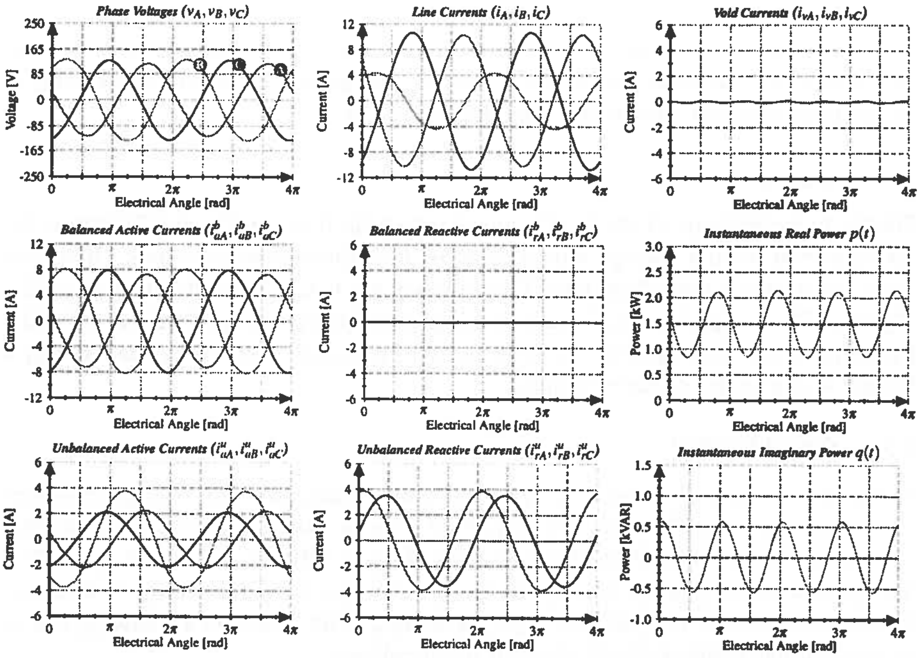

Figure 3.21 – *Case 34 - Unsymmetric D-connected R-load. Resulting line currents are not in-phase with voltages. Load currents contain negative sequence and reactive components.*

3.5.5 Case 36 and 37

Literally switching over to unsymmetric inductive loads. Up to this point there has been a general tendency that phenomenas observed in resistive loads, are also observable for inductive loads. Experiments 36-40 indicate how this *duality*-relation continues even when dealing with unsymmetric bipolars. Inductive reactance in phase A equals to $X_{L_a} = j55\,\Omega$, while being reduced to half in remaining phases $X_{L_{b,c}} = j27.5\,\Omega$.

The three initial cases 36-38 deal with the star-configuration both floating and grounded in IT and TN-environment. In case of floating arrangement the CPT-decomposition is strikingly similar. Acquired currents $\boldsymbol{i}(t)$ are mainly translated as balanced reactive currents $\boldsymbol{i}_r^b(t)$, which are lagging their voltages $\boldsymbol{u}(t)$ by the proper $\varphi \approx$ -90°. However as the line currents are not strictly in quadrature with voltages, this indicate that unbalanced active currents $\boldsymbol{i}_a^u(t)$ must be part of the load current.

Unbalanced active currents $\boldsymbol{i}_a^u(t)$ are detected in phases B and C, $\varphi_{IB} =$ -216° and $\varphi_{IC} =$ -319°, but not in phase A which has the proper phase shift ($\varphi_{IA} =$ -87°). Unbalanced reactive currents $\boldsymbol{i}_r^u(t)$ are credited to all phases as expected. Apparently both $\boldsymbol{i}_r^u(t)$ and $\boldsymbol{i}_a^u(t)$ contain all original negative sequence components ($K_{i^-} = 15.8\,\%$) from the line currents $\boldsymbol{i}(t)$.

Floating unsymmetric inductive loads can be effectively compensated by neutralizing $\boldsymbol{i}_r^u(t)$ and $\boldsymbol{i}_a^u(t)$. This will remove negative sequence currents, along with oscillations in instantaneous powers $q(t)$ and $p(t)$ respectively.

Grounding the unsymmetric inductive load to neutral conductor *(case 37)*, makes all three line currents ***i(t)*** independent. According to **Figure 3.22** currents are now in the familiar quadrature phase shift with voltages ***u(t)***. Consequently unbalanced active currents $i_a^u(t)$ vanish while minor balanced active currents $i_a^b(t)$ are inevitable present. The unbalanced reactive currents $i_r^u(t)$ contain a mix of both negative ($K_{i\text{-}} = 19.8\,\%$) and zero sequence ($K_{i0} = 20.7\,\%$) components. It must be made clear that zero and negative sequence factors applies for measured line currents ***i(t)*** only, and are not valid for current components extracted with the conservative power theory.

Unsymmetric star-connected bipolar loads connected to the neutral conductor, induce zero sequence current components which demands special attention when subjected to shunt compensation.

3.5.6 Case 38 - 40

Results from case 38 are similar to case 36. According to **Figure 3.23** by reconfiguring the load into delta-wiring, is equal to having a floating unsymmetric star-connection.

Thus its been expressly demonstrated that having a π-connected unsymmetric bipolar load, makes the line currents deviate from the expected phase shift; i.e. purely resistive loads draw currents not being in-phase with voltages.

Regarding purely inductive loads currents will not lock in quadrature phase shift with voltages. These interesting phase-shift relations between voltages and currents origins from physical properties, which the CPT elegantly is able to resort.

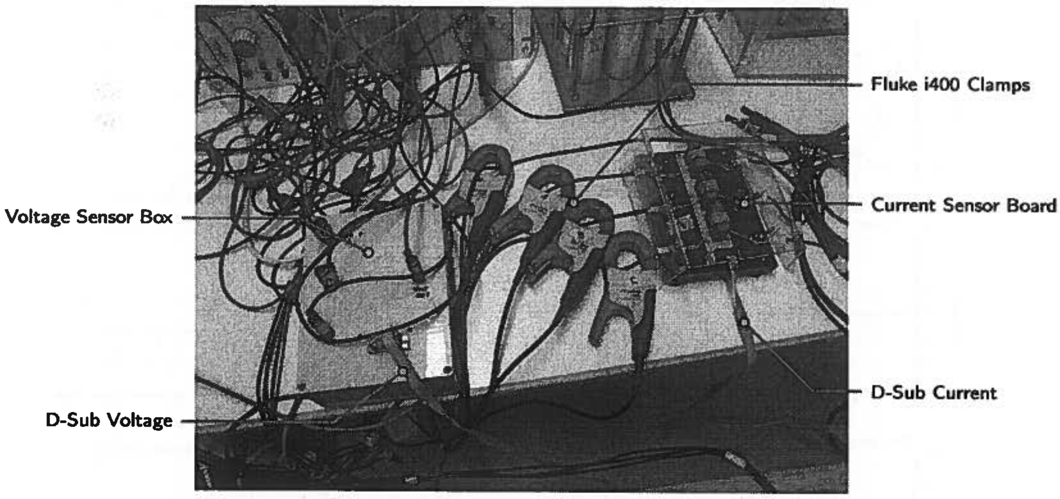

Figure 3.24 – *The Speedgoat target machine does not include any current and voltage acquisition system, consequently this had to be constructed before starting the experiments. LEM sensors are fairly simple putting to use, however it took three weeks assembling these sensor boards. The Fluke current probes can be seen in the middle, being much safer and easier to use.*

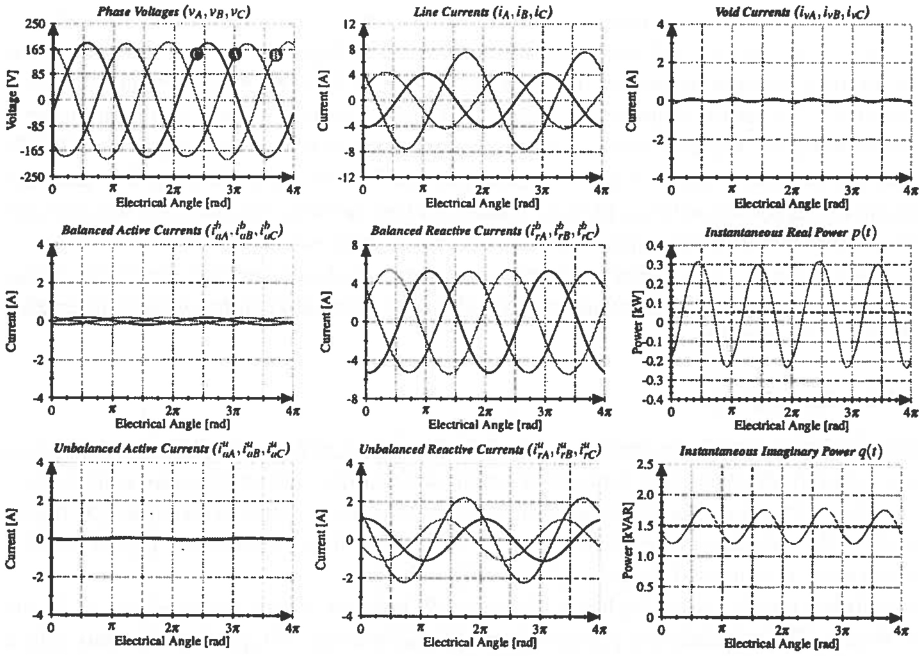

Figure 3.22 – *Case 37 - Unsymmetric YG-connected L-load. Unsymmetric bipolar loads draw positive, negative and zero sequence currents when grounded. Power oscillations increased.*

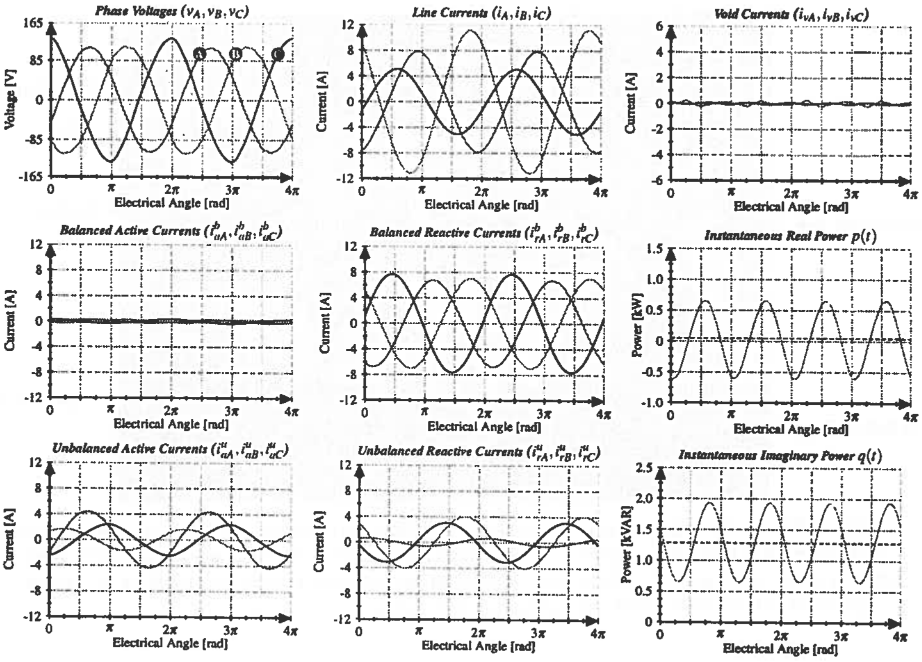

Figure 3.23 – *Case 40 - Unsymmetric D-connected L-load. Unsymmetric floating bipolar loads cause interesting phase relation between currents and voltages, thus both unbalanced active and reactive elements must be expected.*

3.6 Three-phase rectifiers, harmonic voltages

These next ten experiments are of great interest as they deal with three-phase diode and thyristor rectifiers. Passive three-phase rectifiers are typically utilized in large factories and office buildings where DC-power is requested; i.e. facilities for electric drives and electric furnaces to name a few. Active rectifiers grid-interact in a more sophisticated manner, and are considered being not as detrimental power quality wise compared to passive rectifiers. However transistor-based rectifiers are more advanced and expensive thus less commercialized.

The last decades have seen increasing usage of rectifiers in the grid, both in terms of extend and power ratings. One of the challenges related to the future SmartGrid would be the massive introduction of power electronics at consumer level. Single-phase rectifiers are already very common due to the ever expanding usage of electronic consumer products. A representative consumer product is demonstrated in case 68.

By replacing the existing car-fleet with electric vehicles and corresponding decentralized charging stations, might have a tremendous impact on the electric power network. Obviously the transition from fossil to renewable energy will need drastic upgrade of todays power grid. One characteristic of the SmartGrid would be a vast number of power electronic interfaces, decentralized across the entire network giving intricate characteristics potentially more complex than todays operating regimes. Having a power theory that is able to cope with unlinear loads will be essential, and this is where the conservative power theory has proven to be a great contribution.

It must be commented that it was chosen to conduct these experiments under non-sinusoidal voltage regime to make it more interesting, and really put the CPT to the test. Voltage harmonics and voltage imbalance were controlled with the programmable source, however in some occasions the voltage distortion came out of control.
As aforementioned output voltage from the programmable source was not as stiff as intended, clearly visible when testing the thyristor load. As well known commutating thyristors tend to short-circuit the upstream network, causing the characteristic voltage dips or notches especially in case of high inductive network impedance $Z_s \approx j\omega L_s$.

Even if the voltages are more distorted then intended, these cases can be considered as nice examples of how voltages in a critically loaded micro-smart grid might behave. As a comparable reference case thyristor and diode-based rectifiers connected directly to stiff grid voltage, are presented in **Figures 3.40** and **3.41** respectively.

3.6.1 Case 41 - 43

Experiments 41 and 42 introduce the diode rectifier which on the DC-side is connected to a resistive load $R_{DC} = 45.5\,\Omega$. As illustrated in **Figure 3.25** acquired voltages ***u(t)*** appear balanced ($K_{v-} = 0.6\,\%$), and distorted ($THD_v = 14.5\,\%$). According to Fluke FFT (**Figure A.24**) line currents are polluted by 5th, 11th, 13th and 17th harmonics. The harmonic content in line currents ***i(t)*** is altered by the distorted voltages ($THD_i = 22.1\,\%$), when comparing with the same grid-connected diode bridge in experiment 60.

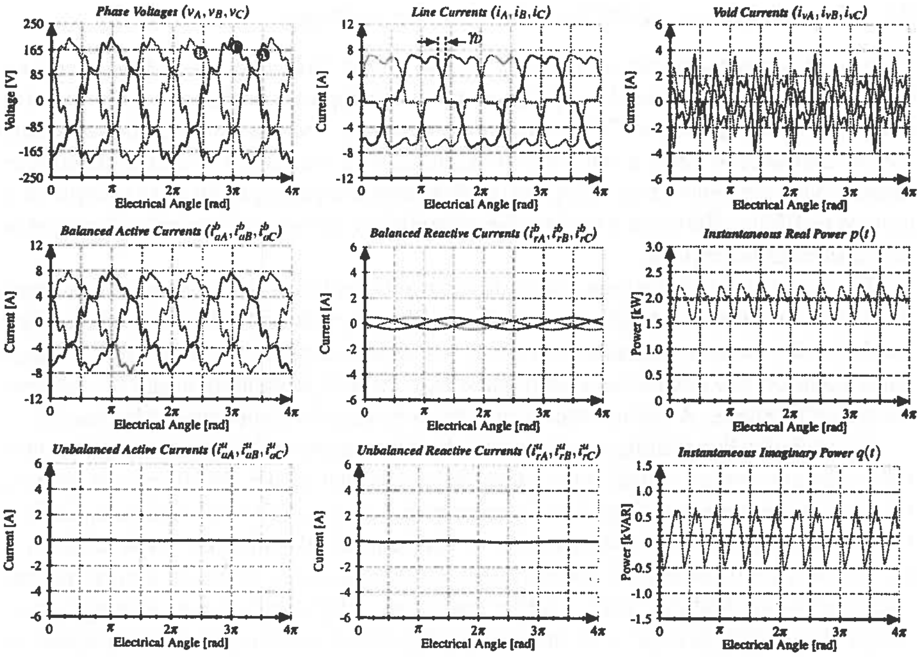

Figure 3.25 – *Case 41 - Diode rectifier feeding R-load. Most of power and current flow are related to active parcels, similar to the classic theory. CPT addresses current harmonics as void terms.*

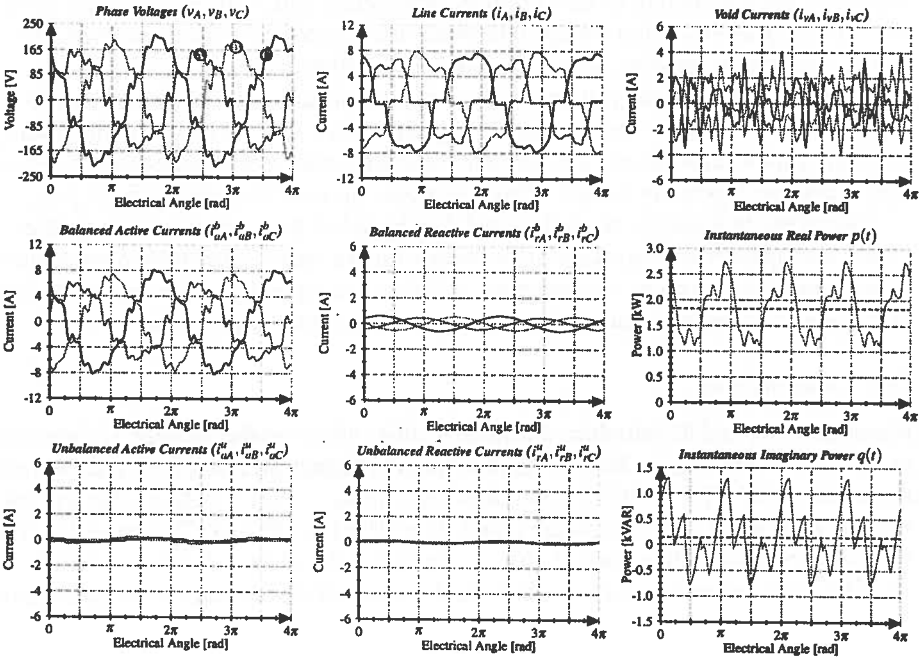

Figure 3.26 – *Case 43 - Diode rectifier with R-load. The Fluke instrument identify reactive elements, while the CPT replaces these with void currents and distortion power.*

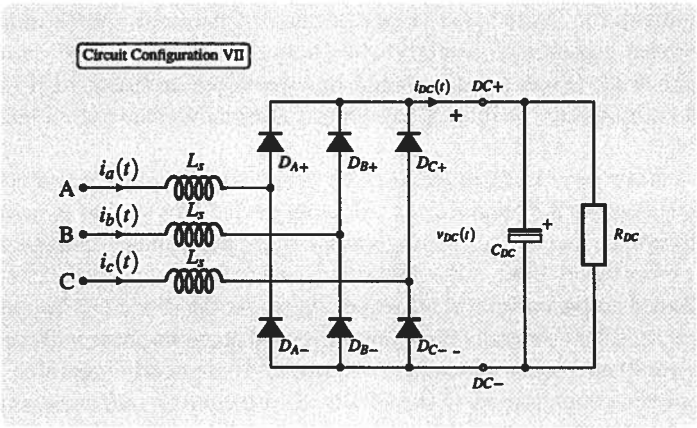

Figure 3.27 – *Load arrangement 7: Three-phase diode rectifier.*

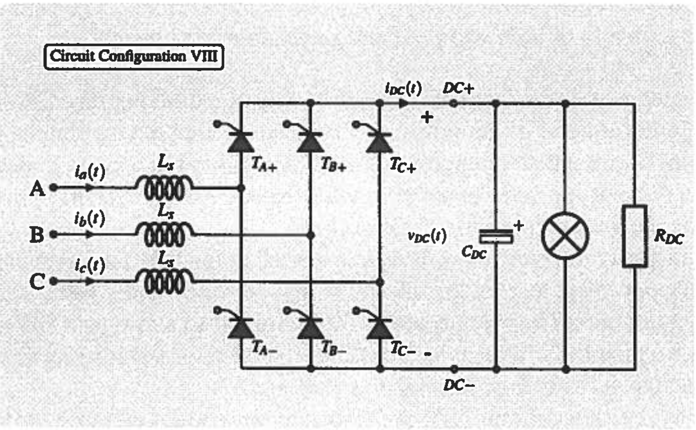

Figure 3.28 – *Load arrangement 8: Three-phase thyristor rectifier.*

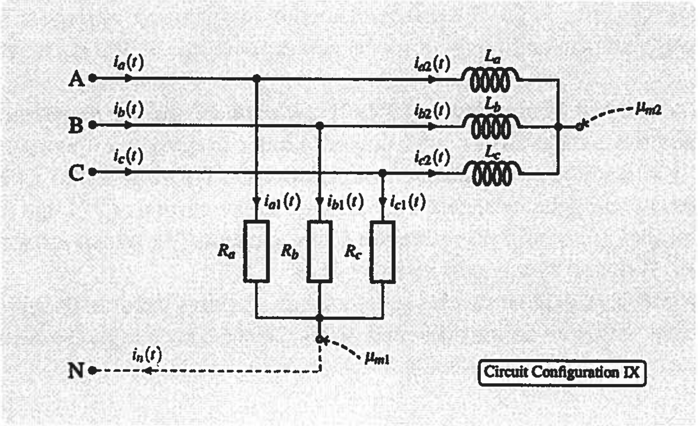

Figure 3.29 – *Load arrangement 9: Parallelled star-connections R- and L-load.*

The commutation angle γ_D is visible because of the large source inductance L_s, while the diodes commutate instantly when being connected to grid (case 60). The harmonic spectrum (**Figure A.24**) would be even more pronounced if the DC-side was loaded by an inductive load, although this alternative was not included in these experiments.

The first two cases results in identical decomposition of powers and currents. The diode bridge (**Figures 3.27** and **A.3**) is a floating device thus similar to passive bipolar loads, no difference can be found using virtual or ground voltage reference. Similar to the classic power theory most of the power and current flow are assorted to active power P, and balanced active currents $i_a^b(t)$ respectively. As the diode is a line-commutated device, diode rectifiers generally draw line currents that are in-phase with voltage. Thus reactive power Q and balanced reactive currents $i_r^b(t)$ are nearly ignorable.

Another interesting property of the CPT is the principle of void currents $i_v(t)$ which comes very handy when analyzing unlinear loads. All harmonic components excepts those common with the voltages are addressed as void currents, suggesting that compensating the void currents would greatly purify the source currents. The void currents are expected to be a mix of both *scattered* and *generative* components.

The concepts of homo-integrals is a clever way of extracting reactive current components. Homo-integral of currents or voltages are computed by simply running the original signals through an integrator block. When plotted in a Bode diagram the integrator has a distinct appearance; the phase shift equals -90° across the entire frequency range, while the gain is constant -20 dB/decade.

As the majority of reactive power is transported at fundamental frequency, the zero of the integrator is set to $z = 2\pi \cdot 50\,Hz = 314.16\,rad/s$. This makes the integrator effectively filter out all harmonics above 50 *Hz* similar to a low-pass filter, while DC-signals are boosted by infinite gain. The CPT-algorithm is sensitive against any offset in the input signals, as will be demonstrated in case 67.

Balanced reactive currents $i_r^b(t)$ are therefore much smoother close to a sinusoidal fundamental waveform. For this floating device negative sequence current components will always project into $i_a^b(t)$ and $i_r^b(t)$. In ordinary operation the diode bridge draws balanced currents ($K_{i\text{-}} = 0.9\,\%$), thus no detection of unbalance current or power terms. Instantaneous real $p(t)$ and imaginary $q(t)$ powers oscillate at 300 *Hz* frequency.

Independently of load characteristics if the network voltages are non-ideal, it is apparent how the conservative power theory (similar to *pq*-power theory) cannot guarantee purely sinusoidal compensated source currents. By utilizing an APF to remove all CPT-current components except the balanced active currents $i_a^b(t)$, the compensated source currents $i_s(t)$ would resemble the *Fryze*-currents[A2], which essentially equals the currents produced by a purely resistive load.

As already extensively demonstrated resistors draw currents linear to the applied voltage, a physical fact which no current-oriented power theory can change. To further improve the quality of voltages and currents a series compensator is needed.

In experiment 43 voltages are further degraded by adding negative sequence voltage components ($K_{v-} = 16.6\,\%$). As depicted in **Figure 3.26** the diode bridge now draws some severely deformed currents, $K_{i\text{-}} = 18.7\,\%$ and $THD_i = 31.1\,\%$.
Nonetheless diode commutation and conduction intervals appear unaltered, and decomposition of currents and powers are arguably very similar to previous two cases.

With non-ideal voltages it is now more evident how the presence of harmonics and unsymmetry in the voltage, affect the waveforms of active $\boldsymbol{i}_a(t)$ and reactive $\boldsymbol{i}_r(t)$ current components. Apparently balanced active currents $\boldsymbol{i}_a^b(t)$ inherit the exact waveform as their corresponding measured voltages $\boldsymbol{u}(t)$. Similarly balanced reactive currents $\boldsymbol{i}_r^b(t)$ inherit the waveforms from homo-integral voltages $\widehat{\boldsymbol{u}}(t)$.

A familiar phenomena regarding instantaneous real $p(t)$ and imaginary $q(t)$ powers, is the $100\,Hz$ oscillation triggered by the voltage unsymmetry. The three-phase diode rectifier drains very little reactive power Q, and even less unbalanced reactive N_q power, making it difficult determining the origin of the fluctuation of $q(t)$. The explanation could be the unbalanced voltage, similar to what observed for bipolar loads.

3.6.2 Case 44 - 46

Moving to experiment 44 it is added an electrolyte capacitor $C_{DC} = 3300\,\mu F$ in parallel with the resistor R_{DC}. This load *(RC-type)* could resemble a front end of an electric drive where the first stage is a rectifier charging the DC-link, and the second stage is some form of controlled converter. In fact this is the same topology used to construct the programmable voltage source. The qualitative and quantitative decomposition of currents and power are very similar to case 42.

The behavior is evidently quite different in experiment 45 where the voltages $\boldsymbol{u}(t)$ are set to unsymmetry. Identical results are observed for case 46, as there is no differentiation using ground or virtual voltage reference when the load is a floating device.
The combination of capacitor load and unbalanced voltages leads to irregular commutation of diodes, resulting in severely unbalanced line currents $K_{i\text{-}} = 69.6\,\%$.

As illustrated in **Figure A.9** *(case 46)* phases B and C draw pulse-shaped capacitative charging currents attempting to energize the DC-link. Moreover the irregular currents $THD_i = 87.3\,\%$ combined with high internal impedance in the source, results in one of the most extreme voltage scenarios presented in this work. This is a good example why the experiments never got to the 10-15 kVA power range. The source handled only around 2 kVA before voltages started degrading, especially when dealing with nonlinear or unsymmetric loads. Dealing with such distorted voltages *u(t)* makes the dissection of CPT-current components challenging. Interestingly the CPT-algorithm detect balanced active currents $\boldsymbol{i}_a^b(t)$ in all phases, even in phase A which is barely conducting any current at all.

It can be noticed that by compensating the load current *i(t)* leaving only the balanced active currents $\boldsymbol{i}_a^b(t)$, would significantly improve the compensated source currents $\boldsymbol{i}_s(t)$, reducing THD_i from 87.3 % to approximately 17.5 %. Hypothetically this would automatically restore much of the voltage quality, which again would purify the balanced active currents floating from the source.

In this special case instantaneous real $p(t)$ and imaginary $q(t)$ powers pulsates strongly with a $\tau_{DC} = 10\,ms$ time constant. Assuming minimal power loss in the diodes, instantaneous real power measured on the input side $p(t)$, must equal the real power on the DC-side $p_{DC}(t)$. Studying $p(t)$ illustrates how the DC-link is rapidly charged and discharged, twice each electrical cycle because of the voltage unsymmetry.

3.6.3 *Case 47 and 48*

Next up is the three-phase thyristor converter (**Figure 3.39**) energized with balanced sinusoidal voltages. This is an old unit designed and built[D44] by NTNU (NTH back then) in the early eighties, used in lab assignments by students specializing on power electronics. As the thyristor is a self-commutated switch, thyristor-based converters covers two quadrants[E53] in the $V_{DC}-I_{DC}$ plane, offering both rectification and inversion operating mode.

The operation is essentially determined by the thyristor gate pulses, and also greatly influenced by the load-configuration on the DC-side. The thyristor can block current both in forward and reversed polarity voltage. Conduction is only initiated when applying a firing pulse on the gate channel. The firing of each of the six semiconducting switches must be synchronized with the applied three-phase voltage.

Conduction state can only initiate when the thyristor is properly forward biased similar to diodes, this instant is termed as $\alpha_{th} = 0°$. The firing pulse can be delayed $\alpha_{th} = 180°$ at the most. This allows various operating features such as working like a conventional diode bridge when $\alpha_{th} = 0°$, then acting as a variable DC-source as α_{th} is increased towards 90 electrical degrees ($V_{DC} = 1.35 V_{LL} \cos \alpha_{th}$). In case of passive DC-loads the thyristor converter cease to conduct beyond $\alpha_{th} = 90°$. Having an active load in the DC-link enables the thyristor converter to operate as an inverter if $\alpha_{th} > 90°$; i.e. electric drives operating in regenerative mode.

Thyristor rectifiers are often found in facilities for temperature and light regulation *(TRIAC)*, welding equipment and motor drives, applications typically found in residents.

Because of the variety of configurations and operations, only one setup is covered in this work for simplicity. The DC-side is loaded with a resistor ($R_{DC} = 32\,\Omega$) connected in parallel with two 60 W bulbs (for entertainment value). The gate pulse generator has not been calibrated after it was put out of service, thus control of α_{th} was fairly inaccurate, thus grossly approximated in these experiments.

According to **Figure 3.30** acquired line currents $\boldsymbol{i}(t)$ appear pulse-shaped almost going into discontinuous current conduction mode, which is typical when the thyristor triggering is delayed ($\alpha_{th} \approx 60°$ in this case). Load currents are noticeably distorted $THD_i = 56.2\,\%$. In addition to the preset harmonics $THD_v = 20.6\,\%$, voltages are further degraded by the thyristor commutation causing characteristic notches. Reactive power Q is dominating the power mix despite having a purely resistive DC-load. In fact this comply with the established power theory, and can be argued from a physical point of view; by introducing a delayed commutation (α_{th}) of the rectifying switches, line currents are equally time shifted compared to their respective voltages, thus thyristor rectifiers draws balanced reactive currents $\boldsymbol{i}_r^b(t)$.

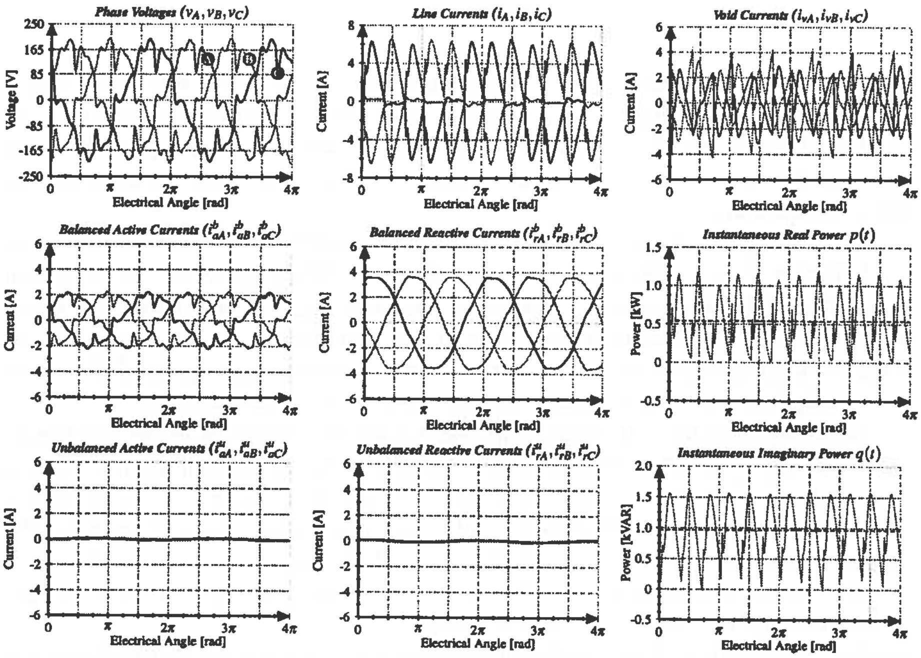

Figure 3.30 – *Case 47 - Thyristor rectifier feeding R-load. Delayed thyristor-firing gives current spikes translates as void currents. Reactive elements are created by nonzero* α_{th}. *Harmonics produce 300 Hz power oscillations.*

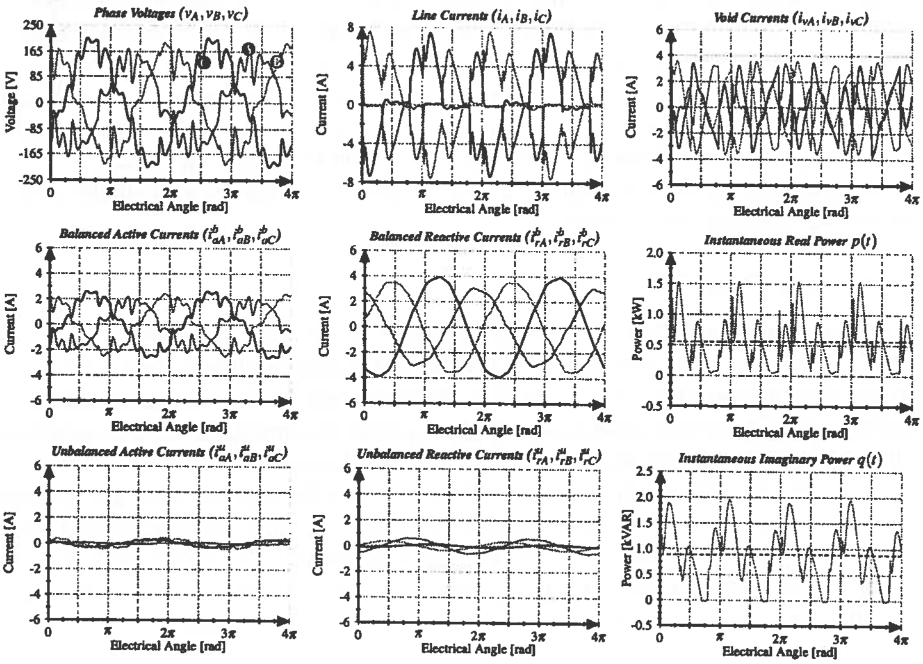

Figure 3.31 – *Case 50 - Thyristor rectifier feeding R-load with unbalanced voltages. High internal impedance in the source causes distorted voltages. Network status could resemble conditions in a micro-smart grid.*

Simultaneously as α_{th} increases line currents become more out-of-phase with voltages, so the impact of active power P and balanced active currents $i_a^b(t)$ must decline. The assumption of having $\varphi_1 = \alpha_{th}$ is strictly valid in the simplified case where $L_s \approx 0$, however it can be used as a gross estimation. Also similar to diode rectifiers, large source inductance $L_s \neq 0$ means that thyristor commutation angle γ_{th} must be taken into consideration.

According to fundamental thyristor converter theory[E53], active and reactive power are defined as $P_{th} = 1.35V_{LL}I_{DC}\cos\alpha_{th}$ and $Q_{th1} = 1.35V_{LL}I_{DC}\sin\alpha_{th}$. It is important to distinguish between active P_{th} and reactive power Q_{th1} in the frequency domain, as active power is related to all contributing harmonics while the reactive power only origin from fundamental frequency components. Also these formulas are deduced with the assumption of having a constant current I_{DC} flowing on the DC-side.

Observing data from the Fluke instrument *(case 48)*, the given active and reactive powers comply with the aforementioned formulas. By approximating the firing angle $\alpha_{th} \approx \cos^{-1}(0.4367\,pu)$ reactive power become $Q \approx \sin(64.11°) = 0.8996\,pu$. Clearly the active power definition still holds true, but reactive power Q from the CPT-algorithm does not fully converge with the classic definition. As most current harmonics are addressed as void currents $i_v(t)$ this means that presence of distortion power D must be expected, on the expense of reactive power.

Dealing with diode and thyristor rectifiers the CPT offers a more nuanced power decomposition, which should be further validated through analytical analysis.

Instantaneous real $p(t)$ and imaginary $q(t)$ powers are clearly affected by the delayed commutation as they oscillate at $300\,Hz$. This type of fluctuating power flow is unfortunate from a power system perspective, as it implies that any electromechanical generator delivering the real power would suffer from severe ripple torque[B21].

Compensating void currents $i_v(t)$ would cancel most of the current harmonics, and improve the instantaneous power flow. By further compensating balanced reactive currents $i_r^b(t)$ only balanced active current $i_a^b(t)$ would flow from the source.

Nonetheless as will be demonstrated in case 71, power oscillation is inevitable as long as network voltages are distorted.

3.6.4 Case 49 and 50

As depicted in **Figure 3.31** voltages $u(t)$ are preset to the usual unsymmetry of $K_{v-} = 16.5\,\%$ giving irregular commutation, similar to the diode rectifier. Line currents $i(t)$ inherit the same unbalance $K_{i-} = 22.0\,\%$ while harmonic content increases to $THD_i = 82.9\,\%$. Despite having unbalanced voltages, power decomposition remain relatively similar to previous cases where the voltages were balanced.

It is now experimentally demonstrated that the way three-phase diode and thyristor rectifiers responds to unbalanced voltages, is greatly influenced by what type of load being connected to the DC-bus. When the load is purely resistive power decomposition remain principally unaffected. However if the DC-load is capacitive unbalanced voltages produce irregular commutation, and severely unbalanced line currents.

In these circumstances unbalanced active N_a and reactive N_q power are detectable along with unbalanced active $i_a^u(t)$ and reactive $i_r^u(t)$ current components. Similarly voltage imbalance triggers considerable $300\,Hz$ oscillation for instantaneous real $p(t)$ and imaginary $q(t)$ power flow when DC-load is capacitive, while $100\,Hz$ oscillation is more prominent with the DC-bus loaded by a resistive impedance. Taking a quick glimpse at case 58 and 60, these present three-phase thyristor and diode rectifiers respectively when being connected to stiff grid voltage. The power decomposition is remarkably similar independently of voltage regime.

Based on these few experiments it have been validated how the CPT is capable of retaining decomposition, independently of voltage regime and choice of voltage reference. As aforementioned three-phase diode and thyristor rectifiers comes in various constellations. Unfortunately only selected scenarios are covered in this work, such that one should be careful not to generalize previous remarks and conclusions.
Because of the multitude of configurations *(both passive and active)* nonlinear loads needs more research, which could be basis for future work. For any serious research it is recommended constructing a new three-phase thyristor converter as the existing units are old, noisy, hazardous and unreliable.

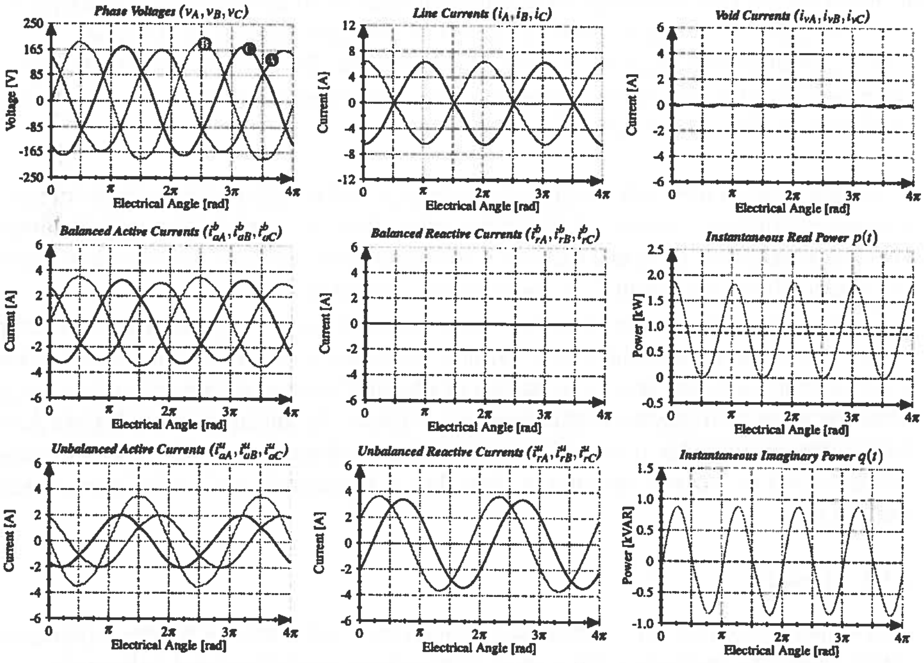

Figure 3.32 – *Case 51 - Single-phasing (R-load) results in notable instantaneous real power oscillation ($\pm 0.9\,pu$). Note how the CPT is able to distribute three equal balanced active currents.*

3.7 More bipolar loads

3.7.1 Case 51 - 54

Inspired by one of the examples in H.Akagis presentation of the pq-theory[B21], experiments 51 and 52 demonstrate how the conservative power theory handles single-phasing when connecting a resistance $R_{ac} = 96\,\Omega$ from phase A to phase C.
This phenomena is probably most common in the low-voltage distribution segment. When planning electrical power systems there are always strived to distribute the loads equally among the phases. However single-phasing and consequent unsymmetry will always occur by the stochastic nature of the way power systems are utilized.

Despite having a resistive single-phase load, power and current decomposition appear similar to previous cases, considering floating three-phase unsymmetric resistive loads. Illustrated in **Figure 3.32** this case must be regarded as a worst-case scenario. Naturally line currents $\boldsymbol{i}(t)$ only flow in phases A and C, and always sum to zero according to KCL causing a massive imbalance $K_{i-} = 100.0\,\%$. As the currents are not aligned with their respective voltages φ_{IA}= -35° and φ_{IC}= -215°, this explain the detection of unbalanced reactive currents $\boldsymbol{i}_r^u(t)$.

It becomes really interesting when observing the balanced active $\boldsymbol{i}_a^b(t)$ and unbalanced active $\boldsymbol{i}_a^u(t)$ currents. The load is not even physically connected to phase B, but according to the CPT-algorithm there must be current in all three phases. Apparently by summing $i_{aB}^b(t)$ with $i_{aB}^u(t)$ these cancel out so that current in phase B vanish.
This is a peculiar case in terms of shunt compensation. By filtering unbalanced active currents $\boldsymbol{i}_a^u(t)$, the APF inject an unbalanced active current into phase B, which then become equivalent to a balanced active current.

Single-phasing makes the instantaneous real $p(t)$ and imaginary $q(t)$ powers oscillate in quadrature phase relation at $100\,Hz$ frequency. This phenomena can only be linked to unbalanced active $\boldsymbol{i}_a^u(t)$ and reactive $\boldsymbol{i}_r^u(t)$ currents respectively, as the voltages $\boldsymbol{u}(t)$ and balanced active currents $\boldsymbol{i}_a^b(t)$ are balanced sinusoidal.

This case represent one of the few instances in this experimental work where the physical interpretation clearly fails. Strictly speaking it should not be expected that the conservative power theory is capable of properly dealing with single-phase loads, when the algorithm operate in the three-phase frame. As further seen in **Figure A.10** connecting an inductor *(case 53 and 54)* between phase A and C evoke the same interpretation of current and power flow, but with reactive and active components shifting role.

3.7.2 Case 55

This scenario is similar to experiment 21 which involved a symmetric star-connection, where the phase impedance was a series-connection of resistance and inductance.
This experiment put a little twist to it as the resistances ($R_{a,b,c} = 96\,\Omega$) and inductances ($L_{a,b,c} = 175\,mH$) are split into two separate floating stars, which then are connected in parallel. Only balanced active $\boldsymbol{i}_a^b(t)$ and reactive $\boldsymbol{i}_r^b(t)$ currents are detectable, due to the symmetric load impedance. The combination of balanced voltages $K_{v-} = 0.1\,\%$

and currents $K_{i-} = 0.2\,\%$, makes instantaneous real $p(t)$ and imaginary $q(t)$ powers flow constant. There is principally no difference in parallel or series configuration when voltages and bipolar impedances are symmetric, as now experimentally verified.

3.7.3 Case 56 and 57

These two are similar to experiments 36 and 37 respectively, but replacing the series unsymmetric star-configurations with parallel-connected stars. In the first scenario both stars are floating, and the resistive part is unsymmetric while the inductive star is symmetric. According to **Figure 3.36** acquired currents $\boldsymbol{i}(t)$ appear unbalanced ($K_{i-} = 21.7\,\%$), and the power decomposition is essentially identical to case 36.

Unbalanced active currents $\boldsymbol{i}_a^u(t)$ are detected in all phases. Unbalanced reactive currents $\boldsymbol{i}_r^u(t)$ are recognized in phase A and B despite having the inductive part of the load isolated from the unsymmetric resistive part. As aforementioned the appearance of $\boldsymbol{i}_r^u(t)$ can be reasoned from the perspective of uneven phase shift among the line currents. Negative sequence components are clearly present in $\boldsymbol{i}_a^u(t)$, while balanced active $\boldsymbol{i}_a^b(t)$ and reactive $\boldsymbol{i}_r^b(t)$ currents contain only positive sequence components (same as voltages). As expected instantaneous real $p(t)$ and imaginary $q(t)$ powers oscillate in a quadrature phase relationship, at rate of twice the fundamental frequency.

Depicted in **Figure 3.37** when the star point μ_{MI} of the unsymmetric resistive part is grounded to neutral conductor *(case 57)*, unbalanced reactive currents $\boldsymbol{i}_r^u(t)$ vanish. The grounding makes line currents $\boldsymbol{i}(t)$ even more unbalanced, containing both negative $K_{i-} = 43.6\,\%$ and zero sequence components $K_{i0} = 46.6\,\%$. Negative and zero sequence components are therefore fully accounted by the unbalanced active currents $\boldsymbol{i}_a^u(t)$. This is exactly same behavior as observed when dealing with the unsymmetric series-connected bipolar loads. Unbalanced active currents $\boldsymbol{i}_a^u(t)$ are detected in all phases. Unbalanced reactive currents $\boldsymbol{i}_r^u(t)$ are recognized in phase A and B despite having the inductive part of the load isolated from the unsymmetric resistive part. As aforementioned the appearance of $\boldsymbol{i}_r^u(t)$ can be reasoned from the perspective of uneven phase shift among the line currents.

Negative sequence components are clearly present in $\boldsymbol{i}_a^u(t)$, while balanced active $\boldsymbol{i}_a^b(t)$ and reactive $\boldsymbol{i}_r^b(t)$ currents contain only positive sequence components (same as voltages). As expected instantaneous real $p(t)$ and imaginary $q(t)$ powers oscillate in a quadrature phase relationship, at rate of twice the fundamental frequency.

Visualized in **Figure 3.37** when the star point μ_{MI} of the unsymmetric resistive part is grounded to neutral conductor *(case 57)*, unbalanced reactive currents $\boldsymbol{i}_r^u(t)$ vanish. The grounding makes line currents $\boldsymbol{i}(t)$ even more unbalanced, containing both negative $K_{i-} = 43.6\,\%$ and zero sequence components $K_{i0} = 46.6\,\%$. Negative and zero sequence components are therefore fully accounted by the unbalanced active currents $\boldsymbol{i}_a^u(t)$. This is exactly same behavior as observed when dealing with the unsymmetric series-connected bipolar loads.

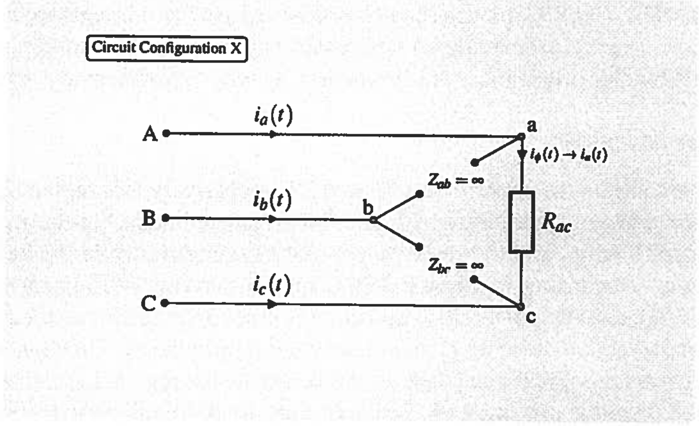

Figure 3.33 – *Load arrangement 10: Single-phasing R-load.*

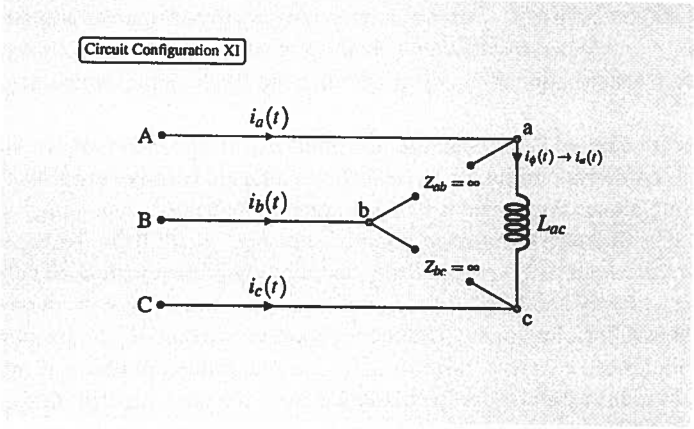

Figure 3.34 – *Load arrangement 11: Single-phasing L-load.*

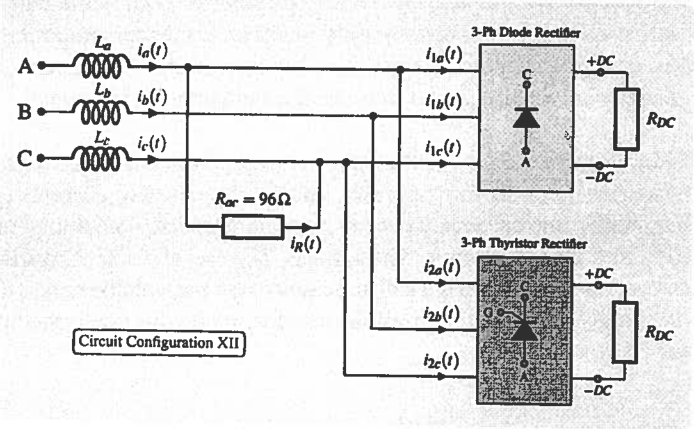

Figure 3.35 – *Load arrangement 12: Mixed load of single-phasing, diode and thyristor rectifiers.*

3.7.4 Case 58 and 59

In the literature[A13–A16] the conservative power theory has mostly been evaluated in context of sinusoidal voltage regimes. For verification and comparison experiments 58 and 59 therefore demonstrate the thyristor rectifier connected to stiff grid voltage.

With the firing angle set to approximately $\alpha_{th} \approx 50°$ line currents $\boldsymbol{i}(t)$ resemble those observed in case 47, the same yields for CPT-decomposition of powers and current components (**Figure 3.40**). The most notable difference is the waveform of current components. As the source voltages $\boldsymbol{u}(t)$ are ideal, balanced active $\boldsymbol{i}_a^b(t)$ and reactive currents $\boldsymbol{i}_r^b(t)$ appear ideally balanced sinusoidal. The triangular shaped line currents contain harmonics $THD_i = 70.7\,\%$ which the CPT-algorithm effectively extracts and categorizes as void currents $\boldsymbol{i}_v(t)$. The experimental results are in fully agreement with simulated results[A1].

By compensating void currents $\boldsymbol{i}_v(t)$ and balanced reactive currents $\boldsymbol{i}_r^b(t)$, network parameters become ideal at the load bus, only sinusoidal balanced active currents $\boldsymbol{i}_a^b(t)$ would be supplied by the grid. Canceling void currents $\boldsymbol{i}_v(t)$ would also remove harmonic powers and therefore make instantaneous real $p(t)$ and imaginary $q(t)$ powers flow constant. Compensating balanced reactive currents would complete the reactive power compensation.

3.7.5 Case 60

Having the same load configuration and parameters as experiment 41 *(three-phase diode rectifier)*, this comparative test replaces the programmable source with stiff grid voltage for reference. Major part of the line currents $\boldsymbol{i}(t)$ are in fact translated (**Figure 3.41**) as sinusoidal balanced active currents $\boldsymbol{i}_a^b(t)$. The void currents $\boldsymbol{i}_v(t)$ accounts for current harmonics $THD_i = 29.5\,\%$, as well as the oscillation of instantaneous real $p(t)$ and imaginary $q(t)$ powers.

Compensating the diode rectifier load in this case should theoretically be a simple task, however it must be commented that low inductive source impedance $Z_s \approx R_s$, cause diodes to commutate almost instantly ($\gamma_D \rightarrow 0°$). At each commutation line currents transitions at very fast rates ($^{di}/_{dt}$), thus line currents must contain high order harmonics.

Once more input and output signals of the CPT-algorithm comply with results from simulated tests[A1], which testify that the conservative power theory is very suitable for load-identification under both ideal and non-ideal voltage regimes. In order to successfully compensate these high order harmonics, the control system must have sufficiently high bandwidth and sample rate, as will be demonstrated later.

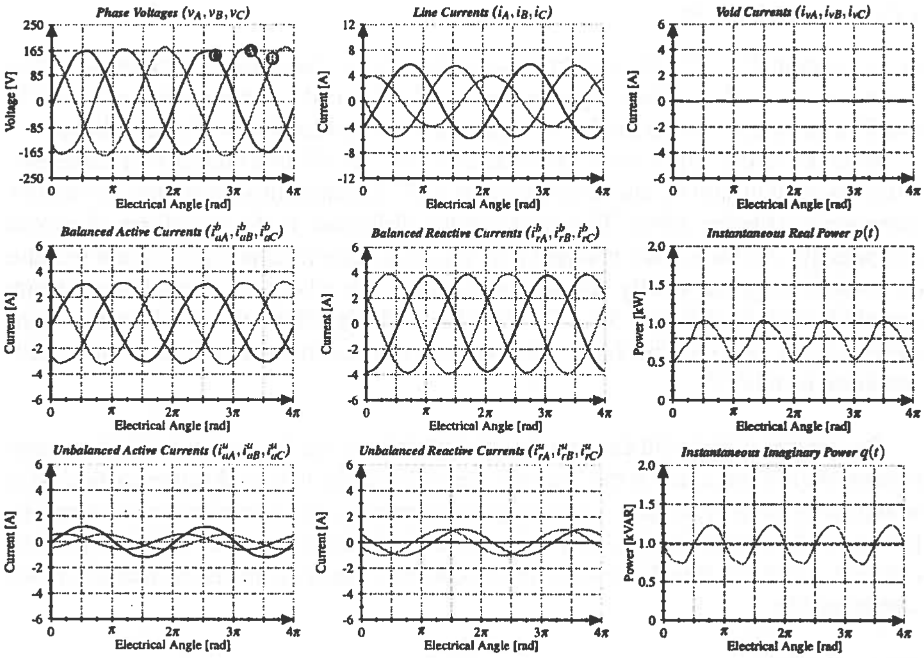

Figure 3.36 – *Case 56 - R(YF) and L(YF)-loads connected in parallel. The floating unsymmetric R-load results in detection of unbalanced reactive currents, similiar to case 36.*

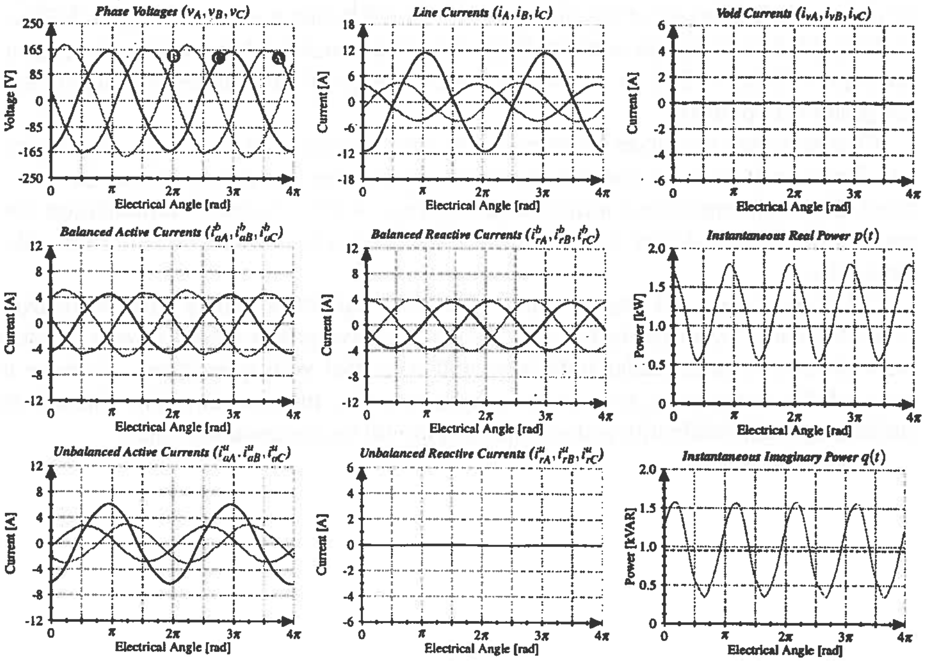

Figure 3.37 – *Case 57 - R(YG) and L(YF)-loads connected in parallel. By grounding the unsymmetric R-load, unbalanced currents terms are only addressed to resistive load part.*

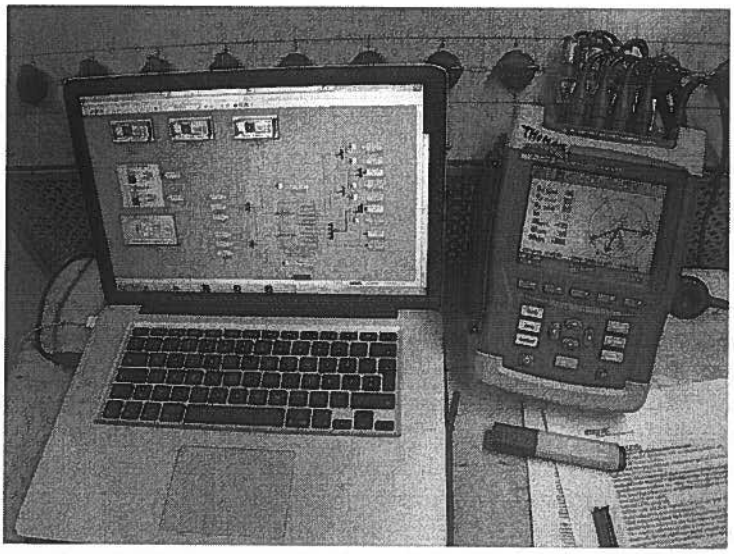

Figure 3.38 – *Close up picture of instrumentation user interface. Left: virtual instrument controlling the output voltage from VSI, and performing real-time decomposition of current and powerflow. Decomposition-algorithms were based on the CPT and PQ-theory.*
Right: state-of-the-art power quality analyzer from market leader Fluke, implementing the classic power theory for benchmark. The Fluke instrument was used both for calibration of the virtual instrument, and measuring harmonics, unsymmetry and RMS values.

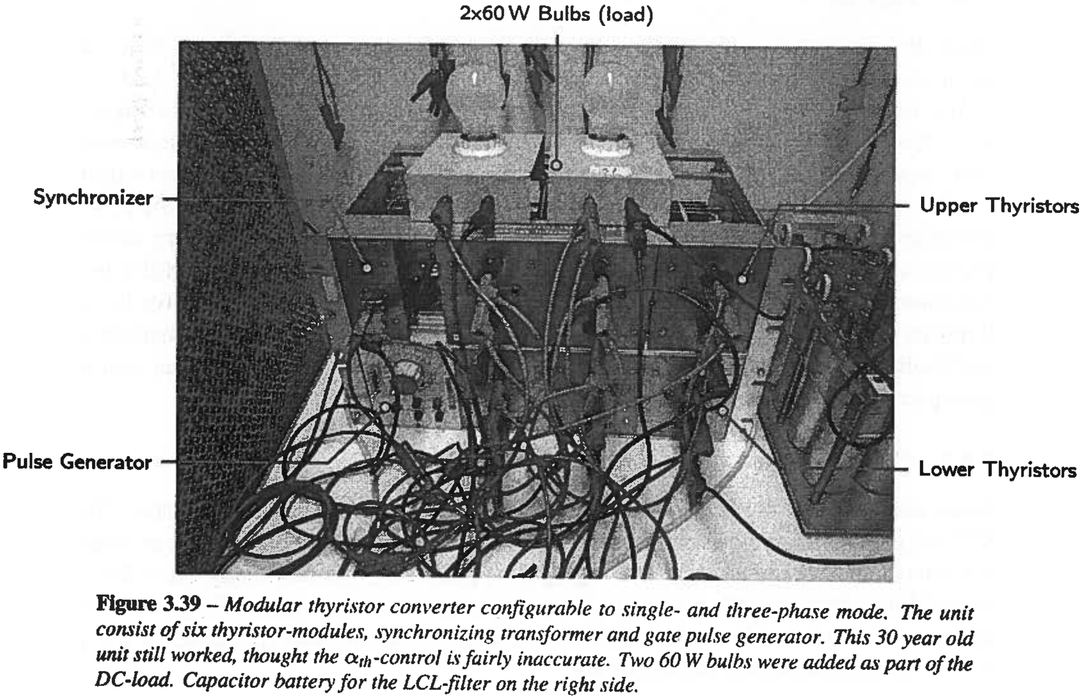

Figure 3.39 – *Modular thyristor converter configurable to single- and three-phase mode. The unit consist of six thyristor-modules, synchronizing transformer and gate pulse generator. This 30 year old unit still worked, thought the α_{th}-control is fairly inaccurate. Two 60 W bulbs were added as part of the DC-load. Capacitor battery for the LCL-filter on the right side.*

3.8 Miscellaneous experiments

3.8.1 *Case 61*

This case is inspired by one of the simulated tests conducted by F.Marafão[B24] incorporating a mixture of three-phase diode and thyristor rectifiers, in addition to a single-phasing resistor $R_{ac} = 96\,\Omega$ between phase A and C.
This could resemble a more realistic scenario where the load possess both unlinear and bipolar unsymmetric characteristics. The load circuitry is connected to stiff grid voltage through a variable transformer (variac).

As depicted in **Figure A.12** line currents $\boldsymbol{i}(t)$ appear abnormal as a result of the combined action of the diode and thyristor rectifiers. Having stiff voltages $\boldsymbol{u}(t)$ all electronic switches commutates in the regular switching-pattern. Delayed commutation of thyristors ($\alpha_{th} \approx 45°$) can be recognized at extrema, while the unsymmetric R-load cause noticeable imbalance of $K_{i^-} = 17.4\,\%$.

Harmonic pollution ($THD_i = 18.0\,\%$) is effectively extracted and classified as void currents $\boldsymbol{i}_v(t)$, leaving remaining current components as purely balanced sinusoidal. Major part of acquired load current $\boldsymbol{i}(t)$ is assorted to balanced active currents $\boldsymbol{i}_a^b(t)$, while reactive currents $\boldsymbol{i}_r(t)$ and unbalanced active currents $\boldsymbol{i}_a^u(t)$ are less prominent. Balanced reactive currents $\boldsymbol{i}_r^b(t)$ are generated by the thyristor bridge *(delayed gate pulses)*. Instantaneous real $p(t)$ and imaginary $q(t)$ powers are significantly distorted, as a result of single-phasing and the 6-pulse rectifiers. The CPT-algorithm decompose line currents very elegantly as long as system voltages $\boldsymbol{u}(t)$ are balanced sinusoidal.

3.8.2 *Case 62*

Using the same setup as in experiment 41 *(diode rectifier)* now connected to infinite bus. Input low-pass filters are adjusted in software by setting the cut frequency $f_c(LP) = 75$ Hz, making resulting input signals $\boldsymbol{u}(t)$ and $\boldsymbol{i}(t)$ sinusoidal as depicted in **Figure A.13**. Consequently the virtual instrument effectively ignore all harmonics in the current flow; void currents $\boldsymbol{i}_v(t)$ and oscillations in real $p(t)$ and imaginary $q(t)$ powers vanish.

Because of the filter damping *(-3 dB @ 50 Hz)*, input gains (K_{Gain}) had to be recalibrated to ensure correct RMS. Balanced active currents $\boldsymbol{i}_a^b(t)$ are notably very similar to case 41. This case is meant as a demonstration of one of the many powerful signal conditioning features available. The Simulink® software contains an extensive list of libraries and blocks. The fact that Simulink® and MATLAB® are mainly mathematical tools, makes it fast and easy to build customized control applications, as well as post-processing of experimental results.

3.8.3 *Case 63 and 64*

Again observing the diode rectifier with input filters set back to nominal parameters. The CPT-algorithm depend profoundly on mean-value operations for computation of homo-variables and average powers. Averaging time period T_{CPT} is nominally set to $20\,ms$, resembling a low-pass filter with cut-frequency equal to the fundamental $f_{CPT} = 50\,Hz$. In high performance shunt-compensating units, extraction of current reference $\boldsymbol{i}^*_{VSI}(t)$ are required to be ideally instantaneous.

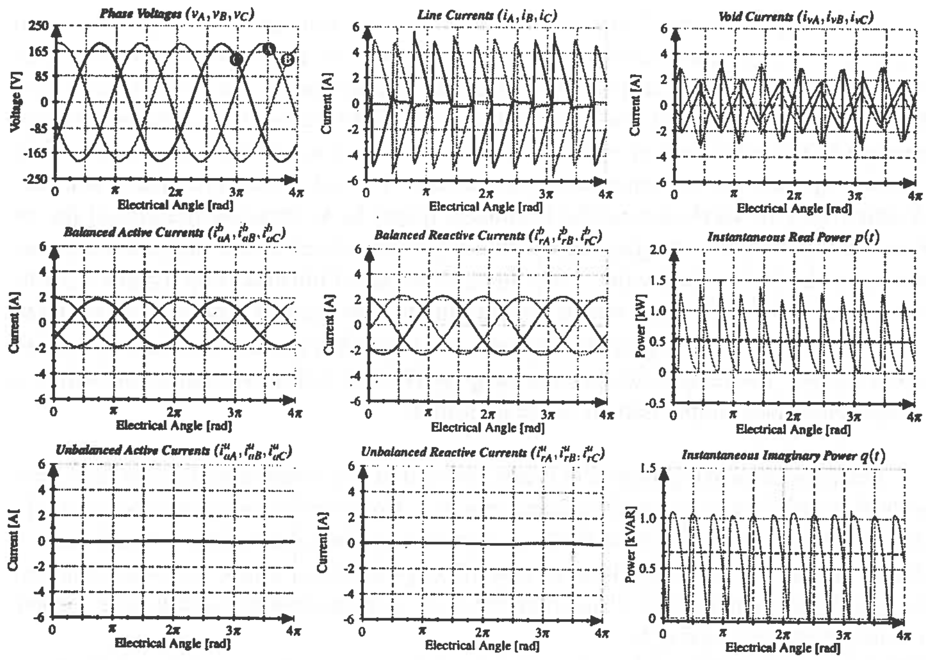

Figure 3.40 – *Case 58 - Same as case 47 (thyristor rectifier). Programmable source replaced by stiff grid voltage. Waveforms and decompositions are identical to ideal results simulated in Simulink®.*

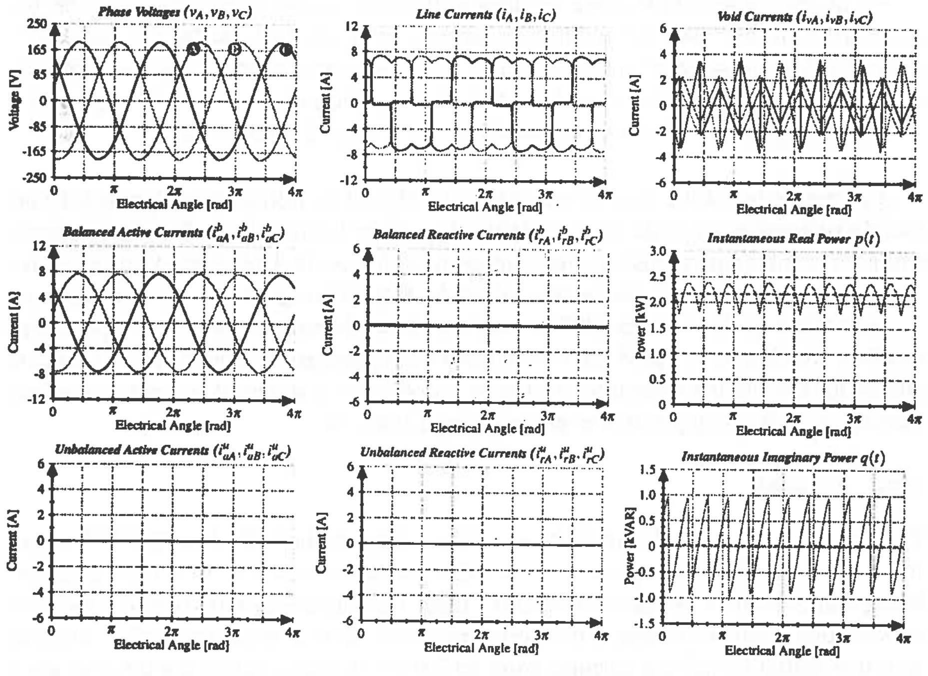

Figure 3.41 – *Case 60 - Same as case 41 (diode rectifier), replacing the programmable source with grid voltage. As the voltage waveforms are sinusoidal the CPT-algorithm effectively separates current harmonics into void currents.*

According to **Figure 2.3** the CPT-algorithm needs minimum 20 *ms (one cycle)* in order for its decomposed current signals to converge, and additional 20 *ms* to compute average powers. This could be a questionable "weakness" of the CPT in this matter, thus H.Paredes suggested a solution to this issue[A5] by replaced the ordinary moving average filters with a lookup table-based method. This is an interesting approach which was attempted to be implemented experimentally, but unfortunately failed to succeed. Another way of work around the limitation might be to increase (decrease) the cut frequency f_{CPT}, and averaging time period T_{CPT} respectively. This suggested approach are tested in the two following cases. In experiment 63 illustrated by **Figure A.14** the f_{CPT} is set to 1.5 kHz which equals an algorithmic convergence time of T_{CPT} =0.67 *ms*.

With this short averaging time period, the algorithm process current components up to the 30th harmonic, thus preserving good fidelity and on the same time offers an almost 30X speed improvement of the algorithm.

Instantaneous real power $p(t)$ is not affected as it is computed directly from products of acquired voltages $\boldsymbol{u}(t)$ and currents $\boldsymbol{i}(t)$. However the imaginary power $q(t)$ is artificial high (8 kVAR), most likely as contribution from harmonics are included. Manipulating the CPT-algorithm clearly affect power and current decomposition. Notably average values active P and reactive Q powers oscillate along with their instantaneous powers $p(t)$ and $q(t)$.
The response from the void currents $\boldsymbol{i}_v(t)$ are interesting as they now apparently contain fundamental as well as high order current harmonics, thus taking larger share of the power flow. Void currents $\boldsymbol{i}_v(t)$ are in anti-phase with respective voltages $\boldsymbol{u}(t)$.

As aforementioned the diode rectifier will under normal circumstances draw balanced line currents, however in this case current flow is partially credited as unbalanced active $\boldsymbol{i}_a^u(t)$ and reactive $\boldsymbol{i}_r^u(t)$ components. Balanced active currents $\boldsymbol{i}_a^b(t)$ are correctly aligned with voltages, however balanced reactive currents $\boldsymbol{i}_r^b(t)$ are not complying with the expected phase relation as they are in fact also aligned with voltages.

In experiment 64 the f_{CPT} is reduced to 100 *Hz* and as indicated in **Figure A.15** this greatly restores most of the phase relationship of the balanced reactive $\boldsymbol{i}_r^b(t)$ currents, while $\boldsymbol{i}_v(t)$ still contain fundamental frequency components. Unbalanced active N_a and reactive N_q power parcels are nearly ignorable. Case 64 might represent a compromise as most of the qualities of the CPT are recovered, while reducing the convergence time to 10 *ms* which still is a good improvement of the algorithms response time. In cases 63 and 64 the CPT fails to decompose currents and powers in a correct and physical related manner, so it is not applicable to power system analysis.

3.8.4 Case 65

This case is included to demonstrate one issue related to the LEM LA 55-P[D40] current transducers. Having no experience with LEM transducers the LA 55-P was considered being a good choice for the experiments. Three current sensor boards were fabricated, all with one number of turns in their primary circuit. However first time this configuration was tested (acquiring currents from an 2.0 *kW* R-load), output signals was not of satisfactory quality. Measured currents were indeed what typically is expected from a resistive load, but there were considerable noise superimposed similar to what shown in **Figure A.20**. After nearly a week of troubleshooting the entire rig, it turned out that the primary currents in the LEMs produced insufficient magnetic flux. The current sensor boards were rebuilt by adding ten turns of smaller wire in the primary circuit. This time the actuators were magnetically saturated at line currents of 4.33 A_{RMS} effective value, resulting in output signals being chopped as visualized in **Figure A.16**. The CPT-algorithm naturally interpret these input signals as void currents similar to a nonlinear load. At the end all experiments were accomplished using a current sensor board having a current loop of five turns, which started to saturate at 7.35 A_{RMS}

The entire rig was designed and constructed to handle the power and currents from the IGBT-based 20 kW VSI. All components were intentionally dimensioned so that it was possible to conduct experiments in the 10.0 - 15.0 kW power range, and that way making the experimental results to be more realistic. However because of safety precautions and hardware limitations, the experiments were scaled down to the 1.0 - 2.0 kW power range, giving a current level that was manageable.

3.8.5 Case 66

In the literature the CPT has been synonymously associated to description of complex loads, having unsymmetric and nonlinear behavior. But to be fully valid in purpose of network analysis, it must be able to properly detect power generating devices. This property is tested with a symmetric resistive load connected to infinite bus. Input and output connections of the current sensor board are interchanged as to mimic a power generating network element.

According to acquired signals presented in **Figure A.17** line currents $\boldsymbol{i}(t)$ are in anti-phase ($\varphi_1 = 180°$) with voltages $\boldsymbol{u}(t)$, which complies with the conventional definition of an electrical voltage source. Amongst current components only balanced active currents $\boldsymbol{i}_a^b(t)$ are detected, which naturally lag/lead their respective voltages by 180 electrical degrees. The instantaneous real power $p(t)$ is correctly negative, however average powers presented in **Table 3.7** are not negative. This is because of the way the algorithm is mathematically implementing the conservative power theory.

Although not included in this experimental work, it would also be equally interesting testing how the CPT-algorithm might respond to reactive power sources. This can be implemented either by connecting the virtual instrument to a capacitor battery, or using an inductive load with interchanged connections on the current sensor board.

3.8.6 Case 67

This scenario illustrated in **Figure A.18**, demonstrate what was the most challenging aspect prior to experimental work. Thought being a hardware-related issue, it was ultimately solved in the software domain. The phenomena can be easily demonstrated by removing the input high-pass filters $f_c(HP) \rightarrow \infty$, revealing a significant DC-component superimposed on the acquired signals. This especially concerns input voltages $\boldsymbol{u}(t)$ where the offset is approximately as much as $V_{bias} = 40.0\,V$.

Bearing in mind the high calibration factors (K_{Gain}) used on voltage channels, this exemplify the sensitivity to biasing when having the Speedgoat IO106 set to "single-ended mode". Utilizing the "differential mode" would most likely strangle the issue, however this option was considered redundant as all input channels were sharing common signal ground with ground in the auxiliary power source[D43].

Similar minor offset is present in acquired line currents $i(t)$. The offset translates into erroneous detection of void currents $i_v(t)$ and distortion power D, even when the load is purely symmetric resistive. It was spent two weeks solving the issue, the challenge was to localize the error. The entire CPT-algorithm was investigated along with the intricate wiring and soldering circuits making up the acquisition system.
There was a milestone in the thesis work when the error was detected and dealt with. It turned out that having high-pass input filters was an absolute premise for the CPT-algorithm to output signals of reasonable and satisfactory quality.

Introducing high-pass and low-pass filters can be justified when dealing with virtual instrumentation, as they in fact might improve the overall performance of the VI. However the reliance on such filters are debatable when considering the control of active power filters. For the APF to compensate successfully it is of the essence that it work as close as possible in phase lock with the load current. As well known from control theory using filters in the control system, ultimately introduces phase shifts in the process *(shunt compensation)* which affect the APFs phase lock. The equivalent time delay can for instance have a detrimental effect on reactive power compensation, and filtering of high-order current harmonics.

It is not clear exactly where the offsets originated from, but they were certainly not generated in the software nor the Speedgoat IO106 AD-card. They are assumed to be related to the badly constructed acquisition system, which must be further investigated. It is strongly recommended that a proper acquisition system is designed and built, as this is considered being the greatest weakness of the Speedgoat solution, compared to other competing brands like dSpace, National Instruments and Opal RT.

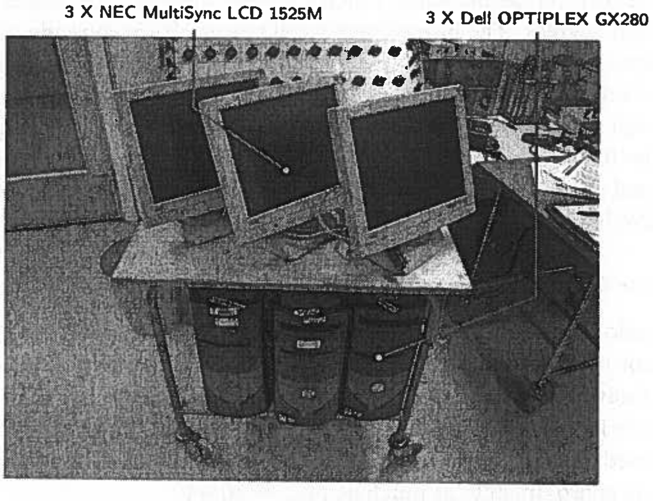

Figure 3.42 – *Electronic consumer products are mostly powered by single-phase diode rectifiers. As such apparatus become increasingly popular and important in the daily life, this imply more passive unlinear loads spread across the electric power grid. A cluster of three PCs and monitors were tested to illustrate the unbalanced distorted line currents these devices induce.*

3.8.7 Case 68

Just to actualize the impact of todays nonlinear loads. **Figure A.19** depict measured line currents $i(t)$ drawn from a very common type of load found nearly anywhere in the distribution power network, scaling from small residents to vast office building. Three PCs (Dell Optiplex GX280) and monitors (NEC MultiSync LCD 1525M) are connected to the grid as presented in **Figure 3.42**.

Electronic consumer products are often powered by typically passive low-power single-phase rectifying units. Designed according to a low-budget philosophy rather than concerning about the eventual impact on the upstream network, these units consequently drain highly distorted currents. Single-phase units are in certain ways worse than three-phase rectifiers, as they do not draw balanced three-phase line currents.

Evidently vast computer clusters located in for instance office buildings, cause detrimental effect on the power quality if these issues are not properly neutralized. The CPT performs current and power decomposition similar to previous described cases dealing with passive rectifier loads.

3.8.8 Case 69

Exemplifying one characteristic of the LEM LV 25-600 voltage transducer[D41]. It was found that voltage applied across the primary circuit must be above a minimum level of $V_{min} = 130.0\, V_{RMS}$ to avoid noise (**Figure A.20**) in the output signal. Notably similar behavior were observed with the LA 55-P current transducer in case of primary currents drastically lower than nominal primary current. Additionally the performance of the LEM transducers proved to be very dependent on the voltage stability of the TRACO auxiliary power supplies. The acquisition system was designed with a supply voltage of $V_{aux} = 30.0\, V$ while the LEM modules can retain their accuracy with up to $\pm 5\%$ variation in the supply voltage.

Prior to the experimental work it was serious problems with the auxiliary power. The unit could only power up to six LEM modules before the auxiliary voltage collapsed. It was eventually discovered that a damaged diode on one of the SINTEF acquisition cards[D36], short circuited the auxiliary power source. Initially these acquisition cards were kept as a part of the acquisition system as they featured some very practical voltage monitors for the LEM supply voltage.

The combination of low voltages $u(t)$ and currents $i(t)$ result in apparent power of only $A = 6.0\, VA$. Proving how the virtual instrument including hardware and software, is able to operate correctly in a broad scope of currents and powers.

3.8.9 Case 70

This experiment is meant as a comparative test to case 13, and all other similar cases dealing with pure inductive loads. The programmable voltage source is replaced with stiff grid voltage through a variable transformer. The qualitative and quantitative decomposition of currents and powers are similar to case 13, thus confirming the previous results.

3.9 Symmetric bipolar loads, harmonic voltages

These final twenty experiments will be dedicated to selected scenarios from case 1-40 involving basic bipolar loads, but now in the context of distorted voltage regime. Before presenting the results, some important remarks regarding harmonics generally is needed.

3.9.1 Voltage harmonics

Considering a triplet-set of basic sinusoidal network voltages $x_{a1}(t)$, $x_{b1}(t)$ and $x_{c1}(t)$ represented by vector $\boldsymbol{x}_1(t)$ at the fundamental frequency $f = 50.0\,Hz$, or equivalently angular frequency $\omega = 2\pi f = 314.16\,rad/s$. For simplicity these voltages are presumed being ideal, hence possessing symmetrical properties such that all three phases have effective value X_1 and mutually phase shifted by 120 °. Rotating according to the conventional positive phase sequence yields:

$$\boldsymbol{x}_1(t) = \begin{bmatrix} x_{a1}(t) \\ x_{b1}(t) \\ x_{c1}(t) \end{bmatrix} = \begin{bmatrix} \sqrt{2}X_1 \sin(\omega t + \phi_{a1}) \\ \sqrt{2}X_1 \sin(\omega t + \phi_{b1}) \\ \sqrt{2}X_1 \sin(\omega t + \phi_{c1}) \end{bmatrix} = \begin{bmatrix} \sqrt{2}X_1 \sin(314.16{\cdot}t + 0) \\ \sqrt{2}X_1 \sin(314.16{\cdot}t - \frac{2\pi}{3}) \\ \sqrt{2}X_1 \sin(314.16{\cdot}t + \frac{2\pi}{3}) \end{bmatrix} \tag{3.1a}$$

In network conditions of non-ideal voltages, multiple triplet-sets of harmonics $\boldsymbol{x}_h(t)$ of the h-th order may be superimposed onto the fundamental voltage $\boldsymbol{x}_1(t)$. Again for simplicity each non-fundamental harmonic triplet is here restricted to symmetry.

In context of this thesis work harmonics may be categorized into two main groups which are referred to simply as *homo-sequential harmonics* $\boldsymbol{x}_h^{\psi}(t)$, and *hetero-sequential harmonics* $\boldsymbol{x}_h^{\sigma}(t)$. To rationalize the notation, vector quantity $\boldsymbol{\phi}$ is introduced incorporating phase offsets for all three phases:

$$\boldsymbol{\phi} = \begin{bmatrix} \phi_{a1} \\ \phi_{b1} \\ \phi_{c1} \end{bmatrix} = \begin{bmatrix} 0 \\ -\frac{2\pi}{3} \\ \frac{2\pi}{3} \end{bmatrix} \tag{3.1b}$$

The difference between the two categories can be seen in the argument containing the angular frequency ωt and phase shift $\boldsymbol{\phi}$. Regarding homo-sequential harmonics $\boldsymbol{x}_h^{\psi}(t)$ only the angular frequency is manipulated by the h-th harmonic order $(\omega_h^{\psi} + \boldsymbol{\phi}_h^{\psi}) = (h\omega t + \boldsymbol{\phi})$. In hetero-sequential harmonics $\boldsymbol{x}_h^{\sigma}(t)$ both angular frequency and phase shift *(whole argument)* are altered by the h-th harmonic order $(\omega_h^{\sigma} + \boldsymbol{\phi}_h^{\sigma}) = (h\omega t + h\boldsymbol{\phi})$. Despite treating both quantities $\boldsymbol{x}_h^{\sigma}(t)$ and $\boldsymbol{x}_h^{\psi}(t)$ as harmonic voltages, they however obtain quite different characteristics. Observing a non-ideal voltage $\boldsymbol{x}(t)$ polluted by a series of homo-sequential harmonics gives:

$$\boldsymbol{x}(t) = \sum_{h \in \mathbb{Z}_{\psi}} \boldsymbol{x}_h^{\psi}(t) = \sum_{h \in \mathbb{Z}_{\psi}} \sqrt{2}X_h \sin(h\omega t + \boldsymbol{\phi}), \quad \mathbb{Z}_{\psi} \in \{\mathbb{N}\} = \{1, 2, 3 \dots\} \tag{3.2}$$

So the homo-sequential harmonics $\boldsymbol{x}_h^{\psi}(t)$ always translate into same phase sequence *(positive)* as the fundamental voltage $\boldsymbol{x}_1(t)$.

Thus resulting voltage $x(t)$ appear distorted as harmonic components get superimposed to the fundamental component, but with the phase sequence and consequently voltage symmetry intact. Next examining a voltage $x(t)$ degraded exclusively by hetero-sequential harmonics:

$$x(t) = \sum_{h \in \mathbb{Z}_\sigma} x_h^\sigma(t) = \sum_{h \in \mathbb{Z}_\sigma^+} x_h^{\sigma+}(t) + \sum_{h \in \mathbb{Z}_\sigma^-} x_h^{\sigma-}(t) + \sum_{h \in \mathbb{Z}_\sigma^0} x_h^{\sigma 0}(t) \tag{3.3a}$$

where terms are defined as

$$\sum_{h \in \mathbb{Z}_\sigma^+} x_h^{\sigma+}(t) = \sum_{h \in \mathbb{Z}_\sigma^+} \sqrt{2} X_h \sin(h\omega t + h\phi), \quad \mathbb{Z}_\sigma^+ \in \{3\mathbb{N} - 2\} = \{1, 4, 7 \dots\} \tag{3.3b}$$

$$\sum_{h \in \mathbb{Z}_\sigma^-} x_h^{\sigma-}(t) = \sum_{h \in \mathbb{Z}_\sigma^-} \sqrt{2} X_h \sin(h\omega t + h\phi), \quad \mathbb{Z}_\sigma^- \in \{3\mathbb{N} - 1\} = \{2, 5, 8 \dots\} \tag{3.3c}$$

$$\sum_{h \in \mathbb{Z}_\sigma^0} x_h^{\sigma 0}(t) = \sum_{h \in \mathbb{Z}_\sigma^0} \sqrt{2} X_h \sin(h\omega t + h\phi), \quad \mathbb{Z}_\sigma^0 \in \{3\mathbb{N}\} = \{3, 6, 9 \dots\} \tag{3.3d}$$

Voltage harmonics $x_h^{\sigma+}(t)$ with the harmonic subset $\mathbb{Z}_\sigma^+ \in \{3\mathbb{N}-2\} = \{1,4,7\dots\}$ translates into positive sequence components. Harmonic voltages $x_h^{\sigma-}(t)$ of subset $\mathbb{Z}_\sigma^- \in \{3\mathbb{N} - 1\} = \{2,5,8\dots\}$ become negative sequence parcells, while voltages $x_h^{\sigma 0}(t)$ of harmonic subset $\mathbb{Z}_\sigma^0 \in \{3\mathbb{N}\} = \{3,6,9\dots\}$ renders zero sequence content.

Custom to hetero-sequential harmonics is that as the harmonic order h increases, the voltages cycle periodically through positive, negative and zero sequence harmonics. In this case resulting voltage $x(t)$ will appear both distorted and unbalanced solely because of harmonics, even when the fundamental component $x_1(t)$ itself is balanced. As harmonics generally are much less profound compared to the fundamental voltage their impact is limited. Harmonics close to the fundamental frequency $h \in \{2\dots6\}$ must be expected to have greatest contribution to such peculiar phenomena.

Positive sequence harmonics $x_h^{\sigma+}(t)$ are expected to behave similar to homo-sequential harmonics, while negative sequence $x_h^{\sigma-}(t)$ and particularly zero sequence $x_h^{\sigma 0}(t)$ ***(triplen-harmonics)***, are of greater interest when dealing with electric power systems. Preliminary simulations reveal new interesting phenomenas related to hetero-sequential voltage harmonics, however these scenarios are beyond the scope of this thesis work:

- The Speedgoat system can easily synthesize PWM-signals from nearly any thinkable control-signal, including homo- and hetero-sequential harmonics.
  The limitation of the experimental setup in its current state is mainly the VSI. Based on a two-level three-phase topology with no midpoint in the DC-link, the VSI is not capable of producing zero-sequence voltage components.

- Analysing homo- and hetero-sequential harmonics imply even more complications and systematic experiments than presented here. Also it would be valuable testing the CPT-algorithm in conjunction with a new generalized sequence components theory, also presented by P.Tenti et al.[tenti2007d]
  The comparison between the pq-theory and CPT-power theory become fully adequate only with cases of combined zero-sequence voltages and currents.

- Testing combinations of zero-sequence voltages and currents, demands a suitable three-phase transformer. The transformer could possibly be discarded if the VSI is properly designed and built, then on expense of the galvanic isolation.

In the previous scenarios dealing with three-phase rectifier loads, and the experiments about to be presented, it is exclusively referred to homo-sequential harmonics $x_h^{\psi}(t)$ whenever voltage harmonics $x_h(t)$ are mentioned. The hetero-sequential harmonics $x_h^{\sigma}(t)$ will not be studied, because of limited time in this already lengthy thesis work, as well as the aforementioned practical constraints.

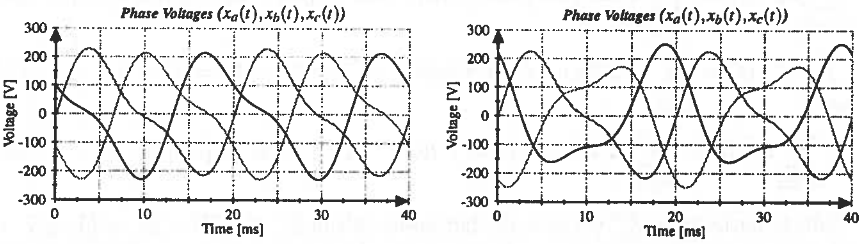

Figure 3.43 – *Symmetric 50 Hz voltage (1.0 pu) degraded by 100 Hz (2nd) harmonics (0.5 pu). Left side: homo-sequential harmonics $x_2^{\psi}(t)$. Right side: hetero-sequential harmonics $x_2^{\sigma}(t)$. The amplitude of harmonics is exaggerated for clarity. Voltages are severely deformed.*

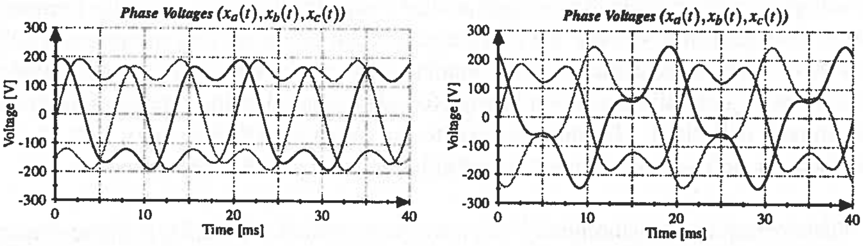

Figure 3.44 – *Symmetric 50 Hz voltage (1.0 pu) degraded by 150 Hz (3rd) harmonics (0.5 pu). Left side: homo-sequential harmonics $x_3^{\psi}(t)$. Right side: hetero-sequential harmonics $x_3^{\sigma}(t)$.*

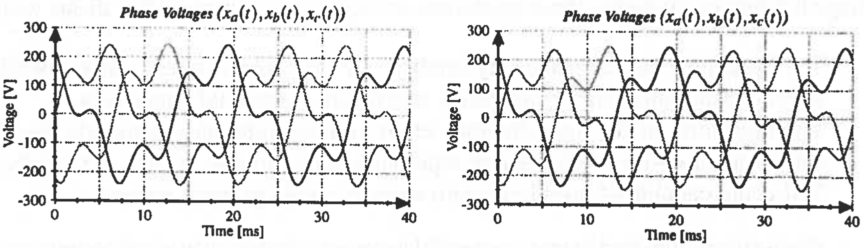

Figure 3.45 – *Symmetric 50 Hz triplet voltages (1.0 pu) degraded by 200 Hz (4th) harmonics (0.5 pu). Left: homo-sequential harmonics $x_4^{\psi}(t)$. Right: hetero-sequential harmonics $x_4^{\sigma}(t)$. Homo- and hetero-sequential harmonics are identical for $h = \{3N - 2\}$ harmonic orders.*

To underline the importance of differentiating between homo- and hetero-sequential harmonics, a non-ideal voltage is modeled in Simulink using plugin SimPowerSystems™. For the three cases illustrated in **Figure 3.43** to **3.45** it is evident how homo-sequential harmonics $\boldsymbol{x}_h^{\psi}(t)$ adds up to the fundamental voltage in the usual expected fashion. The outcome from adding hetero-sequential harmonics $\boldsymbol{x}_h^{\sigma}(t)$ is more dramatic as the voltage become unbalanced as well as distorted.

The impact of these harmonics will be much less in practical scenarios than what is illustrated with the Simulink simulation. In the most general case each triplet-set in voltage $\boldsymbol{x}(t)$ may also have unsymmetric properties, and there might be a mix of homo- and hetero-sequential harmonics.

3.9.2 Case 71 - 73

Introductorily cases 71 to 73 compares directly to experiments $1, 3$ and 7 respectively dealing with symmetric purely resistive loads. In cases 71 and 72 the load is a star-configuration altering between floating and grounded star point μ_M.
As the load impedances are being symmetric $R_{a,b,c} = 23\,\Omega$, line currents sum to zero ($K_{i^-} = 0.7\,\%$) at each instant of time, making the neutral conductor theoretically redundant ($I_N = 0.10\,A$). System voltages $\boldsymbol{u}(t)$ are preset having elements of 7th, 13th and 16th harmonics (**Figure A.28**), resulting in harmonic content of $THD_v = 19.7\,\%$. Resulting line currents $\boldsymbol{i}(t)$ possess exact same harmonic content (**Figure 3.46**) as found in voltage, as expected from a resistive load.

All three cases yields identical power and current decomposition simply because the load impedance is symmetric. Line currents $\boldsymbol{i}(t)$ are adequately classified as balanced active currents $\boldsymbol{i}_a^b(t)$, having exact distorted waveform as respective voltages. Instantaneous real $p(t)$ and imaginary $q(t)$ powers oscillate at frequency $300\,Hz$ remarkably similar to what are observed for three-phase rectifiers. Distorted line currents and instantaneous power flow origins exclusively from the distorted voltage, thus the conservative power theory cannot offer any improvements in this context.

3.9.3 Case 74 - 76

Case 74 to 76 corresponds to experiments 11, 13 and 17 which presented various constellations of a symmetric inductive load. As illustrated in **Figure 3.47** applying the same distorted voltages $\boldsymbol{u}(t)$ as previous cases, the purely inductive load responds differently to non-ideal voltages. Line currents $\boldsymbol{i}(t)$ appear much smoother ($THD_i = 3.7\,\%$), while the voltage distortion has doubled ($THD_v = 41.5\,\%$) compared to the resistive load. This can be reasoned by the natural filtering action of the inductances.

Having a reactance of inductance value $L = 175\,mH$, means that any current harmonics will be heavily dampened. The coil filters these current harmonics by self-inducing harmonic voltages across its terminals, thus aggravating the presence of 7th , 11th , 13th and 16th harmonics in the voltage.

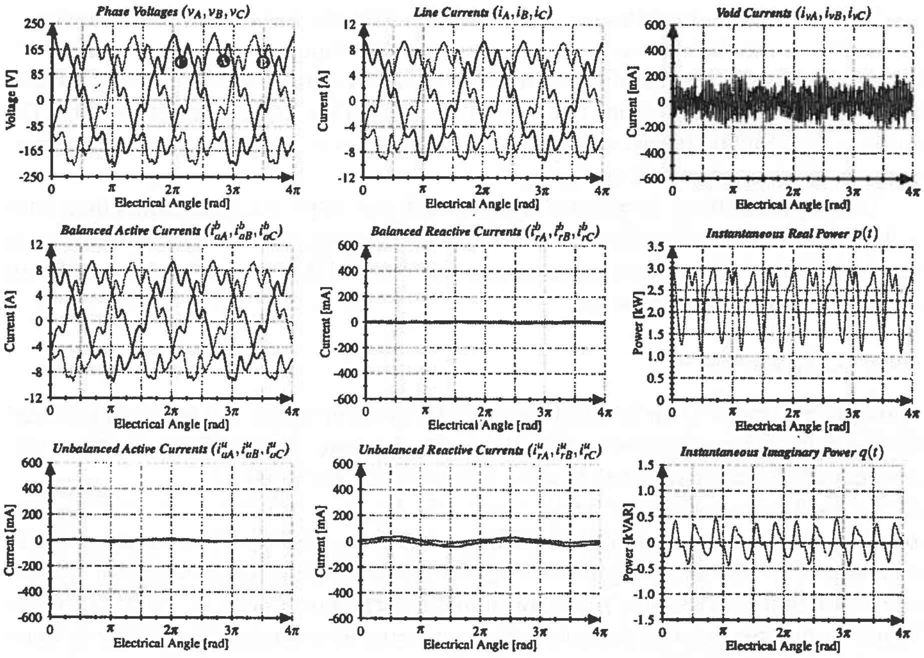

Figure 3.46 – *Case 71 - Symmetric YF-connected R-load. Only balanced active currents detected, other terms are negligible. Instantaneous real power flow oscillates despite having symmetric load.*

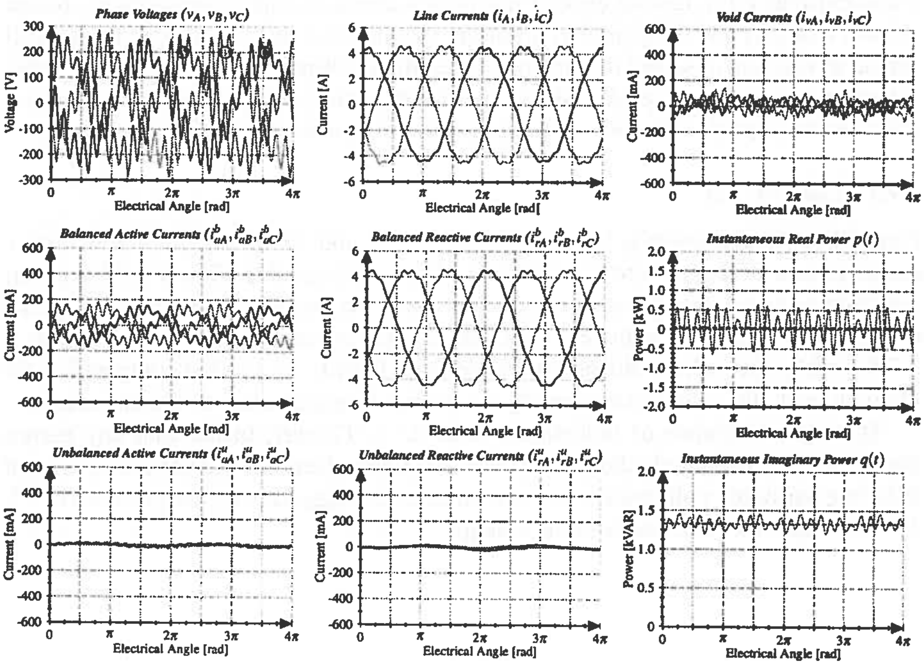

Figure 3.47 – *Case 74 - Symmetric YF-connected L-load. Currents possess different harmonic spectrum than voltages. Difficult determining exact origin of void currents.*

Acquired line currents $\boldsymbol{i}(t)$ are mostly associated to balanced reactive currents $\boldsymbol{i}_r^b(t)$, as well as some less profound balanced active $\boldsymbol{i}_a^b(t)$ and void currents $\boldsymbol{i}_v(t)$. As the acquired line currents posses considerably less harmonics than the voltages, this imply that void currents contain no generated current components. Therefore it must be assumed that void currents are mainly composed of active and reactive scattering currents, accounting for harmonic powers in the instantaneous real $p(t)$ and imaginary $q(t)$ powers.

As numerously demonstrated in the ideal voltage regime, delta and star-configurations produce identical power and current decomposition for symmetric inductive loads. This property is now experimentally verified for the distorted voltage regime as well.

3.9.4 Case 77 - 79

These are comparative tests for experiments 21-23 dealing with symmetric series connected RL-loads. According to **Figure 3.48** same behavior can recognized from previous cases; the inductive reactance dominates the load impedance effectively providing filtering of line currents $\boldsymbol{i}(t)$. Load inductances induce harmonic voltages boosting the original harmonic content of voltages $\boldsymbol{u}(t)$ into $THD_v = 37.6\,\%$, which ultimately purify the line currents $THD_i = 4.4\,\%$.

Having exact same load parameters as cases 21-23, measured line currents $\boldsymbol{i}(t)$ are decomposed similar to experiment 21. The magnitude of balanced reactive $\boldsymbol{i}_r^b(t)$ and balanced active $\boldsymbol{i}_a^b(t)$ currents, grossly reflects the ratio between parameters $R_{a,b,c}$ and $L_{a,b,c}$. One important difference is the detection of void currents $\boldsymbol{i}_v(t)$ and associated distortion power $D^{[A6]}$. The fluctuation of instantaneous real $p(t)$ and imaginary $q(t)$ powers are strikingly similar to those presented in **Figure 3.47**.

3.9.5 Case 80

This scenario is derived from experiment 33 where the load incorporated an unsymmetric resistive load, connected in floating star-configuration. The resulting line currents $\boldsymbol{i}(t)$ and corresponding current decomposition (**Figure 3.49**) look very similar to case 33. As the load impedance is unsymmetric ($R_{a,b} = 96\,\Omega$ and $R_c = 25\,\Omega$) and floating, line currents become phase shifted and contain negative sequence components. This is accounted for by the unbalanced active currents $\boldsymbol{i}_a^u(t)$. The respective phase shifts φ_{IA}= -21°, φ_{IB}= -99° and φ_{IC}= -241° explain the presence of $\boldsymbol{i}_r^u(t)$ in phases A and B, but not in phase C where current is in phase-lock with its voltage.

The important difference from case 33 is that active balanced $\boldsymbol{i}_a^b(t)$ and unbalanced $\boldsymbol{i}_a^u(t)$ currents holds same harmonics as distorted voltages $\boldsymbol{u}(t)$, while unbalanced reactive currents $\boldsymbol{i}_r^u(t)$ are more close to a 50 *Hz* sinewave. Same properties were observed when examining three-phase rectifiers.

Instantaneous powers $p(t)$ and $q(t)$ oscillate at 100 *Hz* in quadrature phase relation, as well as the notable presence of superimposed harmonic powers. The 2nd order harmonic power is induced by the load unsymmetry, while remaining harmonic powers are created by the non-ideal voltages.

3.10 Unsymmetric bipolar loads, harmonic voltages

3.10.1 *Case 81 and 82*

Pursuing the unsymmetric resistive load, by grounding the load star point μ_M to source neutral μ_N, line currents $\boldsymbol{i}(t)$ become independent and now contain both negative ($K_{i-} = 60.8\,\%$) and zero sequence ($K_{i0} = 60.6\,\%$) components. Most of negative and zero sequence current components are located (**Figure 3.50**) in the unbalanced active currents $\boldsymbol{i}_a^u(t)$. Waveforms of balanced active currents $\boldsymbol{i}_a^b(t)$ possess same symmetric and harmonic qualities as network voltages $\boldsymbol{u}(t)$, this is strictly speaking based on a qualitative rather than quantitative observation. Line currents are aligned with respective voltages causing unbalanced reactive currents $\boldsymbol{i}_r^u(t)$ to vanish.

Observing instantaneous real $p(t)$ and imaginary $q(t)$ powers, 2nd order harmonic powers appear doubled in amplitude, making high order harmonic powers less profound. As network voltages $\boldsymbol{u}(t)$ and balanced active currents $\boldsymbol{i}_a^b(t)$ are fairly balanced ($K_{v-} = 5.0\,\%$), compensating $\boldsymbol{i}_a^u(t)$ would make line currents balanced, and at the same time improve instantaneous real $p(t)$ power flow by cancelling the $100\,Hz$ harmonic power. By reconfiguring the resistive load into delta-wiring evoke same results as experiment 34. Notably unbalanced active N_a and reactive N_q power are reduced because of the presence of distortion power D.

3.10.2 *Case 83 - 85*

Having an unsymmetric purely inductive load ($L_a = 87.5\,mH$ and $L_{b,c} = 175\,mH$), altering between delta or floating and grounded star-configuration, generally yields same results as in the sinusoidal voltage regime. The purely inductive load act as a low-pass filter ($THD_i = 4.8\,\%$), strongly opposing any current harmonics (**Figure 3.51**) above the fundamental $50\,Hz$ component.

The filtering action is clearly visible when considering voltages $\boldsymbol{u}(t)$ measured at the load bus. The preset voltage harmonic content of $THD_v \approx 17.0\,\%$ is amplified to $THD_v = 43.8\,\%$ because of the natural current filtering by the load.

As anticipated with the floating star-topology, unbalanced line currents $\boldsymbol{i}(t)$ will not lock in the usual $\varphi_1 \approx$ -90° phase shift *(case 86 and 87)*. Both active N_a and reactive N_q unbalance terms are therefore detected, despite the fact that load impedance is close to an symmetric ideal inductor.

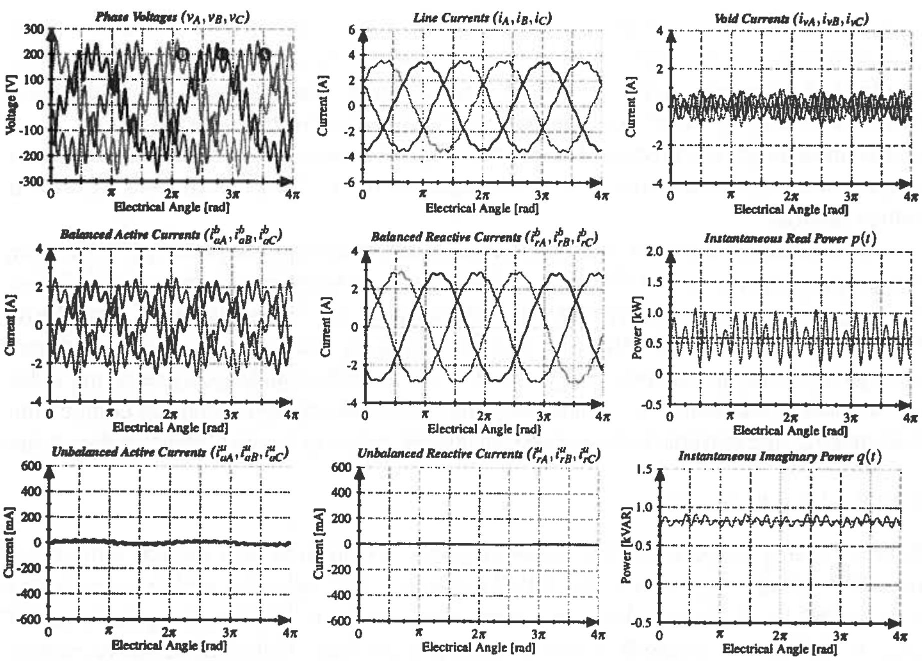

Figure 3.48 – *Case 77 - Symmetric YF-connected RL-load. Similar to case 21 most of currents are addressed as balanced active and reactive terms, which inherit waveforms from voltages and homo-integrated voltages respectively.*

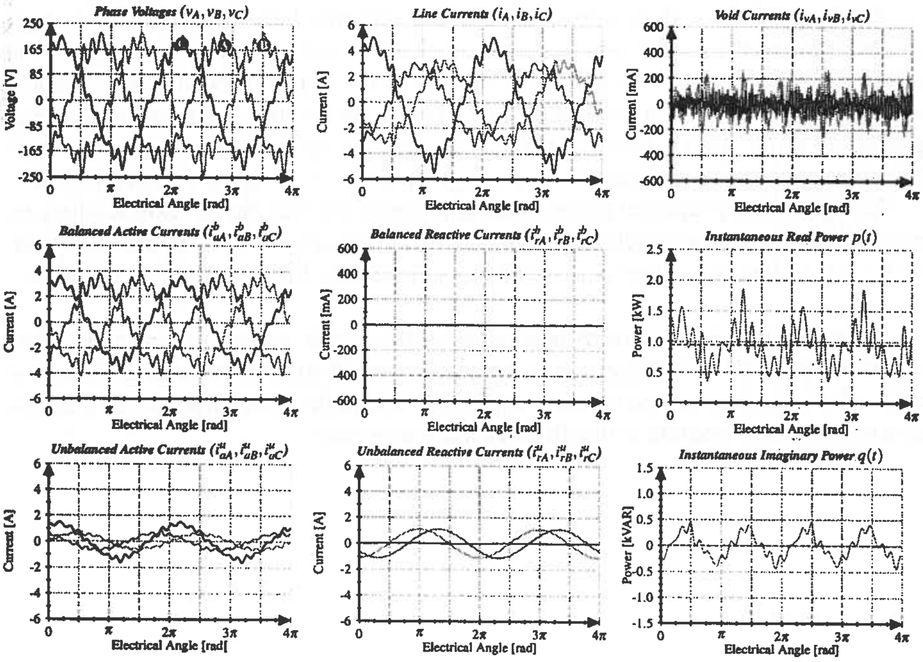

Figure 3.49 – *Case 80 - Unsymmetric YF-connected R-load. The same characteristic line current decomposition as observed during sinusoidal voltage conditions.*

Unbalanced active power N_a and unbalanced active currents $i_a^u(t)$ vanish when the load star point μ_M is connected to neutral conductor *(case 85)*. This can be reasoned on physical properties as the grounding makes all three line currents independent, and therefore restore the familiar phase-relationship between voltages and currents. Unbalanced reactive currents $i_r^u(t)$ contain negative sequence components in case of floating load, in the addition to zero sequence currents when the load is grounded to source neutral.

A confusing phenomena is the oscillation of instantaneous real power $p(t)$, swinging at high rate between $\pm\, 1.0\, kW$ even in absence of any significant presence of balanced active $i_a^b(t)$, unbalanced active $i_a^u(t)$ or void currents $i_v(t)$. The explanation could be the highly distorted voltages ($THD_v = 47.8\,\%$), which in that case can only be mitigated through series compensation. Independent of star or delta-topology, by injecting unbalanced reactive currents $i_r^u(t)$ would neutralize zero and negative sequence components, thus making line currents balanced and imaginary power $q(t)$ most likely unidirectional.

3.10.3 Case 86 and 87

Single-phasing in the distorted voltage regime yield results very similar from the sinusoidal voltage regime. As illustrated in **Figure 3.52** balanced active currents $i_a^b(t)$ are credited to all phases when connecting a resistor *(case 86)* between phase A and C ($R_{ac} = 96\,\Omega$), even phase B which is running at no-load. Unbalanced active currents $i_a^u(t)$ account for negative sequence currents, while unbalanced reactive currents $i_r^u(t)$ are linked to the phase shift. Instantaneous powers $p(t)$ and $q(t)$ oscillate at the familiar $100\,Hz$ frequency. By connecting an inductor in experiment 87 ($L_{ac} = 175\,mH$) evoke similar results (**Figure 3.53**), but with active and reactive parcels shifting role.

In cases dealing with distorted voltages, it is difficult determining the exact origin of distortion power D and void currents $i_v(t)$ without further analytical analysis. The analysis may had been easier and more correctly if these quantities were not presented as unitary variables; i.e. dividing distortion power D into voltage and current distortion powers $D = D_v + D_i$. Also it could be valuable having the void currents $i_v(t)$ split into generated, active and reactive scattering currents $i_v(t) = i_g(t) + i_{sa}(t) + i_{sr}(t)$.

Like previously reported single-phasing is one of few but rare occasions where the physical interpretation is highly questionable. It can for certain be stated that the conservative power theory in three-phase mode lose its validity for these specific scenarios.

Once more it must be underlined that all observations, comments and conclusions regarding the distorted voltage regime, cannot cover all possible scenarios. Thus more elaborate research is needed before it is possible concluding how effective the conservative power theory operate in the distorted voltage regime.

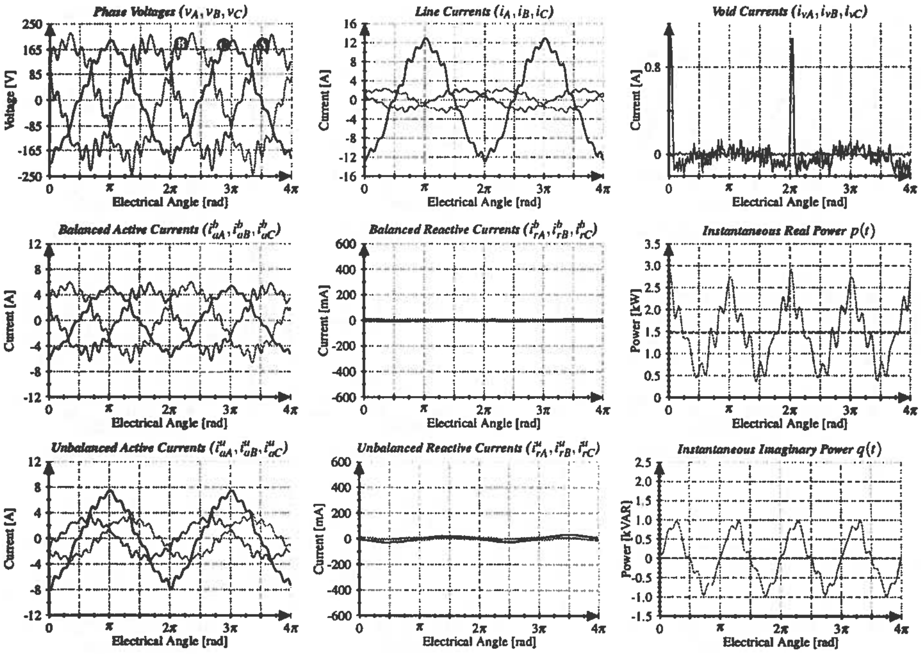

Figure 3.50 – *Case 81 - Unsymmetric YG-connected R-load. As anticipated grounding the load retain the more familiar phase-relationship. Voltage harmonics inherited by decomposed active currents.*

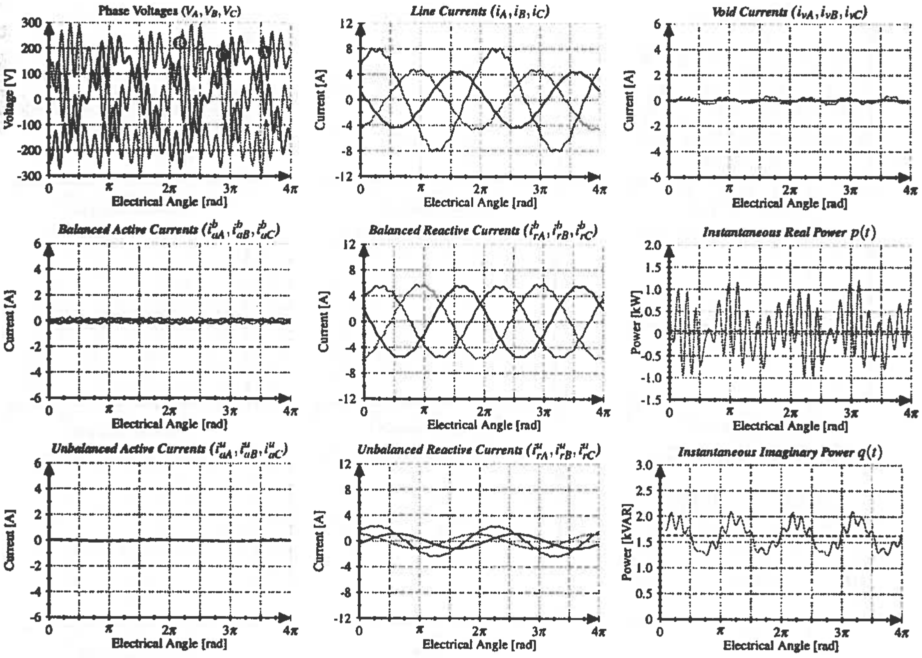

Figure 3.51 – *Case 83 - Unsymmetric YG-connected L-load. Line currents appear close to sinusoidal because of the smoothing action by the inductors.*

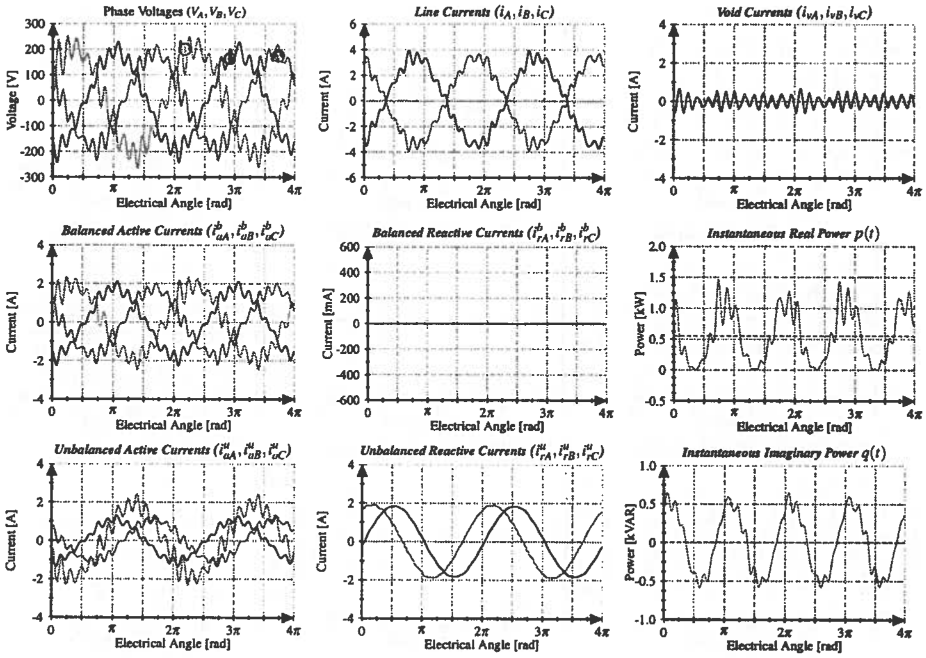

Figure 3.52 – *Case 86 - Resistor between phase A and C. Current decomposition is exclusively related to circuit elements rather than voltage condition. This case demonstrate invalid CPT-decomposition.*

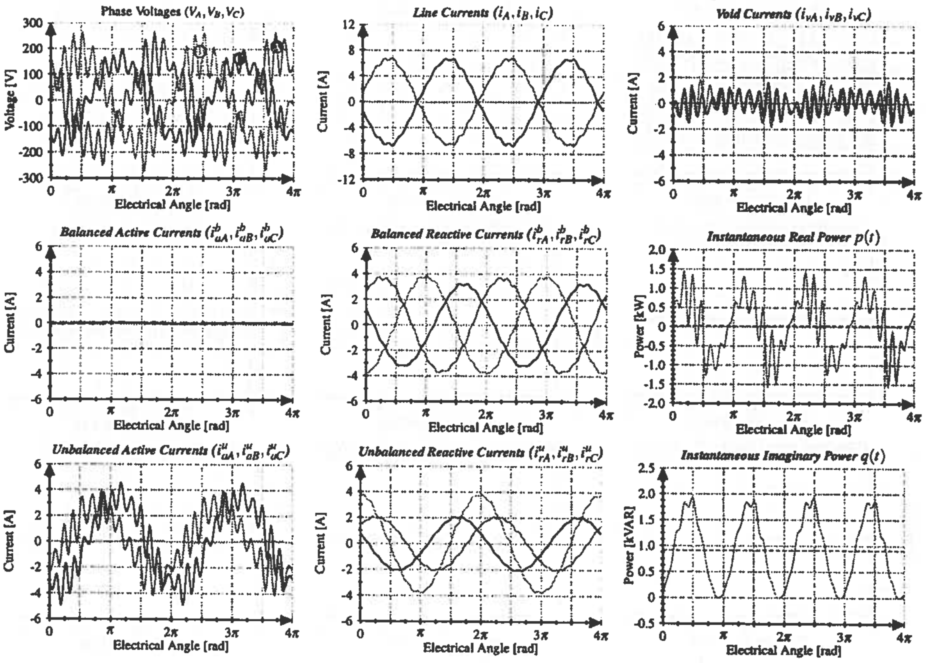

Figure 3.53 – *Case 87 - The conservative power theory performs decomposition of line currents for a single-phasing load, combined with challenging voltage condition.*

3.11 Final remarks

Major part of this thesis work *(6 months)* has been devoted to producing the results presented in this chapter. Conducting the almost 100 experiments was completed in three lab sessions, each lasting about eight hours. The real challenge was to arrive at the point where the experiments were feasible.

Going from a theoretic context to a fully practical experimental implementation, has been a challenging, but very fun and instructive process. There could probably had been said a lot about the various obstacles that were encountered, however here is discussed the most important.

Using the Noratel three-phase dYN11-transformer[D50] was a constant challenge. Rated at $S_n = 80.0\,kVA$ and designed for a maximum frequency $f_{max} = 63.0\,Hz$, it was seldom run at optimum state. The power level in most of the conducted experiments was around $S \approx 2.0\,kVA$, which is only 2.5 % of the rated transformer capacity. The primary side is rated at $V_{pn} = 230\,V$, while the voltage source inverter was only capable of producing half that line voltage before going into over-modulation. Obviously the magnetic core was not sufficiently energized, so the magnetic flux conditions were not optimal. Secondly when performing tests under non-ideal voltage regimes *(distortion and unsymmetry)*, this was clearly difficult dealing with by the transformer. Mechanical vibration and loud audible noise were registered. In general this transformer is not a good match with the 20 *kW* NTNU/SINTEF voltage source inverter.

The transformer was attractive to include in the experiments, as it made it possible having the inverter output to be presented as a star-configuration. With access to the neutral point this offered a wider range of tests to be included, both in a simulated TN and IT-environment. One of the most original contributions from this thesis work is the testing of unsymmetric bipolar loads, which had not been possible without the transformer. Moreover using the transformer as a galvanic isolation between the source and the load circuitry, has been an important safety measure. Lastly it would not been possible achieving 230 V voltage level at the LCL-filter output, without the step-up property of the transformer, $a = {}^{400\,V}/_{230\,V}$.

In the event of future experimental work, it is highly recommended to invest in one or several purpose-built transformers. The technical specifications should be specifically adopted for use in power electronics applications. This could include a low transformation ratio ($a \approx 2$) and adequate power level ($S_n \approx 10 - 20\,kW$). Star-wiring on both primary and secondary side with access to neutral points would be suitable. Most importantly the transformer should be able to handle high-order voltage and current harmonics. If the department is going to focus the experimental research on SmartGrid and power electronics, the next investments should be into proper HF-transformers, as there are currently none or very few transformers available for such purposes.

Retrospective it can be concluded that the low-pass LCL-filter was not optimally designed. The filtering action worked precisely as intended, combined with the VSI it was possible to generate balanced or unbalanced sinusoidal and harmonic voltages. However as demonstrated several occasions, the programmable voltage lacked *stiffness*.

In case of non-linear or unsymmetric loads the output voltage became degraded, even at relatively low current levels. Studying the measured phase voltages in various experiments, its evident that the equivalent series impedance Z_f of the LCL-filter was relatively high. Assembling the LCL-filter was one of the most troublesome hardware related issues. The 3-ph transformer was less important in terms of harmonic filtering, and utilized primarily by reasons discussed above. The filtering was mainly performed by the capacitor bank and the smoothing inductors, connected before the transformer. The challenge was to obtain three matched high-frequency inductors having a proper inductance value, and that were constructed for power electronics applications.

This proved to be impossible as only three matched sets were found, but none could be used in the experiments as their inductance value were either out of range, or they were constructed with an air core. By a pure lucky strike some old bulky inductors (**Figure 3.10**) of value $L_f = 175\,mH$ were found stuffed away, and was employed through most of the project work. However their inductance value were almost 100 times higher than required, moreover they are constructed for $50\,Hz$ applications, consequently not working optimal with the VSI switching at frequency $f_{sw} = 18.0\,kHz$.

One month before project stop there was a milestone as special Siemens HF-inductors were acquired from SINTEF. These were used to replace the $L = 175\,mH$ coils, which then were used to emulate various inductive loads. The overall performance improved dramatically after the replacement. The Siemens HF-inductors are reconfigurable from $L_f = 0.125 - 2.0\,mH$, all these settings were tested however resulting in the same weak output voltage. It was ultimately concluded that the issues originated from the 3-ph dYN11-transformer, thus no more time was dedicated to this aspect.

Regarding harmonic filtering usually a minimum of three inductors are required per three-phase converter in order to make an LC-filter. Many times the properties of an LCL-filter are preferred, which then requires six inductors. Apparently a batch of only 12 of these special purpose inductors are available at campus, which is most likely far less than what is demanded by NTNU and SINTEF researchers. This is such a vital part of power electronics applications, that purchasing more of these HF-inductors should be top priority. Capacitors are less crucial as they are standardized and easy available components.

The general impression is that the Department of electric power engineering, has many good facilities regarding lab and experimental research activities. Most of the equipment that were employed during the project work, are high quality state-of-the-art. Working extensively with workshopping and experimental tests, one will very early learn to appreciate high-standard equipment. It improves the work flow in so many aspects.

3.12 Accuracy and credibility

In the industry the Fluke™ company is recognized as being among the leading manufacturers of field-applied digital instrumentation, in a wide range of technical fields. Their products dedicated for electrotechnical instrumentation, are first and foremost characterized by ruggedness and reliability. Most of these instruments do not offer ultra high-precision measurements, as such characteristics are more common in special lab appliances, and less relevant for field instrumentation.

When calibrating the analog input channels on the virtual instrument, using RMS measurements was regarded as the fastest and most reliable procedure. Notably when comparing RMS-readings from digital multimeters of three different manufactures, these were all individually different. However comparison between several Fluke 177 Digital Multimeters and the Fluke 434 Power Quality Analyzer, revealed matched RMS values. Consequently only Fluke meters were used to ensure consistent calibration. Moreover as its assumed that Fluke 434 performs power calculations based on RMS values, the VI had to be calibrated with Fluke meters. Only then it would be reasonable to anticipate similar power readings, both from the virtual instrument and Fluke 434 scope.

According to its manual the Fluke 434 complies with standards EN 61010-1 2nd edition *Safety Requirements for Electrical Equipment for Measurement, Control, and Laboratory Use* and the document EN 61326 - 2002 *Electrical equipment for Measurement Control and Laboratory use EMC requirements.* The measurement methods and performance are based on standards IEC61000-4-30 *(class A & B)* and EN50160. Frequency bandwidth of both voltage and current input channels, is minimum $f_s > 10.0\,kHz$ and maximum $f_s \approx 100.0\,kHz$ for transient measurements. Resolution of RMS readings is $0.10\,V_{RMS}$ for voltage inputs, and equivalently $0.10\,A_{RMS}$ for current inputs. Power related quantities are computed by two significant decimals resolution.

The Fluke 434 is based on *true RMS* which implies that root-mean-square calculations, are including harmonic contribution from the entire frequency range. Low-end digital multimeters typically tend to perform RMS readings only at the fundamental frequency, which is not the correct physical interpretation of the effective value of an electrical quantity. Moreover active power P^* is calculated based on contribution from all harmonics, while the reactive power Q^* is computed by the fundamental phasors.

Regarding resolution of the virtual instrument this is something that is not fully perceived. The sampling frequency of all analog input channels was fixed $f_s = 10.0\,kHz$, which is matching the performance of Fluke 434, and must be considered as very satisfactory for virtual instrumentation. Signals and blocks within the entire Simulink model were based on *double-precision floating point data type (double)*, which is the default number format in any Simulink model.[G77] The double is also a common datatype in modern PCs and offers the best dynamic range, and maximum resolution of up to 17 significant decimals.

All per-unit numbers from the CPT-algorithm could theoretically have been presented in their full resolution, however it was concluded that using two significant decimals gave satisfactory accuracy, any resolution beyond this had no appreciable advantage. In most electric power engineering applications, this can be considered a convenient resolution. The excellent accuracy was demonstrated in case 69 where the power level was only 6.0 *VA*, but still maintaing correct power and current decomposition.

This experimental work is essentially founded on equipment and methodology very similar to what utilized by H.Paredes and P.Tenti, in their virtual instrumentation-based research. They employed LEM® voltage and current transducers connected to National Instruments™ hardware, then using LabVIEW® software to produce the output data. Therefore the scientific results presented in this chapter must be regarded having the same accuracy and credibility as data presented by H.Paredes et al.

The Speedgoat and xPC Target software proved to have excellent performance for applications like virtual instrumentation. But as one of the main purposes of virtual instrumentation is typically to develop and prototype new types of instruments, it may be difficult having the VI to comply with the requirements from industry standards, as these are established on well-known and accepted technology specifically.

3.13 Conservative power theory

Based on the presented per-unit power data it can be concluded that the conservative power theory, has the ability to deal with scenarios of extreme voltage unsymmetry and distortion. Studying the power decomposition its apparent that the relative amount of power components remain essentially unaltered, irrespective of voltage regimes. For correct power measurement and monitoring this is an highly valuable property. As the CPT power mix is independent of network voltage conditions, this automatically implies that the relative share of current parcels must remain unaltered as well. On the other hand this study has demonstrated that voltage condition affects current decomposition *qualitatively* wise.

What type of current components that are detected is not determined by voltage regime, however their appearance *(symmetric and harmonic qualities)* are closely related to the voltage status. Ultimately this property will have important impact on shunt compensation applications.

It must be underlined that CPT power and current decomposition, does not necessarily mirror the exact characteristics of the load. This is because certain load configurations tend to evoke special physical phenomenas, as well demonstrated for three-phase floating bipolar loads. However the physical interpretation of various current and power components is very promising.

A general observation made during experiments was that all power and current components were always present, even at cases where they theoretically should not. Indeed the same phenomena was partly observed in simulative work.[A1] The difference from simulated and real-time applications is that these errors are much more evident when running the CPT-algorithm in real-time. This could be due to round-off or arithmetic errors within the real-time target machine, even if the system was run at maximum possible precision. Also in case of practical power circuits there are always some parametric variation; i.e. one cannot expect 100 % matched impedance in all three phases, and there may always be stray inductance present. Overall the badly constructed acquisition system is considered being the most significant source of error, but was greatly compensated by using discrete LP and HP-filters. Nonetheless the relative amount of unexpected power components approach idealistic zero values, when being scaled in the per-unit system. Similarly the appearance of current components of course depends on their relative scaling, as demonstrated in the introductory experiments.

During the experiments there was systematically alternated between floating and ground voltage reference, in the expectation of getting differentiated results. In respect to the virtual instrument and the CPT this was not the case, as it appeared to produce a large number of duplicate results. Retrospective it can be concluded that the usage of neutral conductor in this study is questionable. The resistance of the neutral line was measured to be $R_N \approx 2.5\,\Omega$, which is far less than impedance Z_f in the ABC lines. Also in TN-mode the voltage reference was always connected to load-end of the neutral conductor. Different results may have been obtained if the voltage reference was connected to transformer neutral point, or by inserting an extra resistance in the neutral line. In the scope of this work it can be concluded that proposed current and power decomposition, is not affected by chosen voltage reference.

Another important conclusion from this study is that **todays digital "smart" power meters, are measuring the power consumption correctly**. These meters are logging active power exclusively as according to the tariffs, the customers shall only be attributed for the active or real part of their power consumption.
In event of future scenarios including network conditions of non-ideal voltage regimes and unlinear loads, new tariffs and grid codes may be a necessity in order to maintain optimal performance of the power network. In these cases more advanced power metering will be crucial, and todays state-of-the-art power meters will not meet the requirements.

3.14 Fluke 434 Scope

The experimental data from the Fluke 434 Power Quality Analyzer was not given much attention in the previous discussion. Comparing the power decomposition from the CPT and Fluke instrument, these proved to be reasonably consistent in the initial experiments incorporating various constellations of symmetric bipolar loads. By starting with network scenarios where the readings from the Fluke 434 are predictable and reliable, this was exploited to confirm the credibility of output data from the virtual instrument.

Notably data from the virtual instrument were always overestimated compared to the Fluke 434 device, despite having the RMS readings from both instruments perfectly matched. RMS-computation on the virtual instrument was implemented by using a dedicated discrete block from the SimPowerSystems® Simulink package. In the aftermath it became clear that this block does not implement true RMS, which may explain why the CPT power components were overestimated.

Classic apparent power S^* is always matching apparent power A from the CPT. However when calculating the apparent power manually $S^*_{Sum} = \sqrt{P^* + Q^*}$ certain scenarios revealed significant deviation, thus suggesting that S^* is most likely calculated according to formula $S^* = \sqrt{3}VI$. The power metering implemented by the Fluke 434 proved to have remarkable failures in multiple occasions, most evidently when dealing with unsymmetric three-phase or single-phasing bipolar loads. In these cases significant variation is observable, depending on if the Fluke instrument was preset to TN or IT-mode. Its very important to bear in mind that it is reasonable to expect correct operation by the Fluke 434 **only** when its being properly configured. During initiation and configuration the instrument offers a myriad of optional circuit arrangements, spanning from three to single-phase systems, various alternations of TN and IT-wiring etc. Retrospective it must be concluded that Fluke 434 Power Quality Analyzer was not operated correctly. The power acquisition capabilities was not fully exploited, as it was slavishly alternated between only two out of totally twelve different available measuring methods.

The consequence is that power measurements in certain experiments have questionable validity, this apply particularly for reactive power Q^*. The active power is fully valid because its always computed as the summed contribution from all three phases $P^* = P_A^* + P_B^* + P_C^*$. Not even the CPT in three-phase mode was able to correctly decode the power and current flow under single-phasing network conditions. Any experienced technician or engineer would in these special occasions reconfigure the Fluke 434 instrument to obtain enhanced power readings.

3.15 Summary

This entire study of the conservative power theory is fully based on ***qualitative analysis***, and must be evaluated thereafter. Any statements and conclusions made should be further consolidated analytically for ***quantitative confirmation***.
For convenience this section summarizes all observations regarding CPT-variables made throughout the chapter. Results are presented in the following pages in table format.

Table 3.10 – *Summarizing experimental results.*

$i_a^b(t)$ *Balanced active currents*

- Always detected exclusively in the presence of active power $P = \|u\|^2 \cdot \|i_a^b\|^2$.
- Fully reproduce current $i_a^b(t) = i(t)$ drawn by symmetric pure R-loads. This applies independently of voltage regime, voltage reference and circuit-topology.
- Adopts symmetric qualities from voltage $u(t)$ independently of load characteristics. Consequently $i_a^b(t)$ may appear unbalanced despite its name suggest differently, depending solely on the negative and zero sequence content in voltage.
- Also adopt entire frequency spectrum from load bus voltage $u(t)$ irrespective of load type and voltage reference. The fact that $i_a^b(t)$ inherit both symmetric and harmonic characteristics from respective voltage, resemble the *Fryze*-currents.
- Major part of current drawn by three-phase diode rectifiers is credited as $i_a^b(t)$. Dealing with thyristor rectifiers the appearance of $i_a^b(t)$ depends on firing angle α_{th}. These observations appropriately comply with the establish power theory, and can be argued by electro-physical means.
- Currents $i_a^b(t)$ are always anti-phased ($\varphi_1 = 180°$) in respect to voltage $u(t)$ for a source delivering active power P. Dealing with loads draining active power P, balanced active currents $i_a^b(t)$ always align with their respective voltages ($\varphi_1 = 0°$).

$i_a^u(t)$ *Unbalanced active currents*

- Always detected exclusively in the presence of unbalanced active power $N_a = \|u\|^2 \cdot \|i_a^u\|^2$.
- Fully accounts for negative sequence currents induced by unsymmetric floating R-loads. Likewise $i_a^u(t)$ fully reproduce negative and zero sequence current components generated by unsymmetric grounded R-loads. This yields irrespective of voltage regime.
- Adopts harmonic content from load bus voltage $u(t)$, similar to balanced active currents.
- The presence of unbalanced active currents generally induce 2nd order harmonic oscillation in instantaneous real power $p(t)$, similar to unbalanced voltages.
- Non-existing unbalanced active current detected in open-running phase during single-phasing R-loads. The only obvious instance were the CPT-interpretation clearly fails. This comes as a result of attempting to running the algorithm in three-phase mode, while the actual load is a single-phase circuitry.
- Surprisingly detected in context of floating unsymmetric L-loads. The hypothesis is that KCL is satisfied when two out of three line currents become independent, while the third line current becomes dependent. The independent currents notably tend to deviate from the $\varphi_1 = 90°$ phase shift usually expected from inductive loads. Unbalanced active currents $i_a^u(t)$ are therefore detected specifically in those phases only where this quadrature phase shift is violated.
- When an unsymmetric L-load is grounded, all three line currents lock into the familiar quadrature phase relation with respective voltage. Consequently $i_a^u(t)$ disappear for grounded L-loads. This phenomena should be further validated through analytical analysis.
- Notably two out of three line currents always align in anti-phase with respective voltage ($\varphi_1 = 180°$), while the third line current always align in-phase with its respective voltage $\varphi_1 = 0°$. This yields irrespective of floating or grounded loads. Opposite behavior were encountered in experiments 34, 46, 51, 61 and 86.

continued on next page . . .

... continued from previous page

$i_r^b(t)$ ***Balanced reactive currents***

- Always detected exclusively in the presence of reactive power $Q = \|u\|^2 \cdot \|i_r^b\|^2$.
- Fully reproduce currents $i_r^b(t) = i(t)$ drawn by symmetric pure L-loads. This applies independently of voltage regime, voltage reference and circuit-topology.
- Adopts symmetric qualities from load bus voltage $u(t)$ independently of load characteristics. Consequently $i_r^b(t)$ may appear unbalanced despite its name suggest differently, depending solely on the negative and zero sequence content in voltage.
- Inherit harmonic content from voltage homo-integral $\widehat{u}(t)$. Balanced reactive currents $i_r^b(t)$ will therefore always render close to a 50 Hz fundamental sinewave.
- Balanced reactive currents retain their importance in context of bipolar loads. Dealing with unlinear loads the CPT generally seem to put aside $i_r^b(t)$ in favor of void currents $i_v(t)$. The exception is thyristor converters where $i_r^b(t)$ reflect the actual phase shifting caused by delayed commutation, $\varphi_1 \approx \alpha_{th}$.
- Ideal as a current reference for reactive power compensating units *(APFs)*, in both sinusoidal and non-sinusoidal voltage regimes.
- Always appear in a fixed quadrature phase relation with respect to voltage $u(t)$. For a reactive power source $i_r^b(t)$ lead voltage by $\varphi_1 = 90°$.
  Dealing with reactive power loads, balanced reactive currents lag respective voltages by $\varphi_1 = -90°$.

$i_r^u(t)$ ***Unbalanced reactive currents***

- Always detected exclusively in the presence of unbalanced reactive power $N_q = \|u\|^2 \cdot \|i_r^u\|^2$.
- Fully accounts for negative sequence currents induced by unsymmetric floating L-loads. Likewise $i_r^u(t)$ reproduce negative and zero sequence current components generated by unsymmetric grounded L-loads. This yields irrespective of voltage regime.
- Inherit harmonic content from voltage homo-integral $\widehat{u}(t)$, meaning that any possible unsymmetric susceptance at higher frequencies are neglected.
- The presence of unbalanced reactive currents induce 2nd order harmonic oscillation in instantaneous imaginary power $q(t)$, similar to unbalanced voltages.
- Non-existing unbalanced reactive currents detected in open-running phase during single-phasing L-loads. The only obvious instance were the CPT-interpretation clearly fails. This comes as a result of attempting to run the algorithm in three-phase mode, while the actual load is a single-phase circuitry.
- Surprisingly detected in context of floating unsymmetric R-loads. The hypothesis is that KCL is satisfied when two out of three line currents become independent, while the third line current becomes dependent. The independent currents notably tend to deviate from the $\varphi_1 = 0°$ phase shift usually expected from resistive loads. Unbalanced reactive currents $i_r^u(t)$ are consequently detected specifically in those phases only where this aligning phase relation is violated.
- When an unsymmetric R-load is grounded, all three line currents lock into the familiar aligned phase shift relation with respective voltage. Consequently $i_r^u(t)$ disappear for grounded R-loads. This phenomena is recommended for further validation through analytical analysis.
- Hypothetically in case of unsymmetric loads where $i_r^u(t)$ are detected, true reactive compensation *(making line currents aligned with voltage)* can only be accomplished by compensating both balanced and unbalanced reactive currents simultaneously.
- Unbalanced reactive currents always appear in a quadrature ($\varphi_1 = \pm 90°$) phase shift relation in respect to load bus voltage $u(t)$.

continued on next page ...

... *continued from previous page*

$i_\upsilon(t)$ *Void currents*

- Always detected exclusively in the presence of distortion power $D = \|u\|^2 \cdot \|i_\upsilon\|^2$.
- In case of sinusoidal voltage conditions, the void currents prove to be a very effective method for extraction of current harmonics induced by unlinear loads. Consequently $i_\upsilon(t)$ are a powerful aid for neutralizing current harmonics and related fluctuation of instantaneous real and imaginary power flow.
- Produce high-order oscillations in instantaneous real power $p(t)$ and imaginary power $q(t)$. Relative impact is usually less compared to voltage and current unbalance.
- Void currents are often detected in case of abnormalities in the CPT-algorithm input signals: i.e. superimposed contamination like DC or external noise. Even saturated voltage and current actuators may translate as void currents. These are phenomenas typically originated from the acquisition system.
- Surprisingly detected when dealing specifically with RL-loads energized by harmonic voltages. Further analytical analysis is recommended.
- Evaluation of void currents is generally more demanding in cases where both voltages and currents are distorted. A possible enhancement of the CPT-algorithm would be splitting the void current into generated and scattering parcels for clarity.

$p(t)$ *Instantaneous real power*

- Flows constant in case of balanced sinusoidal voltages and currents. Real power equals active power in this context $p(t) = P$, and become negative if the network element produces real power.
- Become equal to total instantaneous powerflow for pure R-loads exclusively. This applies irrespective of voltage regime and wiring-topology.
- Oscillate around a bias-value recognized as active power $\bar{p}(t) = P$. This strictly yield loads only as $\bar{p}(t)$ become negative when dealing with sources.
- Sensitive against harmonics in voltages and currents. High order harmonic powers are generated when either voltage or current are distorted:
  - Three-phase diode and thyristor rectifiers *(6-pulse bridge)* clearly induce 300 Hz power oscillation, which must origin from void currents *(active scattering currents)*.
  - Voltage harmonics induce 300 Hz oscillation when energizing bipolar loads. This is particularly evident for R-loads as the tendency is that, harmonics in balanced active currents translates into harmonics in real power $p(t)$.
- Sensitive against imbalance in voltages and currents, causing 100 Hz oscillation whenever fundamental voltage or current are unbalanced:
  - Oscillate whenever voltages are unbalanced non-regarding type of load. This is verified for symmetric and unsymmetric bipolars and unlinear loads.
  - Single-phasing bipolar loads *(yield both R and L-loads)* induce 100 Hz oscillation, irrespective of symmetric and harmonic voltage characteristics.
  - Unexpected 2nd order oscillation occur for unbalanced line currents containing no active currents *(scattering, balanced or unbalanced)*. Documented both for floating and grounded L-loads independently of voltage regime.
- Always oscillate in a quadrature phase relation with imaginary power $q(t)$. Phase relation become less evident when voltages or line currents are distorted.

continued on next page ...

... continued from previous page

$q(t)$ ***Instantaneous imaginary power***

- Becomes unidirectional in case of balanced sinusoidal voltages and currents. Imaginary power equals reactive power in this context $q(t) = Q$, and becomes negative if the network element produces imaginary power.
- Equal to total instantaneous powerflow for pure L-loads exclusively. This applies irrespective of voltage regime and wiring-topology.
- Oscillate around a bias-value recognized as reactive power $\bar{q}(t) = Q$. This strictly yield loads only as $\bar{q}(t)$ become negative when dealing with reactive sources.
- Imaginary power is equally sensitive towards current harmonics as found for real power $p(t)$, while less influenced by voltage harmonics:
  - Three-phase diode and thyristor rectifiers *(6-pulse bridge)* clearly induce 300 Hz power oscillation, which must origin from void currents *(reactive scattering currents)*.
  - Voltage harmonics have limited impact on $q(t)$ as the quantity is computed partly by the homo-integrated voltage. The only encountered exception is R-loads energized by harmonic voltages.
- Sensitive against imbalance in voltages and currents, inducing 100 Hz oscillation whenever fundamental voltage or current are unbalanced:
  - Oscillate when voltages are unbalanced non-regarding type of load. This is verified for symmetric and unsymmetric bipolars and unlinear loads.
  - Single-phasing bipolar loads *(yield both L and R-loads)* induce 100 Hz oscillation, irrespective of symmetric and harmonic voltage characteristics.
  - Unexpected 2nd order oscillation occur for unbalanced line currents containing no reactive currents *(scattering, balanced or unbalanced)*. Documented both for floating and grounded R-loads, independently of voltage regime.
- Always oscillate in a quadrature phase relation with real power $p(t)$. Phase relation become less evident when line currents are distorted.
- Unbalance in voltages and currents at the fundamental frequency, generally tend to have greater impact on instantaneous power flow, compared to harmonic pollution.

A ***Apparent power***

- According to Tables 3.1 to 3.9 apparent power A_{Sum} has been manually calculated as the norm of remaining subset of powers. The results coincide with A produced by the CPT-algorithm.
  Always summing up to 100 % suggests that proposed power terms are truly mutually orthogonal in all tested network scenarios.
- Orthogonal power decomposition also imply that CPT current decomposition is truly orthogonal, independent of voltage regime and load characteristics.
- Equals to measured and calculated traditional apparent power $A = S^* = S_{Sum}$ when dealing with symmetric bipolar loads, both in the sinusoidal and distorted voltage regimes.

P ***Active power***

- Always exclusively related to the appearance of balanced active currents $i_a^b(t)$. *See paragraph regarding $i_a^b(t)$ for conditional appearance.*
- Fully reproduce total powerflow for symmetric purely resistive loads ($P = A$). This applies independently of voltage regime, voltage reference and wiring-topology.

continued on next page ...

... continued from previous page

- Coincide with instantaneous real power ($P = p(t)$) when network elements drain real power, and both voltages and currents are balanced sinusoidal.
- Equals the average value of real power ($P = \bar{p}(t)$) only in case of true loads. Does not coincide $P \neq \bar{p}(t)$ when dealing with network elements generating real power. $p(t)$ is negative in these cases, while P is always computed as a positive quantity.
- Notably active power P always coincide with the classic definition of active power, irrespective of voltage regimes and types of load *(both bipolar and unlinear)*. Its therefore the **only** proposed CPT-variable that unambiguously comply with the classic power theory.
  This is in fact expected as active power always has a precise physical interpretation, thus its been universally adopted by all power theories.
- The fact that active power P coincides with the traditional definition (P^*) in all tested scenarios, suggests that it must be a conservative power quantity.

Q Reactive power

- Always detected exclusively in the presence of balanced reactive currents $i_r^b(t)$. *See paragraph regarding $i_r^b(t)$ for conditional appearance.*
- Fully recreate total powerflow for symmetric purely inductive loads ($Q = A$). This applies independently of voltage regime, voltage reference and wiring-topology.
- Coincide with instantaneous imaginary power ($Q = q(t)$) when network elements drain imaginary power, and both voltages and currents are balanced sinusoidal.
- Equals the average value of imaginary power ($Q = \bar{q}(t)$) only in case of reactive loads. Q is always computed as a positive quantity, meaning that when dealing with reactive power sources $Q \neq \bar{q}(t)$.
- The new discovery is that Q generally tend to have a less important part of the power mix when dealing with unlinear loads *(both sinusoidal and harmonic voltage regime)*. This is mainly because of the introduction of distortion power D.
- The variation between Q and Q^* is generally larger compared to P and P^*. Nonetheless the new and old interpretation of reactive power does in fact match very closely, both for symmetric and unsymmetric bipolars *(independently of voltage regime and wiring-topology)*. Exceptions are case 35, 40, 52, 54, 61 and 80.
- The fact that reactive power Q coincides with the traditional definition Q^* in most tested scenarios, suggests that it must be a conservative power quantity.
- For diode rectifiers the CPT attributes distortion power D rather than reactive power Q, while reactive power seem to partially retain its significance for thyristor converters. This is due to the physically delayed commutation inducing phase-shifting of line currents ($\varphi_1 \approx \alpha_{th}$) at the fundamental frequency. Results do not comply with fundamental thyristor theory, however more research is needed before stating any final conclusion.

N_a Unbalanced active power

- Always detected exclusively in the presence of unbalanced active currents $i_a^u(t)$. *See paragraph regarding $i_a^u(t)$ for conditional appearance.*
- Generated fully by negative sequence currents *(floating loads)*, in addition to zero sequence currents in case of grounded loads.
- Detected if three-phase diode and thyristor rectifiers are loaded by capacitative DC-load, and energized by unbalanced voltage.

continued on next page ...

... continued from previous page

- When dealing with floating unsymmetric loads the N_a become numerically equal to N_q. This applies independently of load type *(both bipolar and unlinear)*.
- Hypothetically in combinations of zero sequence voltages and currents, would N_a become equal to $\bar{p}_0$ known from the pq-theory? This is something that deserves further investigation.

N_q *Unbalanced reactive power*

- Always detected exclusively in appearance of unbalanced reactive currents $\boldsymbol{i}_r^u(t)$. *See paragraph regarding $\boldsymbol{i}_r^u(t)$ for conditional appearance.*
- Generated fully by negative sequence currents *(floating loads)*, in addition to zero sequence currents in case of grounded loads.
- Uncertain why the N_q and N_a are credited equally for floating unsymmetric loads. Analytical analysis would give further answers.
- In scenarios involving unsymmetric loads *(both bipolar and unlinear)*, N_q and N_a provides orthogonal power decomposition.
- Detected if three-phase diode and thyristor rectifiers are loaded by capacitative DC-load, and energized by unbalanced voltage.

D *Distortion power*

- Always detected exclusively along with the presence of void currents $\boldsymbol{i}_v(t)$. *See paragraph regarding $\boldsymbol{i}_v(t)$ for conditional appearance.*
- Difficult determining the precise origin of D in certain cases of harmonic voltages. Splitting into D_v and D_i is advisable in future work.
- Detected under sinusoidal voltage conditions for certain bipolar loads *(single-phasing, D and YG-configurations)*. Further analytical investigation is recommended.
- Energizing RL-loads under harmonic voltage regimes leads to notable detection of D. Analytical analysis would probably give deeper knowledge.
- Takes large share of the power mix for unlinear loads, partially replacing what presumably has been interpreted as reactive power Q^* in the classic power theories.
- In scenarios involving non-linear loads D provides orthogonal power decomposition, by including power transport from high order current harmonics.
- May origin exclusively by characteristics related to the voltage/current probes and acquisition system, rather than the power load itself: i.e. saturated actuators, superimposed external noise and DC-offset.

λ *Power factor*

- The new definition of power factor is not as straight forward relating to as the classic interpretation. The traditional $\cos\varphi$ gives quick and intuitive information regarding the network utilization. However λ involve six variables *(compared to three)*, making the significance of λ abstracted.
- Comparing λ and $\cos\varphi$ they are practically identical in nearly all tested scenarios. Thus λ is the only CPT quantity second to active power P that coincides with the classic definition. This is an unexpected discovery which needs further analysis.
- According to aforementioned arguments λ provides limited information regarding power quality, and should be complemented by other quality measures.

3.16 Brief evaluation of the Speedgoat system

As currently being the first and only at NTNU with hands-on knowledge of using the xPC Target Turnkey, it is here presented a brief evaluation and further recommendations based on the gained user experience.

Having a control system developed and tested in a Simulink simulation environment, which then is converted into a real-time algorithm, is an attractive engineering concept. But transforming a Simulink algorithm from simulation to real-time application will most likely be a disappointing affair, if not the proper preparations are made prior to the transition. Because of the inherent limitations in the Speedgoat TM hardware, model optimization is an absolute premise, or even the simplest control application will consume most of the hardware capacity.

Right after completing three months of hardware assembly, the following process of exploring the xPC Target Turnkey was characterized by serious problems; the main issue was overloaded TCPU which often led to several seconds response time, or in most attempts application shut down. For optimal performance the designer must do a careful tradeoff between functionality and performance requirements. There are several design aspects that need optimization as will be discussed in the following.

3.16.1 Discrete time-domain

The Speedgoat real-time TM is like any other microprocessor-based devices, carrying out instructions (the application C/C++ code) in a sample-based execution method. Thus all internal signals within the Simulink model exist as discrete time-domain variables, and not continuous states which students normally associate with a Simulink workflow. When eventually realizing this it was undoubtedly the most important milestone in this entire thesis work. It ultimately made it possible to implement the conservative power theory in real experiments. Moreover same design philosophy was applied with great success when modeling shunt compensation, as will be demonstrated in next chapter.

Usually when students are using Simulink to model and demonstrate some sort of power electronics concept or the control related to it, the model is most likely built up from standard blocks and standard parametrized. The problem is that its a continuous system, thus little practical for real-time applications. This issue is relatively easily solved by some minor adjustments which in the end prepares the Simulink model to operate as a discrete system.

The process of discretization is completed in three steps, and is initiated by defining global settings which effectively forces the application to behave as a discrete system. Relevant parameters are found by choosing *"Simulation"* in the main menu, then select *"Configuration Parameters"*. Under the pane *"Solver options"* the *"Type"* must be set to *"Fixed-step"*, and lastly *"Solver"* should be *"discrete(no continuous states)"*.

Next important adjustment is to select a base sample time T_s, or equivalently base sampling frequency $f_s = T_s^{-1}$. The sampling interval T_s is probably the most influential global parameter, which dramatically affect how much processing power that is allocated. Setting T_s to low will be in the risk of rapidly overloading the TCPU within the first sampling intervals. There are no quick rules for determining an optimal base sampling frequency, as it among others depends greatly on how good the model design is optimized for discrete time-domain, and the number of physical input and output channels utilized by the application.

The probably best method is to let the TM tune the fundamental sampling frequency automatically. After completed the above discretization procedure and uploaded the application, issuing *xpcbench('model_name')* in the MATLAB command window, the TM will perform a series of consecutive tests where T_s is gradually reduced towards TCPU overloading. This method which only takes few minutes, is much more effective than attempting to manually dial the optimal sample time. The practical sampling frequency is usually a little lower than what is found in the xPC benchmark test.

In the third step it will be good practice to split the real-time application into subdomains, dictated by respective sampling rate requirements. Many control applications do not require relatively high sampling rate, so that running these facilities on high sampling frequency, would only be a pointless waste of TCPU resources. Running the entire application on minimum base sampling interval T_s predetermined by the benchmarking, is equivalent to running the TCPU close to its limit. There is consequently very little resource *headroom*, and the application will most likely have several seconds response time. In the following some practical examples are given, they should not be regarded as absolute requirements, but as guidelines based on what worked well in this project.

Higher sampling frequencies naturally require larger share of processing and memory resources. Speed critical parts are processor intensive on the expense of compromising the potential size and functionality of the overall application. Low-speed functions frees up processor resources, and thus make possible having more content and functionality to be implemented by the application.

The model content must be set to operate at discrete time steps simply by setting all blocks to a fixed sample time, where the ratio to the base sample time is normally N orders of magnitude $T = T_s \cdot 10^N$. Many Simulink blocks are available both as a continuous and discrete time-domain version. Using blocks tailored for discrete systems is vitally important in real-time applications, as they are much more TCPU resource efficient. If a certain block cannot be discretized, it is beneficial resorting to customized blocks handwritten in an appropriate programming language.

- **Low-sample rate applications**
  Functions that typically implement interaction between operator and the control system, often referred to as human-machine interface *(HMI)*. This can also be various types of external physical devices (switches, buttons, rotary encoders, auxiliary status signals from contactors etc.) sending control signals to the analog and digital inputs (IO106 and IO203), which then triggers an event or manipulate the real-time algorithm in some way. Correspondingly this category include low-speed connections from the analog and digital outputs (IO110 and IO203). For instance signals controlling various electromechanical actuators (relays, contractors etc.), or signals intended as feedback to the user (LEDs, lights etc.) reporting status of important system variables. For these functions an update rate of $T_s = 500.0 - 100.0\,ms \sim f_s = 2.0 - 10.0\,Hz$ was found to work satisfactory.

Also the refresh rate of target and host scopes have an appreciable impact on CPU headroom, and may vary depending on what signal to be displayed. The human visual system has a perception of frame rates up to grossly $f_{rate} \approx 60.0\,Hz$, which grossly limit the relevant refresh rate of target and host scopes. Nonetheless the signal acquisition and visualization capabilities of a virtual instrument, are far less compared to high-end digital oscilloscopes. It was found that the Speedgoat system must always be supplemented by a digital oscilloscope, if there is needed to study for instance fast-transient PWM signals.

- **Mid-sample rate applications**
  Functions providing mid-range sampling rate introduces applications associated to electric power engineering. Required sampling frequency may vary significantly depending on the intended purpose. Many applications are related to measurement and computation of variables specifically at the fundamental network frequency, where a sampling interval of $T_s = 200.0\,\mu s \sim f_s = 5.0\,kHz$ is sufficient. Nonetheless dealing with passive and particularly active power electronic devices, these possess fast transient voltage and current characteristics. Algorithms working in this frequency range require highest possible sampling rate to ensure satisfactory resolution of HF components. In this project the CPT-algorithm was run at sampling rate $T_s = 100.0\,\mu s \sim f_s = 10.0\,kHz$, making it possible to detect current harmonics as demonstrated in **Figure 3.41**. Very demanding applications such as active harmonic filtering, are only possible with low-latency algorithms, but on the expense of loading the TCPU. It was found that running extensive algorithms at this sample rate could easily overload the TCPU.

- **High-sample applications**
  Applications that require highest sampling rate are those related to generation of switching functions for power electronic devices. This could for instance be open-loop control *(voltage controlled converters)*, and closed-loop regulation *(current controlled converters)*. These are processes generally characterized by very fast dynamics, depending on the type of power electronic device in question (thyristors, GTOs, IGBTs or MOSFETs). Insulated gate bipolar transistors are the common choice for VSCs, which typically operate at switching frequency $f_{sw} \approx 10.0 - 25.0\,kHz$. Part of the Simulink model that takes care of modulation should operate at sampling rate $f_s = 500.0\,kHz$, which is regarded as the minimum limit. These strict requirements can only be met by field-programmable gate array devices *(FPGAs)*, working at sampling frequencies in the megahertz range. Therefore the latency is extremely low and speed of FPGAs typically approximates an analog circuit. Despite the highly specialized architecture of an FPGA, its in fact capable to implement a variety of both logical and mathematical applications. The difference from DSPs and regular real-time computer systems is primarily the speed advantage. Traditionally FPGAs are also differentiated from DSPs in terms of programming, as this is accomplished using a low-level hardware description language *(HDL)* which requires highly skilled personnel. Fortunately MathWorks provides a software package HDL Coder™which is based on principles similar to xPC Target. The HDL Coder is a tool offering rapid prototyping of applications

implemented in the FPGA-domain, without having to actually handwrite the code manually. Based on a Simulink model the designer can focus on functionality and optimizing the performance, while the HDL Coder compiles a FPGA bistream which is then transferred to the FPGA chip.

3.16.2 Choosing data format

Selection of datatypes is an important Simulink feature that has come into light after the experiments were completed. In computer science a signal or variable can be presented in a variety of data formats, the most common main types are *integers, fixed-point numbers, floating-point numbers, characters and boolean.* Each format has specific advantages and disadvantages in terms of accuracy, dynamic range, memory and processing requirements. In the same way as fine-tuning sampling frequency can greatly improve the overall performance of the TM, assigning signals and blocks to a proper datatype may boost the algorithmic efficiency in a dramatical manner. If a Simulink algorithm is intended for code generation to a real-time applications, optimizing datatypes must be considered to be among the most important aspects during the design process. In this project the entire application was using *double-precision floating-point (double)* numbers, which is the native format for MATLAB and Simulink. As MATLAB is an high-end mathematical tool for research and engineering, it relies on the 64-bit double format as this offers best floating-point accuracy of approximately 16 significant decimals. When using double-precision the MathWorks software have a dynamic range[1] from $min = 2.2251 \cdot 10^{-308}$ to $max = 1.7977 \cdot 10^{308}$. Even if the Speedgoat TCPU architecture is capable of 64-bit operations the disadvantage is obviously handling of large data quantities, on the expense of resource efficiency. Double-precision provides accuracy and numerical range for special mathematical applications, which are most likely far more than what is required by real-time experiments, especially in electric power engineering where extreme accuracy is not necessarily the most critical performance criteria.

The *single-precision floating number (single)* format is a 32-bit datatype providing approximately 7 significant decimals. The dynamic range spans $min = 1.1755 \cdot 10^{-38}$ to $max = 3.4028 \cdot 10^{38}$ which is probably satisfactory for electric power engineering. Implementing the real-time algorithm with single-precision effectively reduces the data quantity to half of what is used in double-precision, with consequent speed improvement. Moreover most of the installed Speedgoat I/O-subsystems operate at *half-precision,* meaning that input signals from LEM voltage and current transducers are A/D-converted by the IO106 analog input *(PMC66-16AI64SSA/C)* at "only" 16-bit resolution. Same yield for IO110 analog output *(TPMC553),* and IO203 digital I/O *(TPMC681).* Only the IO311 FPGA module *(PMC-DX2001)* operate directly at 32-bitstream resolution. Notably all peripheral I/O-cards are connected to the cPCI-bus, which run at 32-bit resolution. If there is during the design process confirmed that internal variables will never exceed the dynamic range offered by single-precision, this appear to be a much more efficient data format. As aforementioned there are alternative formats optimal for other purposes, for instance boolean for pulse-width-modulation, and using fixed point instead of floating point data format. These are aspects that will be extensively tested

---

[1] Provided by MATLAB functions **realmin** and **realmax**.

in the near future, and hopefully demonstrate improvements in the speed performance. One of the advantages using Simulink as prototyping environment, is the possibility to test and verify optimal selection of data formats and sampling frequencies, prior to application deployment.

3.16.3 Selecting number of I/O-channels

Another design aspect which is as equally important as discretizing the real-time application, is the careful selection of I/O-channels which interface the Simulink model with the real physical world. The Speedgoat CPU module *(EKF System CCM-62RD-BOOGIE)* is expanded by four peripheral external I/O-subsystems, providing 192 individual digital or analog inputs and outputs. The vast number of available channels testify the great potential and flexibility offered by the Speedgoat system. The I/O-facilities suggest that the TM can theoretically implement relatively large and sophisticated real-time control systems. Unfortunately the disadvantage is that a certain inherent latency is introduced for each channel added. The total accumulated latency T_{delay} can seriously compromise the practical maximum achievable base sampling frequency f_s, or in the worst case overload the TCPU.

Initially as the latency was not mentioned in any of the Speedgoat documentation, there was not any awareness of this issue when constructing the Simulink model. Thus the subsystem driver blocks were configured to activate all 192 channels, thought only 25.0 % was actually transferring signals between the application and peripheral I/O-subsystems. The real-time implementation of the CPT was firstly permitted after Simulink model discretization, however maximum base sampling frequency was only $f_s = 1.0\,kHz$ as nearly all TCPU resources was accommodated to manage the I/O-connectivity. Resulting input signals were consequently high-pass filtered similar to experiment 62 (**Figure A.13**). At the end of the project period the Speedgoat company was confronted with this rather disappointing performance. After examined the algorithm implementing the virtual instrument, the Speedgoat support team recommended to deactivate all I/O-channels that were not actually used, which made the final milestone moving the base sampling frequency up to $f_s = 12.0\,kHz$.

The Speedgoat I/O-subsystems are interconnected to the CPU module via the cPCI-bus, and apparently the inherent latency is mainly related to this data transmission process. In their reply the Speedgoat support team supplied a paper describing how the latency in each I/O-subsystem can be precisely calculated; writing input data to the cPCI-bus adds $T_{write} = 1.4\,\mu s$ delay, while the read process has an execution time of $T_{read} = 0.2\,\mu s$. And lastly common to all subsystems is the latency related to Simulink S-Functions[2] as the function needs an overhead of $T_{SFnc} = 1.0\,\mu s$. As an example it will be calculated the total delay T_{delay} assorted exclusively to I/O-subsystems, when half the channel capacity of each system is engaged. Formulas are given by Speedgoat.

- **Speedgoat IO106**
  64 single-ended A/D analog inputs. Activating $N = 32$ input channels give:
  - $T_{IO106} = 7.2 + 1.4 \cdot \frac{N}{2} = 7.2 + 1.4 \cdot \frac{32}{2} = \underline{29.6\,\mu s}$

---

[2] The S-Function is a Simulink block described in code MATLAB, Fortran, C or C++. Among others used to establish connection between external physical devices and Simulink environment *(driver blocks)*.

- **Speedgoat IO110**
  32 D/A analog outputs. Utilizing $N = 16$ output channels add:
  - $T_{IO110} = 1.0 + 0.2 \cdot N = 1.0 + 0.2 \cdot 16 = \underline{4.2\,\mu s}$
- **Speedgoat IO203**
  64 bidirectional TTL digital I/O-channels. Channel independet latency:
  - $T_{IO203} = \underline{2.4\,\mu s}$
- **Speedgoat IO311**
  32 TTL selectable FPGA and digital I/O. Utilizing $N = 16$ channels give:
  - $T_{IO311} = 8.2 + 2.0 \cdot N = 8.2 + 2.0 \cdot 16 = \underline{40.2\,\mu s}$

In total the latency originated from external I/O-modules increases the minimum achievable base sample time by $T_{delay} = 76.4\,\mu s$, or equivalently reduces maximum base sampling frequency by approximately $f \approx 13.0\,kHz$, which is a considerable reduction in the sampling frequency. Notably this must be regarded as a sort of worst-case scenario, as most of the loss of sampling rate origins from IO106 and IO311, and can be greatly reduced in more practical scenarios.

Using ten analog input channels would probably cover most needs for voltage and current measurements. The significant latency generated by the IO311 is because the PWM driver block allows the user to dynamically update up to ten parameters on the FPGA during application runtime. However strictly speaking it is only needed to feed the driver block with the reference signal $v_{ref}(t)$ *(A and B-compare count)*. There should also be possible to alter VSI switching frequency f_{sw} *(period-compare count)*, so that in a stripped down version the total hardware related latency is reduced to half $T_{delay} \approx 38.0\,\mu s$. Nonetheless its somewhat contradictory offering 192 channels when they take up majority of the processing power, making it impossible to implement an algorithm of such size and complexity that can utilize all channels. This can only indicate that the performance will be immensely improved through proper algorithm optimization.

3.16.4 Required user skills

Saying that any average MATLAB/Simulink user will manage to get the xPC Target Turnkey up and running easily, would be a serious overstatement. The Speedgoat real-time target machine is placed under the regular performance restrictions common to all CPU-based rapid prototyping systems. To exploit the full potential the user will first and foremost need in-depth expertise on all the finesses associated to MATLAB and Simulink. Most students studying electric power engineering often resort to other modeling software *(PSCAD® or PSIM™etc.)*, rather then relying on the Simulink environment, as these are often considered more easy to utilize. The MATLAB/Simulink engine comprise a myriad of parameter adjustments, which typically need fine-tuning in order to produce decent simulation results.

This can be argued as both the weak and strong side of the Simulink platform; it provides comprehensiveness and versatility so that it can be employed in a wide range of technical fields, while simultaneously the performance, accuracy and results are in the control of the algorithm designer. The downside however is that in order to fully master the MATLAB and Simulink environment, there is a steep learning curve and all the effort tend to move the focus away from power electronics. In other more specialized software packages like PSIM or PSCAD, all these finesses are hidden from the user under the user interface, enabling the user to focus entirely on the electric power engineering.

When doing rapid prototyping with xPC Target Turnkey this comprehensiveness become the key element to success, and the possibilities are therefore highly constricted by the users experience with MATLAB and Simulink. Additionally NTNU holds license of totally 52 *MATLAB and Simulink Toolboxes*[3] which to various purposes can be employed in order to optimize the real-time application:

- **DSP System Toolbox™**
  Provides algorithms and tools for designing signal processing systems deployed in rapid prototyping and embedded systems. Includes design methods for specialized FIR and IIR filters, FFTs, multirate processing and other common DSP functionalities. Filters implemented using computationally efficient architectures. Tools for signal generation, spectral analysis, and interactive visualization offers analysis of system behavior and performance.

- **HDL Coder™**
  Generates portable, synthesizable VHDL® and Verilog® code from MATLAB functions, Simulink models, and Stateflow charts. Provides a workflow advisor that automates the programming of Xilinx® and Altera® FPGAs. Offers control of HDL architecture and implementation, highlight critical paths, and generate hardware resource utilization estimates. Provides traceability between the Simulink model and the generated HDL code, simplifying code verification.

- **Parallel Computing Toolbox™**
  Make possible to solve computationally and data-intensive tasks using multicore processors, GPUs, and computer clusters. High-level constructs, parallel for-loops, special array types, and parallelized numerical algorithms can be turned into paralleled applications for speed enhancements.

- **Signal Processing Toolbox™**
  Provides industry-standard algorithms for analog and digital signal processing (DSP). The toolbox can visualize signals in time and frequency domains, compute FFTs for spectral analysis, design FIR and IIR filters, and implement convolution, modulation, resampling, or other signal processing techniques.

- **SimPowerSystems™**
  No introduction needed, contains various useful discretized control blocks.

- **Simulink Fixed Point™**
  By using *Fixed-Point Advisor* the Simulink control and signal processing algorithm is stepwise converted from a floating-point to fixed-point model. Enables specification of fixed-point data attributes like word length and scaling for signals and parameters. Then observing the effects of limited range and precision through

---

[3] Toolbox descriptions quoted from `http://www.mathworks.com/products`

bit-true simulations. Additional tools can be employed for recommending data types and scaling.

- **Simulink Coder™**
  Generates and executes C and C++ code from Simulink models, Stateflow charts, and MATLAB functions. The source code can be used for real-time applications like rapid prototyping and hardware-in-the-loop testing. Generated code can be monitored and tuned in Simulink or run and altered with the code outside the MATLAB and Simulink environment.

- **Stateflow®**
  Offers a design environment for developing state charts and flow graphs. Stateflow provides the language elements required to describe complex logic in a natural, readable, and understandable form. It facilitate an efficient environment for designing embedded systems that contain control, supervisory, and mode logic like programmable logic controllers *(PLCs)*.

Out of these can *Simulink Fixed Point, Stateflow, Parallel Computing* and *HDL Coder* be immediately identified as interesting tools that will be further investigated. Because of the multidisciplinary approach users of rapid prototyping systems need to work up an extensive knowledge from several technical fields such as computer science, programming in various languages, digital signal processing theory, and be acquainted with DSP and FPGA technology. Having previous experience and knowledge with DSP and FPGA programming will definitely be a great advantage.

Evidently the downside for those who are not well familiar with these engineering disciplines, there will take extra time getting "into the game". Therefore the usage is best suited for PhD students as the technical level and time required to make the system work, exceed to scope of a MSc thesis project. In time when the department has gained more experience, the xPC Target Turnkey solution may also be well fitted to be used on a MSc level. Model-based rapid prototyping is becoming increasingly important in the industry, so that students are benefited from familiarizing with this R&D principle. This thesis work has nearly scratched the surface of what is possible to achieve with the Speedgoat system, and in a long-term perspective it can potentially boost the experimental research and productivity at the department. The next natural step is through extensive testing to formulate a set of design rules, which will empower future users to implement flexible and high-performance applications.

3.16.5 Hardware solution

The Speedgoat hardware is assembled from the best state-of-the-art components available, its rugged and reliable and therefore a pleasure to use. The performance and application design procedure is most likely very similar to what to expect from equipment by other popular brands like Opal-RT, dSPace and National Instruments. In time when getting more experienced with the usage of MATLAB/Simulink and their associated *Toolboxes*, its expected to see improvements in the performance. However based on the experience in this project, there are proposed three possible hardware improvements:

- **Central processing unit**
  The EKF System CPU-module is founded on an Intel® Core™2 Duo 2.26 *GHz*, 6MB level 2 cache processor, which is the hardware component executing the C/C++ code uploaded from the Host machine. The processor supports 64-bit architecture and contain two CPU cores. The 64-bit data format as previously discussed offers highest numeric resolution and range, but not necessarily better speed performance. The multicore feature however can be greatly beneficial in real-time applications, by designing the algorithm for multicore support this ensure to fully utilize the CPU processing power, thought multicore operation was not employed in this thesis work. The Intel Core 2 Duo was introduced back in 2008 and according to benchmark tests performed by Speedgoat, the 2.26 *GHz* target machines are rated midway on the scale in terms of speed. So the onboard CPU provide a decent but not impressive clock rate by todays standards, clock rates of 2.8 *GHz* or more can be seen even in laptops.
  In May 2012 Speedgoat announced that their products support the Intel® Core™ i7 3.4 *GHz* Quad Core processor. The high clock rate and the possibility to partitionate the algorithm into four domains, all executed in parallel by their own dedicated CPU core, would greatly improve the overall TM performance. However there is reason to believe that a CPU-replacement is most likely an expensive upgrade.

- **I/O-connectivity**
  The Speedgoat hardware is provided as a general purpose technical solution, for a wide range of scientific and engineering disciplines *(aerospace, automotive, communications, defense and medical science)*. Correspondingly in this project work the connectivity is considered as being the definitive drawback, compared to alternative solutions offered by for instance dSpace and National Instruments. While competing brands have specialized on hardware that are *"plug-and-play"* for fast and easy setup, the Speedgoat only provide multisignal I/O-cables and simple terminal boards. Consequently the customer will have to devise an own concept in terms of connectivity between the target machine and the physical world. Throughout this entire project there was always struggle interfacing the Speedgoat real-time target machine with other parts of the experimental setup, especially the acquisition system. Despite these interfacing systems are fairly simple in design and functionality, there was spent a great effort firstly to assembling, then later becoming a repeating source of error. At the time there was neither knowledge or resources to build a proper acquisition system. In the future there should be

decided to either purchase or design and construct a robust acquisition system, as this will save project time, eliminate signal errors and provide safety for the user and protection of the expensive Speedgoat hardware.

- **Ultra high-speed applications**
  In the next chapter it will be demonstrated through simulations what to expect from NTNUs Speedgoat target machine, when imitating an hysteresis current controller with the same sampling frequency f_s achieved by the TM. The result was partly confirmed experimentally and concludes that closed-loop current control applications and PWM in general, cannot be implemented in the regular CPU-based part of the algorithm. Even with the best processor available and a fully optimized algorithm, the system will be to slow for purposes like high-performance active power filters. The modulator and the loop measuring the compensator current must operate at sampling frequency of minimum $f_s = 500.0\ kHz$, in order to guarantee correct tracking of high-order current harmonics.
  For very fast control loops the Speedgoat company offers low latency FPGA-based analog-to-digital I/O-subsystems. The Speedgoat IO235 module is based on an FPGA chip from the Xilinx® Virtex™ 4 family. Expanding the real-time target machine with Speedgoat IO235 should be prioritized before any eventual CPU upgrade.

Chapter 4

Shunt Compensation

Introduction

The main purpose of this thesis work was to experimentally validate harmonic and reactive shunt compensation, using the conservative power theory as current reference generator for the active power filter. Unfortunately it became clear during the initial tests, how the Speedgoat real-time target machine cannot provide the sampling rate required to implement an active power filter.

Supported by computer simulations this last chapter will be dedicated to further demonstrate why the experimental work failed, and subsequently what is required in terms of hardware performance to make future experiments viable. Firstly there will be presented selected modeled scenarios of shunt compensation to exemplify what results to expect, in case of successful experiments.

4.1 Harmonic and reactive compensation

4.1.1 Active power filters

The active power filter *(APF)* can be addressed as two main types depending on the structure. The series-connected APF is employed for active voltage compensation *(unbalance, flickr, distortion, sag/swell, interruption or level regulation)*. The counterpart version is the shunt-connected APF utilized for active current compensation *(current harmonics, load unsymmetry and reactive power compensation)*. There are also other options like hybrid APFs or the unified power flow controller *(UPFC)*, which is basically a combined series and shunt active power filter. This thesis only treat the shunt APF, as the focus is towards shunt compensation exclusively.

The shunt APF is essentially a current-controlled DC/AC converter, intended to operate as a controllable current source. There are two available topologies differentiated by the DC-link layout. The current source inverter *(CSI)* relies on an inductive energy buffer L_{DC}, while the voltage source inverter *(VSI)* is based on a capacitor C_{DC} energy storing device in the DC-link. The second design utilizing a polarized capacitor is probably the most commercialized solution in todays APFs, as its the most cost-effective.

Component parameter values, ratings and other specific performance requirements, depend on the assigned compensation target of the APF. Reactive power compensation at the fundamental frequency can be considered demanding in terms of handling of large power and current levels, giving larger and more expensive components. Harmonic compensation on the other hand requires faster and more accurate performance, compared to reactive power compensation applications. Current harmonics are less demanding in terms of current and power handling capability, allowing the APF hardware to be compact and less expensive. Harmonic compensation is considered as the main application for APFs, while reactive power compensation is regarded as secondary functionality. Reactive power compensation has historically been implemented by various other technologies such as passive filter, static var compensator *(SVC)* and thyristor switched capacitor *(TSC)*.[A8,A9,A18] However these methods are associated with detrimental effects when utilized under non-ideal voltage conditions. H.Akagi et al.[B21] have demonstrated with the *pq*-theory that sophisticated high-performance APFs can be employed with great success under harsh voltage conditions, which more primitive technologies cannot tackle. Also by combining APFs with SVCs or TSCs this can form an optimal cost-effective option, and due to the orthogonal properties of the CPT this combination of technical solutions have become even more attractive.

The voltage source inverter used here (**Figure 4.1**) is based on the conventional 2-level design, although VSIs can be expanded to multilevel circuitry with certain advantages. This study is restricted to symmetric floating bipolar and unlinear loads, thus only a three-phase three-wire network and corresponding three-phase three-leg inverter design is considered. Commercial APFs are mostly equipped with insulated-gate bipolar transistors *(IGBTs)* providing wide range of available power and voltage ratings, high power efficiency and relatively high switching frequency. Each transistor must be connected to its antiparallel freewheeling diode, in order to operate in all four quadrants. The APF is modeled using parametric data from the *Semikron SKM400GB123D* data sheet[E59], which is the IGBT/diode module used in the 20.0 *kW* converter.[D30] The control system is based on standard building blocks from the Simulink® library, while power electric circuit is constructed using the SimPowerSystems™ toolbox[G76].
Electrical properties of power transistors and semiconductors in general are not constant, and depend on thermal and electrical operating point of the device. Technical data provided by Semikron[E60] makes it possible to very accurately model the IGBT/diode module. However semiconductor devices in the SimPowerSystems library are modeled only with the most important parameters in mind. The simplified representation is sufficient enough when studying power electronics on a system level[E53]. Nonetheless its possible by using Simulink customized S-function blocks, to very precisely model physical properties of semiconductor devices[G77]. This could be an interesting approach in future work, where more detailed and realistic representation could be used in the study of APF power losses and efficiency, and fully include transient characteristics.

The *IGBT forward voltage drop* V_f set equal to the collector-emitter saturation voltage drop V_{CE}. The *IGBT forward resistance* R_{on} is estimated to be the inverse of forward transconductance g_{fs}, accounting for conductive losses in the IGBT when its being forward biased. Similarly the inverse diode is included as a simple *diode forward*

bias voltage drop** V_{fd}*. An ideal power transistor switches ON and OFF status in sync with the gate signal, however like all realistic semiconductor devices the IGBT needs a finite switching time in order to transition from one state to the other. SimPowerSystems only allow inclusion of turn-off transients, while neglecting the turn-on switching time. The ***turn-off delay time T_f is the time taken for the collector current declining to 90.0 % of the initial load current, while the *tail time* T_t is the time interval taken for collector current dropping from 90.0 % to 10.0 % of the load current.

Its also important to include the *snubbers*, else Simulink will not be happy. The snubber circuit design in Simulink is restricted to simple series RC-circuitry paralleled with each IGBT/diode module. Snubber component values R_{sn} and C_{sn} must be carefully selected, or they can sabotage the APF performance. For simplicity this study uses the same component values as the snubber in the 20.0 kW NTNU/SINTEF converter, which turned out to work well.

The DC-side of the inverter is populated with an ideal variable DC-voltage source V_{DC}, paralleled with a DC capacitor C_{DC}. The decision of placing a constant DC-voltage source in the DC-link, is admittedly the most notable simplification in this simulation model, from a control system perspective. A fundamental and critical concept of active power filters, is that the average power exchange with the upstream grid must be zero, so the DC-link capacitor C_{DC} is only intended acting as a temporary energy storage device[B21]. Subsequently in order to ensure good APF performance, the DC-bus must be regulated to adequate and constant voltage level V_{DC}, or it can seriously compromise the APF operation as later demonstrated. DC-link voltage regulation has traditionally been incorporated into the current reference generator, as secondary outer control loop. Voltage regulation is performed additionally and simultaneously with the harmonic and reactive compensation, so the converter power will at any instant flow bidirectionally.

This study neglects the voltage control scheme, due to the ideal variable DC-voltage source. Moreover the polarized capacitor C_{DC} is strictly speaking obsolete, but included for demonstrating special phenomenas of the APF behavior. Note that the compensator system *(inverter and coupling transformer)* is electrically floating. This topology works as long as the APF is not processing zero-sequence currents. Preliminary simulations revealed that compensation of unbalanced active and reactive currents, is possible **only** when grounding both primary and secondary sides of the transformer. Moreover such compensation target requires the DC-link to be equipped with a grounded midpoint, however these result will be presented in future work.

4.1.2 VSI grid interface

There is another critical element which combined with the inverter, constitute an active power filter. The IGBTs produce pulse train-shaped output voltages at high carrier frequency f_{sw}, thus a passive impedance between the inverter and the point of common connection is needed to transform voltages into output currents. This is implemented preferably by a passive low-pass filter. In this study the output filter is simply a first order L-filter, but more complex high-order filter designs *(LC and LCL)* are favorable as they provide enhanced filtering and their cut frequency can be optimized according to the APF operation. Although this work has not been focusing particularly on the filter design.

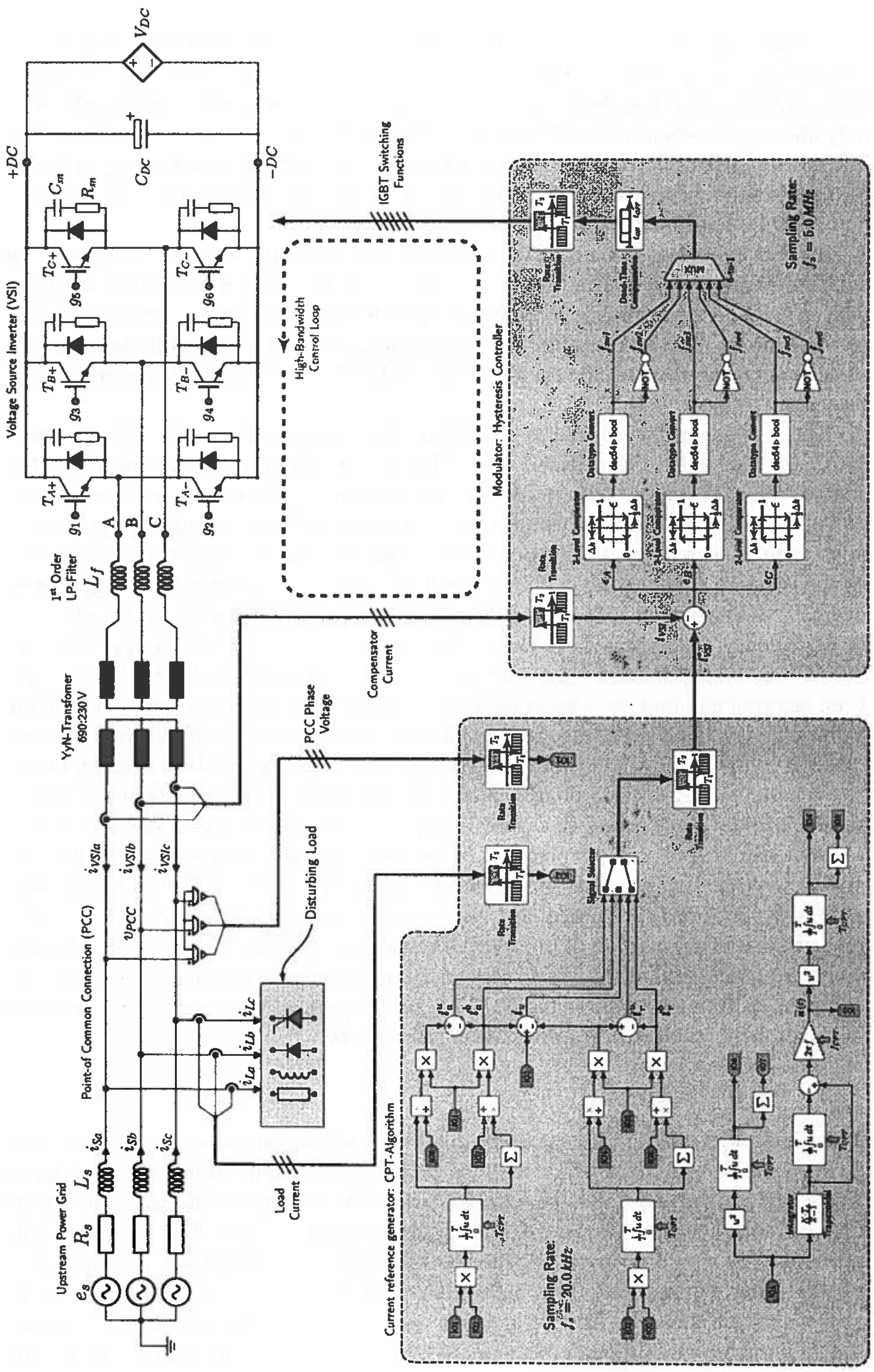

Figure 4.1 – *Electric power circuit and control system for a shunt-connected active power filter.*

The attenuation from the smoothing inductor L_f is constant -20 dB/decade across the full frequency range. As will be demonstrated later APFs based on this filter design generally operate at higher switching frequencies, in order to synthesize output current of desired pureness. The filter properties are important to have in mind, when considering APF performance criteria such as switching frequency f_{sw}, DC-link voltage V_{DC}, tuning of current controller, and the resulting ripple in the output current. It must be clarified that different results and conclusions than what is presented here is to be expected, as filter design may have such a tremendous impact on the APF behavior. Most importantly this study point out that utilizing simple filter design calls for very high switching rate, in some cases beyond the natural limit of IGBTs. Optimal filter design should be thoroughly studied in future work.

Another power component commonly used in the interface, is namely a three-phase *step-up coupling transformer* serving multiple purposes. The stray inductance of the transformer can be designed large enough so that the L-filter can be neglected, while the filtering action is performed entirely by the transformer. Secondly the coupling transformer provides safety and protection, acting as galvanic isolation between the VSI and power network. The most valuable feature however is the step-up transformation which allows the inverter to operate at greatly reduced DC-voltage level, but still maintaining its current tracking capability. Notably if a transformer is to be used in APF applications, it must be specifically designed to handle HF currents and voltages.

One remarkable feature of power transformers from a broad selection of power ratings, is that they share nearly exact same electrical properties, when being transformed to the per-unit system. Technical details for the coupling transformer is based on per-unit data provided by T.Wildi[E61]. Moreover its constructed with a yYN winding configuration, however alternative configurations have proven to work as well.

4.1.3 Electric power network

Representation of the upstream power network is simplified in the form of a Thévenin equivalent. The *internal source voltage* e_s will be manipulated to provoke scenarios of both ideal and unbalanced harmonic voltage waveforms at the load bus. Equivalent source impedance Z_s is the combination of *source resistance* R_s and *source inductance* L_s. Notably $R_s \gg X_s$ and both resistance and reactance are relatively insignificant, so the resulting grid voltage at point of common connection can be assumed as ideally stiff for this work. The dominating resistance R_s contra reactance X_s, corresponds to the characteristics of low-voltage consumer end of the grid.

4.1.4 Control system

The control system utilized in this simulation model (**Figure 4.1**), is very similar to what used in previous work[A1]. However in the project prior to this thesis work, there were challenges related to realistically model an active power filter, so shunt compensation was omitted in that work. The only way to make the active filtering work, was by replacing the power electronic circuitry with an ideal controlled current source. It was spent considerable effort into attempting to implement the APF using power electronics. Some of the issues which were identified and resolved, will be further discussed after demonstrating harmonic and reactive compensation.

In the original simulation model all components both in the electric power circuit and the control system, were run at equal base sampling frequency $f_s = 1.0\,MHz$.[1] When modeling power electronics in Simulink, this is a commonly used sample rate, providing reasonable resolution of signals without demanding to long simulation time. Its not feasible running the control system in the megahertz range, particularly driving the CPT-algorithm at such clock rate is to CPU intensive, resulting in time consuming simulations often terminating with MATLAB engine shutdown. When modeling a system interfaced with some sort of control system, it is to ambitious running both the physical system and controller domain at same sampling rate, particularly when modeling closed-loop feedback systems like an APF. The feedback controller (*hysteresis controller*), is based on the assumption that the physical system has a certain response time, LP-filter time constant τ_f. Its not practical for for the controller to update the PWM-signals before the APF current i_{VSI} has actually responded to the change. This problem is often reported by Simulink as an algebraic loop.[G77]

The simulation first worked when the CPT-algorithm and the hysteresis controller were discretized, allowing to run each domain at separate sampling rates. One crucial detail in this sense is the *Rate Transition block*, which basically replaces the actual A/D and D/A conversion of analog and digital signals, allowing to propagate a signal through subsystems of varying sampling rate. Ultimately this was exploited to downsample the CPT-algorithm to more realistic sample rate $f_{cpt} = 20.0\,kHz$, while the modulator was run at higher clock rate $f_{PWM} = 5.0\,MHz$.

Load current induced by the disturbing load $i_L(t)$ is measured and used as input to the CPT-algorithm, along with the load bus phase voltages $v_{PCC}(t)$. The algorithm decomposes load current $i_L(t)$ into five parcels; balanced active i_a^b, balanced reactive i_r^b, unbalanced active i_a^u, unbalanced reactive i_r^u and void i_v currents, which can be mixed to generate a current reference i_{VSI}^* for the APF. In order to observe the actual change in CPT power mix of the upstream compensated system, an additional identical CPT-algorithm is online with the grid current $i_s(t)$. The importance of selecting correct current sign convention should be mentioned, as there have been lots of challenges with this. Currents related to load, source and APF should be measured with the sign convention indicated in **Figure 4.1**, else the shunt compensation will not work. Note that compensator current i_{VSI} is assigned as injection into the network, which contradicts the sign convention utilized in the pq-theory. This is because the APF in this study is energized by a DER, while the conventional solution has been for the APF to provide energy from the grid, thus the need to reference as a load.

The current controller used in this study is the simple hysteresis controller, which by good reasons is frequently referred to as the *bang-bang* controller. This controller is preferred in many power electronic applications, due to its minimalistic implementation and natural robustness. The greatest drawback of hysteresis current controllers, is that the transistor switching frequency f_{sw} can be unpredictable, making filter design and performance difficult. This controller type is also associated to *limit cycle operation*, meaning that it can generate very high switching rate f_{sw}. There can be found numerous proposals in the literature how to improve the hysteresis controller, however this study

---

[1] Sampling rate is here stated in *'Hz'*, while digital systems often refer to *'Sa/s'*. Thus $f_s = 1.0\,kHz = 1.0\,kS/s \rightarrow 1000$ samples per second, and $f_s = 1.0\,MHz = 1.0\,MS/s \rightarrow 1000000$ samples per second.

is restricted to the original design. Because of the highly non-linear characteristic, the hysteresis controller becomes very dependent on maximum available sampling rate. In the analog domain this is possible using op-amps and comparators, but when implemented as a digital controller the sampling frequency f_{PWM} becomes extremely critical, as will be later discussed. Here the modulator sampling rate was set to $f_{PWM} = 5.0\,MHz$. The power circuit was run at $f_s = 10.0\,MHz$ sampling rate, and the resulting simulation time was reasonably good because of the downsampled CPT-algorithm. Signals are acquired using standard Simulink scopes clocked at $f_s = 500.0\,kHz$ for high definition.

Table 4.1 – *Parameter values for simulation model.*

Quantity	Symbol	Unit	Absolute Value
Voltage source inverter (VSI)			
Transistor type			IGBTs *(Semikron SKM 400GB123D)*
Snubber circuit, resistance	R_{sn}	$[\Omega]$	1.0
Snubber circuit, capacitance	C_{sn}	$[\mu F]$	0.022
Forward resistance (IGBT)	R_{on}	$[m\Omega]$	8.1
Forward voltage drop (IGBT)	V_f	$[V]$	1.0
Antiparalell diode, forward voltage drop	V_{fd}	$[V]$	2.0
Turn-off delay time (IGBT)	T_f	$[ns]$	720.0
Tail time (IGBT)	T_t	$[ns]$	80.0
DC-link capacitance	C_{DC}	$[\mu F]$	3300.0
Output low-pass filter, series resistance	R_f	$[m\Omega]$	100.0
Output low-pass filter, series inductance	L_f	$[mH]$	0.5
Turn-on delay (IGBT)	T_{on}	$[\mu s]$	3.0
Turn-off delay (IGBT)	T_{off}	$[\mu s]$	1.0
Step-up coupling transformer			
Nominal power rating	S_n	$[kVA]$	25.0
Nominal frequency	f_n	$[Hz]$	50.0
Nominal line voltage (primary)	V_{pn}	$[V_{RMS}]$	690.0
Winding resistance (primary)	R_{pri}	$[m\Omega]$	95.2
Winding leakage inductance (primary)	L_{pri}	$[mH]$	0.49
Nominal line voltage (secondary)	V_{sn}	$[V_{RMS}]$	230.0
Winding resistance (secondary)	R_{sec}	$[m\Omega]$	10.6
Winding inductance (secondary)	L_{sec}	$[mH]$	0.05
Magnetic core, resistance	R_m	$[\Omega]$	571.3
Magnetic core, inductance	L_m	$[H]$	952.2
Winding configuration (prim/sec)	-	[-]	Yy *(floating star/star-connected)*
Miscellaneous model parameters			
Resistance, source	R_s	$[m\Omega]$	0.10
Inductance, source	L_s	$[\mu H]$	10.0
Impedance ratio, source	R/X	[-]	15.9
Sampling rate, power circuit	f_S	$[MHz]$	10.0

4.2 Scenario A - Balanced sinusoidal voltage

Electric circuit diagram

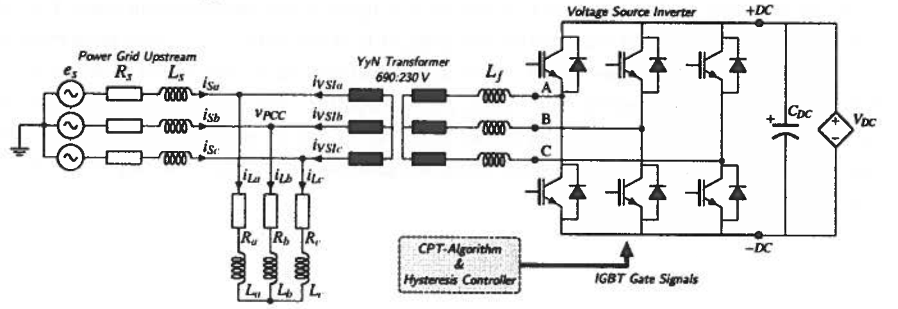

Figure 4.2 – *Shunt compensation of RL-load under ideal balanced sinusoidal voltage regime.*

Oscillograms

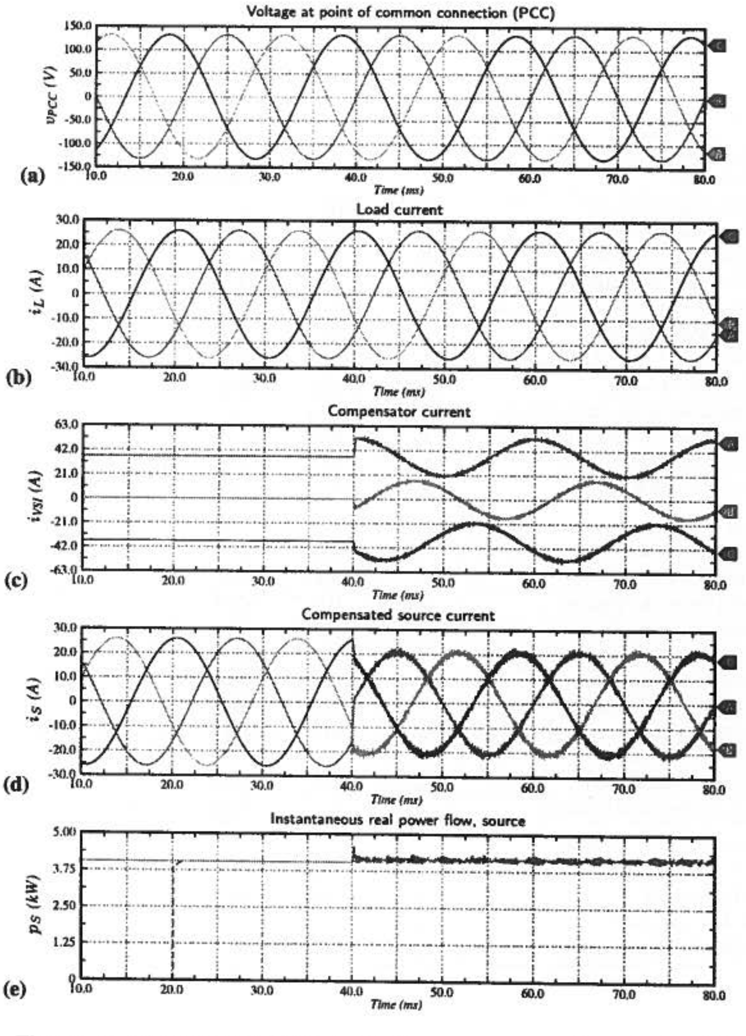

Figure 4.3 – *Demonstration of classic reactive power compensation using the CPT.*

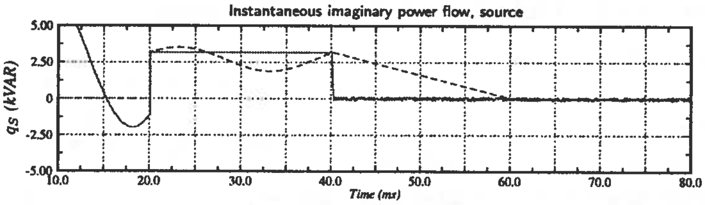

Figure 4.4 – *The reactive power flow is eliminated, optimizing grid utilization.*

Detailed technical data

Table 4.2 – *Scenario A.*

Quantity	Symbol	Unit	APF Off	APF On
VSI Operation Data				
DC-bus voltage	V_{DC}	$[V]$	300.0	
Average switching frequency	f_{sw}	$[kHz]$		10.6, 10.5, 10.6
Hysteresis band	Δh	$[A]$	1.00	
Modulator sampling frequency	f_{PWM}	$[MHz]$	5.0	
CPT Power Mix at Grid Side				
Apparent power	A	$[kVA]$	5.14/100	4.15/100
Active power	P	$[pu]$	78.64	99.98
Unbalanced active power	N_a	$[pu]$	0.0	0.18
Reactive power	Q	$[pu]$	61.77	0.27
Unbalanced reactice power	N_q	$[pu]$	0.0	0.17
Distortion power	D	$[pu]$	0.0	2.15
Power factor	λ	$[-]$	0.79	0.99
CPT algorithm sampling rate	f_{CPT}	$[kHz]$	20.0	
Load Characteristics				
Description	Symmetric YF-connected RL-load			
Phase Resistance	$R_{a,b,c}$	$[\Omega]$	4.0, 4.0, 4.0	
Phase Inductance	$L_{a,b,c}$	$[mH]$	10.0, 10.0, 10.0	

Discussion

Starting simple this first scenario demonstrates how the conservative power theory can be utilized to perform classic power compensation of a symmetric RL-load, under ideal balanced sinusoidal voltage condition. Initially due to the inductive impedance, line currents $i_S(t)$ are lagging respective voltages by approximately $\varphi_1 = \cos^{-1}(\lambda) =$ -37.8°. Correspondingly the reactive power constitute almost 61.77 % of the total power flow. The observation is supported by the non-unity power factor $\lambda = 0.79$. As network voltages and currents are sinusoidal, the instantaneous real $p(t)$ and imaginary powers $q(t)$ flow constant, as expected from previous chapter.

The APF is turned on at $t_{on} = 40.0\,ms$ injecting symmetric sinusoidal currents $i_{VSI}(t)$ that are leading the load bus voltage $v_{PCC}(t)$ by exactly $\varphi_1 = +90°$. Consequently the APF acts as a reactive source, producing same amount of Q as consumed by the RL-load. Source currents become instantly in-phase with respective voltages and obtain minimum amplitude, as the balanced reactive component $i_r^b(t)$ is eliminated. Instantaneous imaginary power is accordingly reduced to zero, while real power is flowing unaltered from the source to the RL-load. After compensation the active power is dominating the power flow $P = 99.98\,\%$, leading to optimal power factor $\lambda = 0.99$.

4.3 Scenario B - Unbalanced sinusoidal voltage

Electric circuit diagram

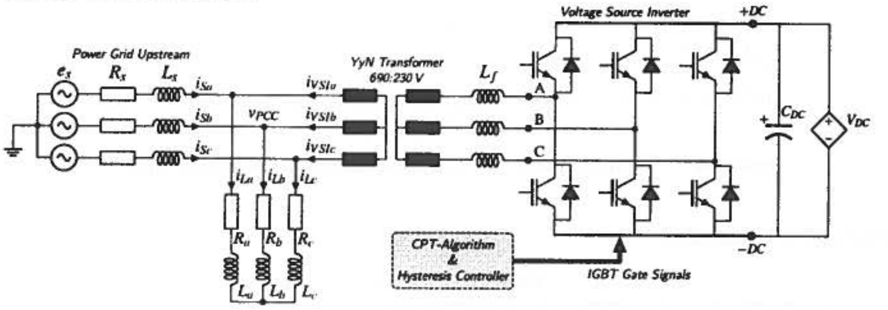

Figure 4.5 – *Shunt compensation of RL-load having unbalanced sinusoidal voltage regime.*

Oscillograms

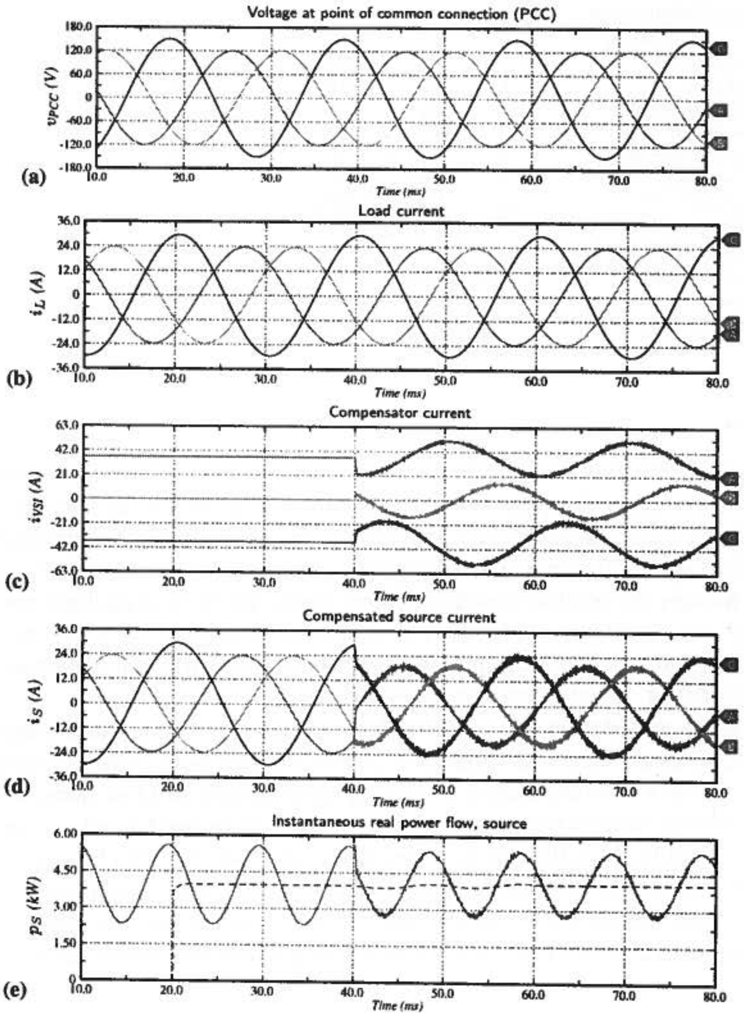

Figure 4.6 – *Unbalanced voltages induce power oscillations and current unsymmetry.*

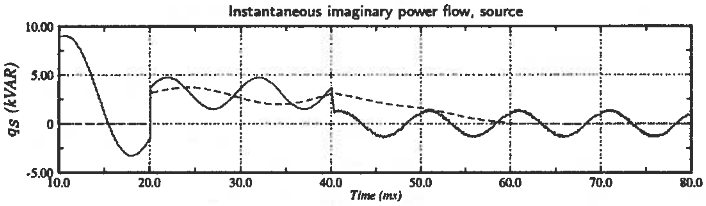

Figure 4.7 – *Bidirectional instantaneous imaginary power flow due to unbalanced voltage.*

Detailed technical data

Table 4.3 – *Scenario B.*

Quantity	Symbol	Unit	APF Off	APF On
VSI Operation Data				
DC-bus voltage	V_{DC}	$[V]$	300.0	
Average switching frequency	f_{sw}	$[kHz]$		11.8, 11.9, 9.3
Hysteresis band	Δh	$[A]$	1.00	
Modulator sampling frequency	f_{PWM}	$[MHz]$	5.0	
CPT Power Mix at Grid Side				
Apparent power	A	$[kVA]$	5.04/100	4.07/100
Active power	P	$[pu]$	78.64	99.98
Unbalanced active power	N_a	$[pu]$	0.0	0.17
Reactive power	Q	$[pu]$	61.77	0.20
Unbalanced reactice power	N_q	$[pu]$	0.0	0.14
Distortion power	D	$[pu]$	0.0	2.12
Power factor	λ	$[-]$	0.78	0.99
CPT algorithm sampling rate	f_{CPT}	$[kHz]$	20.0	
Load Characteristics				
Description	Symmetric YF-connected RL-load			
Phase Resistance	$R_{a,b,c}$	$[\Omega]$	4.0, 4.0, 4.0	
Phase Inductance	$L_{a,b,c}$	$[mH]$	10.0, 10.0, 10.0	

Discussion

As expected having unbalanced sinusoidal voltages $v_{PCC}(t)$ at the point of common connection, makes the instantaneous real $p(t)$ and imaginary powers $q(t)$ oscillate in a quadrature phase relation at 100.0 Hz frequency. As the load is a symmetric RL-impedance load currents $\boldsymbol{i}_L(t)$ are having same symmetric qualities, but phase shifted by proximately $\varphi_1 \approx$ -36.0° to their respective voltages. Nonetheless the CPT power mix is pretty much unchanged compared to previous scenario, reactive power $Q = 61.77\,\%$ reduces the power factor to $\lambda = 0.78$.

As the APF starts injecting balanced reactive currents $\boldsymbol{i}_r^b(t)$ at $t_{on} = 40.0\,ms$ reactive power is practically eliminated $Q = 0.20\,\%$, boosting the power factor to unity $\lambda = 0.99$. Compensated source current $\boldsymbol{i}_S(t)$ becomes aligned with respective voltages, now only transporting active power $P = 99.98\,\%$. Quantitatively the reactive compensation works just as intended, however as previously suggested current and power waveforms will always be degraded by the unbalanced voltage irrespective of shunt compensation. Notably unsymmetry in source currents and the oscillation of instantaneous powers remain unaltered, thought the offset value of the imaginary power has been removed due to compensation of reactive power.

4.4 Scenario C - Balanced harmonic voltage

Electric circuit diagram

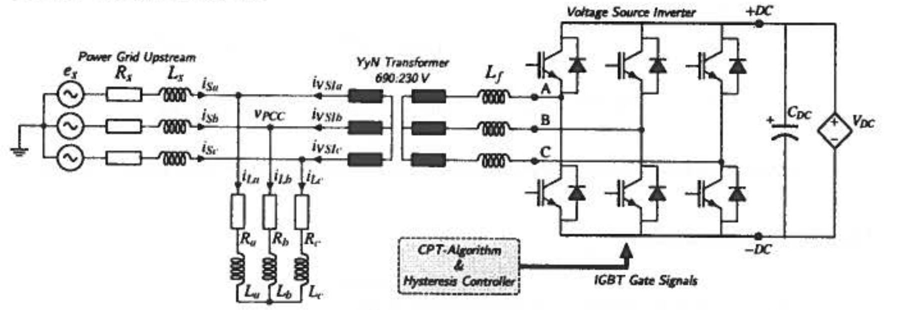

Figure 4.8 – *Shunt compensation of RL-load under balanced harmonic voltage regime.*

Oscillograms

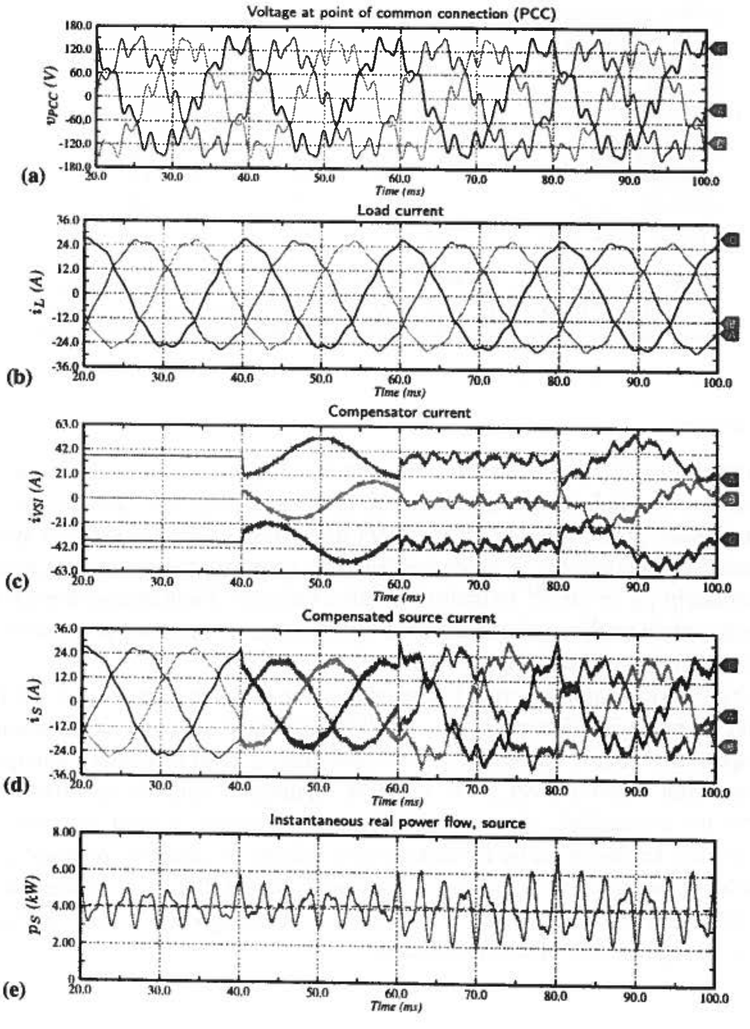

Figure 4.9 – *Similar to pq-theory, the CPT cannot optimize all objectives simultaneously.*

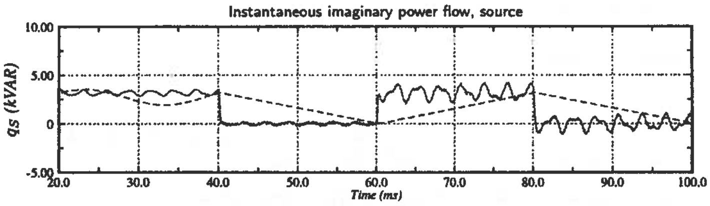

Figure 4.10 – *Inevitable power harmonics under distorted voltage regime.*

Detailed technical data

Table 4.4 – *Scenario C*

Quantity	Symbol	Unit	APF Off	Period 1	Period 2	Period 3
VSI Operation Data						
DC-bus voltage	V_{DC}	$[V]$	300.0			
Average switching frequency	f_{sw}	$[kHz]$		12.0, 12.2, 11.8	14.5, 13.6, 14.9	13.3, 12.9, 13.8
Hysteresis band	Δh	$[A]$	1.00			
Modulator sampling frequency	f_{PWM}	$[MHz]$	5.0			
CPT Power Mix at Grid Side						
Apparent power	A	$[kVA]$	5.25/100	4.23/100	5.19/100	4.16/10
Active power	P	$[pu]$	77.15	98.19	77.89	99.80
Unbalanced active power	N_a	$[pu]$	0.0	0.06	0.06	0.13
Reactive power	Q	$[pu]$	61.79	0.21	62.53	0.31
Unbalanced reactice power	N_q	$[pu]$	0.02	0.06	0.06	0.12
Distortion power	D	$[pu]$	15.14	18.93	4.81	6.31
Power factor	λ	$[-]$	0.77	0.98	0.78	0.99
CPT algorithm sampling rate	f_{CPT}	$[kHz]$	20.0			
Load Characteristics						
Description	Symmetric YF-connected RL-load					
Phase Resistance	$R_{a,b,c}$	$[\Omega]$	4.0, 4.0, 4.0			
Phase Inductance	$L_{a,b,c}$	$[mH]$	10.0, 10.0, 10.0			

Discussion

Energizing the symmetric RL-load by harmonic voltages creates an interesting phenomena, as distortion power $D = 15.14\,\%$ is surprisingly detected. The shunt compensation is performed in three stages: 1) $40.0 - 60.0\,ms \rightarrow i_r^b(t)$, 2) $60.0 - 80.0\,ms \rightarrow i_v(t)$, 3) $80.0 - 100.0\,ms \rightarrow i_r^b(t) + i_v(t)$. The resulting load currents $i_L(t)$ appear relatively sinusoidal despite the distorted grid voltage $v_{PCC}(t)$, due to the inductive impedance $L_{a,b,c} = 10.0\,mH$ of the load. Instantaneous real $p(t)$ and imaginary powers $q(t)$ flow initially unidirectional with a superimposed $300.0\,Hz$ oscilllation.

As the balanced reactive current $i_r^b(t)$ is injected, source current remain close to sinusoidal but in phase with voltage. The reactive power is eliminated $Q = 0.21\,\%$, greatly improving the power factor $\lambda = 0.98$. Interestingly in the second period the source current $i_S(t)$ becomes severely distorted, thought the harmonic content is not matching corresponding voltages. Method 2 appears to be less interesting as the CPT power mix and power factor, reminiscence the uncompensated system. In the last cycle grid current becomes aligned and adopt same waveform as PCC voltage. The first method gives best result as currents are close to sinusoidal, and the imaginary power is eliminated and less distorted compared to methods involving injection of void current.

4.5 Scenario D - Unbalanced harmonic voltage

Electric circuit diagram

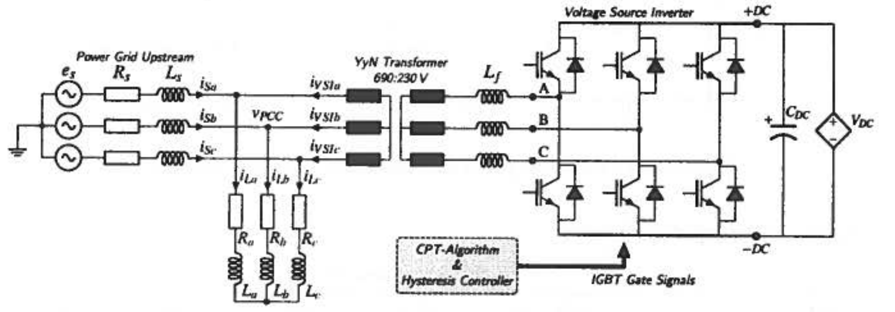

Figure 4.11 – *Shunt compensation of RL-load under unbalanced harmonic voltage regime.*

Oscillograms

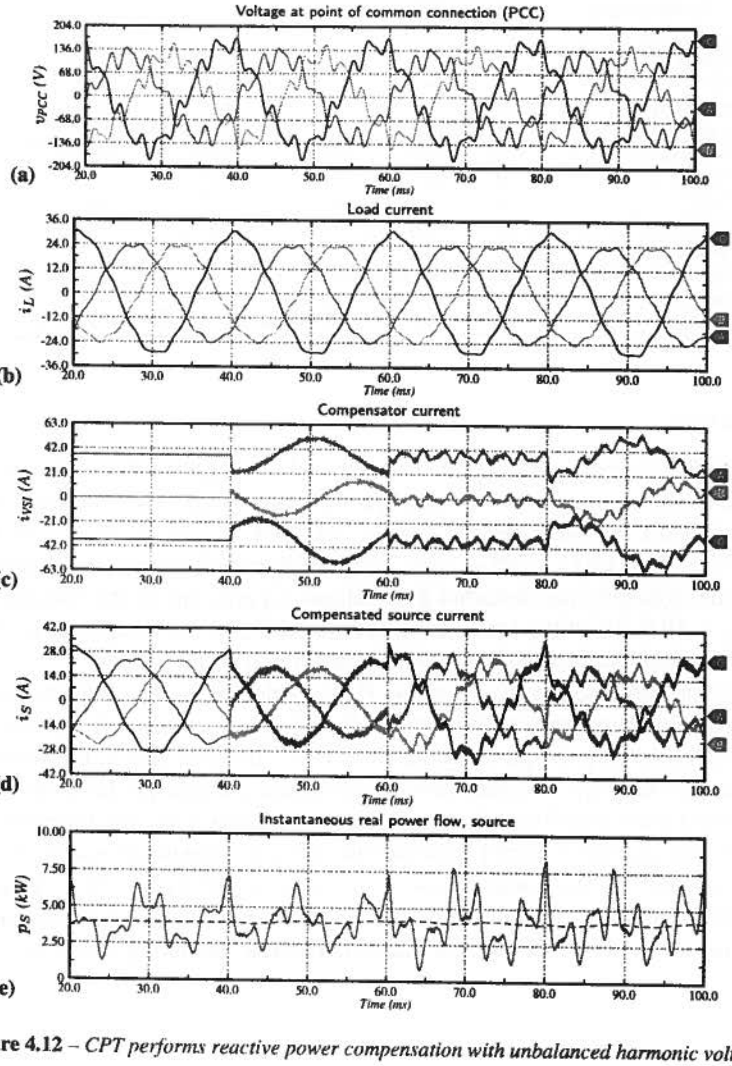

Figure 4.12 – *CPT performs reactive power compensation with unbalanced harmonic voltage.*

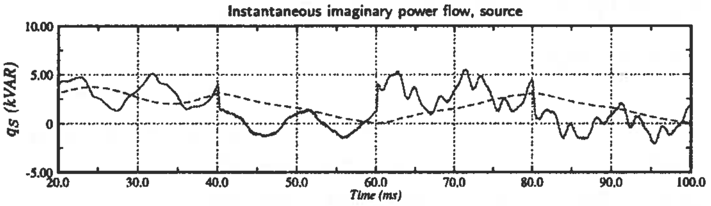

Figure 4.13 – *Deteriorated instantaneous power flow due to harmonic voltages.*

Detailed technical data

Table 4.5 – *Scenario D.*

Quantity	Symbol	Unit	APF Off	Period 1	Period 2	Period 3
VSI Operation Data						
DC-bus voltage	V_{DC}	$[V]$	300.0			
Average switching frequency	f_{sw}	$[kHz]$		11.8, 11.5, 10.0	8.4, 8.5, 15.6	8.0, 8.7, 15.6
Hysteresis band	Δh	$[A]$	1.00			
Modulator sampling frequency	f_{PWM}	$[MHz]$	5.0			
CPT Power Mix at Grid Side						
Apparent power	A	$[kVA]$	5.15/100	4.16/100	5.11/100	4.10/10
Active power	P	$[pu]$	77.12	98.18	78.12	99.82
Unbalanced active power	N_a	$[pu]$	0.61	0.82	0.27	0.29
Reactive power	Q	$[pu]$	61.79	0.27	62.24	0.32
Unbalanced reactice power	N_q	$[pu]$	0.01	0.18	0.31	0.34
Distortion power	D	$[pu]$	15.26	18.99	4.82	5.95
Power factor	λ	$[-]$	0.77	0.98	0.78	0.99
CPT algorithm sampling rate	f_{CPT}	$[kHz]$	20.0			
Load Characteristics						
Description	Symmetric YF-connected RL-load					
Phase Resistance	$R_{a,b,c}$	$[\Omega]$	4.0, 4.0, 4.0			
Phase Inductance	$L_{a,b,c}$	$[mH]$	10.0, 10.0, 10.0			

Discussion

After the APF initially turned off the first two cycles, the shunt compensation is proceeded in the following sequence: 1) $40.0 - 60.0\,ms \rightarrow i_r^b(t)$, 2) $60.0 - 80.0\,ms \rightarrow i_v(t)$, 3) $80.0 - 100.0\,ms \rightarrow i_r^b(t) + i_v(t)$. Despite having a load bus voltage $v_{PCC}(t)$ that is simultaneously unbalanced and distorted, the behavior of the compensated system matches the previous case. Whenever balanced reactive current $i_r^b(t)$ is injected, the reactive power becomes fully eliminated $Q \approx 0$, and distortion power D is greatly reduced by eliminating void currents $i_v(t)$. In the third period the original apparent power A is reduced by 20.4 %, mostly because of the reactive compensation. Correspondingly when compensating both $i_r^b(t)$ and $i_v(t)$, the source current is corrected to be aligned with and having same waveform as PCC voltage *(Fryze currents)*.

Evidently as long as the voltage is non-ideal; i.e. unbalanced or distorted, the CPT cannot provide a solution which approach the current and power flow into idealized state. Harmonics origin solely from the load bus voltage, thus only solvable by a series compensator or an unified power flow controller *(UPFC)*. Nonetheless thanks to homo-integrated voltage, the CPT is capable of generating a solid and credible current reference for reactive power compensation independently of the networks voltage condition.

4.6 Scenario E - 3-Ph Thyristor Rectifier

Electric circuit diagram

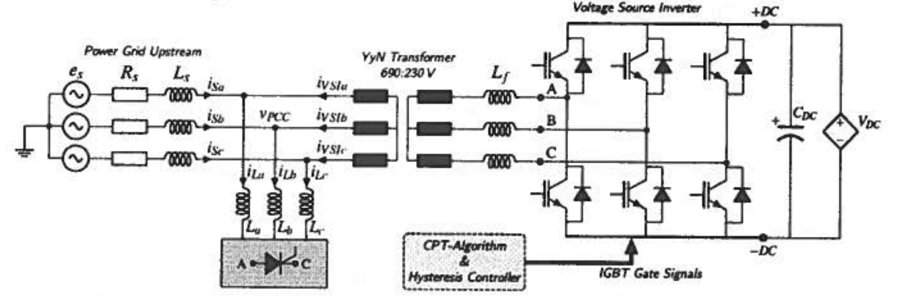

Figure 4.14 – *Shunt compensation of 3-ph thyristor rectifier under balanced sinusoidal voltage.*

Oscillograms

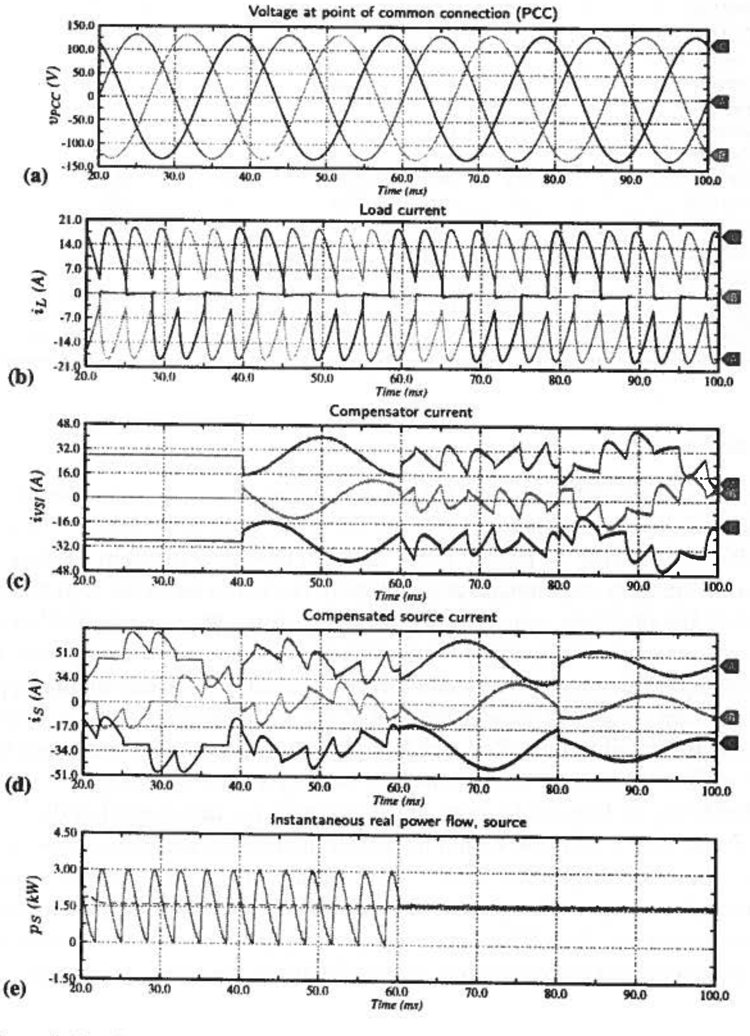

Figure 4.15 – *CPT performs reactive and harmonic filtering of an electronic unlinear load.*

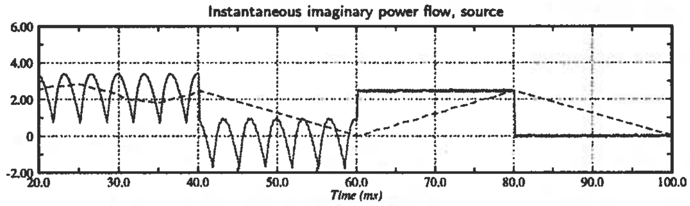

Figure 4.16 – *Fundamental and harmonic reactive power eliminated.*

Detailed technical data

Table 4.6 – *Scenario E.*

Quantity	Symbol	Unit	APF Off	Period 1	Period 2	Period 3
VSI Operation Data						
DC-bus voltage	V_{DC}	$[V]$	400.0			
Average switching frequency	f_{sw}	$[kHz]$		62.4, 62.5, 62.4	58.9, 58.1, 60.0	56.4, 56.3, 56.4
Hysteresis band	Δh	$[A]$	0.50			
Modulator sampling frequency	f_{PWM}	$[MHz]$	5.0			
CPT Power Mix at Grid Side						
Apparent power	A	$[kVA]$	3.21/100	2.06/100	2.94/100	1.60/10
Active power	P	$[pu]$	49.75	77.65	54.52	99.94
Unbalanced active power	N_a	$[pu]$	0.0	0.02	0.34	0.09
Reactive power	Q	$[pu]$	76.70	0.18	83.81	0.11
Unbalanced reactice power	N_q	$[pu]$	0.0	0.02	0.34	0.09
Distortion power	D	$[pu]$	40.51	63.01	2.05	3.36
Power factor	λ	$[-]$	0.49	0.78	0.55	0.99
CPT algorithm sampling rate	f_{CPT}	$[kHz]$	400.0			
Load Characteristics						
Description	3-Ph thyristor rectifier load					
DC-bus load resistor	R_{DC}	$[\Omega]$	8.0			
Front end inductance	$L_{a,b,c}$	$[mH]$	2.0, 2.0, 2.0			
Thyristor delay angle	α_{th}	$[°]$	60.0			

Discussion

This scenario demonstrate several important aspects regarding the CPT and shunt compensation in general. A three-phase thyristor rectifier is energized by balanced sinusoidal voltages $v_{PCC}(t)$. The DC-bus is loaded with resistance $R_{DC} = 8.0\,\Omega$ and by delaying the firing angle to $\alpha_{th} = 60.0°$, the rectification will induce considerable amount of reactive power $Q = 76.70\,\%$. Simultaneously due to fast commutating switches, the network is polluted with high order current harmonics $D = 40.51\,\%$. Three distinguished methods are evaluated in a sequence adopted from previous scenario: 1) $40.0 - 60.0\,ms \rightarrow i_r^b(t)$, 2) $60.0 - 80.0\,ms \rightarrow i_v(t)$, 3) $80.0 - 100.0\,ms \rightarrow i_r^b(t) + i_v(t)$.

Due to reactive compensation the original apparent power $A = 3.10\,kVA$ is reduced by 35.8 %. However the unaltered void component $i_v(t)$ leaves the source current greatly distorted, but in phase with voltage. In the second compensation cycle current harmonics are effectively neutralized, making source current $i_S(t)$ sinusoidal and lagging the voltage by $\varphi_1 \approx \alpha_{th}$. Notably the violent oscillations in instantaneous power flow are completely removed. In the last stage the compensation is completed by neutralizing both reactive power consumption $Q = 0.11\,\%$, and unwanted current harmonics $D = 3.36\,\%$.

4.7 Scenario F - 3-Ph Diode rectifier

Electric circuit diagram

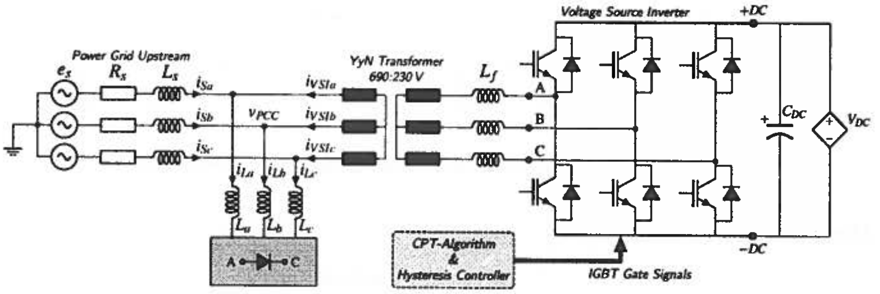

Figure 4.17 – *Shunt compensation of 3-ph diode rectifier under ideal sinusoidal balanced voltage.*

Oscillograms

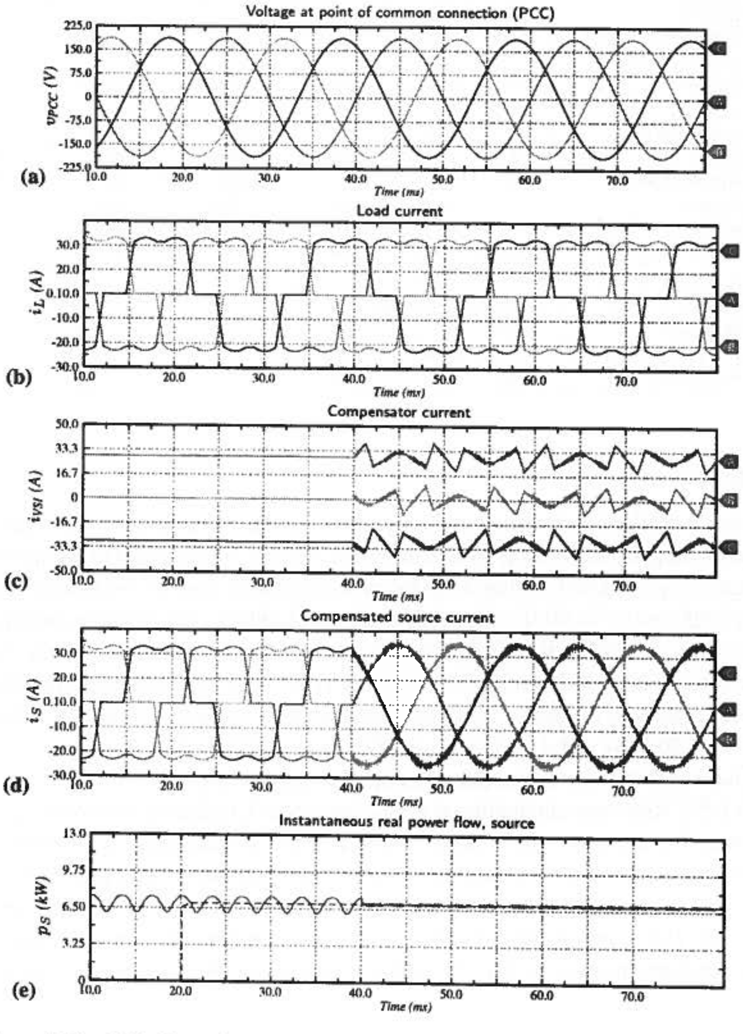

Figure 4.18 – *CPT effectively eliminates void currents giving optimal network performance.*

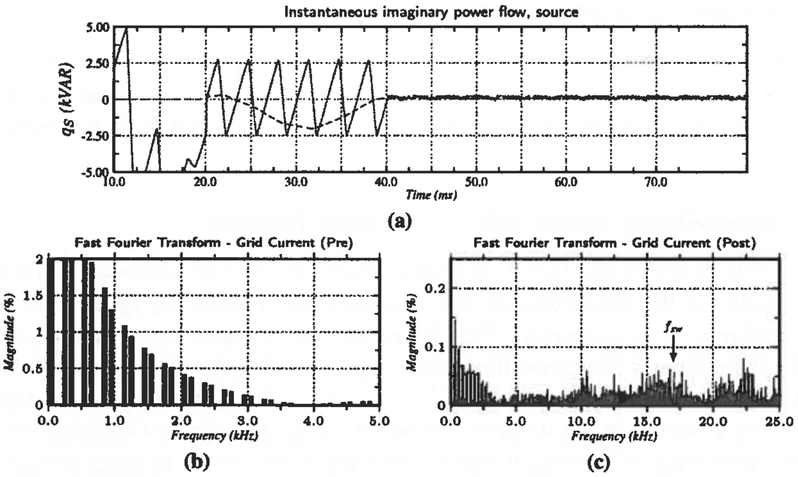

Figure 4.19 – *Reduced harmonic content, thought minor IGBT switching noise present.*

Detailed technical data

Table 4.7 – *Scenario F.*

Quantity	Symbol	Unit	APF Off	APF On
VSI Operation Data				
DC-bus voltage	V_{DC}	$[V]$	300.0	
Average switching frequency	f_{sw}	$[kHz]$		16.1
Modulator sampling frequency	f_{PWM}	$[MHz]$	5.0	
Hysteresis band	Δh	$[A]$	1.00	
CPT Power Mix at Grid Side				
Apparent power	A	$[kVA]$	9.11/100	8.76/100
Active power	P	$[pu]$	96.09	99.92
Unbalanced active power	N_a	$[pu]$	0.0	0.02
Reactive power	Q	$[pu]$	0.24	0.51
Unbalanced reactice power	N_q	$[pu]$	0.0	0.02
Distortion power	D	$[pu]$	27.70	3.88
Power factor	λ	$[-]$	0.96	0.99
CPT algorithm sampling rate	f_{CPT}	$[kHz]$	20.0	
Load Characteristics				
Description	3-Ph diode rectifier load			
DC-bus load resistor	R_{DC}	$[\Omega]$	5.0	
Front end inductance	$L_{a,b,c}$	$[mH]$	10.0, 10.0, 10.0	

Discussion

The last scenario demonstrates classic shunt compensation of distorted load current $\boldsymbol{i_L(t)}$, generated by a three-phase diode rectifier. Loaded by a resistance $R_{DC} = 5.0\,\Omega$ and energized with balanced sinusoidal voltages, it produces characteristic square-shaped current waveforms highly polluted by odd-integer harmonics. Associated to the current harmonics is the distortion power $D = 27.70\,\%$, reducing the power factor to $\lambda = 0.96$.

At time $t_{on} = 40.0\,ms$ the APF starts to inject void components $\boldsymbol{i_v(t)}$ extracted from the load current. The compensated source current $\boldsymbol{i_S(t)}$ immediately becomes sinusoidal and with lowest possible RMS-value. Correspondingly the instantaneous complex power $\boldsymbol{s(t)}$ flow unidirectionally with the well known $300.0\,Hz$ oscillations cancelled.

4.8 Hysteresis controller reviewed

The statement that hysteresis controllers are self-adjusting is only true as long as they are run at sufficient sampling rate. The overall performance of the inverter also depends on DC-link voltage, filter properties and the hysteresis band as will be reviewed in this section.

4.8.1 Importance of current reference sampling frequency

In digital signal processing theory the Nyquist theorem[E58] is of fundamental importance for determining the sampling rate of a discrete signal processing system. According to the theorem can a continuous time-based signals be correctly reconstructed in the discrete time domain, if the sampling frequency f_s is minimum *(Nyquist rate)* twice the maximum frequency component $f_s > 2 \cdot f_{max}$ within the sampled signal. Its important to note that actual sampling frequency should be much greater than Nyquist rate, or the highest harmonics will not be accurately presented. Moreover in order to recover the original sampled input signal, this requires proper reconstruction techniques *(Shannon's interpolation method).*

Engineers working with the Speedgoat system are not concerned with the fundamental mechanisms and procedures related to the sampling process of analog input signals. Voltage and current transducers in the hardware domain are simply connected to the Speedgoat IO106 analog-to-digital input card[D46], and the sampled signals become directly available in the Simulink domain from the Speedgoat IO106 driver block[D28]. This simplicity is one of the main advantages when utilizing rapid-prototyping systems compared to say DSP systems, where signal acquisition and conditioning can be complicated.

On the other hand the simplification also has some disadvantages as there exists no conceptual description of how the sampling is executed. So the overall process becomes abstracted from the real-time application designer, which can be confusing especially for users who are not familiar with DSPs and digital signal processing theory. Nonetheless because of the aforementioned CPU constraints (**Section 3.16**), the real-time application will run at finite sampling frequency. So the appearance and precision of input and output signals from the application, and ultimately the performance of the APF, are directly related to the raw sampling rate provided by the real-time target machine.

The importance of sampling rate can be demonstrated when commanding the current-controlled VSI to output a sine wave current $i^*_{VSI} = 8.0 \sin(314.16t)$, and then altering the sampling frequency (f_{ref}) of the tone generator. In **Figure 4.20a** the sampling rate is set to $f_{ref} = 500.0\, Hz$, suggesting that a fundamental waveform is sampled 10 times per cycle, which is five times the Nyquist rate. The synthesized current has low resolution of stairway-like appearance ($THD = 14.9\,\%$), and by observing the zero crossing there is an artificial phase shift of $\varphi \approx 67.5°$. If the CPT-algorithm is utilized to compute a current reference for reactive power compensation, this will undoubtedly fail due to artificial time delay and unintended injection of harmonics. Also this imply the need for much higher sampling ratio when dealing with detection of HF current harmonics, as these are relatively small in magnitude, thus even more sensitive to precision if to be employed in active power filtering.

Demo 1: Variation of current reference sampling rate f_{ref}

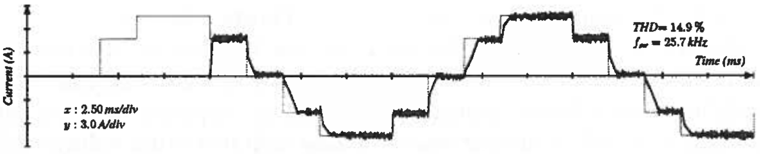

(a) *Sampling rate,* $f_{ref} = 500.0\,Hz$

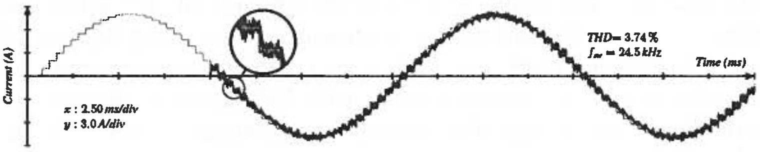

(b) *Sampling rate,* $f_{ref} = 2.5\,kHz$

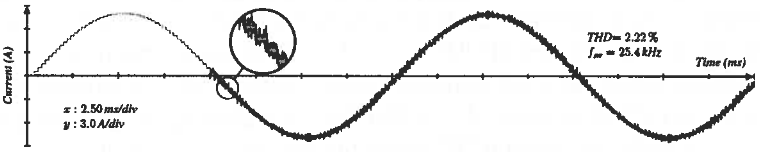

(c) *Sampling rate,* $f_{ref} = 5.0\,kHz$

(d) *Sampling rate,* $f_{ref} = 10.0\,kHz$

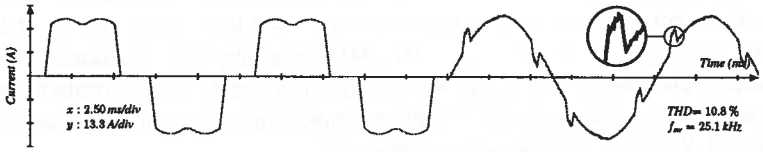

(e) *Sampling rate,* $f_{CPT} = 10.0\,kHz$

Figure 4.20 – *Sampling a continuous time-signal containing high-order harmonics, requires the sampling frequency to be minimum 50 times higher than the maximum frequency component in the sampled signal to ensure authentic reconstruction. Simulation parameters subfigure a) to d),* $L_f = 4.0\,mH$, $R_f = 100.0\,m\Omega$, $V_{DC} = 350.0\,V$, $f_{PWM} = 5.0\,MHz$, $\Delta h = 10.0\,mA$.

Increasing the sampling rate to $f_{ref} = 2.5\,kHz$ (**Figure 4.20b**) the fundamental sine wave is quantized 50 times per cycle, giving an appreciable difference; the resulting output current from the VSI resemble a $50.0\,Hz$ waveform. However the appearance is still stairway-like with a delay of proximately $\varphi \approx 12.1°$. The step time as highlighted, is found as the inverse of sampling rate $T_{ref} = f_{ref}^{-1} \approx 0.4\,ms$.
Similarly when doubling the sampling frequency (**Figure 4.20c**) to $f_{ref} = 5.0\,kHz$, the current reference is sampled 100 times per cycle, leaving the steps and time delay less prominent. Although there is no absolute rule regarding optimal sampling frequency, as this should be adapted for the application in question. Apparently a sampling rate of minimum $f_{ref} = 5.0\,kHz$ is needed when working with first order voltage and current harmonics, meaning that the Speedgoat target machine can easily implement algorithms processing $50.0\,Hz$ signals, with reasonable resolution and CPU resource efficiency.

On the other hand this implies that algorithms working with HF voltage and current harmonics; i.e. active series and shunt compensators, calls for very high sampling rates if there is in interest of having good fidelity and control of harmonic components. For instance having an APF set to compensate up to the 20th harmonic, which is considered a viable goal, this requires an algorithm running at sampling rate $f_s = 50.0\,Hz \cdot 20 \cdot 100 = 100.0\,kHz$, which is far beyond the capacity of the Speedgoat system.

In **Figure 4.20d** the sampling frequency is set equal to what was used in the experimental work $f_{ref} = 10.0\,kHz$. The time delay of the synthesized current is very short, and the waveform close to ideal now as its being sampled 200 times per cycle. Also the total harmonic distortion is acceptable $THD = 1.65\,\%$. Remaining current ripple is not due to restricted sampling rate of the current reference, and can only be reduced by example boosting the switching frequency $f_{sw} > 25.0\,kHz$, or increasing the LP-filter inductance value $L_f > 4.0\,mH$. However a 20th harmonic sampled at $f_{ref} = 10.0\,kHz$, would be quantized only 10 times per period, which is not acceptable for an high-performance APF.

The necessity of running the current reference generator on sufficient sampling rate has been demonstrated, and consequently why the experimental implementation of harmonic filtering was never going to succeed. Notably the extraction of current reference for reactive power compensation is possible as the Speedgoat system provides suitable resolution of $50.0\,Hz$ waveforms. The experimental verification of reactive shunt compensation failed mainly due to lacking sampling rate in the modulator, as will be reviewed later.

During the practical experiments the Speedgoat target machine was able to both acquire fast commutating currents drawn by diode and thyristor rectifiers, and produce harmonic voltages, all at only $f_s = 10.0\,kHz$ sampling rate. Admittedly it must be commented that limited sampling rate was real noticeable when configuring the programmable voltage source, as the VSI often jumped into overmodulation mode depicted in **Figure A.8a**, when adding voltage harmonics.

If an harmonic component is reconstructed with satisfactory resolution at sampling rate say 50 times its own frequency $f_s = 50 \cdot f_{max}$, this imply that running a programmable voltage source at $f_s = 10.0\,kHz$ would guarantee linear control of harmonics only up to $200.0\,Hz$ (4th order). Attempting to produce voltage harmonics above this limit was of course possible, as the experiments demonstrated components up to $800.0\,Hz$ (16th order). The fundamental $50.0\,Hz$ voltage responded linearly when parametrized from

Demo 2: Variation of DC-link voltage level V_{DC}

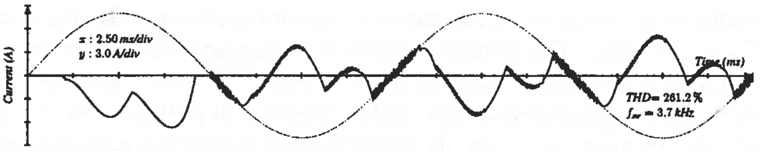

(a) *DC-link voltage,* $V_{DC} = 300.0\,V$

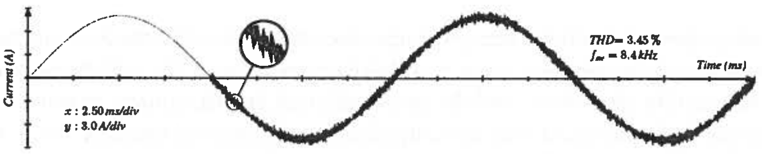

(b) *DC-link voltage,* $V_{DC} = 350.0\,V$

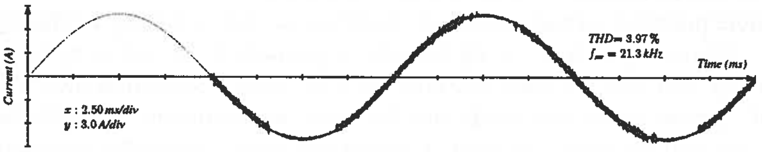

(c) *DC-link voltage,* $V_{DC} = 500.0\,V$

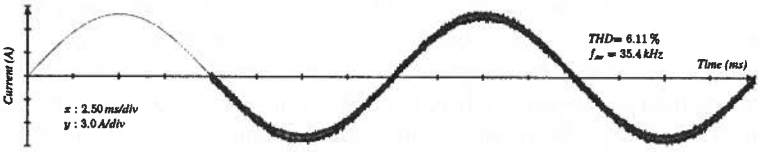

(d) *DC-link voltage,* $V_{DC} = 800.0\,V$

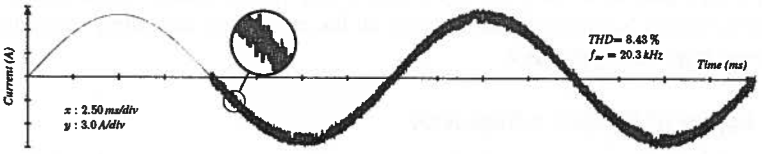

(e) *DC-link voltage,* $V_{DC} = 800.0\,V$ *and tolerance band,* $\Delta h = 1.0\,A$

Figure 4.21 – *DC-link voltage control on a current-controlled VSI is an important operation parameter. If the voltage is to low the VSI will not be able to correctly follow its current reference; the tracking will be lost around extrema. Setting the voltage to stiff will push the inverter into higher switching frequencies, thus increasing current ripple and total harmonic distortion. Simulation parameters,* $L_f = 4.0\,mH$, $R_f = 100.0\,m\Omega$, $f_{PWM} = 5.0\,MHz$, $f_{ref} = 500.0\,kHz$, $\Delta h = 500.0\,mA$.

0 to 1.0 per-unit, but when superimposing harmonic components above 200.0 Hz, these were set in the range of 0.00001 per-unit to ensure inverter operating in linear mode. To demonstrate the limited resolution a sine wave of frequency $f = 1.0\,kHz$ corresponding to 20th order, was generated in a real-time application running at sampling rate of $f_{ref} = 10.0\,kHz$. The reference signal was then sent into the driver block of the Speedgoat IO110 digital-to-analog output module[D48]. The analog output signal was probed with a digital oscilloscope and as depicted in **Figure A.8b**, the signal is quantized only 10 times per cycle. In future work it is recommended to implement the programmable voltage source exclusively in the FPGA domain, as this provides excellent performance.

In **subsections 4.6** and **4.7** there was demonstrated successful reactive and harmonic compensation of three-phase diode and thyristor rectifiers. The compensated source current was purely sinusoidal, and the associated real and imaginary power flow, went from violent 300.0 Hz oscillation to being ideally nullified and unidirectional. Notably an important fact is that these results were obtainable by assuring that diodes and thyristors commutated slowly. Also boosting the sampling rate of the CPT-algorithm to $f_{CPT} = 20.0\,kHz$, enhances the fidelity of void currents.

In more practical scenarios limited sampling rate and frequency bandwidth of the current reference generator can be an issue, especially if the active or passive load commutates very fast. In such circumstances the control system of the APF cannot "see" HF currents beyond the bandwidth. Moreover the maximum obtainable frequency components will not appear correctly reconstructed, and consequently attenuated by the APF.

When studying APFs in the literature and particularly harmonic cancelation of rectifier loads from an experimental point of view, there are many examples of either insufficient or in certain cases deliberate limited sampling frequency of the reference generator. Subsequently the compensated source current appear with characteristic notches at the high ${}^{di}/_{dt}$ regions, where the APF is unable to follow up. This phenomena is presented in **Figure 4.20e** as all system parameters equals scenario F (**Table 4.7**), but with the sampling rate of the CPT-algorithm reduced to $f_{CPT} = 10.0\,kHz$. Harmonic cancellation is only partially completed ($THD = 10.8\,\%$). Conclusively what characterize an high-performance APF is the capability to accurately attenuate HF current harmonics, which is ultimately depending on the maximum sampling frequency f_{ref} of the current reference generator.

4.8.2 Impact of DC-link voltage level

The voltage level on the DC-link V_{DC}, has an interesting impact on the APF operation. In **Figure 4.21a** the DC-voltage is decreased to $V_{DC} = 300.0\,V$, which is less than level provided by the antiparalleled diodes; $V_{DC} = 1.35 \cdot V_{LL} = 1.35 \cdot 230.0\,V = 310.5\,V$. Subsequently the diodes will automatically start to conduct current into the converter *(opposite of reference)*, attempting to energize the DC-link capacitor C_{DC}. In this example the inverter is capable of tracking the reference only around the zero crossing region, while approaching extrema there is not enough inertia in the DC-link forcing the current into desired direction. Notably this example must be considered as a worst case.

Demo 3: Variation of hysteresis band Δh

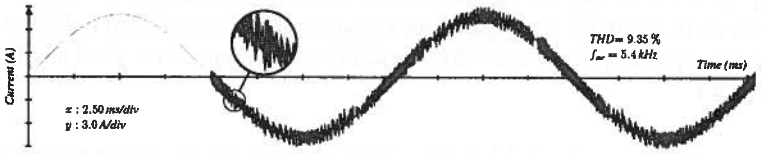

(a) *Tolerance band,* $\Delta h = 1.50\,A$.

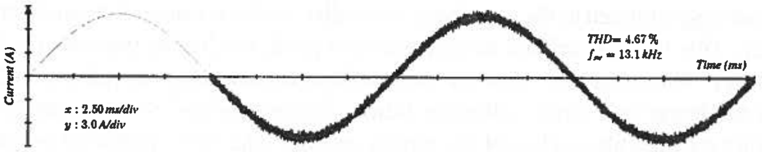

(b) *Tolerance band,* $\Delta h = 500.0\,mA$.

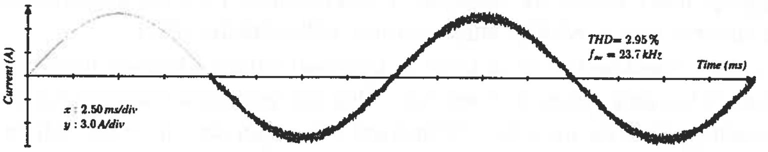

(c) *Tolerance band,* $\Delta h = 100.0\,mA$.

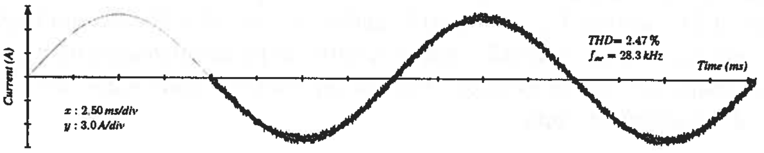

(d) *Tolerance band,* $\Delta h = 1.0\,mA$.

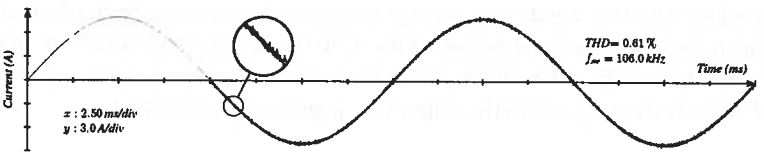

(e) *Tolerance band,* $\Delta h = 1.0\,mA$ *and modulator sample rate,* $f_{PWM} = 10.0\,MHz$.

Figure 4.22 – *The hysteresis current controller is a simple self-adjusting controller. Second to the DC-link the hysteresis band is the only operational parameter. By adjusting the hysteresis tolerance band this will dramatically affect the switching frequency of the IGBTs. By setting the tolerance very low combined with very high sampling rate in the controller, the output current approaches idealistic characteristics. The switching rate however becomes excessive. Simulation parameters,* $L_f = 2.0\,mH$, $R_f = 500.0\,m\Omega$, $f_{PWM} = 5.0\,MHz$, $f_{ref} = 2.0\,MHz$, $V_{DC} = 350.0\,V$.

Similar phenomena occurs when the current reference reach an appreciable level. The inverter delivers more power and consequently higher DC-voltage is needed $E_{DC} = \frac{1}{2}C_{DC}V_{DC}^2$, in order to keep the output current locked to the reference. Else the output current will be deformed at the negative and positive peaks, as depicted in **Figure 4.24a**. The tracking capability is restored (**Figure 4.21b**) when increasing the DC-voltage to $V_{DC} = 350.0\,V$.

As the error tolerance band Δh is the only tunable parameter in the hysteresis current controller, the overall performance of the active power filter is very dependent on the joint action of the error tolerance band Δh, and the DC-link voltage level V_{DC}. One of the well known challenges related to the bang-bang controller, is that it causes excessive switching frequency. This is partly related to the hysteresis band, but just as important is the DC-voltage level. When V_{DC} increases the switched current trajectory travels more violently between the lower and upper tolerance limits. Setting the DC-voltage unnecessarily high in fact reduces the quality of the output current. The APF operation proves to be very sensitive against increased V_{DC} as this will boost the switching frequency, and consequently the output current ripple. Put in a different way the excessive switching noise injected into the network, translates as void currents $i_v(t)$ and distortion power D, which is more or less inevitable when working with realistic APFs.

To achieve good performance there must be maintained a balance between the DC-link voltage V_{DC}, and hysteresis band Δh . This will guarantee tracking capability, but simultaneously limit the switching frequency and output current ripple. There has not been found any proposal in the literature, how this control is implemented in practice. Voltage V_{DC} should not be set randomly, but perhaps as a function of the amplitude or *RMS* value of the reference current, thus not very complicated to realize.
In **Figure 4.21d** setting $V_{DC} = 800.0\,V$ makes $f_{sw} = 35.4\,kHz$ extend beyond the typical frequency range of IGBTs, however this can be compensated by relaxing the hysteresis band Δh. Wider hysteresis band is depicted in **Figure 4.21e** with the disadvantage of considerable ripple.

The experience gained during simulations and what was partly verified under experiments, is that the hysteresis controller might act brutal on the current-controlled VSIs. Controlling the DC-link voltage V_{dc} has not been paid much attention in this thesis work, but as this is such an important aspect of the APF operation, more focus on this topic is required in future work. The active power filter becomes more precise and versatile in terms of current shaping capability when V_{DC} is properly controlled.

4.8.3 Impact of the hysteresis band

The first two examples (**Figure 4.22a** and **4.22b**) resemble a $50.0\,Hz$ current waveform typically seen in the literature. The hysteresis band is set wide $\Delta h = 18.9\,\%$ allowing the appearance of ripple, resulting in $THD = 9.35\,\%$. Thus IGBTs switch at relatively low rate $f_{sw} = 5.4\,kHz$. The DC-link voltage is at minimum level and output filter values are static, so only way to improve the performance is by confining Δh. Setting the error tolerance to $\Delta h = 6.25\,\%$ gives a moderate operation in terms of current ripple, $THD = 4.67\,\%$ and $f_{sw} = 13.1\,kHz$. Further restricting the error tolerance to

Demo 4: Importance of current controller sampling rate f_{PWM}

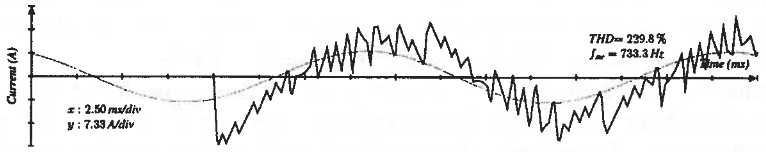

(a) *Sampling rate,* $f_{PWM} = 10.0\,kHz$.

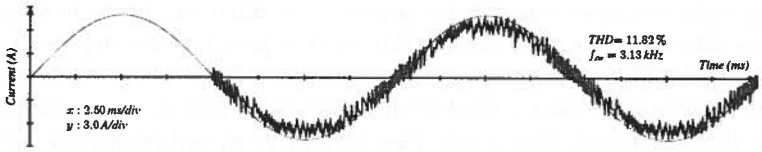

(b) *Sampling rate,* $f_{PWM} = 50.0\,kHz$.

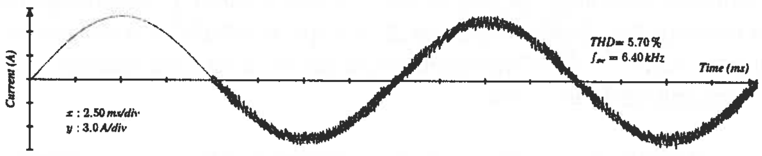

(c) *Sampling rate,* $f_{PWM} = 100.0\,kHz$.

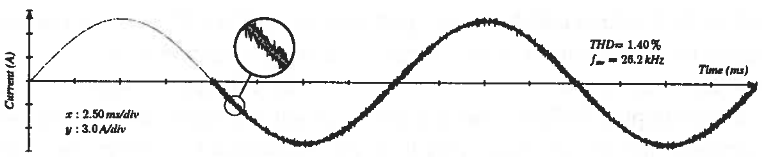

(d) *Sampling rate,* $f_{PWM} = 500.0\,kHz$.

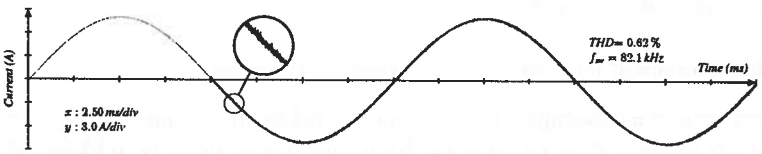

(e) *Sampling rate,* $f_{PWM} = 1.0\,MHz$.

Figure 4.23 – *For past and future this is a very important and unquestionable result. It demonstrates that an hysteresis controller starts to operate properly firstly when run at sampling rates beyond 500.0 kHz. The Speedgoat system should be expanded with additional FPGA subsystems in order to implement modulation techniques. Simulation parameters,* $L_f = 4.0\,mH$, $R_f = 100.0\,m\Omega$, $\Delta h = 10.0\,mA$, $f_{ref} = 200.0\,kHz$, $V_{DC} = 350.0\,V$.

$\Delta h = 1.25\,\%$ switching frequency $f_{sw} = 28.3\,kHz$ extends beyond the IGBT limit, but making $THD < 3.0\,\%$. The smallest possible error tolerance Δh_{min} depends on the sampling rate f_{PWM} of the modulator. With a restricted sampling frequency the controller forms a natural lower limit Δh_{min}, and narrowing below this limit has no noticeable effect on neither switching frequency or current ripple.

In **Figure 4.22e** the hysteresis controller is operated at $f_{PWM} = 10.0\,MHz$ clock rate. This gives the controller high fidelity, making it possible to keep track of very fast switching transients. Thought more theoretical and less feasible in practical experiments, the low-latency update time makes it possible setting hysteresis band to $\Delta h = 0.013\,\%$. As a results the VSI produces a close to ideal output current $THD = 0.61\,\%$. The disadvantage is the execssive switching frequency $f_{sw} = 106.0\,kHz$, which is not realistic in terms of IGBTs. In order to achieve this level of performance, the inverter must be based on MOSFETs. These devices have traditionally not been associated with APFs, and one particular issue related to MOSFETs is the high on-state resistance R_{on}, leading to significant conduction losses. Thus MOSFETs are best compatible with lower voltage levels, and their usage from a power loss standpoint, can only be justified if the transistor switches in excess of $f_{sw} = 30.0 - 100.0\,kHz$[E53]. Thanks to advancements in semiconductor technology MOSFETs are now viable building components for APFs, and more recently there has been presented concepts of MOSFET-based active power filter in the literature.[E55–E57] Experimental realization of this new concept could be an interesting project for future work.

Previous examples demonstrate how the switching frequency f_{sw} is closely related to the error tolerance band Δh of the hysteresis current controller. Setting Δh to strictly can easily make f_{sw} go beyond the limit of IGBTs, however the tolerance band cannot be too relaxed as the tracking capability and performance of the APF become compromised. This is especially important in terms of harmonic shunt compensation.

It must be commented that the low-pass filter design is probably not so optimal for low current output. Reduced switching frequency and ripple is observed when the current increases $i_{VSI} \gg 5.0\,A_{RMS}$, simply as the filtering action improves. This imply that a flexible APF is accomplished if the modulator and transistors are run at high frequency $f > 100.0\,kHz$. This provides better current tracking, independently of the filter design and DC-link voltage level.

4.8.4 Importance of current controller sampling frequency

These very important examples demonstrate the behavior of an hysteresis current controller, when manipulating its sampling frequency f_{PWM}. Initially in **Figure 4.23a** the current feedback loop and the modulator are run at sampling frequency equal to the Speedgoat system capacity $f_{PWM} = 10.0\,kHz$. Clearly the performance is not satisfactory as there is very large ripple giving unacceptable $THD = 229.8\,\%$. The synthesized output current has low fidelity and incorrect amplitude, moreover there is an artificial phase shift of $\varphi \approx 22.5°$. Note that a relatively large current reference amplitude must be used compared to other examples, otherwise the ripple would be to dominating and the output current would appear as random noise.

Further in **Figure 4.23b** ramping up to $f_{PWM} = 50.0\,kHz$ provides the controller better accuracy. Switching rate f_{sw} increases which consequently recovers most of the phase lag and current ripple $THD = 11.82\,\%$, the amplitude on the other hand is not tracking the reference as intended.

At sampling rate $f_{PWM} = 100.0\,kHz$ the tracking comes closer to the reference, **Figure 4.23c**, however still the magnitude is not correct before pushing the clock rate to $f_{PWM} = 500.0\,kHz$, as depicted in **Figure 4.23d**. Another noticeable difference is the narrow error tolerance band $\Delta h = 0.13\,\%$ gets more effective as modulator sample rate increases. Finally at $f_{PWM} = 1.0\,MHz$ update rate the output current becomes close to what is an idealistic waveform, **Figure 4.23e**. The general observation is that when f_{PWM} increases while Δh, V_{DC} and L_f are fixed, the IGBT switching frequency speeds up. When dealing exclusively with fundamental waveforms one could get away with sampling rates of $f_{PWM} = 100.0 - 500.0\,kHz$, nonetheless in order to properly control an APF the sampling should be in the megahertz range.

At lower modulator sampling frequencies f_{PWM}, the output current travels outside the preset error tolerance band Δh. The switching logic becomes more random so the fundamental conditional rules which the hysteresis current controller are based on, become violated due to insufficient sampling rate. In general the higher sampling rate provides a much more versatile controller, and the APF can operate with enhanced accuracy, in wider operational range of current output, while being less dependent on other system parameters.

The regular software-based Speedgoat IO106 analog-to-digital input module simply cannot provide these extreme sampling rates. Although there is not stated any absolute upper sampling frequency in the xPC Target manual[G74], but the general impression is that sampling rates of $f_s = 20.0 - 200.0\,kHz$ are plausible with the Speedgoat real-time target machine, notably under very restricted circumstances.[2]

The requested signal processing speed can only be achieved either with analog circuitry, or most preferably in the FPGA domain. Expanding the Speedgoat real-time target machine with several Speedgoat IO325 FPGA-based low-latency analog inputs, would open for wider range of application areas such as closed-loop control of converters; i.e. implementation of high-performance active power filter.

---

[2] Algorithm code must be executed in polling mode, and the model size and I/O-complexity must be low. Processor performance in the Speedgoat real-time target machine is vitally important.

4.8.5 Experimental implementation of hysteresis current controller

This section presents recorded oscillograms of current waveforms produced by the voltage source inverter when operated in current-control mode, thus confirming restricted performance of the Speedgoat real-time target machine.

The practical arrangement of the experiment was as following; the ABC outputs of the VSI were connected to stiff grid voltage through a series first order low-pass RL-filter, in chain with a three-phase variable transformer. At the time the experiment was conducted, the only filter inductors available were those of value $L_f = 175.0\,mH$. This is as previously mentioned grossly 50-100 times more than what is usually employed for APF applications. Moreover as the coils were not magnetically designed and compatible with high-frequency applications, they generated considerable acoustic noise. The high inductance value made the time response of the output filter τ_f, slow enough for the modulator to keep track of the output current, thus partially compensating for the unsatisfactory sampling frequency f_{PWM}. Rheostats connected in series with the inductors were set unrealistic high $R_f = 50.0\,\Omega$, limiting the LP-filter time constant $\tau_f = \frac{L_f}{R_f}$ into reasonable order. The 7.5 kVA variable yYN0-transformer was set to transformation ratio $a = 1$, and used primarily as galvanic isolation between the power grid and experimental setup. The inverter DC-link C_{DC} was energized through a passive rectifier circuit connected directly to the power grid as well. The charging circuitry was built as a series-connection of a soft starter, diode rectifier and the 80.0 kVA dYN11-transformer. The transformer was connected to the power grid via the soft starter, and the secondary output of the transformer V_p was fed into the diode rectifier providing a DC-voltage level of $V_{DC} = 230.0\,V \cdot \frac{400}{230} \cdot 1.35 \approx 540.0\,V$, which was necessary to overcome the large filter inductance L_f.

For generation of current reference, the CPT-algorithm was replaced by a simple tone generator. The signal generation was synchronized with the power grid using a standard discrete phase-lock loop (*PLL*) from the SimPowerSystems library. Normalized phase voltages measured with LEM voltage transducers were fed into the PLL, and the angular frequency ωt output from the PLL further utilized to generate three 120.0° mutually phase shifted reference currents of adjustable amplitude and frequency. The output currents from the VSI were measured using LEM current transducers, then fed directly to the hysteresis current controller. Both the tone generator and the hysteresis controller were run at the regular $f_s = 10.0\,kHz$ sampling frequency.

To supplement the experimental results, the experiment and associated parameters are recreated in the Simulink environment. The control algorithm in the simulation is identical to the one used in the real-time application. The only difference is the real power circuit which is replaced by an equivalent arrangement using SimPowSystems library. Notably by comparing the simulated and experimental results, this will importantly confirm the physical realism and validity of all previous simulation results and observations presented in this chapter.

In **Figure 4.24a** and **4.24e** the inverter is set to produce a 50.0 Hz current sine wave, and the simulated and experimental results are indeed quite similar. As expected the constricted sampling rate of the hysteresis current controller f_{PWM} makes the current tracking inaccurate. The logic state of each IGBT is evaluated every $T_{PWM} = f_{PWM}^{-1} =$

100.0 μs. Consequently the switching rate becomes very low $f_{sw} = 1.2\,kHz$, making the filtering action less effective and resulting in massive current ripple, $THD = 14.23\,\%$. Based on these results there could be possible to perform reactive power compensation, notably with considerable power loss in R_f and injection of unfiltered switching noise.

In **Figure 4.24b** and **4.24f** the DC-link voltage is reduced to $V_{DC} \approx 480.0\,V$ by adjusting the threshold on the DC-bus breaking chopper. There is obviously not enough inertia in the DC-link E_{DC} for the inverter to track the current reference, tracking capability is lost around extrema as previously reported. This demonstrates the drawback of using high filter value L_f and limited sampling rate f_{ref}, as the APF can only operate in a narrow power range before performance is further compromised.

Figure 4.24c and **4.24g** the reference is changed to 250.0 *Hz* current sine wave. The current reference has decent precision, however the synthesized waveform is severely phase shifted and deformed. Interestingly what is observed both in the simulated and experimental result, is what appears to be a 50.0 *Hz* power oscillation between PCC and the DC-bus.

Lastly in the final example depicted in **Figure 4.24d** and **4.24h**, there is attempted to synthesize a composite waveform of 50.0 *Hz* fundamental superimposed with 250.0 *Hz* harmonic. Not surprisingly the rendering lacks precision, and the modulator is unable to generate high switching frequency f_{sw}, due to its own limited clock rate f_{PWM}.

Active power filter solutions in various power and voltage ratings, are offered by industry leading companies like ABB and Siemens. The PQF active power filters[E62] marketed by ABB can compensate harmonics up to $2.5\,kHz = 50^{th}$ order, where the degree of attenuation of the first 20th orders is individually programmable. The PQF APF guarantees 10.0-90.0 % filtering within typically two network cycles.

The active power filter from Siemens SIVACON S8 technology[E63], can compensate harmonics of maximum $4.0\,kHz = 80^{th}$ order. Active filtering of the first 16 harmonic orders can be customized to specific needs. The Siemens APF is guaranteed to filter 95.0 % and current ripple $THD_i < 3.0\,\%$ notably at *nominal* current. The current reference generator in the Siemens controller is running at sampling rate $f_{ref} = 192.0\,kHz$, meaning that highest order harmonic is digitized 48 times per cycle, see **Figure 4.20b** for reference. Nonetheless operating at $f_{ref} = 192.0\,kHz$ gives very good resolution of the more important harmonics in the lower part of the frequency spectrum. By natural reasons neither ABB or Siemens state any details regarding what algorithms used to extracts current reference for the converter, but its reasonable to believe they are utilizing selective harmonic control similar to what presented by P.Mattavelli[E64].

Demo 5: Demonstrating restricted performance of the Speedgoat system

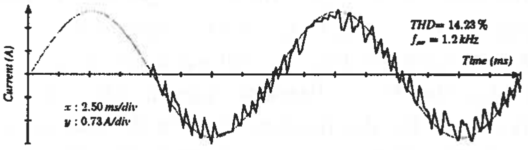

(a) *Simulation result,* 50.0 *Hz sine wave.*

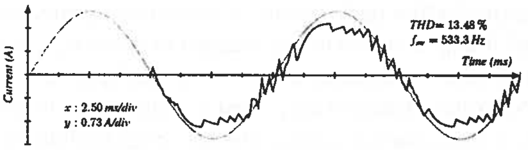

(b) *Simulation result,* 50.0 *Hz sine wave,* $V_{DC} = 480.0\,V$.

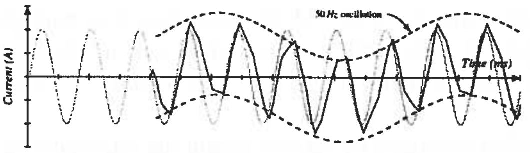

(c) *Simulation result,* 250.0 *Hz sine wave.*

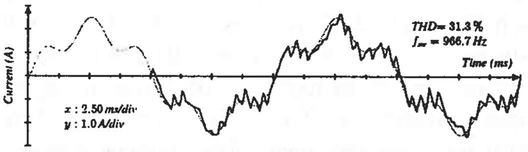

(d) *Simulation result,* 50.0 *Hz and* 250.0 *Hz composite.*

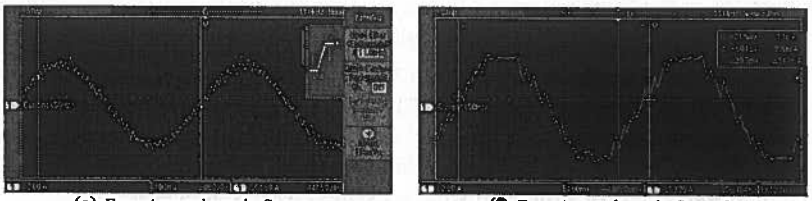

(e) *Experimental result, figure a.* **(f)** *Experimental result, figure b.*

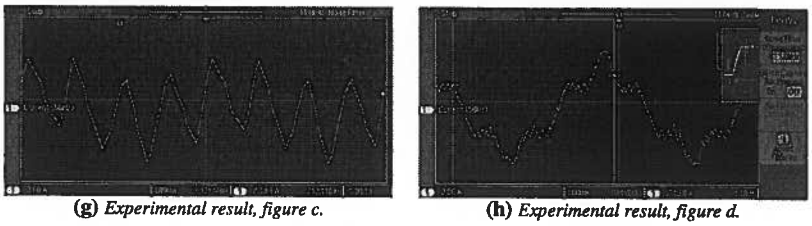

(g) *Experimental result, figure c.* **(h)** *Experimental result, figure d.*

Figure 4.24 – *Experimental results from attempt to operate a current-controlled voltage source inverter, using hysteresis current controller. Simulation parameters,* $L_f = 175.0\,mH$, $R_f = 50.0\,\Omega$, $f_{ref} = 10.0\,kHz$, $f_{PWM} = 10.0\,kHz$, $V_{DC} = 540.0\,V$ *and* $\Delta h = 100.0\,mA$.

Chapter 5

Conclusion and Future Work

5.1 Speedgoat system

The Speedgoat real-time target machine operates on principles similar to a digital signal processing system, consequently any algorithm must be designed accordingly. The Simulink solver and model must be set to operate at discrete time steps, and its good practice splitting the algorithm into subdomains assigned to appropriate sample rates. What sample rate to be used should be evaluated based on what purpose each respective domain is serving. During algorithm design there must also be paid attention towards using proper data format. Similar to sample rate each subdomain of the algorithm should be dedicated to the data format which ensures requested resolution, but minimizes CPU loading. Native format for the MATLAB engine is double-precision floating point numbers, however alternative more efficient formats like singe-precision or fixed-point should be considered, as this is expected to enhance the performance. To achieve high performance real-time applications, sample rate and datatype are probably the two most important design considerations.

Another feature which should be further investigated is the xPC Target multicore support, however once again the algorithm must be specifically designed for such purpose. By fully exploiting the Dual Core CPU in the Speedgoat processor module, the application can be executed on a separate core, while the secondary core provides ancillary functions such as resource demanding target-host communication.

The number of activated input and output channels greatly affect the maximum base sampling frequency f_s, particularly when operating in interrupt mode where the sampling rate is already drastically reduced. Excessive channel number takes larger share of CPU resources, which in the initial work was challenging.

Users of the Speedgoat system should be well acquainted with DSP and FPGA technology, thus PhD students will benefit most as DSP and FPGA systems are not covered by the electric power engineering master programme. Secondly the designer needs thorough experience with MATLAB and Simulink software. Optimized real-time algorithms can be achieved using MathWorks Toolboxes such as Simulink Fixed™, Stateflow®, Parallel Computing™ and HDL Coder™. For users familiar with all these aspects, the Speedgoat system becomes a very powerful tool, without needing to spend time on writing exhaustive C/C++ code. Eventually rapid prototyping systems can make the department more productive in terms of experimental research. Overall the entry level of the Speedgoat system is challenging for inexperienced users, as there exist none or very little literature explaining how to use and design efficient real-time algorithms. Major well established brands like dSpace and National Instruments are superior on these issues, providing extensive documentation making their products much easier putting into use.

Theoretically the xPC Target software and Speedgoat hardware can reach 200.0 *kS/s* sampling rates for an highly optimized algorithms, which is very satisfactory in most applications, including sampling and processing of HF voltage or current harmonics. However for closed-loop applications such as DC-link voltage regulation or current-controlled power converters, it is highly recommended expanding the target machine with Speedgoat IO325 FPGA-based analog-to-digital acquisition system. Enabling sampling rates and algorithmic implementations in the megahertz range, this fulfills even the most demanding control applications such as APFs. In purpose of synthesizing programmable harmonic voltages, improved performance can be achieved implementing the entire control in the FPGA domain.

The Speedgoat company does not supply any plug-and-play acquisition systems, so a custom solution was assembled becoming a repeatedly source of error. Either purchasing or constructing a solid reliable voltage and current acquisition system, would be the second major important hardware upgrade.

The xPC Target software comes with computer programs that through the target-host communication link, can be used to perform basically all kinds of real-time operations; tuning system parameters, reading off values and monitor signals on scopes. However the provided software was experienced as little user-friendly, and culminated into programming an own custom graphical user interface (*GUI*) greatly enhancing the user experience. GUIs are probably less important in the current state, as the scientific focus should primarily be towards functionality. On the sidenote technical solutions from dSpace and National Instruments provide very user-friendly solutions, superior to Speedgoat system.

5.2 Virtual instrumentation

Although most of the important discoveries have already been covered by P.Tenti and H.Paredes et al., and experimental results from this work are principally consistent with and support previous research. Detailed conclusions regarding experimental results are comprehensively reproduced in **Table 3.10**. As the virtual instrumentation was based on equipment and methodology very similar to what utilized by P.Tenti and H.Paredes et al, the obtained experimental results are considered to be of corresponding accuracy and credibility. Rapid prototyping systems can implement high-precision instruments, mainly limited by properties of the acquisition hardware. DC-offset on the analog input channels caused problems, which eventually were solved in the software-domain using high-pass input filters. Careful attention should be paid to the LEM voltage and current transducers, as they must be ensured working in their linear range. The CPT-algorithm was tested and proved reliable performance down to power level of $A = 6.0\,VA$. By mimicking an active power source the algorithm was confirmed being able to identify generative elements; active currents $\boldsymbol{i}_a$ were anti-phased with respective voltages, and instantaneous real power $q(t)$ turned negative. Average power components however cannot distinguish between sources or sinks. The setup was tested assembling a cluster of three standard PC workstations and monitors, so to demonstrate the realism of the conservative power theory and virtual instrument.

When dealing with symmetric bipolar loads the CPT fully agrees with the classic power theory, irrespective of voltage conditions. It offers more nuanced power and current decomposition when observing nonlinear diode and thyristor rectifiers, particularly reactive power Q tends to have less importance than what previously assumed. New interesting and promising characteristics were demonstrated in context of unsymmetric bipolar loads. The existence of negative and zero sequence currents, and their relation to unbalanced active $\boldsymbol{i}_a^u$ and reactive $\boldsymbol{i}_r^u$ components was documented. Notably N_a and N_q always occur in pair if the unsymmetric load is floating. Distortion power D and void currents $\boldsymbol{i}_v$ were surprisingly detected for RL-loads subjected to harmonic voltages. Evaluation of distortion power and void currents are particularly challenging in case of non-sinusoidal voltage regimes. The power decomposition and consequently current decomposition, were proven to be orthogonal for all voltage regimes and load characteristics. Apparent power A and active power P are the only CPT quantities that always coincide with equivalents from the classic power theory.

This project has through comprehensive tests demonstrated how the CPT exclusively reflects the load interaction with the grid, irrespective network voltage conditions. Its truly hard to come up with any scenario where the power and current decomposition fail. When it comes to analyzing and understanding the power network **from a physical perspective, the CPT stands out as a better alternative than to the popular *pq*-theory**. The physical interpretation suggested by the conservative power theory when dealing with single-phasing bipolar loads, is however highly questionable. Its currently the only case one can safely conclude that the CPT fails. This is of course an issue only when the CPT-algorithm is run in polyphase mode. Similarly the Fluke state-of-the-art power quality analyzer showed problems interpreting single-phasing loads correctly, notably this was due to incompetent usage of the device.

5.3 Active shunt compensation

Modeling both the physical and control system in Simulink at equal sample rate is not a realistic approach. The key concept for successful simulations was to distinguish the two systems using Rate Transition blocks. These blocks prevent algebraic loops and moreover options to model the hysteresis current controller and CPT-algorithm in discrete time domain at practical sample rates, adding realism to simulation results. The conservative power theory can provide excellent reactive and harmonic compensation under balanced sinusoidal voltage conditions. By compensating the reactive parcels, source current becomes in phase with voltages, and imaginary $q(t)$ and reactive power Q canceled. In case of harmonic currents induced by unlinear loads, these can be made sinusoidal with minimum RMS value, when injecting void currents. This will simultaneously eliminate oscillations in instantaneous real $p(t)$ and imaginary power $q(t)$. Reactive and distortion power are therefore nullified greatly reducing apparent power A, which minimizes loading of the power network making power factor unity.

Usability of the CPT under unbalanced non-sinusoidal voltage regimes, is however more questionable. Utilizing the same compensation strategy in distorted voltage regime, effectively produces *Fryze currents* having same waveform as non-sinusoidal voltages. Reactive power Q can still be eliminated making the average value of imaginary power zero $\int q(t)\,dt = 0$. Due to the invention of homo-integral voltage, the CPT provides robust reactive compensation of both inductive and thyristor rectifier loads, independent of voltage regime. However 2nd and 6th order power oscillations both in instantaneous real and imaginary power are inevitable, due to voltage related unsymmetric and harmonic properties in the current. The comparative pq-theory can provide additional compensation strategies such as sinusoidal source current and constant instantaneous power flow, notably not all objectives simultaneously. Apparently the CPT is less versatile than its counterpart particularly in harsh voltage conditions, conclusively the **CPT cannot provide more efficient shunt compensation than the pq-theory.** Under sinusoidal voltage regimes the pq-theory can selectively damp oscillations in instantaneous real and imaginary power. By further splitting the void current active and reactive into scattering components, its expected that the CPT can perform similar functionally as long as the voltage is balanced sinusoidal.

Dealing with RL-loads energized by distorted voltages it might not be appropriate filtering void currents, as the source current is closer to a sinusoidal waveform when leaving void currents unaltered. Simulations also revealed difficulty accomplishing a fully compensated system; there will always be minor presence of residual distortion power and associated void currents, due to switching ripple from the active power filter. This issue can be dealt with equipping the APF with higher order output filters, or as proposed replacing IGBTs with MOSTFETs enabling higher switching frequencies.

The response time of the conservative power theory matches similar methods. In case of load dynamics with steady state voltage, the CPT-algorithm needs 20.0 *ms (one cycle)* for the output to converge, whilst in case of simultaneously changing load and voltage, the convergence time may take up to 60.0 *ms (three cycles)*. Sampling rate of the CPT-algorithm should be set 100 times the maximum harmonic component of interest, in order to guarantee proper compensation. This implies 5.0 *kS/s* for fundamental components, and 100.0 *kS/s* or more for good resolution of 20th order harmonics. Restricted sample rate of the reference generator makes the APF incapable of fully cancel out harmonics, which will be evident in regions where the unlinear load commutates at high rate.

Utilizing an hysteresis current controller as pulse-width-modulator turned out to work nicely. Simulations demonstrated how the hysteresis band Δh effectively dictates the converter switching frequency f_{sw}. Narrowing the error tolerance band can easily push the switching frequency into extreme levels. Minimum achievable Δh is closely related to the sample rate f_{PWM} of the controller, as low sampling rate will drastically degrade the controller performance. The switching logic becomes random and conditional switching rules are violated. Results suggest sample rate of $f_{PWM} = 0.5\,MS/s$ as the absolute minimum. Very low error tolerance will result in output currents close to an ideal current source, having minimized ripple on expense of transistors switching at high rate.

Inverter DC-link voltage V_{DC} must be high enough or the APF tracking capability becomes lost. Required voltage level increases with the amplitude of APF current reference, and reactive compensation requires higher DC-link inertia compared to harmonic filtering. DC-voltage level also has considerable impact on switching frequency, causing excessive switching rate and increased current ripple in case of DC-link overvoltage. Using a single pole output filter led to very high switching rates, in some occasions much greater than what is generally presented in the literature. It must be underlined that other results is expected if alternative filter designs were implemented. This study has focused extensively on the importance of sampling frequency, as its such a critical performance measure of active power filters. All the gained knowledge will have great practical value in future experiments.

5.4 Recognized contribution

In the research field of the conservative power theory and shunt active power filtering, the author recognizes the following items as valuable contributions:

- The CPT has been tested experimentally in a comprehensive qualitative survey, based on virtual instrumentation. The scope of this study is overall more extensive and detailed than what is presently available in the literature.
- Apparently the first third party independent review of the CPT framework, but results principally support previous research by P.Tenti and H.Paredes.
- This project has experimentally verified the orthogonal decomposition of current and power flow, irrespective of load characteristics or voltage regimes.
- The conservative power theory was confirmed being able to identify an active generative network element.
- Contrary to the literature this research has intentionally focused on scenarios where the physical interpretation of the conservative power theory clearly fails.
- Due to splitting the unbalanced currents and unbalanced power into active and reactive components, new yet undisclosed properties have been revealed
- Behavior of instantaneous real and imaginary powers for various combinations of loads and voltages, have been presented in greater detail than what currently found in the literature.
- Available literature has mostly investigated balanced sinusoidal voltage regimes, while this work brings the CPT in context of all possible voltage conditions.
- Symmetric and unsymmetric bipolar loads in star, delta, floating, grounded, series and parallel configurations have been systematically tested. Also typical diode and thyristor rectifier loads have been investigated in various voltage regimes, in purpose of demonstrating the robustness of the conservative power theory.
- This thesis is richly provided with detailed waveforms from current and power flow. Combined with average power values this gives the reader an impression of the conservative power theory which previously has not been shown.

5.5 Future work

This project work has inspired the author to continue in academia. When hopefully becoming hired as a Scientific Assistant at the department of electric power engineering, there are several relevant topics that deserves further investigation:

- The ultimate goal is to experimentally implement active shunt compensation in non-sinusoidal voltage regimes, using a variety of both reactive, unsymmetric and unlinear loads. This will include one converter operated as a programmable voltage source, and possibly two converters constituting the active power filter.
- In-depth literature study regarding DSP and FPGA technology, will be the first and most important step towards implementing highly efficient real-time algorithms. More effort is also required getting experienced with all the capabilities of Simulink and associated Toolboxes; Simulink Fixed, Stateflow, Parallel Computing and HDL Coder.
- Control system related to the programmable voltage source should be developed in the FPGA-domain for enhanced performance. The alternative is to purchase a purpose-built controllable voltage source, which will be quite expensive.
- Improving the acquisition system should be highly prioritized. Designing and constructing such a system in-house will be a time consuming assignment, if not a prefabricated unit is purchased.
- This study proposes new implementation of active power filters, based on using MOSFETs for enhanced flexibility and performance. This new voltage source inverter should also provide access to a DC-link midpoint, enabling inclusion of zero sequence currents and voltages.
- Future experiments should investigate compensation of floating and grounded unsymmetric bipolar loads, as these are sparsely documented in the literature.
- The full potential of the CPT should be exploited. This involves splitting void current into its three parcels; generated, active and reactive scattering currents. Distortion power should be decomposed into current and voltage distortion power.
- Analysis and shunt compensation of the neutral conductor, as these topics are little mentioned in the literature.
- In context of APF there should be shed more light on how the conservative power theory handles load and voltage dynamics.
- Fundamental mathematical properties of the CPT are already extensively covered, however more in-depth analytical examples would be of valuable contribution.
- Alternative high-order power filters should be investigated, as the first-order filter proved to be less suited for active power filtering applications.
- DC-link voltage regulation will be an important part of the APFs control system, and alternative current controllers should be examined.

- Distributed reactive and local harmonic compensation through coordinated use of APFs, SVCs and TSCs, is hardly covered in the literature and should be reviewed.
- Revisited definition of sequence components have been proposed by Tenti et al.[C25]. Paired with the CPT this might open for improved shunt compensation in context of unsymmetric non-sinusoidal voltage regimes.

References

Conservative Power Theory

[A1] T.S.Haugan. *TET5500 - Specialization Project. Reactive Power Compensation in Non-Sinusoidal Regimes.* Research Report. NTNU, 2010.

[A2] E.Tedeschi. "Cooperative Control of Distributed Compensation Systems in Electric Networks Under Non-Sinusoidal Operations". PhD. Thesis. Università degli Studi di Padova, 2009. URL: `https://sites.google.com/site/elitedeschi/family-recipes/available-papers` (visited on 07/05/2012).

[A3] P.Tenti, P.Mattavelli, and E.Tedeschi. "Compensation Techniques Based on Reactive Power Conservation". In: *Electrical Power Quality and Utilization, Journal* XIII.1 (2007), pp. 17–24.

[A4] P.Tenti and P.Mattavelli. "Third-Order Passive Load Identification Under Non-Sinusoidal Conditions". In: *European Trans. on Electrical Power Engineering (ETEP)* 12.2 (2002-04), pp. 93–100. DOI: `10.1002/etep.4450120203`.

[A5] H.K.M.Paredes, A.Costabeber, and P.Tenti, eds. *Application of Conservative Power Theory to Cooperative Control of Distributed Compensators in Smart Grids.* International School on Nonsinusoidal Currents and Compensation (ISNCC) (June 15–18, 2010). Lagow, Poland, pp. 190–196. DOI: `10.1109/ISNCC.2010.5524488`.

[A6] P.Tenti, P.Mattavelli, and H.K.M.Paredes, eds. *Conservative Power Theory, Sequence Components and Accountability in Smart Grids.* International School on Nonsinusoidal Currents and Compensation (ISNCC) (June 15–18, 2010). Lagow, Poland, pp. 37–45. DOI: `10.1109/ISNCC.2010.5524473`.

[A7] P.Tenti and P.Mattavelli, eds. *A Time-Domain Approach to Power Term Definitions under Non-Sinusoidal Conditions.* Sixth International Workshop on Power Definitions and Measurements under Non-Sinusoidal Conditions (Oct. 13–15, 2003). Milano, Italy, pp. 1–10.

[A8] E.Tedeschi, P.Tenti, P.Mattavelli, and D.Trombetti, eds. *Cooperative Control of Electronic Power Processors In Micro-Grids.* Power Electronics Conference

(COBEP) (Sept. 27–Oct. 1, 2009). Brazil, pp. 1–8. DOI: `10.1109/COBEP.2009.5347596`.

[A9] P.Tenti, D.Trombetti, E.Tedeschi, and P.Mattavelli, eds. *Compensation of Load Unbalance, Reactive Power and Harmonic Distortion by Cooperative Operation of Distributed Compensators.* 13th European Conference on Power Electronics and Applications (EPE) (Sept. 8–10, 2009), pp. 1–10. ISBN: 978-1-4244-4432-8.

[A10] P.Tenti, D.Trombetti, E.Tedeschi, and P.Mattavelli, eds. *Cooperative Operation of Active Power Filters by Instantaneous Complex Power Control.* International Conference on Power Electronics and Drive Systems (PEDS) (Nov. 27–30, 2007), pp. 555–561. DOI: `10.1109/PEDS.2007.4487756`.

[A11] P.Tenti, E.Tedeschi, and P.Mattavelli, eds. *Optimization of Hybrid Filters for Distributed Harmonic and Reactive Compensation.* International Conference on Power Electronics and Drive Systems (PEDS). Vol. 1. 2005, pp. 292–297. DOI: `10.1109/PEDS.2005.1619701`.

[A12] E.Tedeschi and P.Tenti, eds. *Cooperative Design and Control of Distributed Harmonic and Reactive Compensators.* International School on Nonsinusoidal Currents and Compensation (ISNCC) (June 10–13, 2008). Lagow, Poland, pp. 1–6. DOI: `10.1109/ISNCC.2008.4627482`.

[A13] H.Paredes, F.P.Marafão, D.I.Brandao, and I.S.Diniz, eds. *Conservative Power Theory Discussion and Evaluation by Means of Virtual Instrumentation.* Power Electronics Conference (COBEP) (Sept. 27–Oct. 1, 2009). Brazil, pp. 423–430. DOI: `10.1109/COBEP.2009.5347670`.

[A14] H.K.M.Paredes, F.P.Marafão, and L.C.P.da Silva, eds. *Selective Current Compensators Based on the Conservative Power Theory.* PowerTech Conference (June 28–July 2, 2009). Bucharest, Romania, pp. 1–7. DOI: `10.1109/PTC.2009.5282113`.

[A15] F.P.Marafão, D.I.Brandao, H.K.M. Paredes, and L.da Silva, eds. *Possible Shunt Compensation Strategies Based on Conservative Power Theory.* International School on Nonsinusoidal Currents and Compensation (ISNCC) (June 15–18, 2008). Lagow, Poland, pp. 162–167. DOI: `10.1109/ISNCC.2010.5524498`.

[A16] H.K.M.Paredes, F.P.Marafão, T.M.Terrazas, and P.J.A.Serni, eds. *Harmonic, Reactive and Unbalance Compensation by Means of CPT Framework.* Power Electronics Conference (COBEP) (Sept. 27–Oct. 1, 2009). Brazil, pp. 741–748. DOI: `10.1109/COBEP.2009.5347610`.

[A17] M.Jafar, M.Molinas, and P.Tenti, eds. *Application of Conservative Power Theory for Active Power Filtering of Line-Commutated HVDC for Offshore Wind Power.* PowerTech Conference (June 19–23, 2011). Trondheim, Norway, pp. 1–8. DOI: `10.1109/PTC.2011.6019464`.

[A18] E.Tedeschi, P.Tenti, and P.Mattavelli, eds. *Synergistic Control and Cooperative Operation of Distributed Harmonic and Reactive Compensators.* Power

Electronics Specialists Conference (PESC) (June 15–19, 2008), pp. 654–660. DOI: `10.1109/PESC.2008.4592004`.

[A19] P.Tenti, H.K.M.Paredes, and P.Mattavelli, eds. *Conservative Power Theory, a Framework to Approach Control and Accountability Issues in Smart Micro-Grids.* Power Electronics, IEEE Transactions on. Vol. 26. 3. 2011, pp. 664–673. DOI: `10.1109/TPEL.2010.2093153`.

[A20] P.Tenti, H.K.M.Paredes, Fernando P. Marafão, and P.Mattavelli, eds. *Accountability and Revenue Metering in Smart Micro-Grids.* Applied Measurements For Power Systems (AMPS), 2010 IEEE International Workshop on (Sept. 22–24, 2010). Aachen, 2010, pp. 74–79. DOI: `10.1109/AMPS.2010.5609516`.

PQ Power Theory

[B21] H.Akagi, E.H.Watanbe, and M.Aredes. *Instantaneous Power Theory and Applications to Power Conditioning.* 1st ed. John Wiley & Sons Inc., 2007. Chap. 1-4. ISBN: 978-0470107614.

[B22] H.K.M.Paredes, F.P.Marafão, and L.C.P.da Silva, eds. *A Comparative Analysis of FBD, PQ and CPT Current Decompositions – Part I: Three-Phase Three-Wire Systems.* PowerTech Conference (June 28–July 2, 2009). Bucharest, Romania, pp. 1–8. DOI: `10.1109/PTC.2009.5282173`.

[B23] H.K.M.Paredes, F.P.Marafão, and L.C.P.da Silva, eds. *A Comparative Analysis of FBD, PQ and CPT Current Decompositions – Part II: Three-Phase Four-Wire Systems.* PowerTech Conference (June 28–July 2, 2009). Bucharest, Romania, pp. 1–6. DOI: `10.1109/PTC.2009.5282169`.

[B24] F.P.Marafão, H.Paredes, and L.da Silva, eds. *Critical Evaluation of FBD, PQ and CPT Current Decompositions for Four-wire Circuits.* Power Electronics Conference (COBEP) (Sept. 27–Oct. 1, 2009). Brazil, pp. 49–57. DOI: `10.1109/COBEP.2009.5347595`.

Power Theories

[C25] P.Tenti, J.L.Willems, P.Mattavelli, and E.Tedeschi. ''Generalized Symmetrical Components for Periodic Non-Sinusoidal Three-Phase Signals''. In: *Electrical Power Quality and Utilisation, Journal* XIII.1 (2007), pp. 9–15.

[C26] J.Machowski, J.W.Bialek, and J.R.Bumby. *Power System Dynamics: Stability and Control.* 2nd ed. John Wiley & Sons Inc., 2008. ISBN: 978-0-470-72558-0.

[C27] K.R. Padiyar. *FACTS Controllers in Power Transmission and Distribution.* 1st ed. New Age International Publishers Ltd., 2007. ISBN: 978-81-224-2541-3.

Experimental Setup

[D28] Speedgoat GmbH. *Modular-Large Real-Time Target Machine. User's Manual (SN1415-1416).* 2011.

[D29] Speedgoat GmbH. *Custom FPGA Bitstream and xPC Target Driver Blockset. User's Manual).* 2011.

[D30] H.Kolstad and K.Ljøkelsøy. *20 kW IGBT-Converter - Description.* 3rd ed. AN 01.12.12. SINTEF/NTNU. Sept. 20, 2002.

[D31] K.Ljøkelsøy. *Brake Chopper Control Board v2.1 - Documentation.* 2.1. AN 00.12.48. SINTEF. Nov. 24, 2000.

[D32] K.Ljøkelsøy and R.Lund. *Driver Interface Board v4.0 - Documentation.* 2nd ed. AN 00.12.49. SINTEF/NTNU. Nov. 24, 2000.

[D33] K.Ljøkelsøy. *Driver Interface v2.2.* 2nd ed. AN 08.12.04. SINTEF. Jan. 11, 2008.

[D34] K.Ljøkelsøy. *Driversignal Testcard v1.0 - Description.* AN 08.12.11. SINTEF. Feb. 12, 2009.

[D35] T.Rogne and K.Ljøkelsøy. *Gatedriver SMD2.* AN 01.12.17. SINTEF. June 6, 2001.

[D36] H.Kolstad. *Acquisition Card v1.0 - Description.* AN 02.12.61. NTNU. Mar. 21, 2001.

[D37] Fluke. *Fluke 434/435 - Three Phase Power Quality Analyzer.* Fluke Corporation. Apr. 2006. URL: `http://www.elfa.spb.ru/uploads/tdpdf/aa434-435_manual_en.pdf` (visited on 09/02/2011).

[D38] Tektronix. *MSO/DPO2000 Mixed Signal Oscilloscope Series.* URL: `http://www.tek.com/oscilloscope/mso-dpo2000`.

[D39] LEM. *Isolated Current and Voltage Transducers. Characteristics - Applications - Calculations.* 3rd ed. URL: `http://www.lem.com/images/stories/files/Products/P1_5_1_industry/CH24101E.pdf` (visited on 05/09/2011).

[D40] LEM. *Current Transducer LA 55-P.* URL: `http://www.lem.com/docs/products/la\%2055-p\%20e.pdf` (visited on 05/09/2011).

[D41] LEM. *Voltage Transducer LV 25-600.* URL: `http://www.lem.com/docs/products/lv\%2025-600\%20e.pdf` (visited on 05/09/2011).

[D42] Welwyn Components TT electronics. *Aluminimum Housed Wirewound Resistors. WH Series - Specifications.* Welwyn Components Limited. (Visited on 06/01/2011).

[D43] TracoPower. *Enclosed Power Supplies - TXL Series*, pp. 1–10. URL: `http://www.tracopower.com/products/txl.pdf` (visited on 05/04/2011).

[D44] NTNU. *3Ph Thyristor Bridge - Documentation.* Sept. 22, 1989.

[D45] EKF System. *CCM-BOOGIE-Core™ 2 Duo CompactPCI® CPU. High Performance Dual Core Processor.* Sept. 2010.

[D46] General Standards Corp. *PMC66-16AI64SSA/C. 64-Channel, 16-Bit Simultaneous Sampling PMC Analog Input Board.* Version 092307. Sept. 2010.

[D47] TEWS Technologies. *TPMC681. 64 Digital Inputs/Outputs (Bit I/O).* Nov. 2006.

[D48] TEWS Technologies. *TPMC553. 32/16 Channels of 16 Bit D/A.* Sept. 2008.

[D49] Acromag. *PMC-DX501/DX2001 - Reconfigurable FPGA With TTL I/O.* June 2005.

[D50] Noratel AS. *3Ph Transformer - Mounting Guide.* Apr. 28, 2009. URL: `http://noratel.no/content/download/3468/348844/file/3fase_montasje.pdf` (visited on 07/18/2011).

[D51] Klockner Moeller. *Contactors - Technical Specifications.* Apr. 28, 2009.

[D52] Crydom. *DRA & DRS Series.* Apr. 28, 2009. URL: `http://www.crydom.com/en/Tech/crydom_drac.pdf` (visited on 06/11/2011).

Power Electronics

[E53] N.Mohan, T.M.Undeland, and W.P.Robbins. *Power Electronics - Converters, Applications and Design.* 3rd ed. John Wiley & Sons Inc., 2002. ISBN: 978-0471226932.

[E54] B.K.Bose. *Power Electronics and Variable Frequency Drives: Technology and Applications.* 1st ed. IEEE Press, 1996. ISBN: 978-0780310841.

[E55] K.Sangsun and P.N.Enjeti. "A New Hybrid Active Power Filter (APF) Topology". In: *Power Electronics, IEEE Transactions on* 17.1 (2002), pp. 48–54. DOI: `10.1109/63.988669`.

[E56] P.Vaibhav and K.Sanjiv. *Simulation of Shunt Active Power Line Conditioner (APLC) for Three Phase AC/DC Converter.* VSRD International Journal of Electrical, Electronics & Communication Engineering. 2011, pp. 504–513. ISBN: 2231-3346. URL: `http://www.vsrdjournals.com/EEC/Issue/2011_11_Nov/Web/2_Vaibhav_Purwar_480_Research_Article_Nov_2011.pdf` (visited on 01/29/2012).

[E57] Z.Chen, Y.Luo, and M.Chen. "Control and Performance of a Cascaded Shunt Active Power Filter for Aircraft Electric Power System". In: *IEEE Transactions On Industrial Electronics* 59.9 (2012), pp. 3614–3623. DOI: `10.1109/TIE.2011.2166231`.

[E58] F.J.Taylor. *Digital Filters: Principles and Applications with MATLAB: (IEEE Press Series on Digital and Mobile Communication).* 1st ed. Wiley-IEEE Press, 2012. ISBN: 978-0470770399.

[E59] Semikron. *Data Sheet - SEMITRANS® M IGBT Modules SKM400GB123D.* SEMIKRON International GmbH, pp. 195–200. URL: `http://www.digchip.com/datasheets/download_datasheet.php?id=872985part-number=SKM400GB123D` (visited on 02/10/2012).

[E60] Semikron. *Application Manual for Semiconductors. Datasheet Rating for MOSFET, IGBT and Thrysitors.* SEMIKRON International GmbH, pp. 131–214. URL: `http://www.semikron.com/skcompub/en/section3_Datasheet_Ratings_for_MOSFET_IGBT_Diodes_and_Thyristors.pdf` (visited on 02/12/2012).

[E61] T.Wildi. *Electrical Machines, Drives and Power Systems.* 6th ed. Prentice Hall, 2005. ISBN: 978-0131776913.

[E62] ABB. *Power Quality Filters PQFI-PQFM-PQFS. Improving Power Quality for efficiency and reliability.* ABB Quality Products. 2012, pp. 1–12. DOI: 2GCS304019A0070. URL: `http://www05.abb.com/global/scot/scot209.nsf/veritydisplay/0238f5978b9eff2bc12579e300284177/$file/2GCS304019A0070-PQF\%20Pamphlet.pdf` (visited on 04/07/2012).

[E63] Siemens. *Reactive-Power Compensation and Active Filter. Lower power costs with the intelligent SIVACON technology.* Siemens AG, Low Voltage Distribution. 2011, pp. 1–4. DOI: 10003-E38-11T-D2091-7600. URL: `https://www.hqs.sbt.siemens.com/gip/general/dlc/data/assets/hq/manual/02_pi_ReactivePowerCompensationandActiveFilter_EN_2902.pdf` (visited on 04/07/2012).

[E64] P.Mattavelli. "A Closed-Loop Selective Harmonic Compensation for Active Filters". In: *IEEE Transactions on Industry Applications* 37.1 (2001), pp. 81–89. DOI: 10.1109/28.903130.

Virtual Instrumentation

[F65] R.Berger, ed. *Virtual Instrumentation for Test, Control and Design.* Systems, Applications and Technology Conference (May 2, 2008). Long Island, pp. 1–2. DOI: 10.1109/LISAT.2008.4638952.

[F66] M.Popa, R.Ionel, V.Groza, and M.Marcu, eds. *Educational Virtual Instrumentation Application for System Identification.* Instrumentation and Measurement Technology Conference (IMTC) (Apr. 24–27, 2006). Sorrento, Italy, pp. 842–846. DOI: 10.1109/IMTC.2006.328215.

[F67] H.Goldberg. "What is Virtual Instrumentation?" In: *IEEE Instrumentation & Measurement Magazine* 3.4 (2000-10), pp. 10–13. DOI: 10.1109/5289.887453.

[F68] L.Cristaldi, A.Ferrero, and V.Piuri. "Programmable Instruments, Virtual Instruments and Distributed Measurement Systems. What is Really Useful, Innovative and Technically Sound?" In: *IEEE Instrumentation & Measurement Magazine* 2.3 (1999-09), pp. 20–27. DOI: `10.1109/5289.783108`.

Software

[G69] Speedgoat GmbH. *Speedgoat I/O Moduels: Latency Times Added to the Cycle Time (TET).* 2011.

[G70] Speedgoat GmbH. *PWM FPGA Code Module: Latency Calculation.* 2011.

[G71] MathWorks. *Matlab®7 - Creating Graphical User Interface.* R2011b. The MathWorks Inc. 2011. URL: `http://www.mathworks.se/help/pdf_doc/matlab/buildgui.pdf` (visited on 09/15/2011).

[G72] MathWorks. *Simulink®- Graphical User Interface.* R2011b. The MathWorks Inc. 2011. URL: `http://www.mathworks.se/help/pdf_doc/simulink/slgui.pdf` (visited on 08/08/2011).

[G73] MathWorks. *Simulink®- Reference.* R2011b. The MathWorks Inc. 2011. URL: `http://www.mathworks.se/help/pdf_doc/simulink/slref.pdf` (visited on 07/25/2011).

[G74] MathWorks. *xPC Target™- User's Guide.* R2011b. The MathWorks Inc. 2011. URL: `http://www.mathworks.se/help/pdf_doc/xpc/xpc_target_ug.pdf` (visited on 05/19/2011).

[G75] MathWorks. *xPC Target™- API Guide.* R2011b. The MathWorks Inc. 2011. URL: `http://www.mathworks.se/help/pdf_doc/xpc/xpc_target_api_ugref.pdf` (visited on 08/08/2011).

[G76] MathWorks and hydro Quebec. *SimPowerSystems®- User's Guide.* R2011b. The MathWorks Inc. 2011. URL: `http://www.mathworks.se/help/pdf_doc/physmod/powersys/powersys.pdf` (visited on 02/11/2011).

[G77] MathWorks. *Simulink®- User's Guide.* R2011b. The MathWorks Inc. 2011. URL: `http://www.mathworks.se/help/pdf_doc/simulink/sl_using.pdf` (visited on 05/10/2011).

[G78] MathWorks. *Matlab®- Programming Fundamentals.* R2011b. The MathWorks Inc. 2011. URL: `http://www.mathworks.se/help/pdf_doc/matlab/matlab_prog.pdf` (visited on 08/03/2011).

[G79] MathWorks. *xPC Target Data Logging Methodologies.* May 28, 2009. URL: `http://www.mathworks.com/matlabcentral/fileexchange/17492-xpc-target-data-logging-methodologies` (visited on 10/10/2011).

Appendix A

Supplement to virtual instrumentation

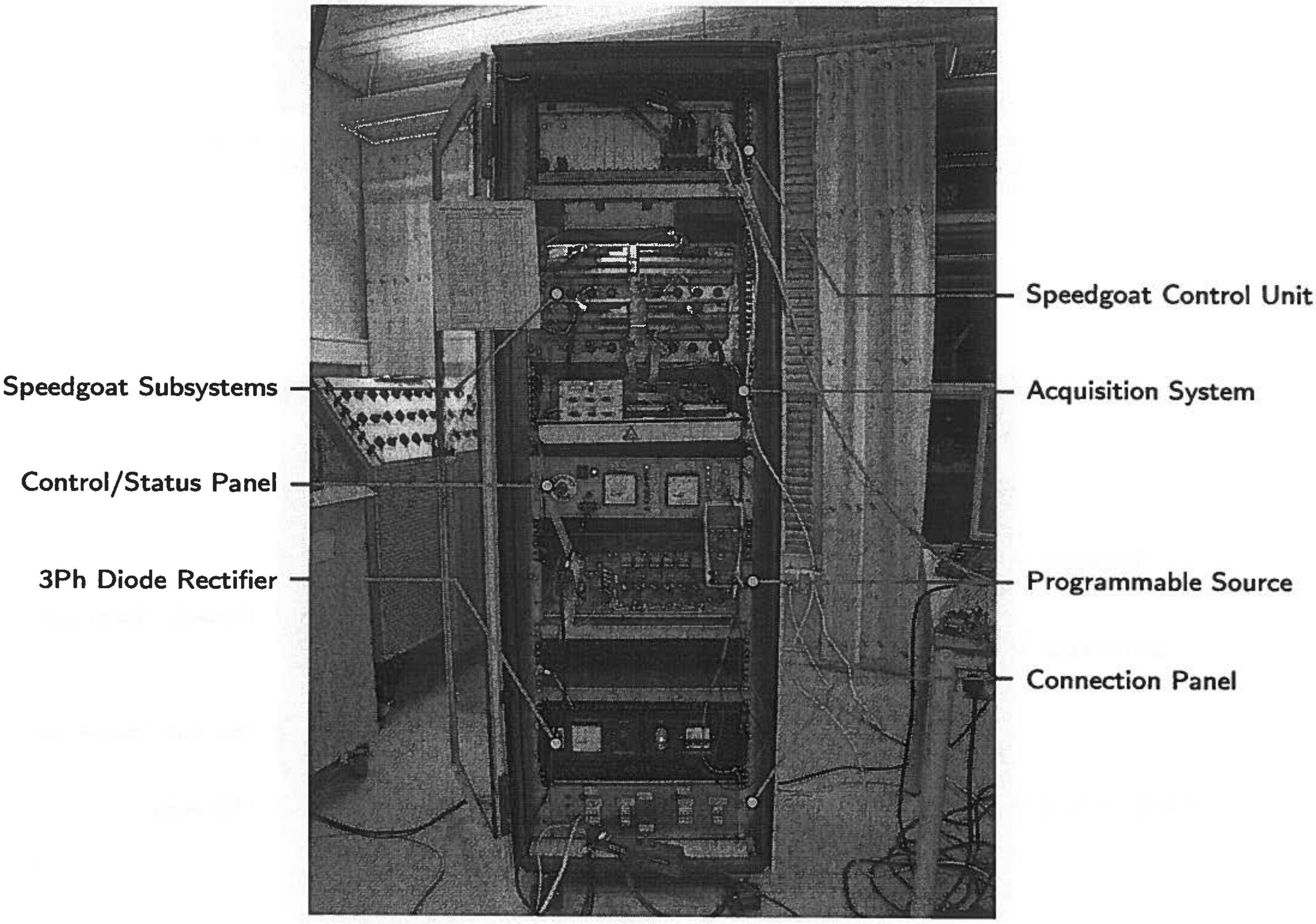

Figure A.1 – *Rack containing Speedgoat real-time target machine implementing the control system, 20 kW voltage source converter operating as programmable source, grid-connected diode rectifier charging VSC DC-link and acquisition system for collecting LEM-signals. Initially when starting the project none of the infrastructure was available, so the entire experimental setup had to be planned and assembled prior to the experiments. This process on its own took three and a half months to complete.*

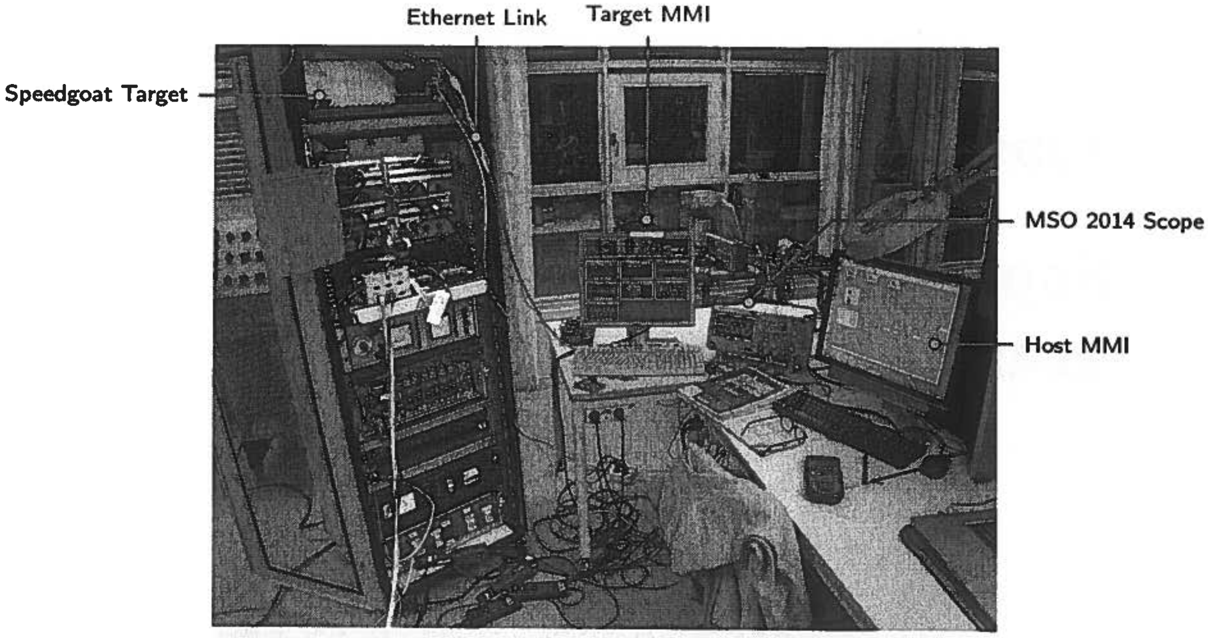

Figure A.2 – *Target machine is equipped with separate keyboard and monitor for direct interaction with the user. Similar and more user friendly functionality is provided on the Host machine connected to the Target via Ethernet Link. However target-host communication is TCPU intensive.*

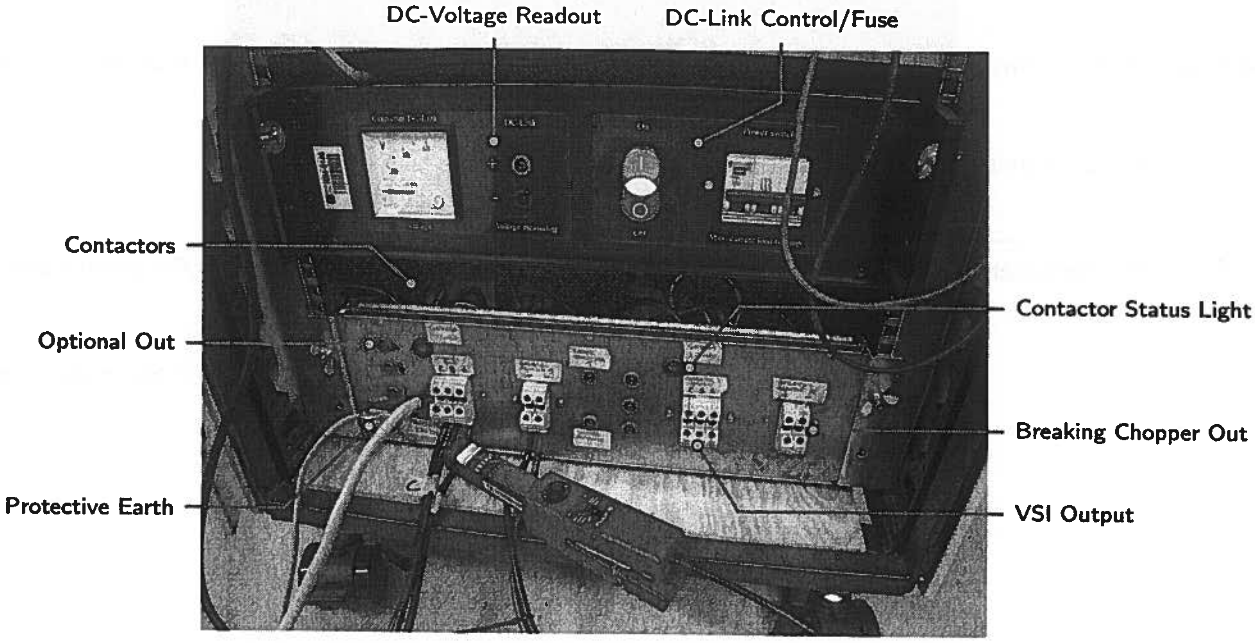

Figure A.3 – *Above: multipurpose unit containing a contactor-based soft starter, which can be used to soft start grid-connected converters. It also includes a diode rectifier intended for energizing converter DC-link. Below: converter interface unit was designed specifically to be controlled by the Speedgoat system, which turned out to be very successful. It was built to include possibly two converters in future.*

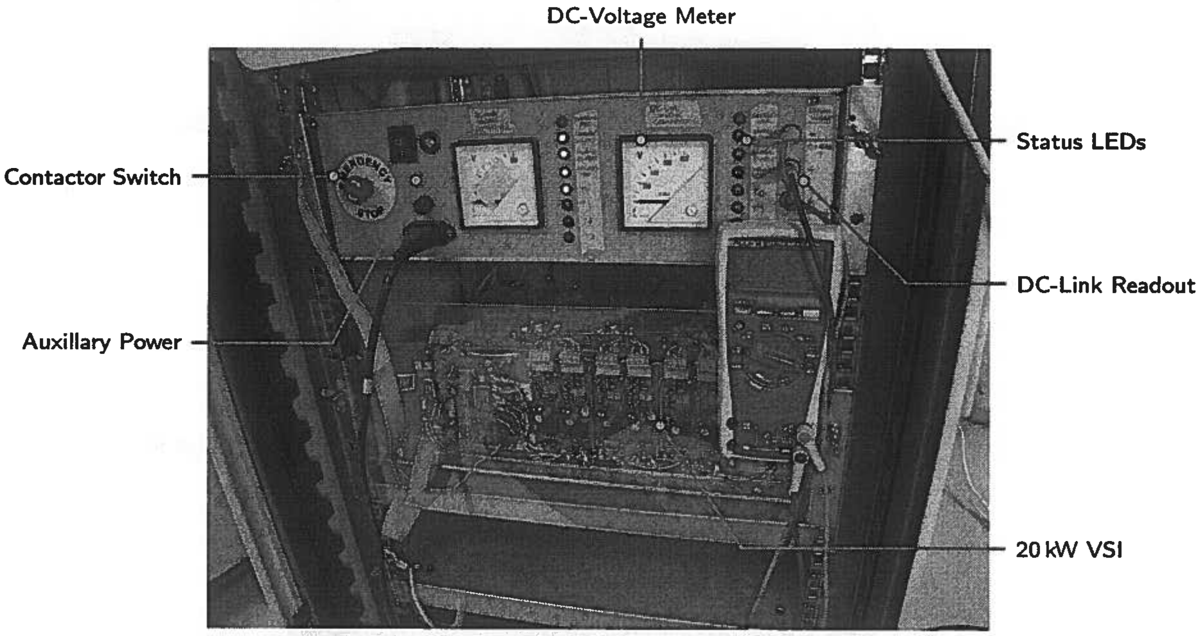

Figure A.4 – *Above: In case of hazardous situations the programmable voltage source could be disconnected and discharged, with an handy emergency stop switch. All auxiliary power for the rack was turned on/off and supplied from this unit. Two optional readouts of DC-link voltage were required by HSE authority. Status LEDs provided visual status of important system parameters. Below: IGBT-based voltage source converter. This is a rugged and good quality unit developed by NTNU/SINTEF.*

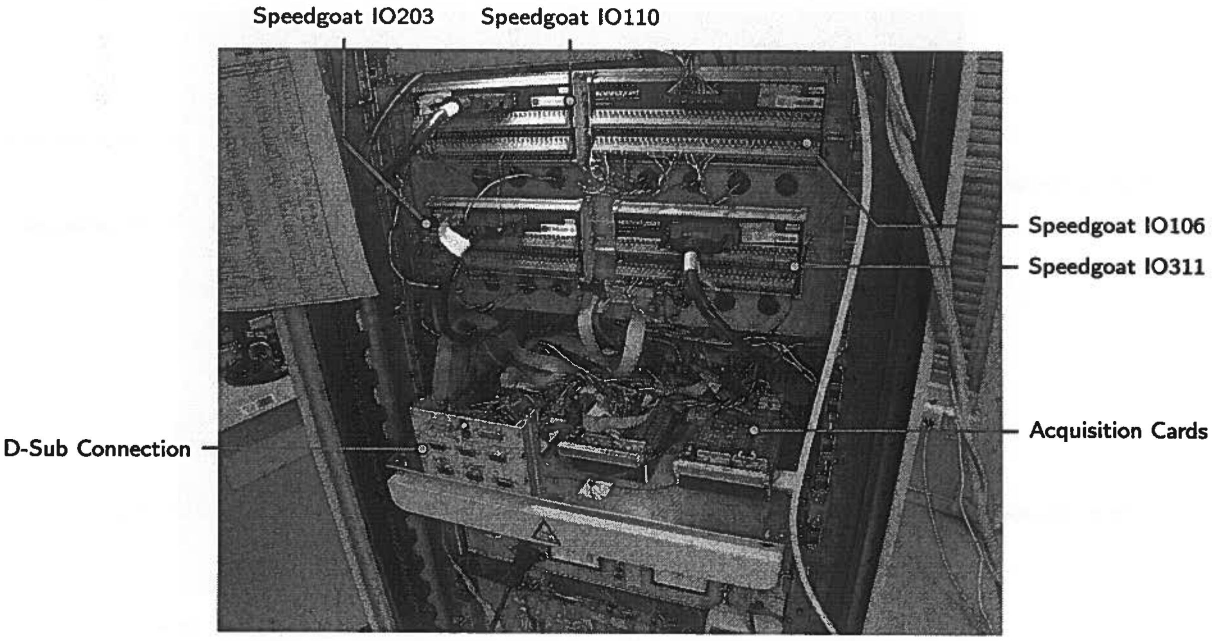

Figure A.5 – *Below: the acquisition system was a constantly source of error and frustration. LEM sensor boards and acquisition system, were interconnected using flat cables and D-Sub connectors. Above: each Speedgoat subsystem is connected to the outside world using terminal boards. Not exactly plug-and-play, but it works.*

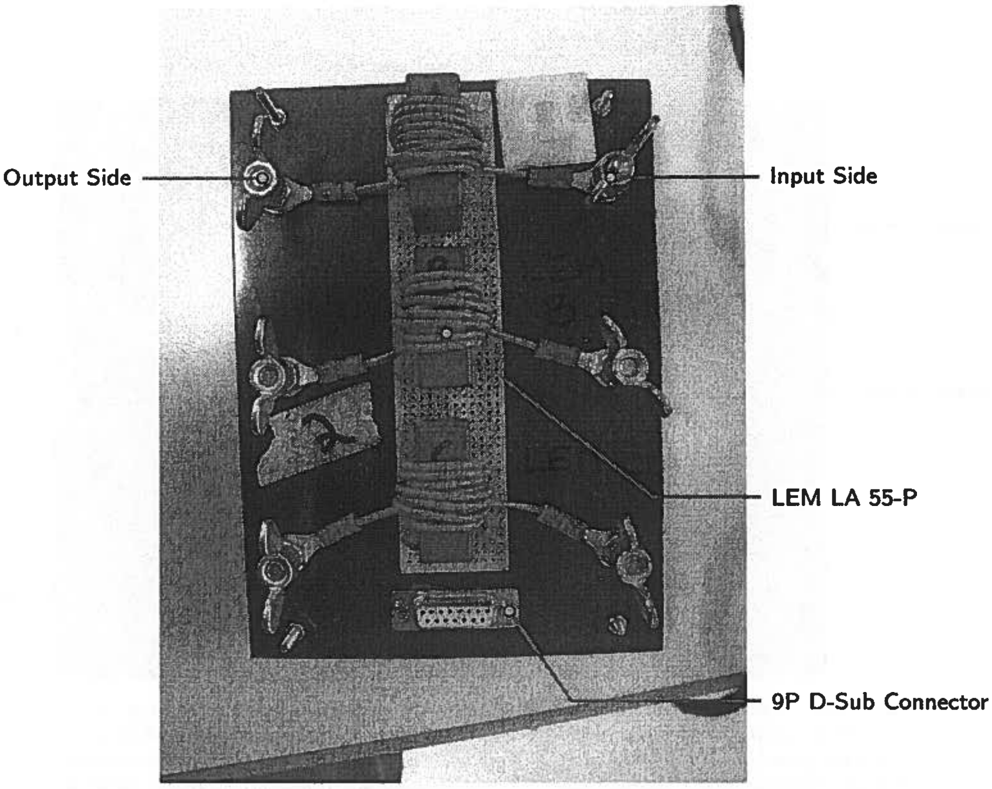

Figure A.6 – *Current inputs for the virtual instrument were measured using LEM hall-effect transducers. The LEM LA 55-P unit is rated for 60 A nominal current. Experiments included load currents at much lower levels, so linear operation was ensured by using multiple turns.*

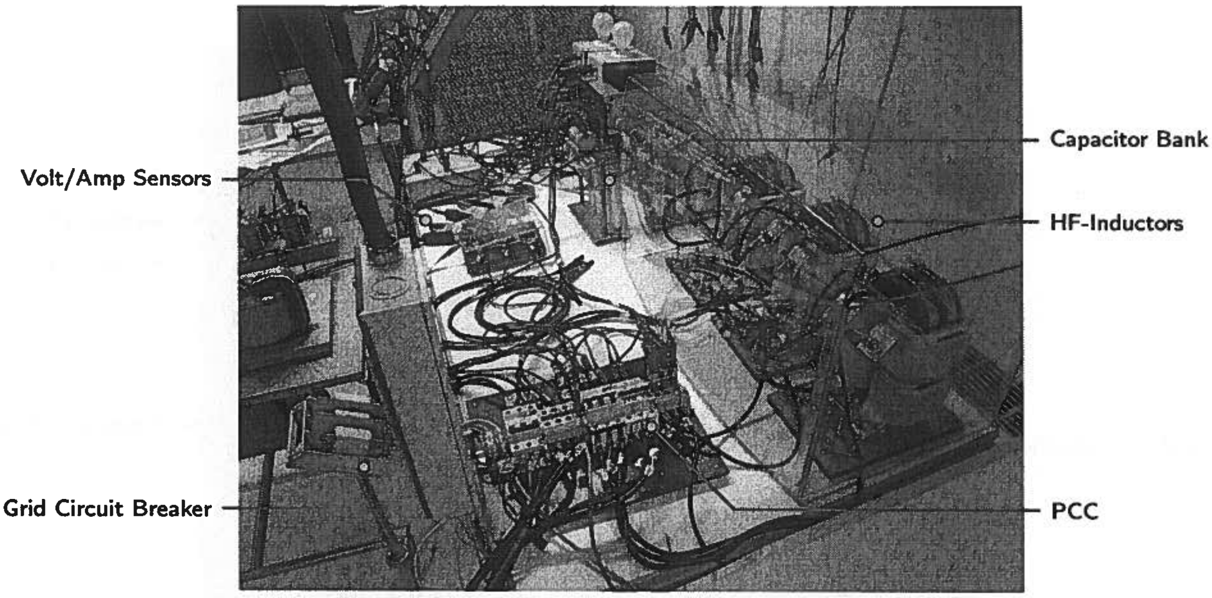

Figure A.7 – *When finally getting hands on special high-frequency inductors this greatly improved to converter performance. All inputs and outputs at the point of common connection was secured by automatic fuses, ensuring safety and protecting the experimental setup.*

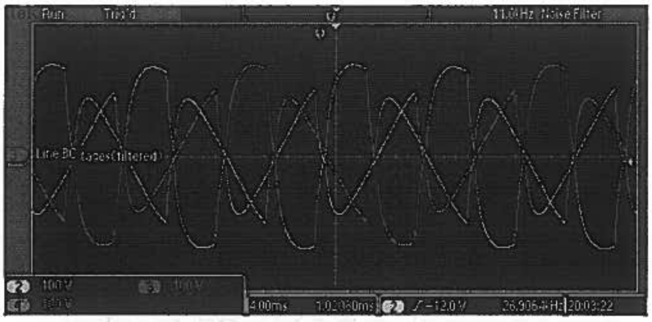

(a) *Voltage source converter forced into overmodulation mode.*

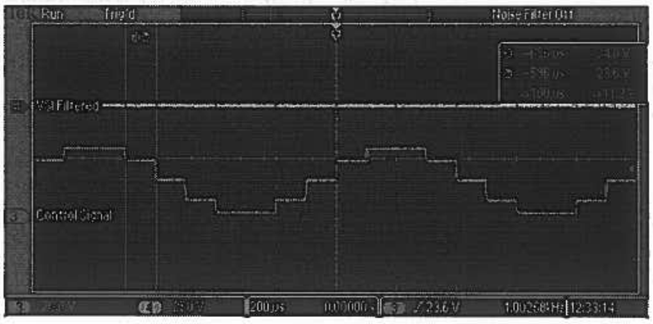

(b) *Synthesizing a 1.0 kHz sinewave at 10.0 kHz sampling rate.*

Figure A.8 – *Demonstrating hardware limitations.*

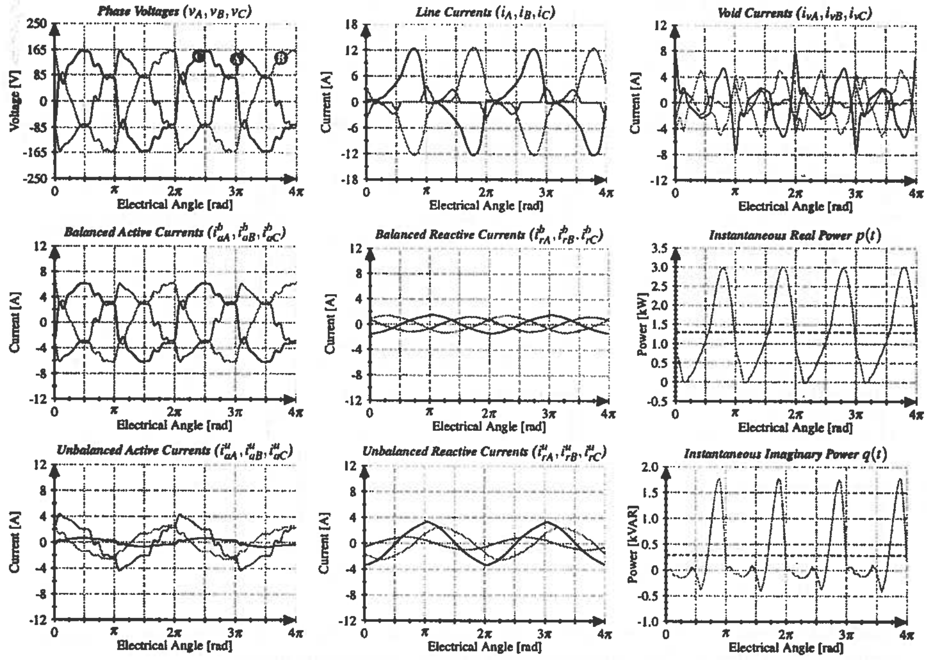

Figure A.9 – *Case 46 - Diode bridge feeding RC-load. Worst case scenario, diodes commutating unnaturally. CPT-decomposition of currents and powers remain unaltered nonetheless.*

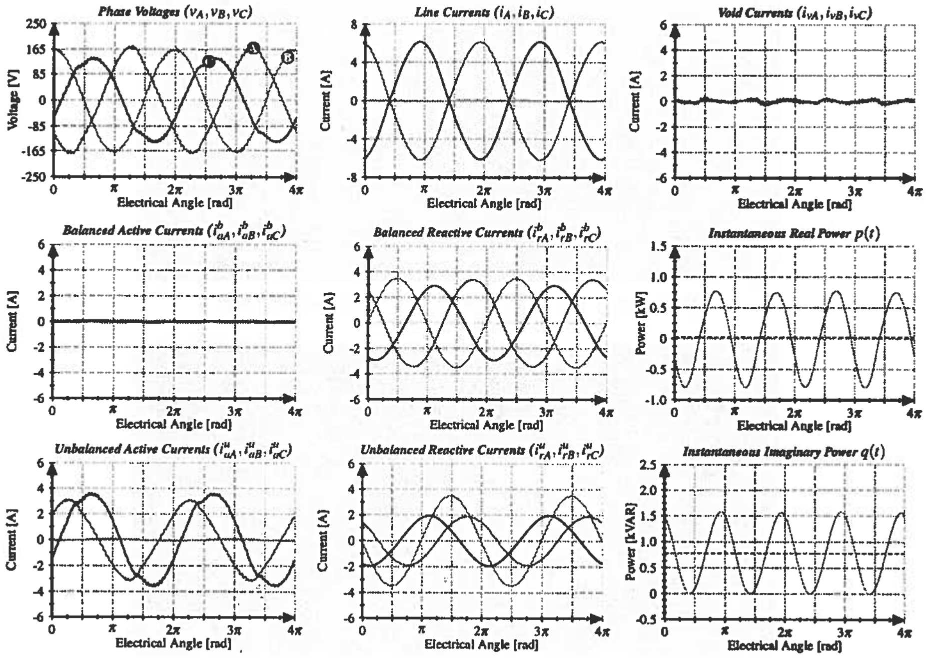

Figure A.10 – *Case 54 - Single-phasing (L-load) similar to case 51. Balanced and unbalanced reactive currents credited to all phases, even phase B which is running open circuit.*

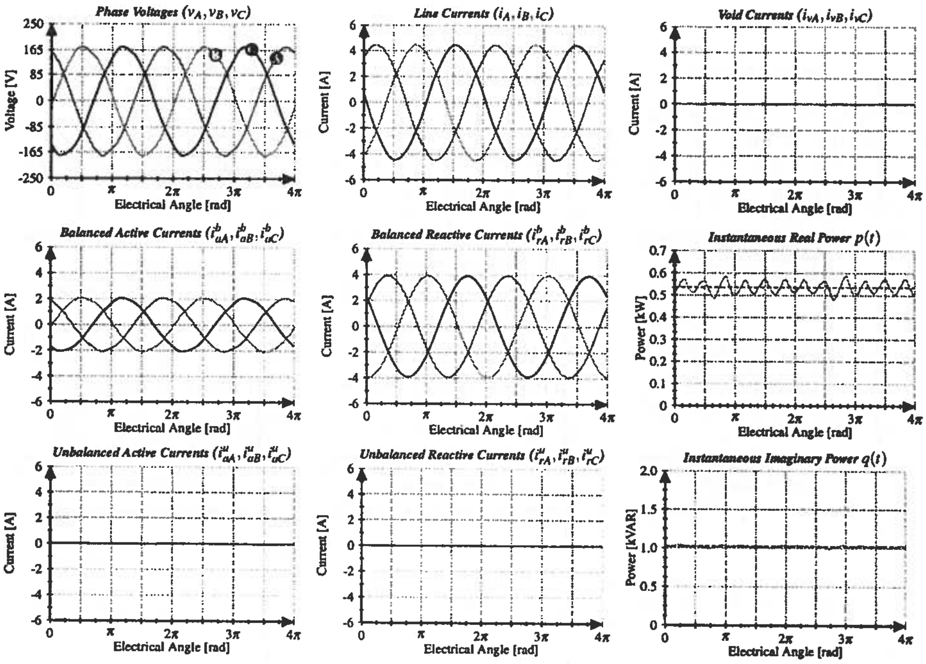

Figure A.11 – *Case 55 - R(YF) and L(YF)-loads connected in parallel. Verifying that series or parallel topologies yields same CPT-decomposition when the load is symmetric bipolar.*

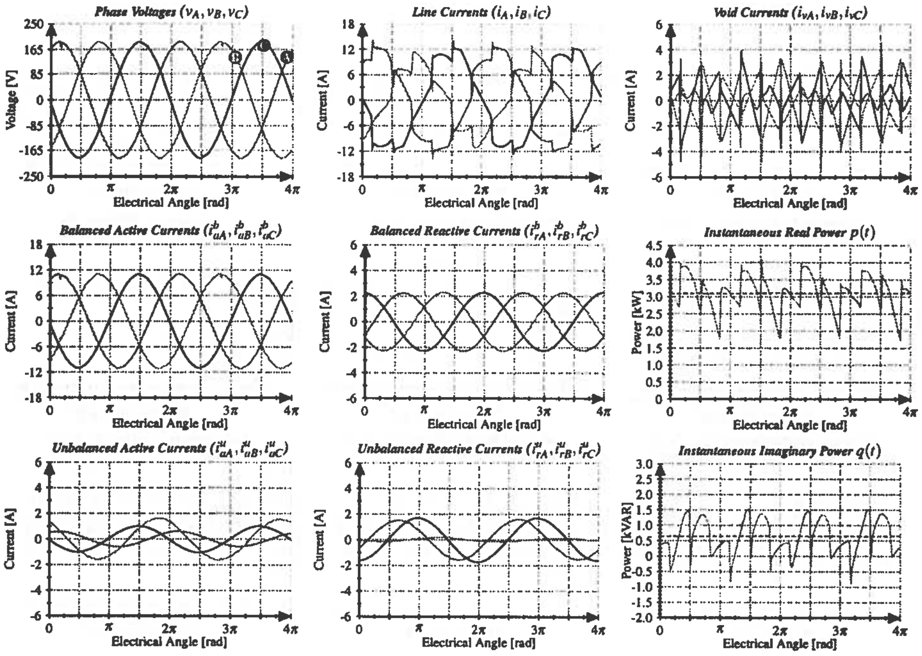

Figure A.12 – *Case 61 - Diode and thyristor rectifiers paralleled with single-phasing R-load. Scenario similar to described in*[B24]*, resulting in highly distorted and unbalanced line currents.*

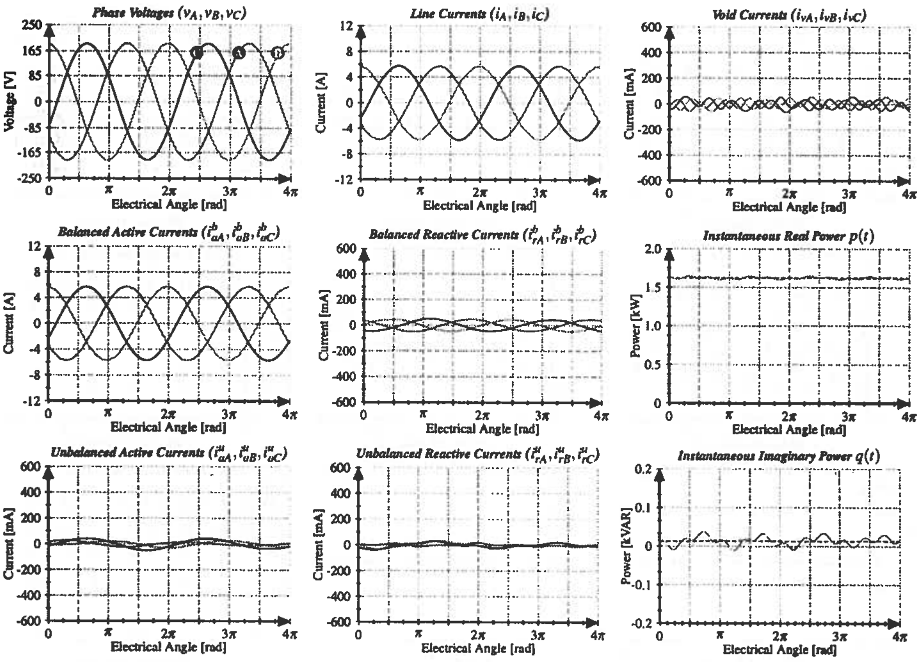

Figure A.13 – *Case 62 - Diode bridge feeding R-load. Cut frequency lowpass filters* $f_C(LP) = 75\,Hz$ *effectively remove all harmonics. Only fundamental active and reactive parts are considered by the CPT.*

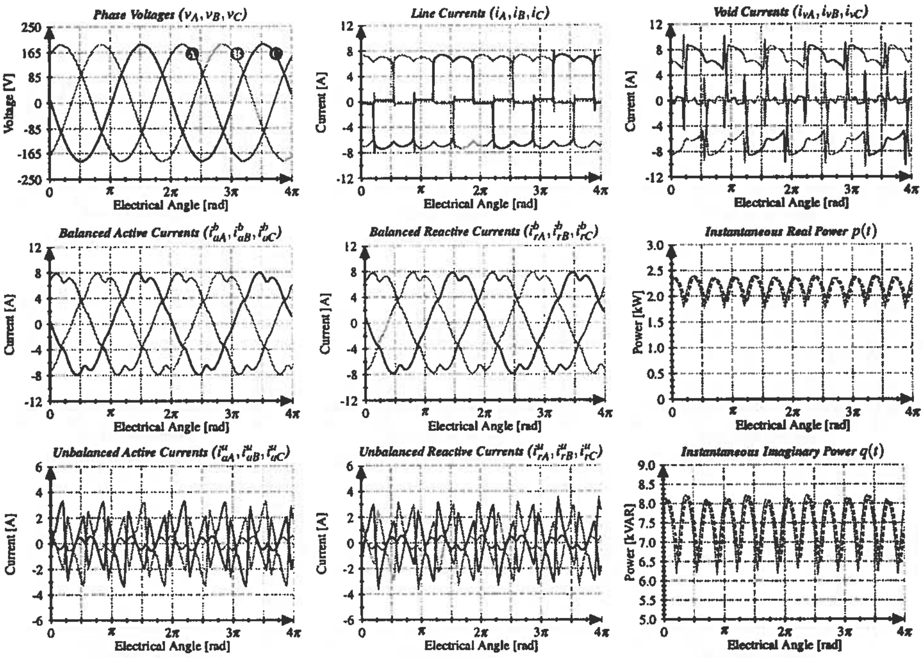

Figure A.14 – *Case 63 - Diode bridge feeding R-load. With $f_{CPT} = 1.5\,kHz$ the CPT-algorithm can work fast with convergence time of $t_{conv} = 0.67\,ms$. Phase sequence and physical interpretation of various parcels are however questionable.*

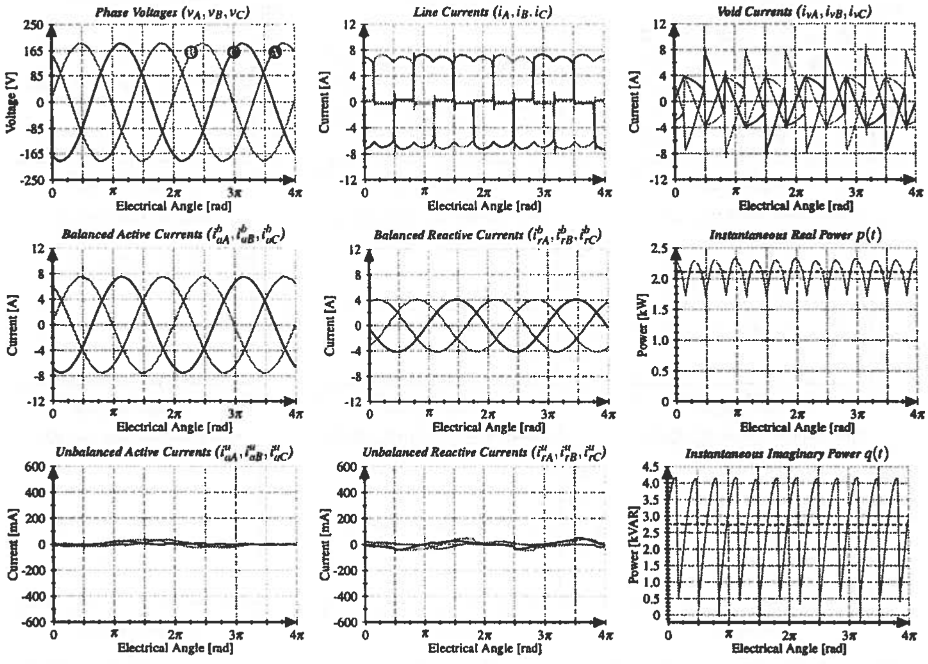

Figure A.15 – *Case 64 - Diode bridge feeding R-load. With $f_{CPT} = 100\,Hz$ results in $t_{conv} = 10\,ms$. This compromise gives fast computation time (2x improvement), and partly restores the phase relationship of CPT current components.*

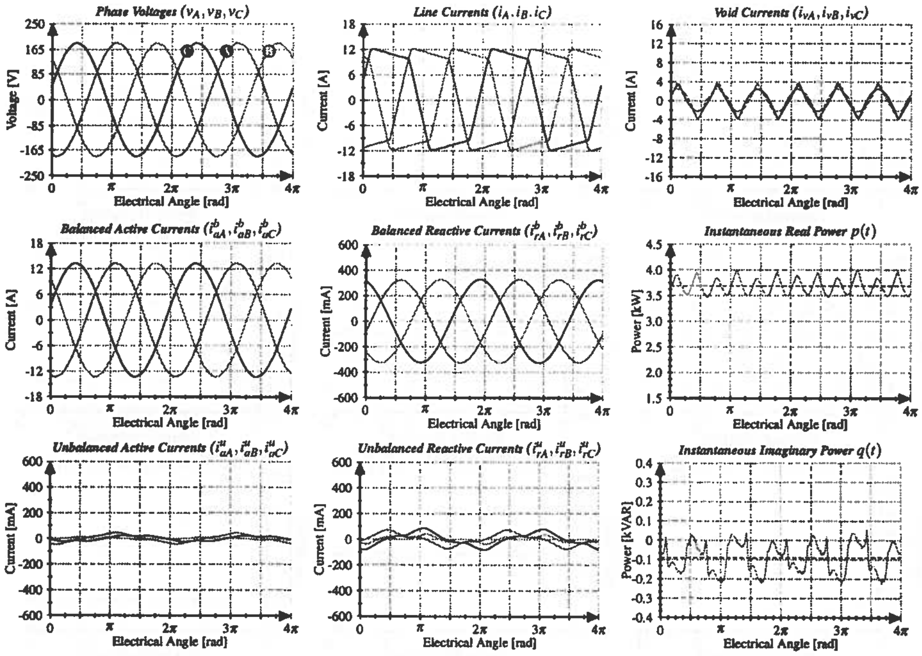

Figure A.16 – *Case 65 - Symmetric R-load. Line currents adjusted high enough to saturate the current actuators. The LEM LA 55-P with 10 turns saturated at $I = 4.33\ A_{RMS}$ resulting in fictive void currents. Defect auxiliary power unit (low voltage) was also part of the issue.*

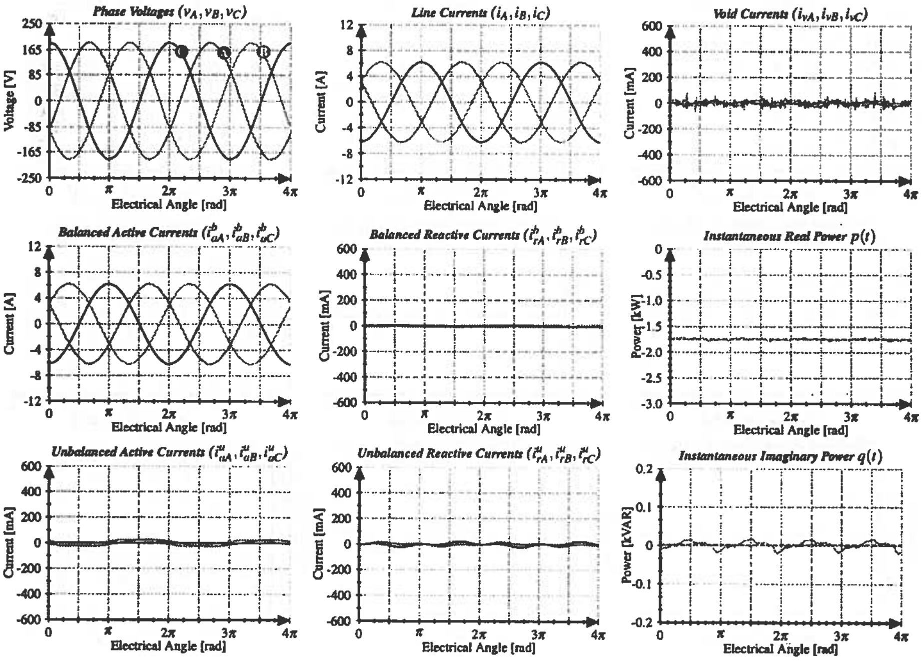

Figure A.17 – *Case 66 - Symmetric R-load. Verifying that the CPT-algorithm can recognize generative elements. Balanced active terms in anti-phase with respective voltages and real power flow $p(t)$ is negative, which is in accordance with the conventional source definition.*

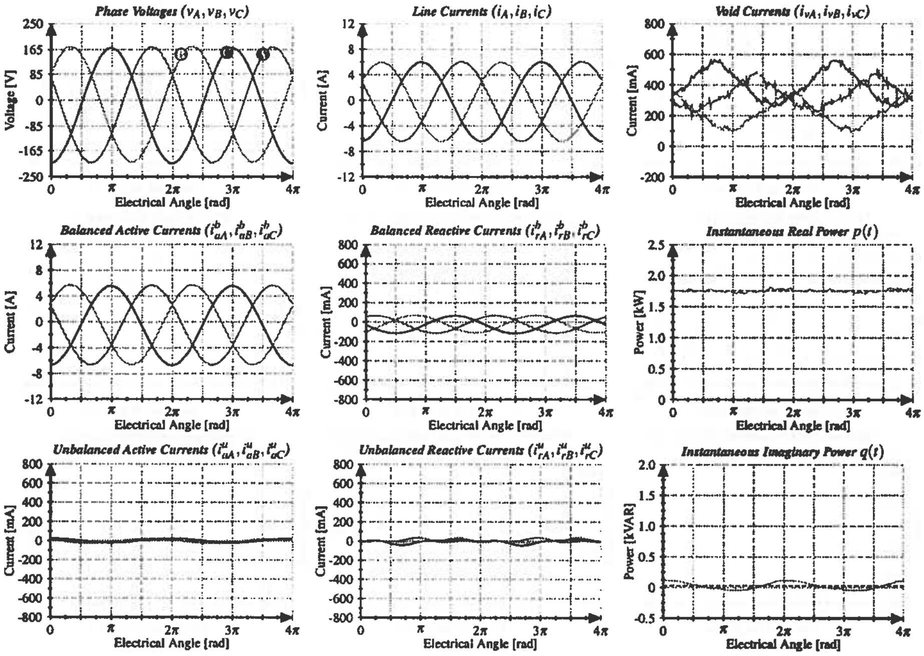

Figure A.18 – *Case 67 - Symmetric grid-connected R-load. Removing high-pass filters reveal significant offset in acquired and decomposed signals. Also invalid detection of void currents and distortion power.*

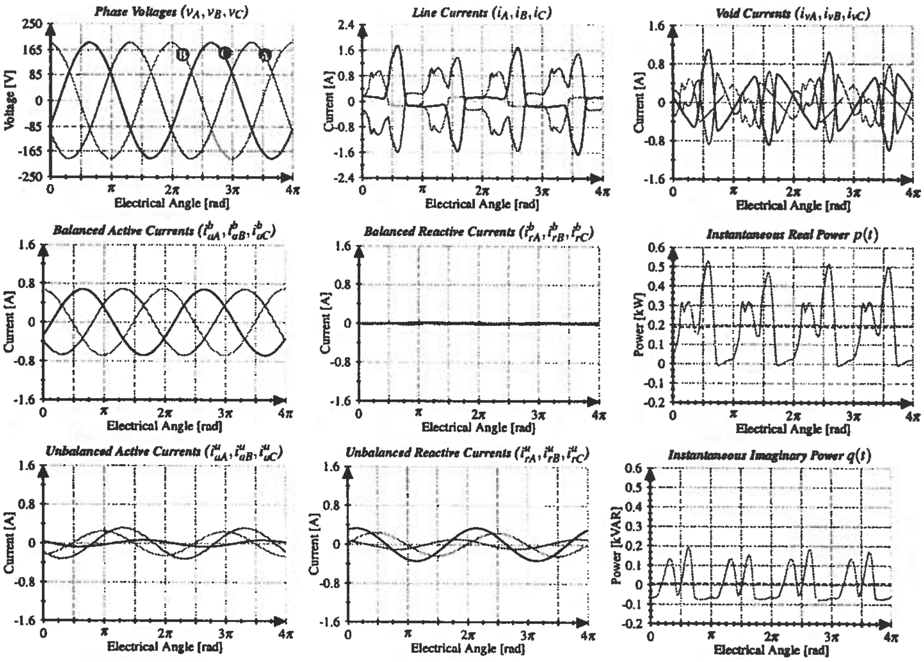

Figure A.19 – *Case 68 - Common type of load, clusters of PCs and monitors cause severely distorted and unbalanced currents. CPT-algorithm easily separate balanced/unbalanced active and void current components.*

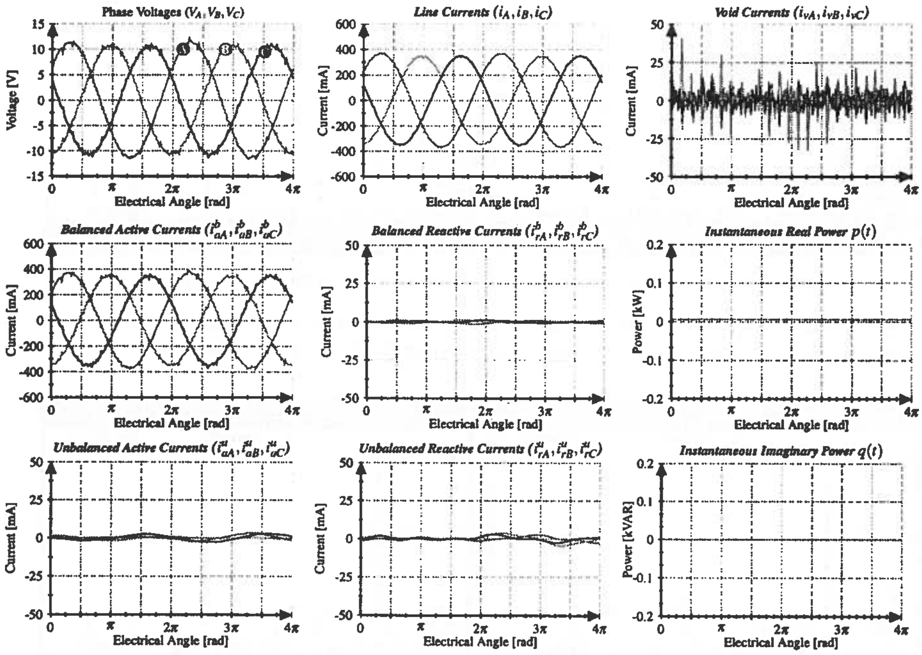

Figure A.20 – *Case 69 - Symmetric grid-connected R-load. The voltages are transformed down to demonstrate irregular output from LEM LV 25-600 voltage transducers. Similar behavior can be observed from LA 55-P current transducers when sensing low primary currents.*

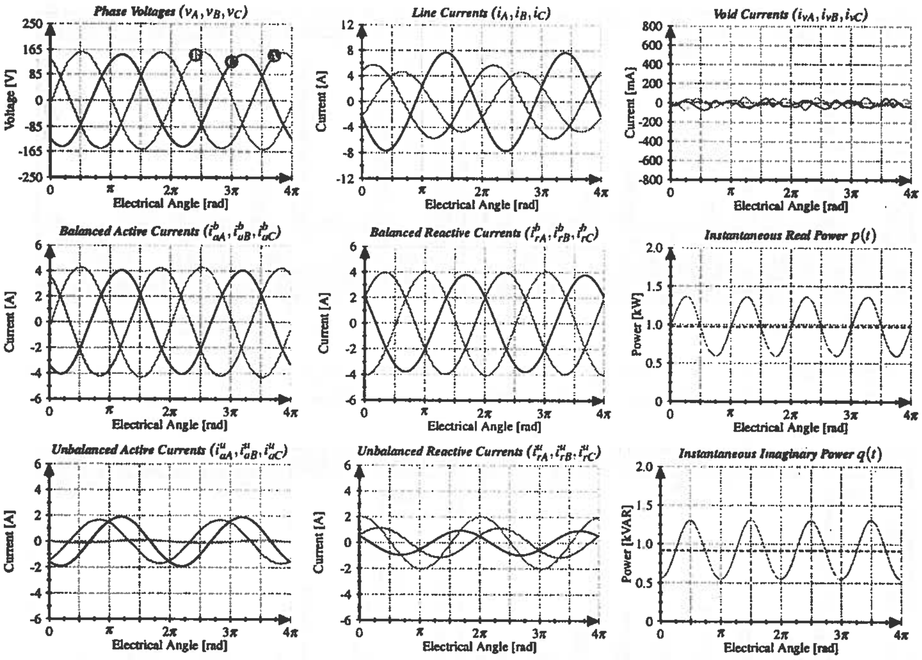

Figure A.21 – *Case 90 - Unsymmetric D-connected RL-load. Unsymmetric delta-topologies always feature this special decomposition because of two independent and one dependent line current.*

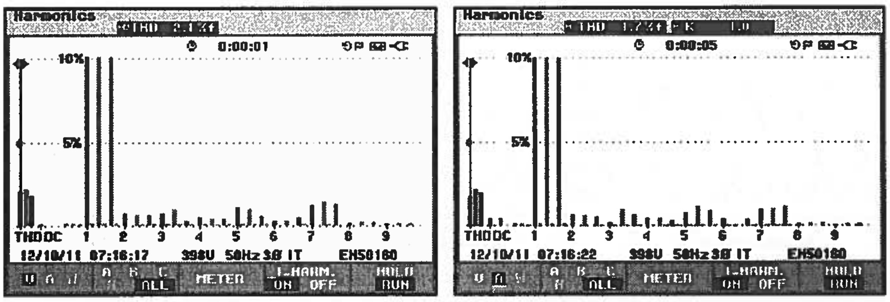

(a) *FFT Line voltages* (b) *FFT Line currents*

Figure A.22 – *Experiment 1: Frequency spectrum for sinusoidal three-phase voltage generated by VSI. Same harmonics are found in line currents as the load is a purely resistive impedance.*

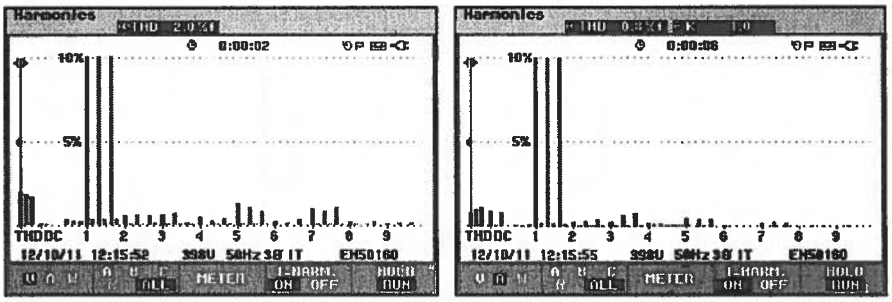

(a) *FFT Line voltages* (b) *FFT Line currents*

Figure A.23 – *Experiment 11: Frequency spectrum for same voltage generated by in case 1. The load is approximately purely inductive, thus damping of current harmonics.*

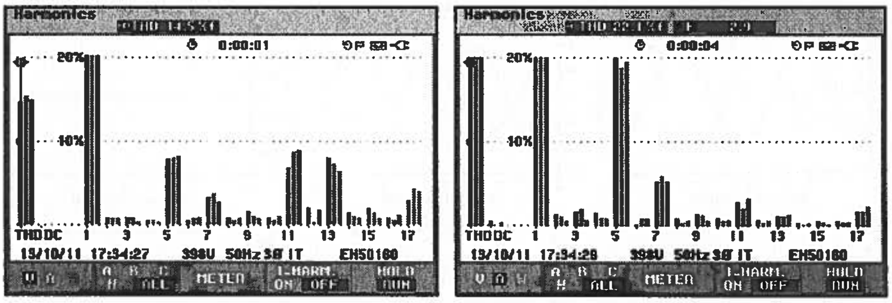

(a) *FFT Line voltages* (b) *FFT Line currents*

Figure A.24 – *Experiment 41: Frequency spectrum for 3-Ph diode bridge under distorted voltage regime. The harmonic difference of voltage and currents is classified as void currents.*

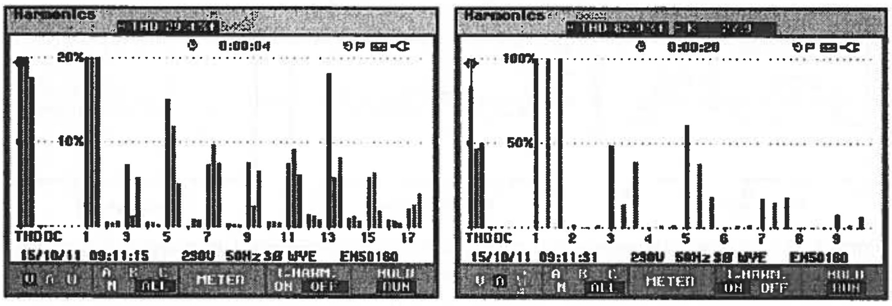

(a) *FFT Phase voltages* (b) *FFT Line currents*

Figure A.25 – *Experiment 50 - Frequency spectrum for 3-Ph thyristor rectifier under unbalanced distorted voltage regime. Line currents are extremely distorted. Compensating void currents would theoretically reduce THD down from 82.9 to 29.4 % or even more.*

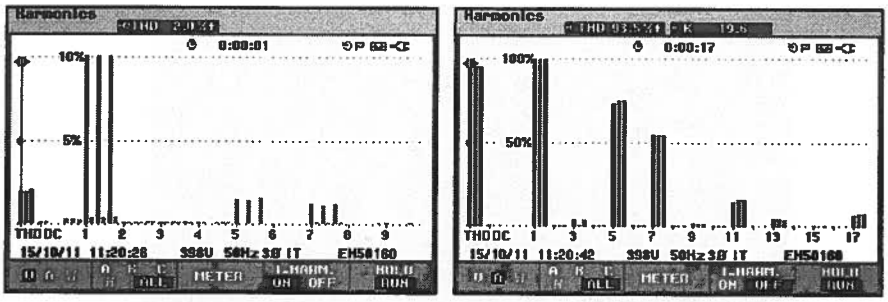

(a) *FFT Line voltages*　(b) *FFT Line currents*

Figure A.26 – *Experiment 59: Frequency spectrum for sinusoidal three-phase voltage generated by VSI. Same harmonics are found in line currents as the load is a purely resistive impedance.*

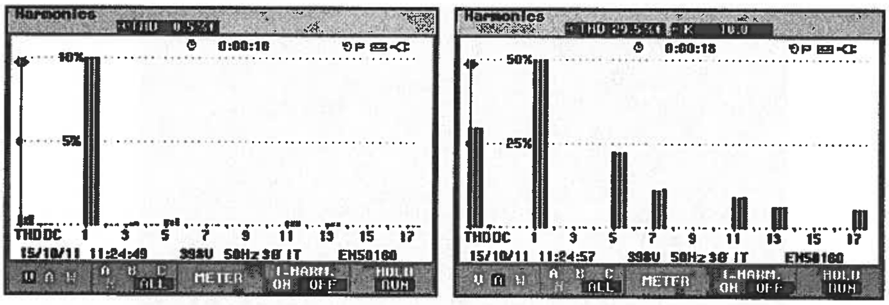

(a) *FFT Line voltages*　(b) *FFT Line currents*

Figure A.27 – *Experiment 60: Frequency spectrum for same voltage generated by in case 1. The load is approximately purely inductive, thus damping of current harmonics.*

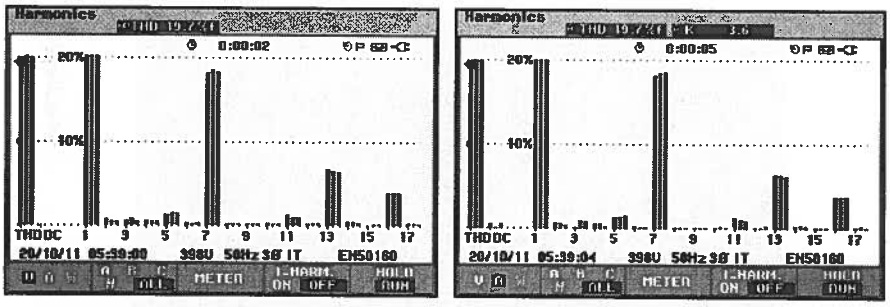

(a) *FFT Line voltages*　(b) *FFT Line currents*

Figure A.28 – *Experiment 71: Frequency spectrum for 3-Ph diode bridge under distorted voltage regime. The harmonic difference of voltage and currents is classified as void currents.*

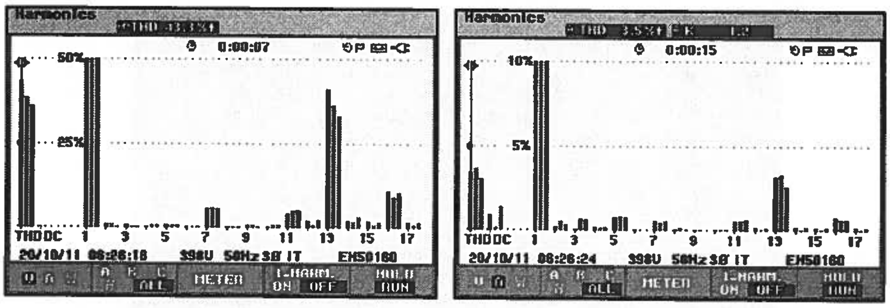

(a) *FFT Line voltages*　(b) *FFT Line currents*

Figure A.29 – *Experiment 74 - Frequency spectrum for 3-Ph thyristor rectifier under unbalanced distorted voltage regime. Line currents are extremely distorted. Compensating void currents would theoretically reduce THD down from 82.9 to 29.4 % or even more.*

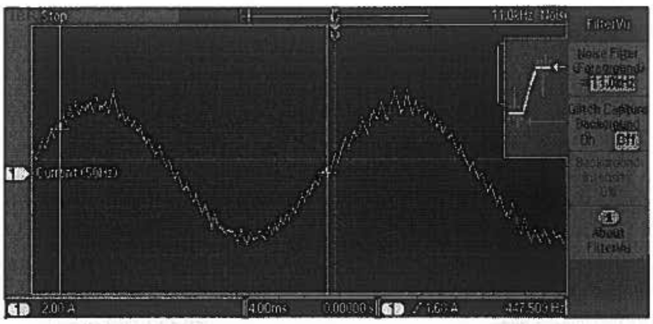

Figure A.30 – *Hysteresis control producing fundamental sinewave.*

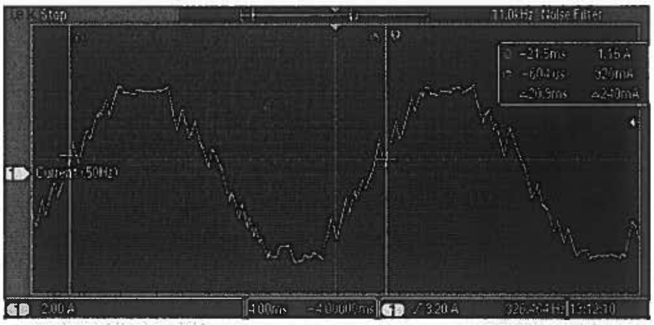

Figure A.31 – *Deformed sinewave due to insufficient DC-link voltage level.*

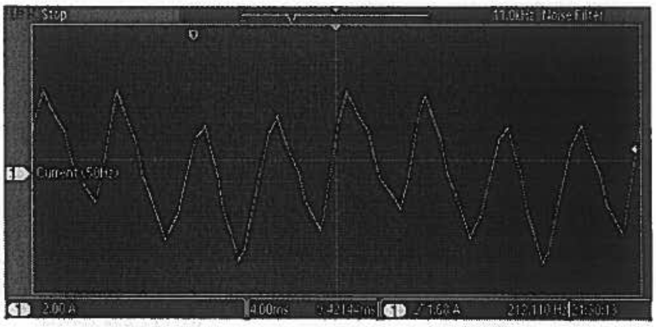

Figure A.32 – *Hysteresis control producing 5th order sinewave.*

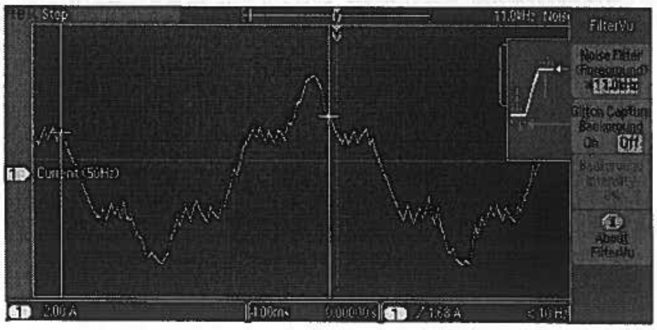

Figure A.33 – *Combined fundamental and 5th order harmonic.*

Appendix B

Miscellaneous documentation

Signal Routing - Acquistion Boards

Acquistion Card 1

Input Channel	Color	Signal	Connected	Rm
A	Purple	Voltage, Converter - Phase A	Dsub 8, LEM A	165Ω
B	Green	Voltage, Converter - Phase B	Dsub 8, LEM B	165Ω
C	Yellow	Voltage, Converter - Phase C	Dsub 8, LEM C	165Ω
D	Blue	Current, Grid - Phase A	Dsub 2, LEM A	100Ω
E	Brown	Current, Grid - Phase B	Dsub 2, LEM B	100Ω
F	Grey	Current, Grid - Phase C	Dsub 2, LEM C	100Ω
G	Pink	Voltage, PCC - Phase B	Dsub 3, LEM B	165Ω
H	White	Voltage, PCC - Phase C	Dsub 3, LEM C	165Ω

Acquistion Card 2

Input Channel	Color	Signal	Connected	Rm
A	Green	Voltage, PCC - Phase A	Dsub 3, LEM A	165Ω
B	Pink	Current, Converter - Phase A	Dsub 4, LEM A	100Ω
C	Blue	Current, Converter - Phase B	Dsub 4, LEM B	100Ω
D	Red	Current, Converter - Phase C	Dsub 4, LEM C	100Ω
E	Grey	Current, Load - Phase A	Dsub 5, LEM A	100Ω
F	Brown	Current, Load - Phase B	Dsub 5, LEM B	100Ω
G	White	Current, Load - Phase C	Dsub 5, LEM C	100Ω
H	Orange	Voltage, Converter - DC-Link	Dsub 8, LEM D	165Ω

Signal Mapping - Module: IO106 PMC66 - 16AI64SSA/C

Pin	Single Ended Mode	Pseudo Differential Mode	Differential Mode	Color
1	Input01: Status_From_1 T0	Input (-):	Input01 (+):	Red
2	Input02: Status_From_1 T1	Input01 (+):	Input01 (-):	Green
3	Input03: Status_From_1 T2	Input02 (+):	Input02 (+):	Orange
4	Input04: Status_From_1 T3	Input03 (+):	Input02 (-):	Yellow
5	GROUND - Driver Card 1			Brown
6	Input05: Status_From_2 T0	Input04:	Input03 (+):	Red
7	Input06: Status_From_2 T1	Input05:	Input03 (-):	Green
8	Input07: Status_From_2 T2	Input06:	Input04 (+):	Orange
9	Input08: Status_From_2 T3	Input07:	Input04 (-):	Yellow
10	GROUND - Driver Card 2			Brown
11	Input09: Drivers_From_1 OK	Input08:	Input05 (+):	White
12	Input10: Drivers_From_2_OK	Input09:	Input05 (-):	White
13	Input11:	Input10:	Input06 (+):	
14	Input12:	Input11:	Input06 (-):	
15	GROUND			
16	Input13:	Input12:	Input07 (+):	
17	Input14: **(A1-Dsub8)** Voltage Phase A_Converter 1	Input13:	Input07 (-):	Purple
18	Input15: **(B1-Dsub8)** Voltage Phase B_Converter 1	Input14:	Input08 (+):	Green
19	Input16: **(C1-Dsub8)** Voltage Phase C_Converter 1	Input15:	Input08 (-):	Yellow
20	GROUND			
21	Input17: **(D1-Dsub2)** Current Phase A_Grid	Input16:	Input09 (+):	Blue
22	Input18: **(E1-Dsub2)** Current Phase B_Grid	Input17:	Input09 (-):	Brown
23	Input19: **(F1-Dsub2)** Current Phase C_Grid	Input18:	Input10 (+):	Grey
24	Input20:	Input19:	Input10 (-):	
25	GROUND - Acquisition Card 1			Black
26	Input21: **(A2-Dsub3)** Voltage Phase A_PCC	Input20:	Input11 (+):	Purple
27	Input22: **(G1-Dsub3)** Voltage Phase B_PCC	Input21:	Input11 (-):	Red
28	Input23: **(H1-Dsub3)** Voltage Phase C_PCC	Input22:	Input12 (+):	White
29	Input24:	Input23:	Input12 (-):	
30	GROUND			
31	Input25: **(B2-Dsub4)** Current Phase A_Converter 1	Input24:	Input13 (+):	Green
32	Input26: **(C2-Dsub4)** Current Phase B_Converter 1	Input25:	Input13 (-):	Yellow
33	Input27: **(D2-Dsub4)** Current Phase C_Converter 1	Input26:	Input14 (+):	Blue
34	Input28: **(E2-Dsub5)** Current Phase A_Load	Input27:	Input14 (-):	Brown
35	GROUND - Acquisition Card 2			Black
36	Input29: **(F2-Dsub5)** Current Phase B_Load	Input28:	Input15 (+):	Grey
37	Input30: **(G2-Dsub5)** Current Phase C_Load	Input29:	Input15 (-):	Red
38	Input31: **(H2-Dsub8)** Voltage DC-Link_Converter 1	Input30:	Input16 (+):	White
39	Input32:	Input31:	Input16 (-):	
40	GROUND			

Signal Mapping - Module: IO106 PMC66 - 16AI64SSA/C

Pin	Single Ended Mode	Pseudo Differential Mode	Differential Mode	Color
41	Input33:	Input32:	Input17 (+):	
42	Input34:	Input33:	Input17 (-):	
43	Input35:	Input34:	Input18 (+):	
44	Input36:	Input35:	Input18 (-):	
45	GROUND			
46	Input37:	Input36:	Input19 (+):	
47	Input38:	Input37:	Input19 (-):	
48	Input39:	Input38:	Input20 (+):	
49	Input40:	Input39:	Input20 (-):	
50	GROUND			
51	Input41:	Input40:	Input21 (+):	
52	Input42:	Input41:	Input21 (-):	
53	Input43:	Input42:	Input22 (+):	
54	Input44:	Input43:	Input22 (-):	
55	GROUND			
56	Input45:	Input44:	Input23 (+):	
57	Input46:	Input45:	Input23 (-):	
58	Input47:	Input46:	Input24 (+):	
59	Input48:	Input47:	Input24 (-):	
60	Input49:	Input48:	Input25 (+):	
61	GROUND			
62	Input50:	Input49:	Input25 (-):	
63	Input51:	Input50:	Input26 (+):	
64	Input52:	Input51:	Input26 (-):	
65	Input53:	Input52:	Input27 (+):	
66	Input54:	Input53:	Input27 (-):	
67	GROUND			
68	Input55:	Input54:	Input28 (+):	
69	Input56:	Input55:	Input28 (-):	
70	Input57:	Input56:	Input29 (+):	
71	Input58:	Input57:	Input29 (-):	
72	Input59:	Input58:	Input30 (+):	
73	GROUND			
74	Input60:	Input59:	Input30 (-):	
75	Input61:	Input60:	Input31 (+):	
76	Input62:	Input61:	Input31 (-):	
77	Input63:	Input62:	Input32 (+):	
78	Input64:	Input63:	Input32 (-):	
79	Synch Return			
80	Synch I/O			

Signal Mapping - Module: IO110 TPMC553-10

Pin	Q-DAC	Signal	Colour
1	1	Output01: Contactor 1 Source Send	Blue
2		Output02: Contactor 2 Source Send	Red
3		Output03: "Faulty Channel"	
4		Output04: Engage Coils 1 Send	Blue
5	2	Output05: Engage Coils 2 Send	Red
6		Output06: Emergency Stop Source Send	Green
7		Output07:	
8		Output08:	
9	3	Output09:	
10		Output10:	
11		Output11:	
12		Output12:	
13	4	Output13:	
14		Output14:	
15		Output15:	
16		Output16:	
17	5	Output17:	
18		Output18:	
19		Output19:	
20		Output20:	
21	6	Output21:	
22		Output22:	
23		Output23:	
24		Output24:	
25	7	Output25:	
26		Output26:	
27		Output27:	
28		Output28:	
29	8	Output29:	
30		Output30:	
31		Output31:	
32		Output32:	
33			
34			

Pin	Q-DAC	Signal	Colour
35		Contactor 1 Source Return	Black
36		Contactor 2 Source Return	Black
37		Engage Coils 1 Return	Brown
38		Engage Coils 2 Return	Brown
39		Emergency Stop Source Return	Black
40		GROUND	
41		GROUND	
42		GROUND	
43		GROUND	
44		GROUND	
45		GROUND	
46		GROUND	
47		GROUND	
48		GROUND	
49		GROUND	
50		GROUND	
51		GROUND	
52		GROUND	
53		GROUND	
54		GROUND	
55		GROUND	
56		GROUND	
57		GROUND	
58		GROUND	
59		GROUND	
60		GROUND	
61		GROUND	
62		GROUND	
63		GROUND	
64		GROUND	
65		GROUND	
66		GROUND	
67		GROUND	
68		GROUND	

Signal Mapping - Module: IO203 TPCMC681

	Pin	In	Out	Signal	Colour	Pin	In	Out	Signal	Colour
Lower Channel Group	1		✓	DIO01: Emergency Stop LED	Red	35		✓	DIO02: Emergency Stop LED	Red
	2		✓	DIO03: Contactor Closed_1 LED	Blue	36		✓	DIO04: Contactor Closed_2 LED	Blue
	3		✓	DIO05: Global Enable_1 LED	Yellow	37		✓	DIO06: Global Enable_2 LED	Yellow
	4		✓	DIO07: Drivers OK_1 LED	Orange	38		✓	DIO08: Drivers OK_2 LED	Orange
	5		✓	DIO09: Status_1 T0 LED	Grey	39		✓	DIO10: Status_2 T0 LED	Grey
	6		✓	DIO11: Status_1 T1 LED	Green	40		✓	DIO12: Status_2 T1 LED	Green
	7		✓	DIO13: Status_1 T2 LED	Purple	41		✓	DIO14: Status_2 T2 LED	Purple
	8		✓	DIO15: Status_1 T3 LED	Pink	42		✓	DIO16: Status_2 T3 LED	Pink
	9			GROUND 1	Black	43			GROUND 2	Black
	10			DIO17:		44			DIO18:	
	11			DIO19:		45			DIO20:	
	12			DIO21:		46			DIO22:	
	13			DIO23:		47			DIO24:	
	14			DIO25:		48			DIO26:	
	15			DIO27:		49			DIO28:	
	16			DIO29:		50			DIO30:	
	17			DIO31:		51			DIO32:	
Upper Channel Group	18			DIO33:		52			DIO34:	
	19			DIO35:		53			DIO36:	
	20			DIO37:		54			DIO38:	
	21			DIO39:		55			DIO40:	
	22			DIO41:		56			DIO42:	
	23			DIO43:		57			DIO44:	
	24			DIO45:		58			DIO46:	
	25			DIO47:		59			DIO48:	
	26			GROUND		60			GROUND	
	27			DIO49:		61			DIO50:	
	28			DIO51:		62			DIO52:	
	29			DIO53:		63			DIO54:	
	30			DIO55:		64			DIO56:	
	31			DIO57:		65			DIO58:	
	32			DIO59:		66			DIO60:	
	33			DIO61:		67			DIO62:	
	34			DIO63:		68			DIO64:	

Signal Mapping - Module: IO311 PMC-DX501

Lower Channel Group					
I/O	Pin	In	Out	Signal	Colour
1	1		✓	PWM1 - A: Driver A1+ On	Orange
2	2		✓	PWM1 - B: Driver A1- On	Red
3	3		✓	PWM1 - Trigger:	
4	4		✓	PWM2 - A: Driver B1+ On	Green
5	5		✓	PWM2 - B: Driver B1- On	Yellow
6	6		✓	PWM3 - A: Driver C1+ On	White
7	7		✓	PWM3 - B: Driver C1- On	Grey
8	8		✓	PWM4 - A: Driver A2+ On	Orange
9	9		✓	PWM4 - B: Driver A2- On	Red
10	10		✓	PWM4 - Trigger:	
11	11		✓	PWM5 - A: Driver B2+ On	Green
12	12		✓	PWM5 - B: Driver B2- On	Yellow
13	13		✓	PWM6 - A: Driver C2+ On	White
14	14		✓	PWM6 - B: Driver C2- On	Grey
15	15		✓	PWM7 - A:	
16	16		✓	PWM7 - B:	
	17			Ground Output 1	Brown
	18			Ground Output 2	Brown
17	19		✓	PWM7 - Trigger:	
18	20		✓	PWM8 - A:	
19	21		✓	PWM8 - B:	
20	22		✓	PWM9 - A:	
21	23		✓	PWM9 - B:	
22	24		✓	PWM10 - A:	
23	25		✓	PWM10 - B:	
24	26		✓	PWM10 - Trigger:	
25	27		✓	PWM11 - A:	
26	28		✓	PWM11 - B:	
27	29		✓	PWM12 - A:	
28	30		✓	PWM12 - B:	
29	31		✓	PWM13 - A:	
30	32		✓	PWM13 - B:	
31	33		✓	PWM13 - Trigger:	
32	34		✓	PWM14 - A:	

Upper Channel Group					
I/O	Pin	In	Out	Signal	Colour
	35			GROUND	
	36				
33	37		✓	PWM14 - B:	
34	38		✓	PWM15 - A:	
35	39		✓	PWM15 - B:	
36	40		✓	PWM16 - A:	
37	41		✓	PWM16 - B:	
38	42		✓	PWM16 - Trigger:	
39	43			PWM17 - A:	
40	44			PWM17 - B:	
41	45			PWM18 - A:	
42	46			PWM18 - B:	
43	47		✓	DIO01: Global Enable 1	Black
44	48		✓	DIO02: Global Enable 2	Black
45	49			DIO03:	
46	50			DIO04:	
47	51			DIO05:	
48	52			DIO06:	
49	53			DIO07:	
50	54			DIO08:	
51	55			DIO09:	
52	56			DIO10:	
53	57			DIO11:	
54	58			DIO12:	
55	59			DIO13:	
56	60			DIO14:	
57	61			DIO15:	
58	62			DIO16:	
59	63			DIO17:	
60	64			DIO18:	
61	65			DIO19:	
62	66			DIO20:	
63	67			DIO21:	
64	68			DIO22:	

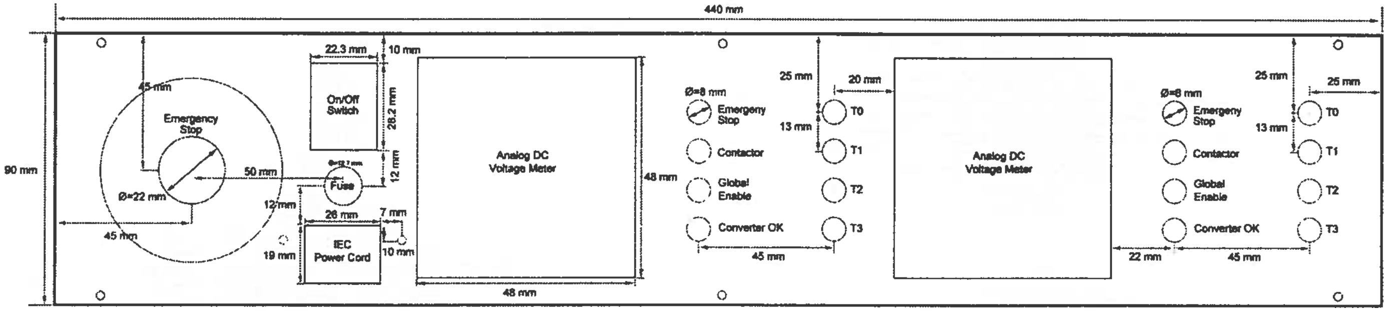
440 mm
90 mm
45 mm
Emergency Stop
Ø=22 mm
45 mm
50 mm
22.3 mm
10 mm
On/Off Switch
28.2 mm
12 mm
Ø=12.7 mm
Fuse
12 mm
26 mm
7 mm
IEC Power Cord
19 mm
10 mm
Analog DC Voltage Meter
48 mm
48 mm
Ø=8 mm
Emergeny Stop
Contactor
Global Enable
Converter OK
25 mm
13 mm
20 mm
T0
T1
T2
T3
45 mm
Analog DC Voltage Meter
22 mm
Ø=8 mm
Emergeny Stop
Contactor
Global Enable
Converter OK
25 mm
13 mm
25 mm
T0
T1
T2
T3
45 mm

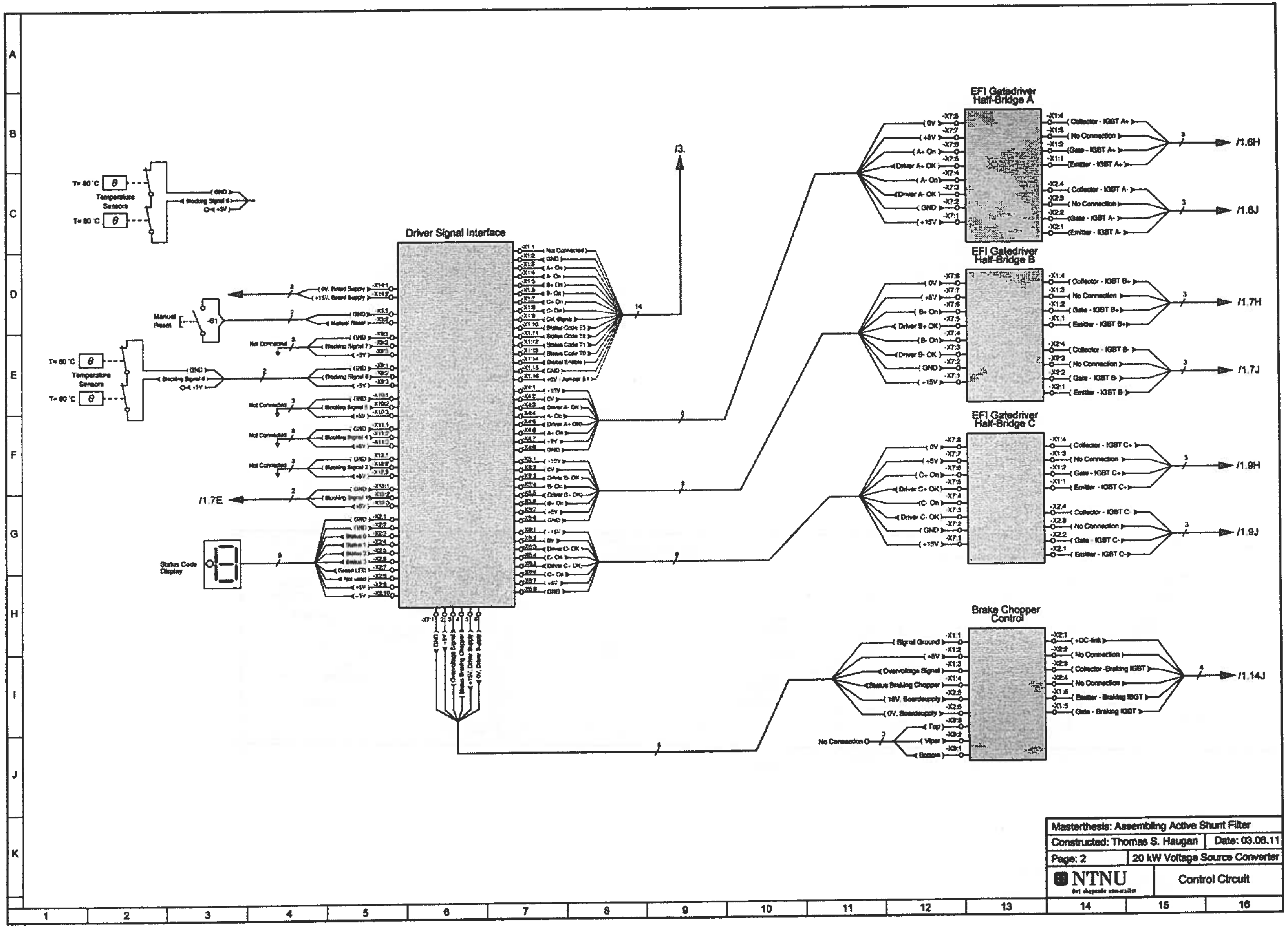

Masterthesis: Assembling Active Shunt Filter
Constructed: Thomas S. Haugan | Date: 03.06.11
Page: 2 | 20 kW Voltage Source Converter
NTNU | Control Circuit

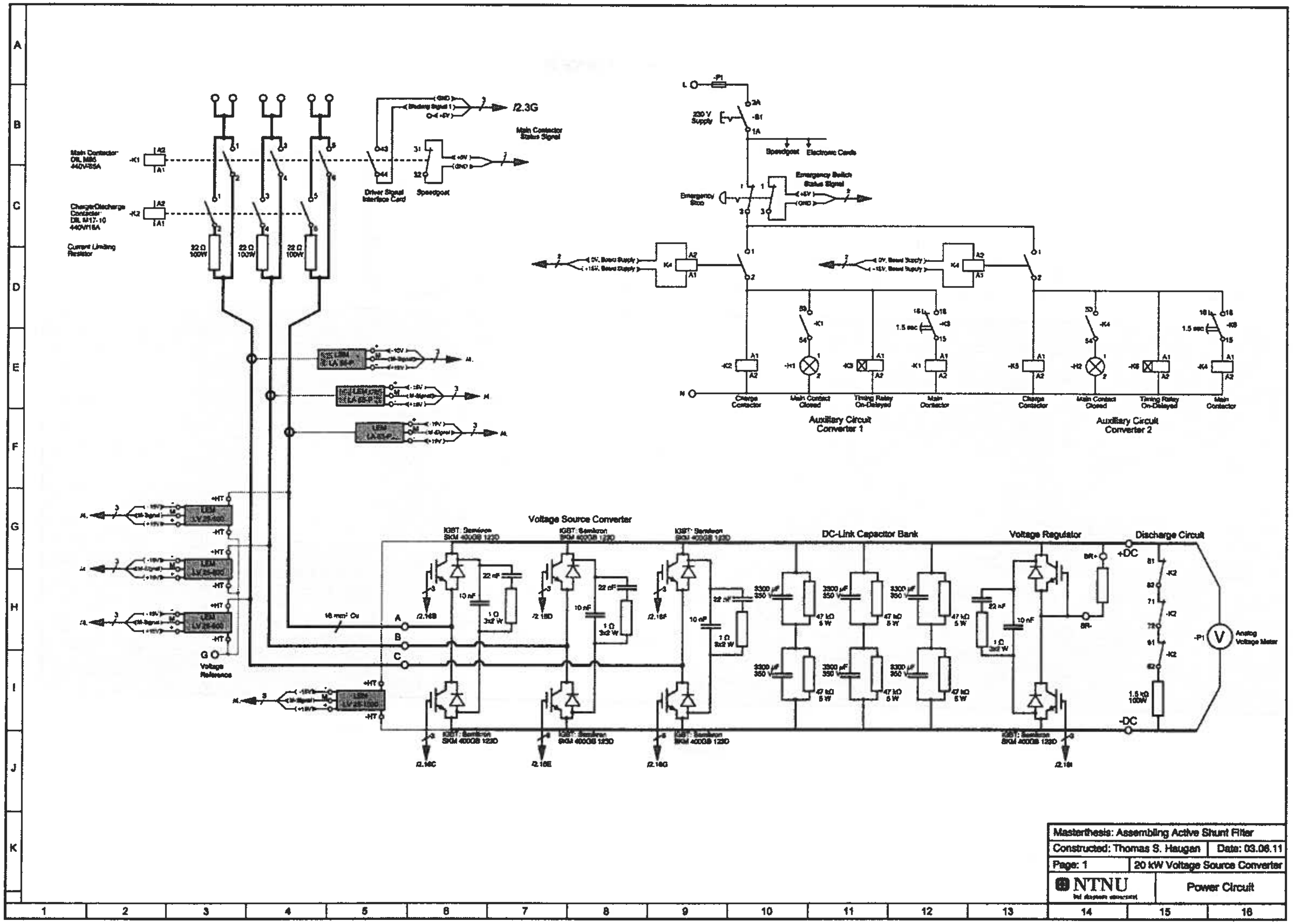

Masterthesis: Assembling Active Shunt Filter
Constructed: Thomas S. Haugan
Date: 03.06.11
Page: 1
20 kW Voltage Source Converter
NTNU
Power Circuit

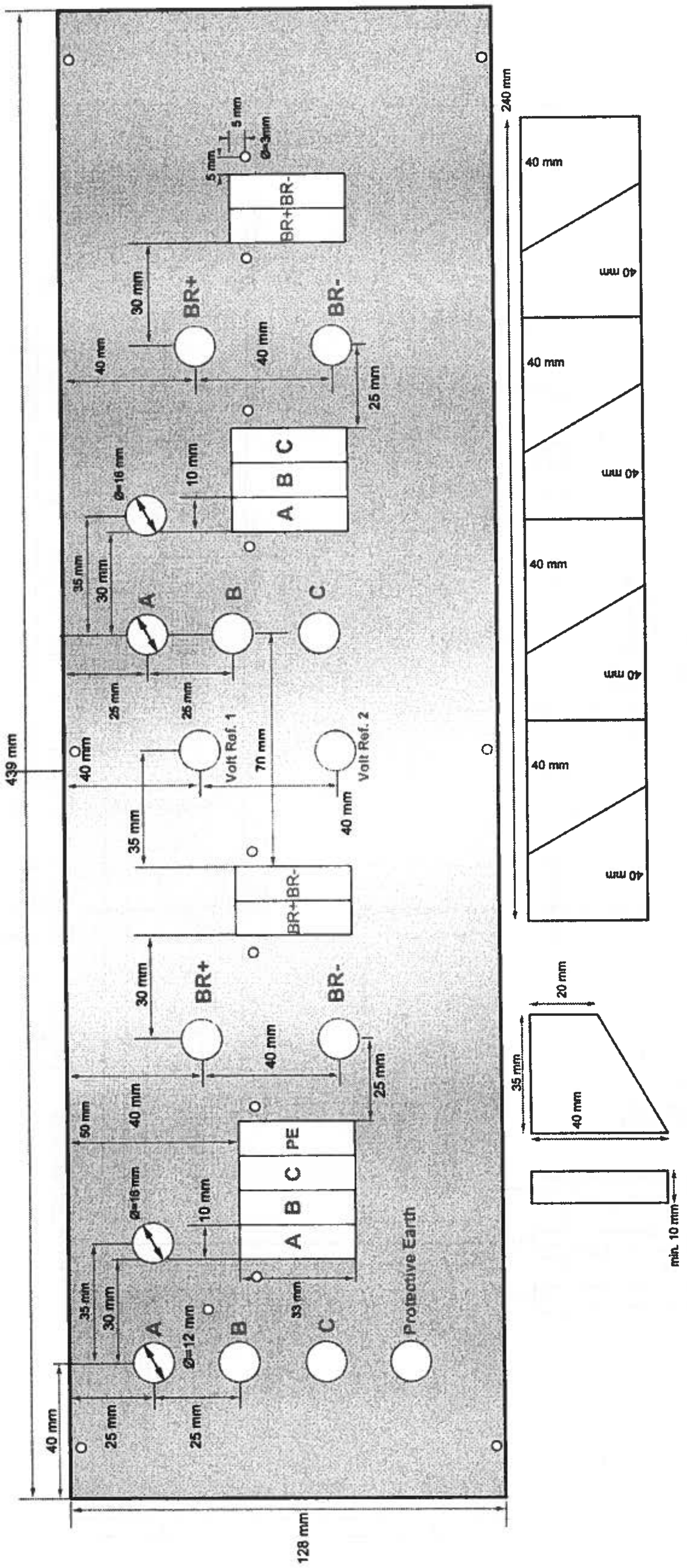
439 mm
128 mm
40 mm
25 mm
25 mm
35 mm
30 mm
A
B
C
Ø=12 mm
Ø=16 mm
10 mm
33 mm
A
B
C
PE
Protective Earth
50 mm
40 mm
BR+
BR-
30 mm
40 mm
25 mm
BR+BR-
35 mm
Volt Ref. 1
Volt Ref. 2
40 mm
70 mm
25 mm
25 mm
35 mm
30 mm
A
B
C
Ø=16 mm
10 mm
A
B
C
40 mm
BR+
BR-
30 mm
40 mm
25 mm
BR+BR-
5 mm
5 mm
Ø=3mm
240 mm
40 mm
40 mm
40 mm
40 mm
40 mm
40 mm
40 mm
40 mm
20 mm
35 mm
40 mm
min. 10 mm

Table B.1 – *List of equipment used during experimental research.*

LAB-No[A]	Equipment	Technical Data
B01-0747	Noratel 3-Ph Transformer [D50]	dYN11-23, $U_{pn}/U_{sn} = 230/400\,V, S_n = 80\,kVA, e_z = 2.96\,\%, e_r = 1.7\,\%, f_n = 47 - 63\,Hz$
B01-0394	Lubecke 3-Ph Variable Transformer	YY0, $U_{pn}/U_{sn} = 230/260\,V, S_n = 7.6\,kVA$
K02-0085	Siemens High-Frequency Inductor	$L = 0.125, 0.50, 2.00\,mH \triangleright I_n = 200, 100, 50\,A, P_n = 2.0\,kVA, f_{max} = 3\,kHz, B_n = 0.5\,T$
K02-0086	Siemens High-Frequency Inductor	$L = 0.125, 0.50, 2.00\,mH \triangleright I_n = 200, 100, 50\,A, P_n = 2.0\,kVA, f_{max} = 3\,kHz, B_n = 0.5\,T$
K02-0090	Siemens High-Frequency Inductor	$L = 0.125, 0.50, 2.00\,mH \triangleright I_n = 200, 100, 50\,A, P_n = 2.0\,kVA, f_{max} = 3\,kHz, B_n = 0.5\,T$
L02-0014	Single-Phase Inductor (NTNU)	$L = 175\,mH, R = 3.0\,\Omega, I_n = 5\,A, f_n = 50\,Hz$
L02-0015	Single-Phase Inductor (NTNU)	$L = 175\,mH, R = 3.0\,\Omega, I_n = 5\,A, f_n = 50\,Hz$
L02-0016	Single-Phase Inductor (NTNU)	$L = 173\,mH, R = 3.0\,\Omega, I_n = 5\,A, f_n = 50\,Hz$
L02-0019	Single-Phase Inductor (NTNU)	$L = 175\,mH, R = 3.5\,\Omega, I_n = 5\,A, f_n = 50\,Hz$
K03-0029	3-Phase Capacitor Bank (NTNU)	3×15 *pcs à* $33\,\mu F, U_n = 450\,V, U_{max} = 640\,V$
K01-0434	Reo Single-Phase Variable Resistor	$R = 0 - 200\,\Omega, I_n = 2\,A$
K01-0443	Reo Single-Phase Variable Resistor	$R = 0 - 200\,\Omega, I_n = 2\,A$
K01-0444	Reo Single-Phase Variable Resistor	$R = 0 - 200\,\Omega, I_n = 2\,A$
K01-0146	Configurable Resistor (NTNU)(See Appendix XX)	$U_{max} = 920\,V, I_{max} = 15.18\,A, P_{max} = 15\,kW, R = 15 - 228\,\Omega$
K01-0149	Configurable Resistor (NTNU)(See Appendix XX)	$U_{max} = 920\,V, I_{max} = 15.18\,A, P_{max} = 15\,kW, R = 15 - 228\,\Omega$
R04-0148	3-Phase Converter switch/charger (NTNU)	Combined diode bridge + soft starter unit $\triangleright U_n = 400\,V, I_n = 63\,A, S_n = 43\,kVA$
R04-0149	3-Phase Converter switch/charger (NTNU)	Combined diode bridge + soft starter unit $\triangleright U_n = 400\,V, I_n = 63\,A, S_n = 43\,kVA$
B03-0258	Single/3-Phase Thyristor Bridge (NTNU)[D44]	Synchronizing unit, gate pulse generator and six thyristors $\triangleright U_n = 600\,V, I_n = 35\,A$
H01-0107	Agilent U1732A Handheld LCR-Meter	Measuring Resistance, Capacitance and Inductance at $f = 100\,Hz, 120\,Hz, 1\,kHz$ and $10\,kHz$
S03-0417	Fluke 177 Digital Multimeter	$V_{max} = 1000\,V, I_{max} = 10\,A, R_{max} = 50\,M\Omega, C_{max} = 1\,mF \triangleright$ AC and DC measurement
S03-0420	Fluke 177 Digital Multimeter	$V_{max} = 1000\,V, I_{max} = 10\,A, R_{max} = 50\,M\Omega, C_{max} = 1\,mF \triangleright$ AC and DC measurement
H02-0124	Fluke 434 3-Ph Digital Power Quality Analyzer[D37]	Waveforms, Phasors, Volts/Amps/Hertz, Dips&Swells, Harmonics, Power Quality&Energy, Flicker, Unbalance
G04-0259	Tektronix TDS 2024B	4-Channel Digital Oscilloscope, 200 MHz Bandwidth, 1 GS/s
G04-0259	Tektronix MSO 2014[D38]	4-Channel Multi Signal Oscilloscope, 100 MHz Bandwidth, 1 GS/s
G04-0356	Tektronix MSO 2014	4-Channel Multi Signal Oscilloscope, 100 MHz Bandwidth, 1 GS/s
P08-0165	Analog Acquisition Card (Midcom/SINTEF)[D36]	4-LEM In/8-analog In,2 relay Out $\triangleright$ Built-in signal conditioning and protection functions
P08-0167	Analog Acquisition Card (Midcom/SINTEF)	4-LEM In/8-analog In,2 relay Out $\triangleright$ Built-in signal conditioning and protection functions
H02-0110	Fluke 43 Single-Phase Power Quality Analysator	Waveforms, Volts/Amps/Hertz, Transients, Power Quality, Harmonics, Sags&Swells
P07-1670	Dell Optiplex 990MT Core™ i5-2400 3.10 GHz[G74][G76]	Host Machine $\triangleright$ Software: Matlab, Simulink, xPC Target, Speedgoat Driver Library, SimPowerSystems
P08-0355	Speedgoat Real-Time Target Machine[D28][D45]	Target Machine $\triangleright$ Intel Core 2 Duo 2.26 GHz, 2048 DDR3 RAM, 32-bit/66 MHz bus, 160GB SATA,BIOS
P08-0361-13	Speedgoat IO110 Analog Output Module[D48]	TEWS Technologies TPMC553 32/16 Channels of 16 Bit D/A
P08-0361-14	Speedgoat IO106 Analog Input Module[D46]	PMC66-16AI64SSA/C 64-Channel, 16-Bit Simultaneous Sampling PMC Analog Input Board
P08-0361-12	Speedgoat IO203 Digital Input/Output Module[D47]	TEWS Technologies TPMC681 64 Digital Inputs/Outputs (Bit I/O)
P08-0361-11	Speedgoat IO311 FPGA Module[D29][D49]	Acromag PMC-DX501/DX2001 - Reconfigurable FPGA With TTL I/O
P08-0354	Speedgoat Electronic Documentation and Software	
P08-0360-06	Speedgoat USB Floppy Disk	
P08-0360-02/03	Speedgoat 68-Pin Cable	
P08-0360-04	Speedgoat 80-Pin Cable	
B03-0440	IGBT Voltage Source Converter (SINTEF/NTNU)[D31][D30]	$P_n = 20\,kW, U_{dc} = 640\,V, I_n = 105\,A, f_s = 0 - 25\,kHz, D = 0 - 100\,\%$, Semikron SKM 400GB 123D IGBTs
P08-0364	PWM Driver Signal Testcard (SINTEF/Midcom)[D34]	Readout of converter PWM-gate pulses via LEDs and tespins
P08-0365	Converter Testcard (SINTEF/Midcom)	Distributing CMOS gatepulses from signal source to VSC to test and verify converter functionality
I04-0477	Fluke 80i-100s Current Clamp	$I_{n1} = 50\,mA - 10\,A, I_{n2}1 - 100\,A$, DC-100 kHz Bandwidth
I04-0376	Fluke 80i-100s Current Clamp	$I_{n1} = 50\,mA - 10\,A, I_{n2}1 - 100\,A$, DC-100 kHz Bandwidth
I04-0375	Fluke 80i-100s Current Clamp	$I_{n1} = 50\,mA - 10\,A, I_{n2}1 - 100\,A$, DC-100 kHz Bandwidth
B02-0478	Traco Power Module TXL 0100-0533T[D43]	DC-Source $\triangleright P_n = 100\,W, V_{in} = 230\,VAC, V_{o1} = +5\,VDC, V_{o2} = +15\,VDC, V_{o1} = -15\,VDC, I_n = 12, 3, 1.5\,A$
B02-0474	Traco Power Module TXL 060-0533	DC-Source $\triangleright P_n = 60\,W, V_{in} = 230\,VAC, V_{o1} = +5\,VDC, V_{o2} = +15\,VDC, V_{o1} = -15\,VDC, I_n = 7, 3, 1\,A$
I06-0492	Tektronix P5200 Differential Voltage Probe	$U_n = 1\,kV_{rms}$ (Differential-CATII), $U_n = 0.6\,kV_{peak+dc}$ (Common-CATIII), 25 MHz Bandwidth
I06-0493	Tektronix P5200 Differential Voltage Probe	$U_n = 1\,kV_{rms}$ (Differential-CATII), $U_n = 0.6\,kV_{peak+dc}$ (Common-CATIII), 25 MHz Bandwidth
I06-0505	Tektronix P5200 Differential Voltage Probe	$U_n = 1\,kV_{rms}$ (Differential-CATII), $U_n = 0.6\,kV_{peak+dc}$ (Common-CATIII), 25 MHz Bandwidth
P08-0368	LEM LV25-600 Hall-Effect Voltage Transducer[D41]	$V_{pn} = 600\,V, V_p = \pm 900\,V, V_d = 4.1\,kV, I_{pn} = 10\,mA \triangleright$ High bandwidth, galvanic isolation
P08-0369	LEM LV25-600 Hall-Effect Voltage Transducer[D41]	$V_{pn} = 600\,V, V_p = \pm 900\,V, V_d = 4.1\,kV, I_{pn} = 10\,mA \triangleright$ High bandwidth, galvanic isolation
P08-0370	LEM LV25-600 Hall-Effect Voltage Transducer[D41]	$V_{pn} = 600\,V, V_p = \pm 900\,V, V_d = 4.1\,kV, I_{pn} = 10\,mA \triangleright$ High bandwidth, galvanic isolation
H02-0107	ELIT SP480 Phase Sequence Meter	$U_n = 110 - 480\,V, f_{max} = 70\,Hz$
P07-1230	Dell OPTIPLEX GX270 Desktop PC	Intel Pentium 4-800 MHz, 4 GB SDRAM, 40GB 5400 RPM, Power Module=250 W Rectifier
P07-1225	Dell OPTIPLEX GX270 Desktop PC	Intel Pentium 4-800 MHz, 4 GB SDRAM, 40GB 5400 RPM, Power Module=250 W Rectifier
P07-0870	Dell OPTIPLEX GX270 Desktop PC	Intel Pentium 4-800 MHz, 4 GB SDRAM, 40GB 5400 RPM, Power Module=250 W Rectifier
P11-0019	Workshop Toolbox	Used during workshop period
P02-0121	Weller WECP-20 Soldering Station	Used during workshop period
P11-0008	Workshop Toolbox	Used during workshop period
P11-0033	Meec Tools 12 V/1.3A Drill 68702	Used during workshop period
P11-0063	XLHD 0560 Crimping Plier	Used during workshop period
P02-0067	PM-1056-D Wire Stripper	Used during workshop period

[A] Detailed technical data for components are available at the institutes online catalogue: `https://tellus.elkraft.ntnu.no/instrumentarkiv/instsokresultat.php` by searching the registration number. Accessing the catalogue is restricted to users with NTNU IP-adresses.

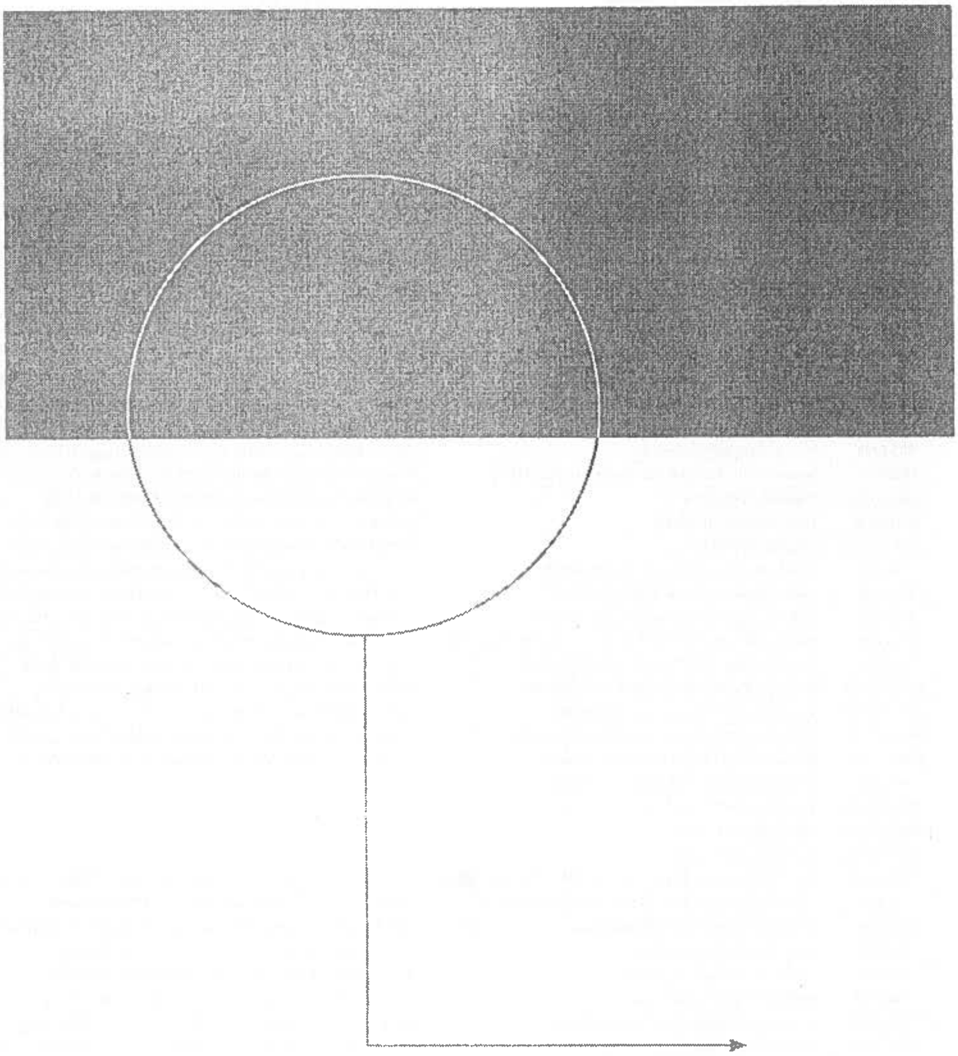

NTNU – Trondheim
Norwegian University of
Science and Technology